U.F.R. Sciences Fondamentales et Appliquées
Laboratoire de Physique des Milieux Denses

Research Center Juelich, Institute of Energy Research (Photovoltaics)

ECOLE DOCTORALE SESAMES

Ph.D. Thesis

written by

Etienne MOULIN

For Awarding the Degree of Doctor of the University Paul Verlaine – Metz
Specialized in the field of **Solid State Physics**

Thin-Film Silicon Solar Cells with Integrated Metal Nanoparticles and Metal Nanostructures for an Enhanced Light Absorption

Impedance Measurements and Simulations of Thin-Film Solar Cells

Ph.D. Thesis defended on the 23rd of February 2009
In presence of the examination committee

U. Kreibig, Professor, University of Aachen	reviewer
S. Siebentritt, Professor, University of Luxembourg	reviewer
A. Slaoui, Professor, InESS-CNRS, Strasbourg	reviewer
O. Pages, Professor, Paul Verlaine University – Metz	examiner
U. Rau, Professor, Research Center Jülich	examiner
F.X. Royer, Professor, Paul Verlaine University – Metz	director of the thesis
H. Stiebig, Doctor, Malibu GmbH & Co. KG	supervisor
J. Sukmanowski, Doctor, Paul Verlaine University – Metz	supervisor

to my parents, Isabelle, Stéphane, Clément, Louise and Jing

Acknowledgements

This study was carried out at the IEF-5 (Institute of Energy Research, Photovoltaics) in the Research Center of Juelich in Germany in collaboration with the Laboratoire de Physique des Milieux Denses of the University of Metz in France and the Institute of Experimental Physics of the Saarland University in Germany. Therefore, I would like to thank the "Region Lorraine" in France and the Research Center Juelich in Germany for their financial support.

I would like to express my gratitude to Prof. Dr. François-Xavier Royer of the University of Metz, to Dr. Joachim Sukmanowski of the Saarland University, to Prof. Dr. Uwe Rau, Dr. Wolfhard Beyer and to my supervisor Dr. Helmut Stiebig of the IEF-5 for having given me the possibility to work on this PhD.

It is a pleasure to offer my sincere thanks to all the people who helped me to carry out this research.

My deepest thanks belong to Dr. Helmut Stiebig for his continuous encouragement and guidance throughout this research. Without his creativeness, his humor, his patience, his many critics, the several Sundays spent together to improve the quality of publications or posters, his contagious passion for solar energy, this work would have been impossible. I have learned many things from him, such as the way of proceeding research and the way of writing publications. Thank you!

I wish to thank Dr. Joachim Sukmanowski for having given me the introduction to the very interesting world of metal nanoparticles. Joachim is also acknowledged for having read and corrected the publications and this manuscript.

I would like to thank Prof. F.X. Royer for his general interest in the work and for having carefully read and corrected this manuscript. F.X. Royer also helped me for the translation of the PhD thesis in French.

I am very grateful to Peiqing Luo for the nice time we had, working together. I thank him for the ideas, interest and technical support he gave me during the last year of my PhD.

I wish to thank Ulrich Paetzold for having performed some of the simulations presented in this work and for having helped me to understand the theory behind plasmonics.

I would like to thank Joachim Kirchhoff, Hilde Siekmann, Wilfried Reetz, Markus Hülsbeck, Andreas Mück, Ralf Schmitz, Jürgen Hüpkes and Hans Peter Bochem for their collaboration and their technical support. I thank them for their professionalism and for their good mood every time I asked depositions or measurements (very often, indeed !).

I would like to extend my thanks to Dr. Reinhard Carius for his general interest in my work, and the helpful discussions, especially on the Raman measurements. I thank Dr. Aad Gordijn for the pieces of advice he gave me concerning the PECVD depositions.

I am very thankful to Prof. Dr. Uwe Kreibig. Uwe Kreibig helped me to improve the quality of this manuscript by giving me clear advices, especially about the theory of metal nanoparticles.
I am grateful to Janine Worbs, Gunnar Schöpe, Alain Doumit, Timo Wätjen and Brigitte Zwaygardt for the depositions of the TCO layers, to Silke Lynen for the depositions of the SiO_2 layers, to Hongbing Zhu and Melanie Schulte for the AFM measurements, to Christoph Zahren for the angle-resolved spectroscopy measurements, to Franz Birmans and Rebecca van Aubel for the help at the sun simulator and to Uwe Zastrow and Astrid Besmehn for the XPS measurements. I would also like to acknowledge Thomas Melle, Sandra Moll, Florian Köhler, Florian Einsele and Frank Pennartz for their technical support.
I am grateful to Andrea Mülheims and Susanne Griesen for the support concerning the administrative things and to Willi Hilgers and Christian Bock for their computing assistance.
I would like to express my great thanks to my colleagues Eerke Bunte, Christian Haase, Kah Yoong Chan, Simonetta Rampu, Toygan Yilmatz, David Wippler and Maurice Nuys for the pleasure I had to share the same office. I thank Eerke and Christian for the introduction they gave me to the fascinating world of photovoltaics and the many illuminating discussions we had together.
I would also like to thank my colleagues of the Saarland University, especially Stefan Griesing and Andreas Englisch, for the discussions. I am grateful to Stefan for having sent me samples and powders of colloids and for having shared his knowledge about the spin coating technique.
I am very thankful to all friends (many are already mentioned before !) I met in Germany and my friends in France for having shared with me the many nice moments of these three last years.
Finally, I thank my parents, my sister and Stéphane who have always been supportive and who have always given me good pieces of advice and helped me to find my way.

Publications related to the thesis

Integration of metallic nanoparticles in thin-film solar cells, E. Moulin, J. Sukmanowski, F.X. Royer, H. Stiebig, 21th European Photovoltaic Solar Energy Conference and Exhibition, Dresden (2006) 1724.

Photodetectors based on amorphous and microcrystalline silicon, H. Stiebig, E. Moulin, B. Rech, Thin Solid Films, Vol. 515 (2007) 7522.

Intégration de nanoparticules métalliques dans des cellules solaires à couches minces, E. Moulin, J. Sukmanowski, F.X. Royer, H. Stiebig, 13^{ième} Colloque National de la Recherche des IUT CNRIUT (2007).

Improved light absorption in amorphous silicon thin-film solar cells by integration of silver nanoparticles and silver nanostructures, E. Moulin, P.Q. Luo, J. Sukmanowski, M. Schulte, F.X. Royer, H. Stiebig, 22nd European Photovoltaic Solar Energy Conference and Exhibition, Milan (2007).

New Management concepts for thin-film silicon solar cells, H. Stiebig, C. Haase, S. Jorke, P. Obermeyer, E. Moulin, M. Schulte, Materials Research Society, Symposium proceedings (2008).

Improved light absorption in thin-film silicon solar cells by integration of silver nanoparticles, E. Moulin, J. Sukmanowski, P.Q. Luo, R. Carius, F.X. Royer, H. Stiebig, Journal of Non-Crystalline Solids, Vol. 354 (2008) 2488.

Thin-film silicon solar cells with integrated silver nanoparticles, E. Moulin, J. Sukmanowski, M. Schulte, A. Gordijn, F.X. Royer, H. Stiebig, Thin Solid Films, Vol. 516 (2008) 6813.

Enhanced infrared response of ultra-thin amorphous silicon photosensitive devices induced by localized surface plasmon, P.Q. Luo, E. Moulin, J. Sukmanowski, F.X. Royer, X.M. Dou, H. Stiebig, Thin Solid Films (2008), *In Process*.

Photoresponse enhancement in the near infrared wavelength range of ultrathin amorphous silicon photosensitive devices by integration of silver nanoparticles, E. Moulin, P.Q. Luo, B. Pieters, J. Sukmanowski, J. Kirchhoff, W. Reetz, T. Müller, R. Carius, F.X. Royer, H. Stiebig, Applied Physics Letters (2008), *In Process*.

Contents

List of Abbreviations

AFM	Atomic Force Microscopy
AM	Air Mass
Arb. u.	Arbitrary unit
a-Si	Amorphous silicon
a-Si:H	Hydrogenated amorphous silicon
ATR	Attenuated Total Reflection
c-Si	Crystalline Silicon
FF	Fill Factor
FWHM	Full Width at Half Maximum
LSP	Localized Surface Plasmon
n-Si	Nanocrystalline Silicon
PDS	Photothermal Deflection Spectroscopy
PECVD	Plasma Enhanced Chemical Vapor Deposition
Poly-Si	Polycrystalline Silicon
RF	Radio-Frequency
RF-PECVD	Radio-Frequency Plasma Enhanced Chemical Vapor Deposition
RT	Room Temperature
QE	Quantum Efficiency
SEM	Scanning Electron Microscopy
SERS	Surface Enhanced Raman Spectroscopy
SP	Surface Plasmon
SR	Spectral Response
SWE	Staebler-Wronski Effect
TCO	Transparent Conductive Oxide
XPS	X-Ray Photoelectron Spectroscopy
µc-Si:H	Hydrogenated microcrystalline silicon

Introduction

Silicon solar cells

Photovoltaic technology offers the possibility of environmentally friendly production of electricity based on an almost infinite source of energy, the sun. Today most commercially available solar cells are made of crystalline or polycrystalline silicon. Such solar cells can achieve efficiencies of up to 24.7 % for unconcentrated light (Green et al., 2006). However, their disadvantages are the high material cost and the high energy consumption during production.

Thin-film silicon solar cells based on hydrogenated amorphous silicon (a-Si:H) and hydrogenated microcrystalline silicon (μc-Si:H) have widely sparked the interest of solar cell manufacturers. The very thin layers constituting the cells (~ 1 μm thick silicon in comparison to hundreds of microns for the wafer-based solar cells) allow a low material consumption. Thin-film silicon technology offers the possibility of large-area in-line processing (modules of up to 1 m² or more). Furthermore, the moderate temperatures (150 – 300 °C) necessary for the production of thin-film silicon solar cells provide a low energy consumption in industrial-scale process and offer the possibility to use a large variety of cheap substrates such as glass, stainless steel and plastic (Deng and Schiff, 2003). As the solar cells are very thin, they can be deposited on a flexible substrate, such as a metal film or a plastic foil. Finally the fact that the integrated series connection is an inherent part of the thin-film module design in contrast to the external line contacts used for crystalline or polycrystalline silicon based modules considerably simplifies the manufacturing process. A disadvantage of the a-Si:H technology is the relatively low efficiency and the light induced degradation of a-Si:H material which leads to a decrease of the initial cell efficiency. Stable efficiencies in the range of 4 – 6 % are generally achieved for single-junction a-Si:H *modules* (Shah et al., 1999). The concept of stacked cells (also called multi-junction cells) is a powerful concept which permits to enhance the cell stability due to the thinner applied layers. Moreover it allows to improve the cell efficiency. Stacked cells consist of two (tandem cells) or more (e.g. triple cells) single cells based on a-Si:H, μc-Si:H or a-Si:H alloys deposited on top of each other. The highest stable efficiency so far using a-Si:H/μc-Si:H tandem structure is 12% for a *cell* made at the University of Neuchatel (Meier et al, 1998). Stabilized efficiencies of more than 13% have been reported (Yang et al., 1997) for e.g. triple-junction a-Si:H alloys solar *cells* (a-Si:H/a-Si:Ge:H/a-Si:Ge:H). However the general objective of the thin-film silicon solar cell

manufacturers is to obtain stable *module* efficiencies larger than 10%. Sharp already commercializes a-Si:H/µc-Si:H tandem *modules* with stable efficiency of 8.5% [1]. United Solar has reported a stable efficiency of 10.5% for small *modules* (0.09 m²) consisting of a-Si:H/a-Si:Ge:H/a-Si:Ge:H (Banerjee et al., 1999).

Motivation of the work

The optimization of the thin-film silicon solar cell performances in combination with a reduction of the production costs remains a key issue for the industrial production. In order to achieve high efficiencies, thin-film silicon solar cells need an efficient light absorption. The most efficient a-Si:H and µc-Si:H solar cells produced today are based on a light-trapping approach which consists of a randomly textured transparent substrate and a highly reflective back contact (Springer et al., 2005). With such light-trapping schemes, light scattered at the rough TCO-silicon interface leads to a prolonged absorption path in the active layer of the cell and consequently results in an increased short-circuit current. Finding new structures or optical concepts as alternative approaches for light trapping in solar cells is a great challenge. In this work, we propose to use metal nanoparticles to enhance the light absorption in thin-film silicon solar cells.

Recently, metal nanoparticles have attracted the attention of the research community, due to their particular optical properties. The origin of their surprising optical behavior was only understood in the 19th century by Faraday (1857). In the 20th century, Mie (1908) calculated the optical response of a spherical nanoparticle in interaction with an incoming electromagnetic wave. Nowadays new optical properties of the metal nanoparticles have been found. The possibility to modify them by changing their structure and environment are at the base of the very broad interest they cause. Metal nanoparticles find an application in a large number of domains such as chemical and biological sensing (Haes and Van Duyne, 2004; Ji et al., 2005), linear and non-linear optics, polarizers (Dirix et al., 1999), nano-optics, optical commutation, optical filtering, photodetectors (Stuart and Hall, 1998), light-emitting diodes (Pillai et al., 2006; Catchpole and Pillai, 2006) and finally solar cells.

The specific optical properties of metal nanoparticles are a consequence of the appearance of a resonance in their absorption and scattering spectra, known as the localized surface plasmon (LSP) resonance. The LSP resonance is due to the collective oscillation of free electrons in the metal. The LSP resonance of small (< 20 nm) silver and gold nanoparticles in air is located in the blue at around 350 nm and in the green at around 520 nm, respectively (Kreibig and Vollmer, 1995). This leads to yellowish and red colourings of small silver and gold nanoparticles in air, respectively. In this thesis, we discuss new approaches based on metal nanoparticles and metal nanostructures for light trapping in thin-film silicon solar cells. The

first approach is based on the strongly enhanced electromagnetic field present in the vicinity of small metal nanoparticles (< 50 nm) when they are irradiated by light of wavelength close to the LSP excitation wavelength. The second approach consists of making use of the light scattering properties of large metal nanoparticles (> 50 nm) and metal nanostructures.

Two approaches for enhancing the light absorption in thin-film silicon solar cells

The *electromagnetic field enhancement* approach

For sufficiently small particles (< 50 nm), the LSP absorption is accompanied by a strong enhancement of the electromagnetic field inside and in the surrounding of the nanoparticles. The first part of this work is motivated by the utilization of this enhanced electromagnetic field. In this approach, we target to confine the light in the active layer of thin-film silicon solar cells. Since the enhanced electromagnetic field is localized in the close vicinity of the nanoparticles, this concept would in addition to the improved light absorption allow to reduce the thickness of the active layer of solar cells (i.e. reduce the silicon consumption) and consequently lower the manufacturing costs.

The existence of a strong electromagnetic field enhancement associated to the LSP is demonstrated by the increased signals found in surface enhanced Raman spectroscopy (SERS) (Nie and Emory, 1997; Kneipp et al., 1997) and scanning near field optical microscopy (SNOM) (Genov et al., 2003; Grésillon et al., 1999 and 2000; Wiederrecht, 2004). Recently, several authors have reported enhancements of the photovoltaic conversion efficiency of organic and dye-sensitized thin-film solar cells by making use of the LSP of metal nanoparticles with diameter smaller than 50 nm (Westphalen et al., 2000; Stenzel et al. 1995; Wen et al., 2000; Rand et al., 2004). The enhanced photocurrent is explained in terms of (i) an improved light absorption in the absorber layer of the cell, due to an enhanced electromagnetic field in the vicinity of the nanoparticles at the LSP resonance or (ii) photoemission from the nanoparticles to their surrounding due to an enhanced electromagnetic field inside the nanoparticles. The positive contribution of surface plasmons (SP) on the photocurrent of inorganic semiconductor/metal Schottky junctions has also been reported by using the method of attenuated total reflection (ATR) (Daboo et al., 1991). In this experiment, the enhanced photocurrent is also explained in terms of photoexcitation of electrons from the metal surface to the semiconductor at the SP resonance.

The *light scattering* approach

The second approach is based on the light scattering of large metal nanoparticles or metal nanostructures. The scattering cross section of metal nanoparticles increases rapidly with their diameter (van Dijk et al., 2006). This effect makes them attractive for photodetectors (Stuart and Hall, 1998), solar cells and light-emitting diodes (Pillai et al., 2006; Catchpole and Pillai, 2006). Several authors have made use of the scattering properties of large metal nanoparticles (~ 100 nm) – deposited on top of c-Si and a-Si:H solar cells – to improve the light in-coupling at the front side of the cells and/or enhance the light path within the cells (Derkacs et al., 2006; Schaadt et al., 2005; Pillai et al., 2006 and 2007). In this work, a different approach is investigated since the nanoparticles (and nanostructures) are introduced at the rear side of the solar devices.

Organization of the thesis

This thesis is organized as follows:

- In Chapter 1, we briefly review the fundamentals of plasmonics of single metal nanoparticles.
- In Chapter 2, we describe the deposition systems and preparation conditions used for the metal nanoparticles, metal nanostructures, samples and solar cells presented in this work. In parallel we discuss the structural and optical properties of the deposited layers and we explain the working principle of thin-film silicon solar cells.
- Chapter 3 presents the main characterization methods used throughout this work and their physical background. These are measurements of the current-voltage characteristics in the dark and under illumination, quantum efficiency, angle-resolved distribution, Raman spectroscopy, etc.
- The experimental results start in Chapter 4. We discuss the structural and optical properties of metal films thinner than 10 nm (necessary to obtain nanoparticles or other metal structures) consisting of Ag, Au or Al deposited on various substrates such as a-Si:H, ZnO:Al and c-Si. The structure and the optical response of the deposited metal films before and after an annealing treatment and for different embedding media are investigated.
- In Chapter 5, we present the optoelectronic properties of a-Si:H solar cells and ultra-thin photosensitive devices integrating silver nanoparticles of diameter below 35 nm.
- In Chapter 6, we investigate the optical properties of large nanoparticles (Ø > 50 nm) in order to find an optimum in terms of light scattering. The nanoparticles are

incorporated at the rear side of μc-Si:H and a-Si:H solar cells in the n-i-p configuration. We demonstrate their positive contribution to the light trapping and discuss their impact on the electrical properties.

- In Chapter 7, we show the optoelectronic properties of μc-Si:H and a-Si:H solar cells in the n-i-p configuration deposited on a so-called nanostructured Ag back reflector. The results are compared with those obtained for cells deposited on a standard textured surface.
- In parallel to the study of the integration of metal nanoparticles and metal nanostructures in thin-film silicon solar cells, a second independent study was conducted: the investigation of the dynamic properties of thin-film silicon solar cells by means of impedance measurements. The results of this study are summarized in Chapter 8.
- We close the thesis by drawing the main conclusions of the work.

Chapter 1

Optical properties of metal nanoparticles: fundamentals

In this chapter we present the fundamentals of the optical response of metal nanoparticles. Firstly, we give a simple description of the interaction of light with metal nanoparticles. Afterwards, we introduce the quasi-static field approximation, valid for describing the optical response of nanoparticles with radius much smaller than the excitation wavelength ($R \leq 0.01\lambda$). With this approach, we determine the condition to obtain localized surface plasmons. A solution of the optical behavior of ellipsoidal nanoparticles is also presented. Then we introduce the Mie theory which can, in contrast to the quasi-static field approximation, be used for spherical particles of any size. In the last part of this chapter, we define and analyse the dielectric functions of bulk metal and metal nanoparticles.

1.1 Simple semi-classical model

A simple semi-classical model to understand the interaction of light with a spherical metal nanoparticle is illustrated in Fig. 1.1. The electromagnetic wave penetrating the particle induces an oscillation of the electronic cloud, i.e. conduction electrons will oscillate at the optical frequency with respect to the positive charge of the lattice ions, creating an oscillating charge at the particle surface. This charge will result in a restoring force inside the nanoparticle. If the frequency of excitation light is in resonance with the eigenfrequency of the collective oscillation, even a small exciting field will induce a strong oscillation. The restoring force is mainly determined by the distance between the surface charges (i.e. the particle size), the polarizability of the conduction electrons and the polarizability of the embedding medium. For nanoparticles with radius much smaller than the excitation wavelength, the alternating surface charges form an oscillating dipole which can be associated with strong field enhancements inside and in the close vicinity of the particle. The nanoparticle then behaves as an “optical antenna”.

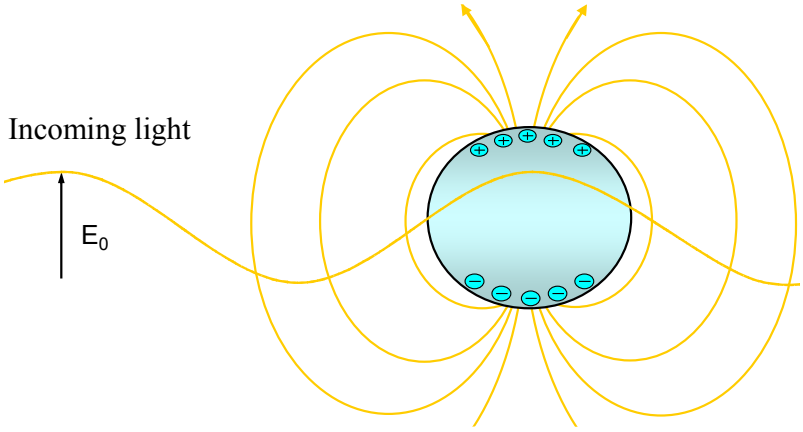

Figure 1.1 : Illustration of the interaction of an electromagnetic wave with a spherical metal nanoparticle in the semi-classical approach.

1.2 Quasi-static optical response of a small sphere

1.2.1 Introduction

The most convenient geometry for describing the optical response of a particle is the case of a homogeneous and isotropic sphere of radius R, where R is much smaller than the wavelength λ of the incoming light. Indeed, for $R \leq 0.01\lambda$, the optical response of a particle can be calculated in the *quasi-static regime* approximation. In this approach, the phase of the harmonically oscillating electromagnetic field is considered as constant over the particle volume. Therefore, one can calculate the spatial field distribution by assuming the simplified problem of a particle in an electrostatic field. The harmonic time dependence can be added to the solution when the field distributions are known. In this case the electrostatic field is considered to vary at a frequency equal to the light frequency. For visible light the quasi-static regime refers to nanoparticle sizes $R \leq$ 5 nm (Kreibig and Vollmer, 1995). For larger particle sizes, retardation effects of the electromagnetic field over the particle diameter become significant and the problem has to be solved using Mie theory. However, in practice, the quasi-static regime approximation describes the optical properties of nanoparticles of dimensions below 20 nm adequately for many purposes (Maier, 2007).

1.2.2 Determination of the localized surface plasmon resonance of a spherical metal nanoparticle

We assume that a sphere of radius R << λ is located at the origin in a uniform, static electric field E_0 along the z axis (Fig. 1.2). The surrounding medium is isotropic and non-absorbing with dielectric constant ε_m. The optical response of the sphere is described by the complex dielectric function (or optical function) $\varepsilon = \varepsilon_1 + i\varepsilon_2$, connected to the complex index of refraction by $n + ik = \sqrt{\varepsilon}$.

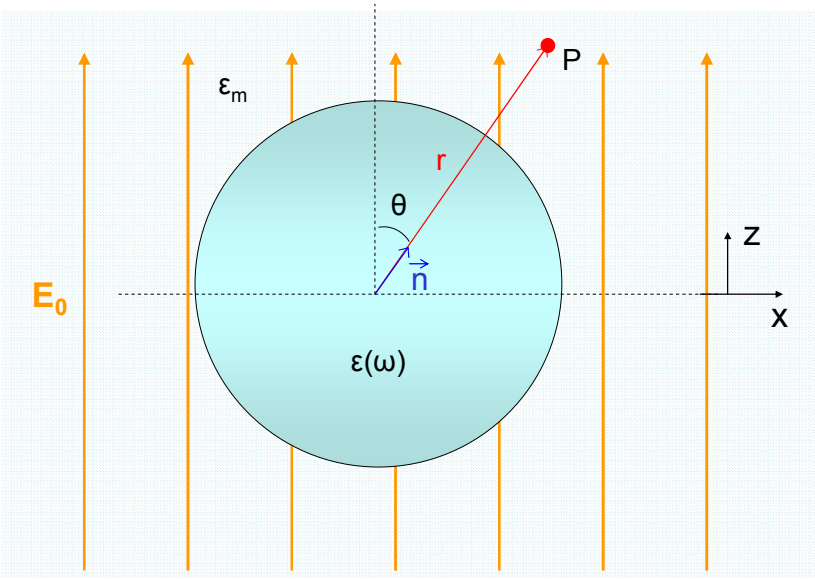

Figure 1.2 : Schematic drawing of the interaction of a spherical particle with an electromagnetic wave in the quasi-static regime approximation.

In the electrostatic approach, we should first solve the Laplace equation of the potential, $\nabla^2\Phi = 0$. The electric field can then be determined using the relation $\vec{E} = -\nabla\Phi$. The general solution is of the form (Jackson, 1999) :

$$\Phi(r,\theta) = \sum_{l=0}^{\infty}[A_l r^l + B_l r^{-(l+1)}]P_l(\cos\theta) \qquad (1.1)$$

where $P_l(\cos\theta)$ are the Legendre Polynomials of order l, and θ is the angle between the position vector r at point P and the z-axis (Fig. 1.2). Due to the boundary condition that the potential remains finite at the origin, the solution for the potentials Φ_{in} inside and Φ_{out} outside the sphere can be written as :

$$\Phi_{in}(r,\theta) = \sum_{l=0}^{\infty} A_l r^l P_l(\cos\theta) \tag{1.2a}$$

$$\Phi_{out}(r,\theta) = \sum_{l=0}^{\infty} [B_l r^l + C_l r^{-(l+1)}] P_l(\cos\theta) \tag{1.2b}$$

Application of the boundary conditions of the tangential component of $\vec{E}$ and the normal component of the displacement at the surface of the sphere leads to :

$$\Phi_{in} = -\frac{3\varepsilon_m}{\varepsilon + 2\varepsilon_m} E_0 r \cos\theta \tag{1.3a}$$

$$\Phi_{out} = -E_0 r \cos\theta + \frac{\varepsilon - \varepsilon_m}{\varepsilon + 2\varepsilon_m} E_0 R^3 \frac{\cos\theta}{r^2} \tag{1.3b}$$

Φ_{out} describes the superposition of the applied field and that of a dipole located at the particle center. Therefore, Φ_{out} can also be written as :

$$\Phi_{out} = -E_0 r \cos\theta + \frac{\vec{p}\cdot\vec{r}}{4\pi\varepsilon_0\varepsilon_m r^3} \tag{1.4a}$$

$$\vec{p} = 4\pi\varepsilon_0\varepsilon_m R^3 \frac{\varepsilon - \varepsilon_m}{\varepsilon + 2\varepsilon_m} \vec{E}_0 \tag{1.4b}$$

where $\vec{p}$ denotes the dipole moment. If we introduce the polarizability α, defined by $\vec{p} = \varepsilon_0\varepsilon_m\alpha\vec{E}_0$, we obtain for α :

$$\alpha = 4\pi R^3 \frac{\varepsilon - \varepsilon_m}{\varepsilon + 2\varepsilon_m} \tag{1.5}$$

The distribution of the electric field $\vec{E} = -\nabla\Phi$ can be determined by the derivation of equations 1.3 :

$$\vec{E}_{in} = -\frac{3\varepsilon_m}{\varepsilon + 2\varepsilon_m} \vec{E}_0 \tag{1.6a}$$

$$\vec{E}_{out} = \vec{E}_0 + \frac{3\vec{n}(\vec{n}\cdot\vec{p}) - \vec{p}}{4\pi\varepsilon_0\varepsilon_m} \frac{1}{r^3} \tag{1.6b}$$

$\vec{n}$ denotes the unit vector in the direction of the point P of interest (see Fig. 1.1).

These solutions of electrostatics can also be applied to small metal spheres in oscillating electromagnetic fields in the quasi-static regime. In this approach the spheres feel a field with spacially constant – though time dependent – phase. Since ε_m is generally taken as a real

constant, only ε has to be replaced by its frequency dependent value $\varepsilon(\omega)$. Both internal and dipolar electric fields experience a resonance, referred to as *localized surface plasmon* (or *dipolar surface plasmon*) resonance when :

$$\left|\varepsilon(\omega) + 2\varepsilon_m\right| = \text{Minimum}, \tag{1.7a}$$

$$\text{i.e. } \left[\varepsilon_1(\omega) + 2\varepsilon_m\right]^2 + \left[\varepsilon_2(\omega)\right]^2 = \text{Minimum} \tag{1.7b}$$

A negative ε_1 is necessary to obtain the localized surface plasmon resonance. This condition can be achieved for metals (see Fig. 1.8 and Fig. 1.9).

For a small or slowly-varying Im[ε] around the resonance, equation 1.7b simplifies to :

$$\text{Re}[\varepsilon(\omega)] = -2\varepsilon_m \tag{1.8}$$

In this case metal nanoparticles exhibit a strong and sharp increase in the light absorption at the localized surface plasmon resonance. The resonant increase in the absorption is accompanied by a strong enhancement of the electric field inside and in the close vicinity of the metal nanoparticle. The field enhancement in the surrounding of the nanoparticle at the localized surface plasmon resonance is addressed by this work to improve the light absorption in thin-film silicon solar cells.

If $\varepsilon_2(\omega) \neq 0$ or ε_2 strongly varies close to the resonance, the internal and external electric fields and the light absorption in the nanoparticle at the localized surface plasmon resonance will be limited by the incomplete vanishing of the term $|\varepsilon(\omega) + 2\varepsilon_m|$.

Equation 1.8 further expresses the strong dependence of the resonance frequency on the dielectric environment. A red-shift of the resonance occurs when ε_m is increased. Thus metal nanoparticles are ideal detectors for optical sensing of changes in refractive index of their surrounding medium. Fig. 1.3 illustrates the dependency of the shape and position of the LSP resonance of small Ag nanoparticles (R=10 nm) on the refractive index *n* of the embedding medium. The optical response of the nanoparticle is calculated in a wavelength range which is relevant for thin-film silicon solar cells. It is expressed in terms of extinction cross section. This parameter corresponds to the sum of both absorption and scattering contributions (see section 1.2.4). The calculations are performed for n = 1, n = 2 and n = 3.6 (after Mie theory, see section 1.3). These values correspond to the refractive indices of air, TCO (ZnO:Al) and a-Si:H, respectively. In reality, the refractive indices of TCO and a-Si:H vary in the investigated range. However the utilization of approximated values already provides a good estimation of the expected effect of these two media on the optical response of nanoparticles. Calculations of Ag nanoparticles of radius 10 nm embedded in air show a LSP resonance at 350 nm. For nanoparticles embedded in TCO, the resonance is red-shifted from 350 nm to 480 nm and the full width at half maximum (FWHM) of the peak broadens from 10 nm to

18 nm. Ag nanoparticles embedded in a-Si:H exhibit a resonance at around 780 nm with FWHM of 24 nm.

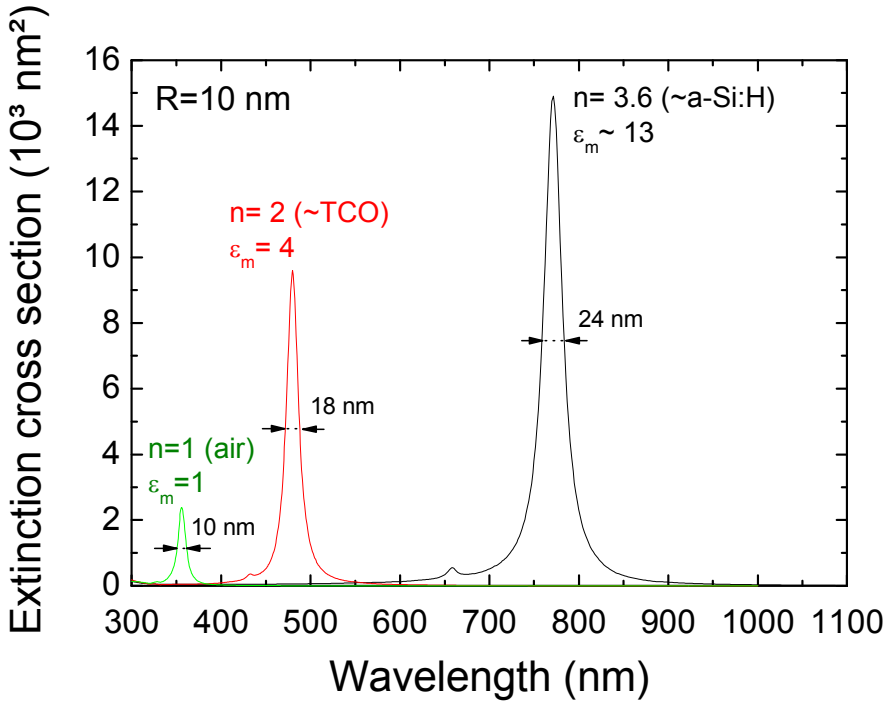

Figure 1.3 : Calculated extinction cross section (absorption + scattering) as function of wavelength for Ag nanoparticles with 10 nm radius embedded in various embedding media (air : n=1; TCO : n=2 and a-Si:H : n=3.6), after Mie theory (see section 1.3). The dielectric constants given by Johnson and Christy (1972) are used for Ag.

The localized surface plasmons introduced above and discussed in the context of this work should in fact be referred to as *localized surface plasmon polaritons* because they are coupled to the outer electromagnetic field and they are different from free plasmons in nanoparticles excited e.g. by fast electrons (Kreibig and Vollmer, 1995). The resonance energies of the free plasmons are for example almost independent of cluster size whereas excitation with light shows phase retardation effects for large particles. Since the distinction between localized surface plasmons and localized surface plasmon polaritons is not central in this work we will use the term *localized surface plasmons* to refer to the coupled excitations of metal nanoparticles.

1.2.3 Electromagnetic fields radiated by a small particle

In the quasi-static regime approximation, a small sphere with radius $R << \lambda$ can be represented as an ideal dipole. Under plane-wave illumination with $\vec{E}(r,t) = \vec{E}_0 e^{-i\omega t}$, the fields induce an oscillating dipole moment $\vec{p}(t) = \varepsilon_0 \varepsilon_m \alpha \vec{E}_0 e^{-i\omega t}$, with α given by equation 1.5. In the near zone ($kr << 1$) of the particle – considered here as a point dipole – the electric and magnetic fields are given by :

$$\vec{E} = \frac{3\vec{n}(\vec{n}\cdot\vec{p}) - \vec{p}}{4\pi\varepsilon_0\varepsilon_m} \cdot \frac{1}{r^3} \tag{1.9a}$$

$$\vec{H} = \frac{i\omega}{4\pi}(\vec{n}\times\vec{p})\frac{1}{r^2} \tag{1.9b}$$

with $k = 2\pi/\lambda$ and $\vec{n}$ the unit vector in the direction of the point P of interest.

We can notice that equation 1.9a is similar to the second term in equation 1.6b. In the near zone of the particle, the fields are predominantly electric in nature, since the magnitude of the magnetic field is about a factor $\sqrt{\varepsilon_0/\mu_0}\,(kr)$ smaller than that of the electric field. For static fields ($kr \to 0$), the magnetic field vanishes.
For $kr >> 1$ (far field), i.e. in the opposite limit of the radiation zone, the dipole fields are of the spherical-wave form :

$$\vec{H} = \frac{ck^2}{4\pi}(\vec{n}\times\vec{p})\frac{e^{ikr}}{r} \tag{1.10a}$$

$$\vec{E} = \sqrt{\frac{\mu_0}{\varepsilon_0\varepsilon_m}}\vec{H}\times\vec{n} \tag{1.10b}$$

1.2.4 Absorption, scattering and extinction cross sections of a small particle

Independently of the particle size, both absorption and scattering (and thus extinction: extinction = absorption + scattering) are strongly enhanced at the localized surface plasmon resonances (Kreibig and Vollmer, 1995). This is revealed by the equations 1.11 (in the case of small nanoparticles). The corresponding cross sections C_{sca} and C_{abs} for scattering and absorption of small nanoparticles can be calculated by the Poynting-vector $\vec{S} = \vec{E}\times\vec{H}$ determined from the equations 1.9 (Bohren and Huffman, 1983) :

$$C_{sca} = \frac{k^2}{6\pi}|\alpha|^2 = \frac{8\pi}{3}k^4R^6\left|\frac{\varepsilon-\varepsilon_m}{\varepsilon+2\varepsilon_m}\right|^2 \quad (1.11a)$$

$$C_{abs} = k\,\mathrm{Im}[\alpha] = 4\pi kR^3\,\mathrm{Im}\left[\frac{\varepsilon-\varepsilon_m}{\varepsilon+2\varepsilon_m}\right] \quad (1.11b)$$

For a sphere of volume V and dielectric function $\varepsilon = \varepsilon_1 + i\varepsilon_2$ in the quasi-static limit, the extinction cross section $C_{ext} = C_{abs} + C_{sca}$ is thus given by :

$$C_{ext} = 9\frac{\omega}{c}\varepsilon_m^{3/2}V\frac{\varepsilon_2}{[\varepsilon_1+2\varepsilon_m]^2+\varepsilon_2^2} \quad (1.12)$$

According to the expressions for C_{sca} and C_{abs} of small particles with $R << \lambda$, the efficiency of absorption (~R^3) dominates over the scattering efficiency (~R^6).

1.2.5 Localized surface plasmon resonance of a non-spherical metal nanoparticle

The electrostatic theory for light scattering by spherical particles with diameters much smaller than the excitation wavelength can be extended to ellipsoidal particles which represent a more general case. Ellipsoidal particles are defined by the three semiaxes $a_1 \le a_2 \le a_3$, specified by $\frac{x^2}{a_1^2}+\frac{y^2}{a_2^2}+\frac{z^2}{a_3^2}=1$ (Fig. 1.4). According to Bohren and Huffman (1983), the expression of the polarizabilities α_i along the principal axes (i=1, 2, 3) is:

$$\alpha_i = 4\pi a_1a_2a_3\frac{\varepsilon(\omega)-\varepsilon_m}{3\varepsilon_m+3L_i(\varepsilon(\omega)-\varepsilon_m)} \quad (1.13)$$

L_i is a geometrical factor related to the shape of the particle given by :

$$L_i = \frac{a_1a_2a_3}{2}\int_0^\infty \frac{dq}{(a_i^2+q)f(q)} \quad (1.14)$$

where $f(q) = \sqrt{(q+a_1^2)(q+a_2^2)(q+a_3^2)}$ and such as $\sum L_i = 1$.

For a sphere $L_1 = L_2 = L_3$ is equal to $\frac{1}{3}$. In this case equation 1.13 eases to equation 1.5. As an alternative, the polarizability of ellipsoids is also often expressed in terms of the *depolarization factors* $\tilde{L}_i$, defined via $E_{1i} = E_{0i} - \tilde{L}_i P_{1i}$, where E_{1i} and P_{1i} are the electric field and polarization induced inside the particle by the applied field E_{0i} along a principal axis *i*, respectively. $\tilde{L}$ is linked to *L* via :

$$\tilde{L}_i = \frac{\varepsilon - \varepsilon_m}{\varepsilon - 1} \frac{L_i}{\varepsilon_0 \varepsilon_m} \tag{1.15}$$

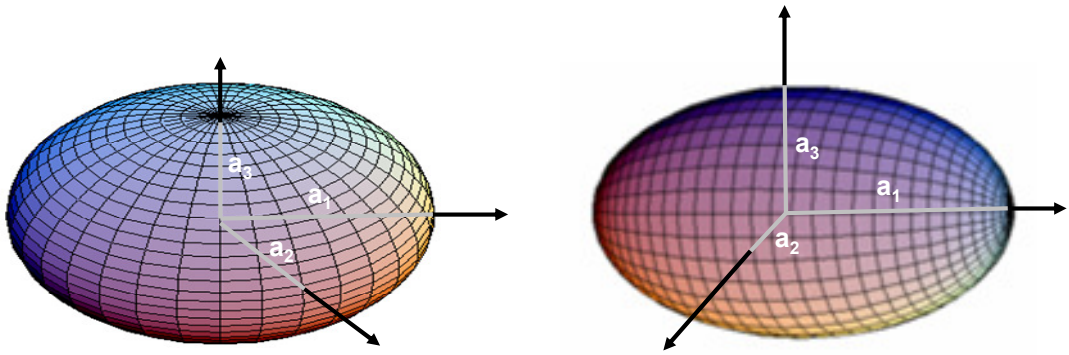

Figure 1.4 : Oblate spheroid (left) and prolate spheroid (right).

Of particular interest is the case of *spheroids*, where two of the three axes of the ellipsoid have identical length. *Oblate spheroids* have their two major axis equal $(a_1 = a_2 > a_3)$ and *prolate spheroids* have their two minor axis of same size $(a_1 > a_2 = a_3)$ (cigar-shaped), as illustrated in Fig. 1.4. Equation 1.13 reveals that a spheroidal metal nanoparticle exhibits two spectrally separated localized surface plasmon resonances, corresponding to oscillations of its conduction electrons along the major or minor axis, respectively. Due to oscillations along the major axis the plasmon resonance can significantly be red-shifted in comparison to the resonance of a sphere of the same volume. Thus, localized surface plasmon resonances are shifted in the near-infrared region using metal nanoparticles with small aspect ratio. However, equation 1.13 can only be used as long as the major axis is much smaller than the wavelength of the incoming light.

Most of the nanoparticles prepared in this work exhibit an oblate shape. If we consider $a_1 = a_2 = a$, $a_3 = b$ and $x = b/a$, we can write :

$$L_1 = L_2 = \frac{x}{2}\left[\frac{\frac{\pi}{2} - \arctan\left(\frac{x}{\sqrt{1-x^2}}\right)}{\left(1-x^2\right)^{3/2}}\right] + \frac{x^2}{2(x^2-1)} \tag{1.16a}$$

$$\text{and } L_3 = \frac{x}{2}\left[\frac{2\arctan\left(\frac{x}{\sqrt{1-x^2}}\right) - \pi}{\left(1-x^2\right)^{3/2}}\right] + \frac{1}{1-x^2} \tag{1.16b}$$

From equations 1.13 and 1.16, the position of the LSP resonances of a small oblate nanoparticle can be determined in the frame of the quasi-static regime approximation. Fig. 1.5 shows calculations of the position of the LSP resonance (for excitation along the major axis) of a small isolated Ag oblate spheroid embedded in a-Si:H for various aspect ratios. By varying the aspect ratio of the ellipsoid from 1 (sphere) to 0.25, the LSP resonance is red-shifted from 760 nm to 1240 nm.

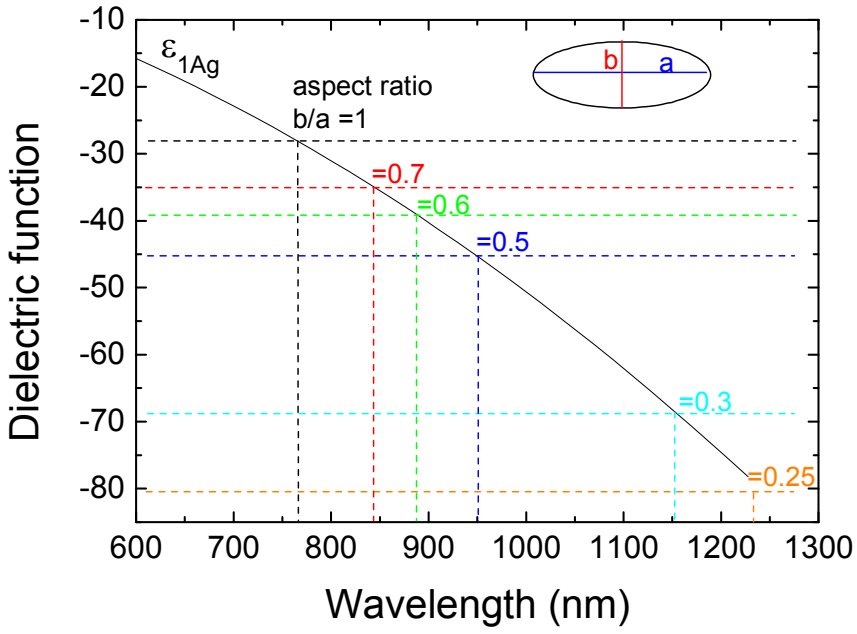

Figure 1.5 : Influence of the aspect ratio of a small isolated Ag oblate spheroid embedded in a-Si:H on the position of the LSP resonance. The calculations are performed in the frame of the quasi-static regime approximation.

1.3 Mie theory

The quasi-static regime serves as a first rough estimation when sufficiently small particles (diameter < 20 nm) are used. For larger particle, retardation effects of the electromagnetic field over the particle diameter become significant and multipole contributions are observed in the extinction spectra. The problem has to be solved in the frame of Mie theory (Mie, 1908). Mie applied Maxwell's equations with appropriate conditions in spherical coordinates using multipole expansions of the incoming electric and magnetic fields. He was not the first to derive a solution of this problem, but the first to apply

it to the problem of light scattering of metal spheres embedded in transparent, non-absorbing media (Logan, 1965). To determine the optical response of a particle embedded in a medium the necessary parameters are the particle size, the optical functions of the particle material and the embedding medium (which should be transparent, non-absorbing). We will briefly summarize the main results of Bohren and Huffman (1983). In the Mie theory, the scattering and extinction efficiencies are given by :

$$Q_{sca}^{(P)} = \frac{2}{x^2}(2P+1)\left(|a_P|^2 + |b_P|^2\right) \tag{1.17a}$$

$$Q_{ext}^{(P)} = \frac{2}{x^2}(2P+1)\,\mathrm{Re}\left(a_P + b_P\right), \tag{1.17b}$$

P is the number of the multipole extension of the fields suggested by the spherical symmetry ($P=1$ corresponding to the case of a dipolar mode as described in the previous sections). x is equal to kr, with k the modulus of the wave vector, r the particle radius and a_P, b_P are the Mie coefficients which are calculated by :

$$a_P = \frac{m\psi_P(mx)\psi_P'(x) - \psi_P(x)\psi_P'(mx)}{m\psi_P(mx)\xi_P'(x) - \xi_P(x)\psi_P'(mx)} \tag{1.18a}$$

$$b_P = \frac{\psi_P(mx)\psi_P'(x) - m\psi_P(x)\psi_P'(mx)}{\psi_P(mx)\xi_P'(x) - m\xi_P(x)\psi_P'(mx)}, \tag{1.18b}$$

with $m = n_{particle}/n_{medium}$ (n the refractive index) and ψ_P and ξ_P the Riccati-Bessel cylindrical functions (Bohren and Huffman, 1983).

Fig. 1.6 presents the optical response (absorption, scattering and extinction cross sections) in a wavelength range relevant for solar cells of Ag spheres of various diameters embedded in a-Si:H (with $n_{a\text{-}Si:H}$=3.6) calculated according to the Mie theory. In these calculations, we don't consider the influence of the particle size on the dielectric constant (see section 1.4.2) for particles smaller than 40 nm. The values of the dielectric functions as measured by Johnson and Christy (1972) are used. For radius R=5 nm, both the absorption and scattering cross sections (and thus the extinction cross section) exhibit a sharp peak at around 750 nm which represents the localized (or dipolar) surface plasmon resonance. The position of the resonance found here is in good agreement with the one calculted above for a small nanoparticle in the frame of the quasi-static regime approximation (see Fig. 1.5 for an aspect ratio of 1). For R=20 nm, the quasi-static approach already collapses. The dipolar resonance is red-shifted and the FWHM (Full Width at Half Maximum) is broader than in the case of a nanoparticle with R=5 nm. A second peak (a quadrupolar resonance) sharper than the dipolar resonance

appears at around 680 nm. Both absorption and scattering cross sections increase (mind the different scales used for various diameters) but the scattering dominates over the absorption in the whole spectral range. By further increasing the particle radius, both dipolar and quadrupolar resonances shift to the red and higher multipole modes appear in the spectrum (octopolar resonance ...). The absorption and scattering cross sections further increase but the absorption becomes negligible compared to the scattering.

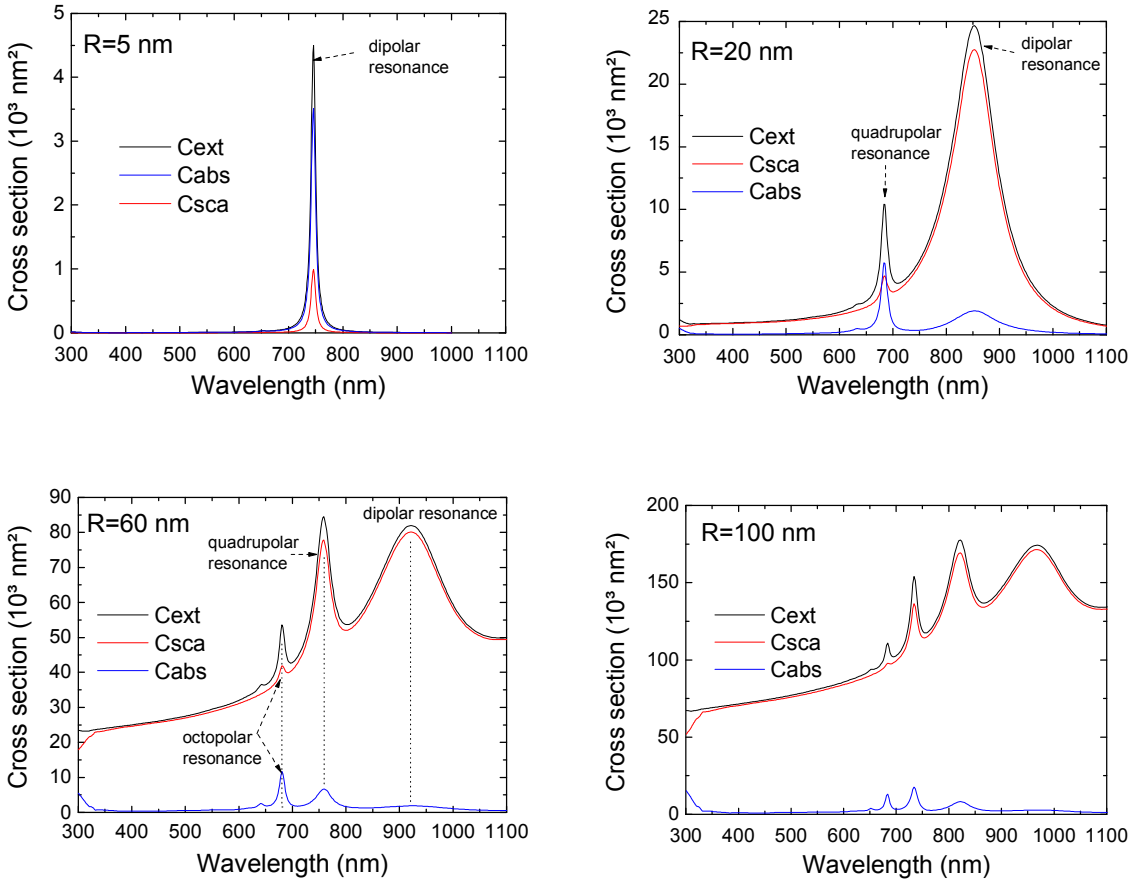

Figure 1.6 : Calculations of absorption, scattering and extinction cross sections of Ag nanoparticles with various radii embedded in a-Si:H ($n_{a\text{-}Si:H}$=3.4) according to the Mie theory. The dielectric constants given by Johnson and Christy (1972) are used for Ag.

1.4 Dielectric function ε(ω) of a metal nanoparticle

For metal nanoparticles with a diameter larger than 40 nm the optical material functions are similar to their bulk metal values and are nearly size independent (Kreibig and Vollmer, 1995). For nanoparticles with a diameter smaller than 40 nm, intrinsic particle-size effects

become more important as the diameter decreases (Pinchuk et al., 2004). The optical material functions themselves have thus to be modified.
In the following sections, the Drude model will be introduced. Basic assumptions of the Drude model as well as clear illustrations of the electronic distribution (conduction and core electrons) in a metal are given in the book written by Ashcroft and Mermin (1981).

1.4.1 Dielectric function of bulk metal and metal nanoparticles

Metals are assigned to free-electron metals if most of their electronic and optical properties are determined by the conduction electrons alone. Example are the alkali metals, magnesium and aluminium. Noble metals, e.g. Ag, Au, Cu, Pd, Pt and Hg, are also considered in some extent as free-electron metals. However their optical function also depends on the electron occupation of deeper energy levels. All of these metals have completely filled valence bands and partially filled conduction bands. A simplified model of the electronic band diagram of noble metals is shown in Fig. 1.7. For free-electron metals like the alkalis, the optical properties are determined mainly by excitation of electrons within the conduction band. This is denoted as *intraband* transitions. In other metals, considerable contributions of *interband* transitions from fully occupied electronic levels to states of the conduction band or from this later to unoccupied bands of higher energy take place.

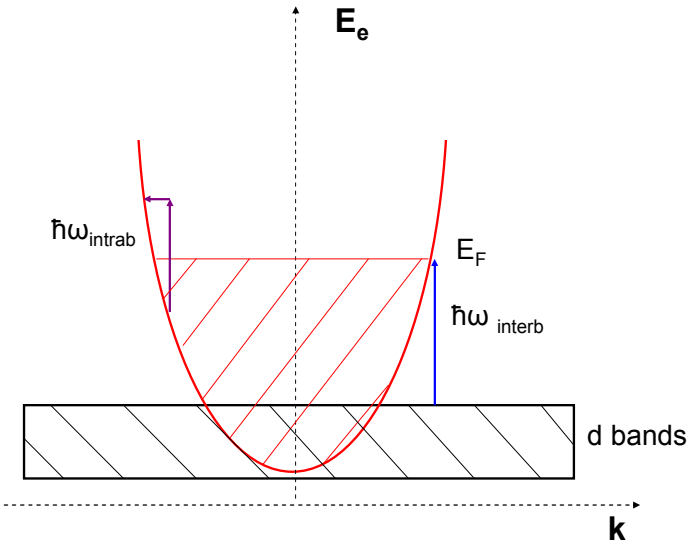

Figure 1.7 : Simplified model of the electronic band diagram of noble metals. The parabolic conduction band $E_e=\hbar^2k^2/2m$ is full up to the Fermi level E_F. Arrows indicate intraband transitions ($\hbar\omega_{intrab}$) and the threshold of interband transitions ($\hbar\omega_{interb}$).

The *intraband* describes an indirect optical excitation without a change of the electronic band (see Fig. 1.7). A direct absorption of a photon by an electron can not occur, due to momentum conservation. A two-step process involving a third particle, a phonon (i.e. a *quantum* or fundamental quasi-particle corresponding to the coordinated vibration of the atoms making up the crystal structure), or another electron is required to assure the conservation of both the energy and the momentum during the optical transition. At room temperature, the interaction electron-phonon dominates. Thus light absorption in a metal is directly correlated with the optical collision frequency γ_0 of the quasi-free electrons of the conduction band.

The *interband* mechanism originates from optical transitions between two different electronic bands, i.e. from lower energy bands into the conduction band or from the conduction band into higher unoccupied levels.

Free-electron optical response (intraband mechanism)

The contribution of the conduction electrons to the optical properties of metal can be determined by using a *plasma model* which considers a gas of free electrons *n* which move collectively against a fixed background of positive ion cores. Collective motion means that all electrons oscillate in-phase, with a phase determined by the one of the incoming light. In this model, known as Drude-Lorentz-Sommerfeld model, we assume that the response of a metal particle can be found by first considering the influence of external forces on one free conduction electron only and then multiplying by the number of electrons to obtain the macroscopic optical response. Details of the lattice potential and electron-electron interactions are not taken into account within this model. The electrons oscillate in response to the applied electromagnetic field and their motion is damped via collisions with the atoms of the lattice or other electrons. A characteristic collision frequency $\gamma_0 = 1/\tau_0$ describes the damping, where τ_0 is the optical relaxation time of the free electron gas. It is typically in the order of 10^{-14} s at room temperature. It has to be noted that τ_0 is frequency dependent (Kaveh and Wiser, 1984; Smith and Ehrenreich, 1982). γ_0 is related to the electron mean free path l by $\gamma_0 = v_F / l$, where v_F is the Fermi velocity. The motion for an electron of mass m_e and charge e of the plasma sea in response to a driving electric field E can be described by the following equation:

$$m_e \ddot{x} + m_e \gamma_0 \dot{x} = eE \tag{1.19}$$

If we consider a harmonic time dependence $E(t)=E_0 e^{-i\omega t}$ of the external field, a particular solution of this differential equation describing the oscillation of the electron is :

$$x(t) = -\frac{e}{m_e \omega(\omega + i\gamma_0)} E(t) \tag{1.20}$$

The displacement of the electrons results in a macroscopic polarization $P = nex$, explicitly given by :

$$P = -\frac{ne^2}{m_e \omega(\omega + i\gamma_0)} E \tag{1.21}$$

The dielectric displacement D is linked via the electric field E and the polarization P by :

$$D = \varepsilon_0 E + P \tag{1.22}$$

where ε_0 is the electric permittivity of the vacuum.

Thus, by replacing the expression for P into equation 1.22, we can write :

$$D = \varepsilon_0 (1 - \frac{\omega_p^2}{\omega(\omega + i\gamma_0)}) E \tag{1.23}$$

where $\omega_p = \left(ne^2 / \varepsilon_0 m_e\right)^{1/2}$ is the *Drude plasma frequency* of the free electron gas. Since $D = \varepsilon_0 \varepsilon E$, the dielectric function $\varepsilon_{\text{int}rab}(\omega) = \varepsilon_{\text{int}rab1}(\omega) + i\varepsilon_{\text{int}rab2}(\omega)$ of the free electron gas, can be expressed by (Drude, 1900):

$$\varepsilon_{\text{int}rab}(\omega) = 1 - \frac{\omega_p^2}{\omega(\omega + i\gamma_0)} \tag{1.24a}$$

$$\varepsilon_{\text{int}rab1}(\omega) \approx 1 - \frac{\omega_p^2}{\omega^2}, \quad \varepsilon_{\text{int}rab2}(\omega) \approx 1 - \frac{\omega_p^2}{\omega^3}\gamma_0 \tag{1.24b}$$

The term *intrab* is used here to stress out that only the contribution from conduction band electrons was considered until now. A coupling of the free electrons to the ion cores can be described by considering the effective mass m_{eff} instead of the electron mass m_e. In this case, ω_p is modified.

For small metal nanoparticles in the dipolar mode, all conduction electrons of the metal will oscillate in phase. The electrons will be excited at the same time and with the same phase. The energy of the excitation light will be then distributed over all electrons taking part in the oscillation. Under these conditions, one cannot use anymore the model based on single-electron transitions presented in Fig. 1.7 since each electron taking part in the oscillation will receive a small fraction of the excitation quantum energy. In this case it is also not relevant anymore to assume indirect optical transitions assisted by a phonon.

The localized surface plasmon resonance of small spherical nanoparticles is found when $\text{Re}[\varepsilon(\omega)] = -2\varepsilon_m$ if Im[ε] only slightly or slowly varies close to the resonance (equation 1.8). If this condition is fulfilled and if the sphere consists of a Drude metal, the particle resonance in air ($\varepsilon_{\text{air}} \sim 1$) is met at the frequency $\omega_0 = \omega_p / \sqrt{3}$.

Contribution from core electrons (interband mechanism)

Up to now we have only considered the interaction of the conduction electrons with the electromagnetic wave. The electrons in deeper levels, i.e. core levels, contribute also to the dielectric function. The dielectric function of the Drude model (equation 1.24) adequately describes the optical response of metals only for energies below the threshold of transitions between individual bands (interband contribution). For alkali metals, the validity of the Drude approach extends up to the ultraviolet. Their interband threshold is given by excitations of conduction-band electrons to higher levels as all filled bands lie far below the conduction band. For Al, the threshold for interband absorption is 1.5 eV. For gold and silver, the interband transitions start to occur for photon energies larger than 2.3 eV (λ ~ 540 nm) and 3.9 eV (λ ~ 320 nm), respectively (Ashcroft and Mermin, 1981). The intraband electron contribution, $\varepsilon_{\text{int}\,rab}(\omega)$, has thus to be complemented with the core electron contribution $\varepsilon_{\text{int}\,erb}(\omega)$ (Del Fatti et al., 2000; Ehrenreich and Philipp, 1962), so that the complete dielectric constant is :

$$\varepsilon(\omega) = \varepsilon_{\text{int}\,rab}(\omega) + \varepsilon_{\text{int}\,erb}(\omega) \tag{1.25}$$

As an example, Fig. 1.8 shows the dielectric function $\varepsilon = \text{Re}[\varepsilon] + \text{Im}[\varepsilon] = \varepsilon_1 + i\varepsilon_2$ of Ag, with both contributions of intraband and interband optical transitions.

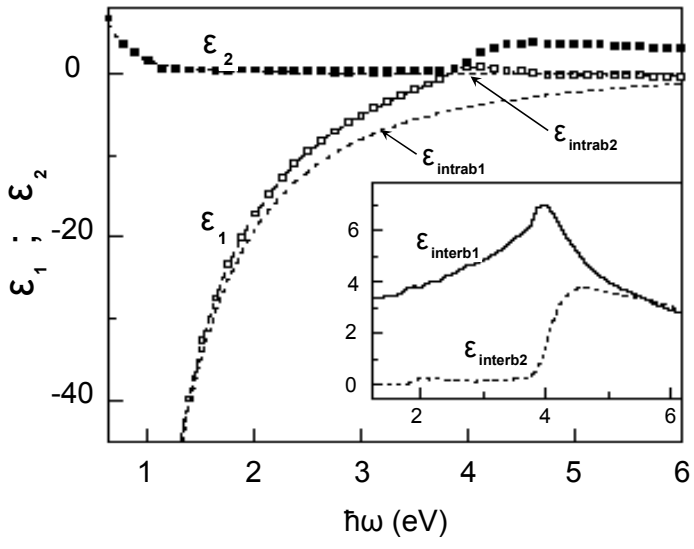

Figure 1.8 : Complex dielectric functions (squares) of Ag, with ε_1 the real part and ε_2 the imaginary part. Contributions of both intraband and interband optical transitions are taken into account. The insert shows the contribution of the interband transitions only.

As gold and aluminium are also investigated in this work, we present the dielectric functions of these metals (Fig. 1.9, left and right, respectively).

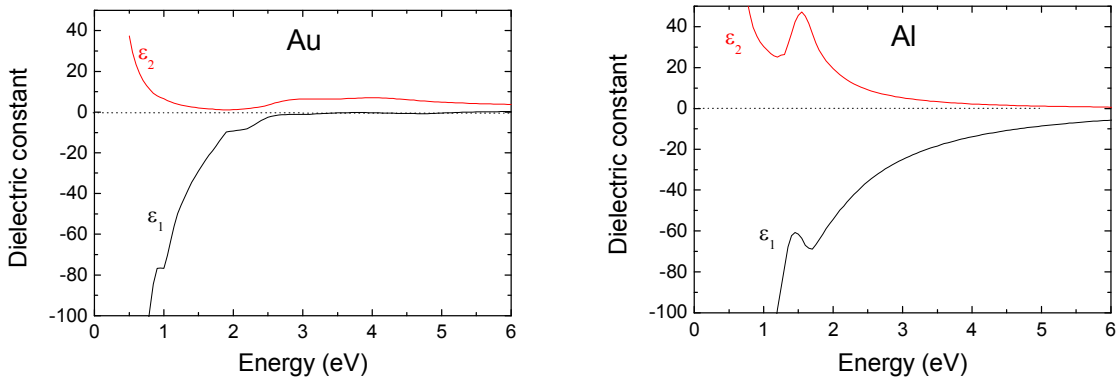

Figure 1.9 : Complex dielectric functions of Au (left) and Al (right), with ε_1 the real part and ε_2 the imaginary part. Contributions of both intraband and interband optical transitions are taken into account (Handbook of Optical Constants of Solids, 1985).

1.4.2 Dielectric function of very small metal nanoparticles

The metal properties that are dominated by the quasi-free electrons in the bulk material will be modified in a nanocrystal by the concomitant breakdown of the lattice periodicity and interaction with the interface. Indeed, the presence of surfaces will significantly influence the optical properties, especially for nanoparticles of dimensions smaller than the mean free path of the electrons $l = v_F \tau_0$ (20 nm < l < 50 nm for metals), where v_F is the Fermi velocity of the electrons. Thus collisions between the electrons and the surface can not be neglected anymore compared to the other interaction processes and have to be considered in the optical collision mechanisms. In the frame of Drude model, the intraband absorption, which can also be assisted by collisions between the electrons and the surface, will increase. The impact of the confinement on the optical properties can be explained by both classical and quantum mechanic approaches. Both concepts lead to the same result that the intraband contribution to the dielectric constant of metal nanocrystal preserves its Drude-type form. Within a simple model a term is introduced that is proportional to the collision frequency with surfaces, i.e. the inverse of the time required by an electron to cross the particle $t_t = D / v_F$. For a sphere of diameter *D*, the collision frequency can be written as :

$$\gamma = \gamma_0^{'} + g\frac{v_F}{D} \tag{1.26}$$

where g is a proportionality factor close to 0.25 (Zaremba et al., 1987; Persson, 1993; Hovel et al., 1993) and $\gamma_0^{'}$ is the intrinsic collision frequency (electrons-electrons and electrons-phonons) for bulk metals. This relation is similar to the bulk frequency but is modified due to the confinement of the particle (Voisin et al., 2000). The second term in equation 1.26 becomes comparable and even larger than the first one as the diameter of the particle decreases. The size dependence of the dielectric function for gold and silver nanoparticles is not negligible for nanoparticles with a diameter D < 40 nm (Pinchuk et al., 2004). The second term in equation 1.26 especially influences the width and the amplitude of the LSP resonance and has only a small effect on the position of the resonance (Kreibig and Vollmer, 1995).
Interband light absorption of gold and silver nanoparticles was studied with regard to particle size (Hovel et al., 1993). The interband dielectric constant of the metal is only slightly modified for particle sizes smaller than 2 nm. Consequently, for metal nanoparticles of sizes smaller than around 40 nm, the main effect of the particle confinement on the dielectric constant is the modification of the collision frequency. By adding the contribution from collisions between electrons and surfaces into equation 1.25, the dielectric constant of a metal nanoparticle can be written as :

$$\varepsilon(\omega) = \varepsilon_{\text{int}erb} + 1 - \frac{\omega_p^2}{\omega[(\omega + i(\gamma_0^{'} + gv_F / D)]} \tag{1.27}$$

1.5 Summary

The optical response of spherical metal nanoparticles is characterized by a resonance in their absorption and scattering spectra. This resonance results from the collective oscillation of the free electrons inside the metal particle and is referred to as localized surface plasmon (LSP). The position and the width of the LSP resonance are determined by the material (i.e. the dielectric function), the shape, the size and the surrounding medium of the nanoparticle. For metal nanoparticles with dimensions much smaller than the excitation wavelength, the optical response – calculated in the frame of the quasi-static regime approximation – is dominated by the absorption. At a frequency corresponding to the LSP resonance, small metal nanoparticles behave as oscillating dipoles and lead to a strong enhancement of the electric field inside and in their close vicinity. The case of small ellipsoidal metal nanoparticles is treated, where spectrally separated LSP resonances depending on the polarization of the excitation light, can be observed.
The scattering cross-section of nanoparticles increases rapidly with their diameter. For nanoparticles larger than 20 nm, retardation effects of the electromagnetic field over the

particle diameter become significant and the problem has to be solved in the frame of the Mie theory.

The dielectric function of a noble metal nanoparticle is given as the sum of two contributions. The first contribution results from the free electrons of the metal and can be determined by using a plasma model (Drude model). The second contribution originates from the core electrons of the metal. It has to be considered for excitation energies above the specific threshold of interband transitions. For metal nanoparticles with a diameter larger than 40 nm, the optical function is similar to the bulk metal value and is nearly size independent. For smaller particles, collisions of the free electrons with the particle surface lead to a modification of the dielectric function which varies as a function of the particle size. This particularly influences the width and the amplitude of the LSP resonance.

Chapter 2

Deposition techniques, material properties and silicon solar cells

This chapter provides a description of the deposition processes used for the preparation of metal nanoparticles, samples and solar cells investigated in this work. Since metal nanoparticles can only be obtained for specific materials and under specific preparation conditions, in this section the general term "metal films" will be used for the description of any realized metal structure with a thickness of a few nanometers. Structural and optical properties of amorphous silicon and microcrystalline silicon are described and compared with those of crystalline silicon. The Plasma Enhanced Chemical Vapor Deposition (PECVD) method used to deposit the silicon layers is explained briefly. The sputtering technique for the preparation of Transparent Conductive Oxide (TCO) films is presented as well. Finally, the structure of crystalline silicon solar cells and thin-film silicon solar cells is shown and their working principle is described. Requirements for the preparation of optimized solar cells are listed.

2.1 Preparation of metal films

A large number of techniques is commonly used for the preparation of metal nanoparticle films, as vapor deposition, sputtering, laser ablation, citric reduction, wet chemical synthesis, electron beam lithography, scanning tunnelling microscopy assisted nano-structure formation, nanosphere lithography. In this work, we used a thermal evaporation process since this method is one of the most inexpensive approaches. Besides, this method is reliable and enables the realization of high quality metal films (Gupta et al, 2002) and the equipment involved is commonly available in material research and production facilities. Thus it can be easily integrated in the fabrication process of thin-film solar cells. Thermal evaporation consists of the evaporation of a small piece of metal placed on a heated tungsten holder in a thin-film deposition system providing a high vacuum. In this work, metal films of Ag, Au, Al and a combination of two of these metals with thicknesses varied between 0.5 and

50 nm were deposited on various substrates such as TCO (Transparent and Conductive Oxide, made of ZnO:Al), a-Si:H, Corning glass and silicon wafer. The thickness of the deposited metal films was controlled by a quartz oscillator. The deposition rate was varied between 0.2 and 10 $Å.s^{-1}$. The influence of the pressure was investigated by depositing the metal film at 5.10^{-4} and 5.10^{-5} mbar. In this range, no significant contribution of the pressure on the formation process of the nanoparticles was found. The effect of an annealing treatment on the morphology of the metal film was studied. The annealing temperature was varied between 150 °C and 300 °C and the duration of the treatment was varied between 30 min and several hours. In the case the metal films were covered with a-Si:H (or µc-Si:H), an "unintentional" annealing treatment was always performed. Indeed, a thermal treatment of approximately 1 h is commonly used prior to the silicon deposition (performed at 180 °C) so that the substrate reaches the desired temperature of 180 °C. This step provides a higher quality of the deposited silicon layers. It was found that annealing the substrates leads to modifications in the structure of the metal films, especially in the case of Ag. All the parameters mentioned above were varied throughout this work to obtain different metal film structures (e.g. small nanoparticles, large nanoparticles and nanostructures), each showing specific optical properties.
To characterize the structure of the metal films, both Scanning Electron Microscopy (SEM) and Atomic Force Microscopy (AFM) were used. In order to judge the performance of the realized devices always a sample without metal film was produced. Instead of using two different substrates (one kept as reference, i.e. with no metal film, another one covered with metal film), we deposited the metal films through a mask on half of the substrate to avoid discrepancies originating from thickness variations and facilitate their structural and optical characterization.

2.2 Material properties and deposition of a-Si:H and µc-Si:H

2.2.1 Structural properties of a-Si:H

The local atomic structure of amorphous silicon (a-Si) resembles the local atomic structure of crystalline phase. However differences can be observed. Crystalline silicon (c-Si) has a diamond lattice structure, i.e. it is a four-fold coordinated atom that is normally tetrahedrally bonded to four neighboring silicon atoms. In c-Si this tetrahedral structure is extended over a large range, forming a well-ordered lattice (crystal) and a strict periodic repetition of an unit cell (Fig. 2.1, left). In a-Si, variations in bond lengths and angles lead to a lack in the long range order and the atoms form a continuous random network (Fig. 2.1, right). Due to the disordered nature of the material, the periodic bonding requirements are not

met for all atoms. This leads to *dangling bonds*, i.e. bonds which are not bonded to the neighboring silicon atom. These dangling bonds represent defects in the continuous random network, when they are not passivated with hydrogen. Hydrogen can bond to the dangling bonds and thus reduce the dangling bond density by several orders of magnitude from 10^{25}-10^{26} to 10^{21}-10^{22} m^{-3} (Willemen, 1998). Hydrogenated amorphous silicon (a-Si:H) has a low amount of defects (10^{22} m^{-3}). However, the hydrogen is unfortunately associated with light induced degradation of the material that is known as Staebler-Wronski effect (Staebler and Wronski, 1977). One of the main advantages of a-Si:H over c-Si is based on its production technique (see section 2.2.4). Moreover, it can be doped by similar materials to c-Si to form p- or n-type layers, which is a prerequiste to realize electronic devices.

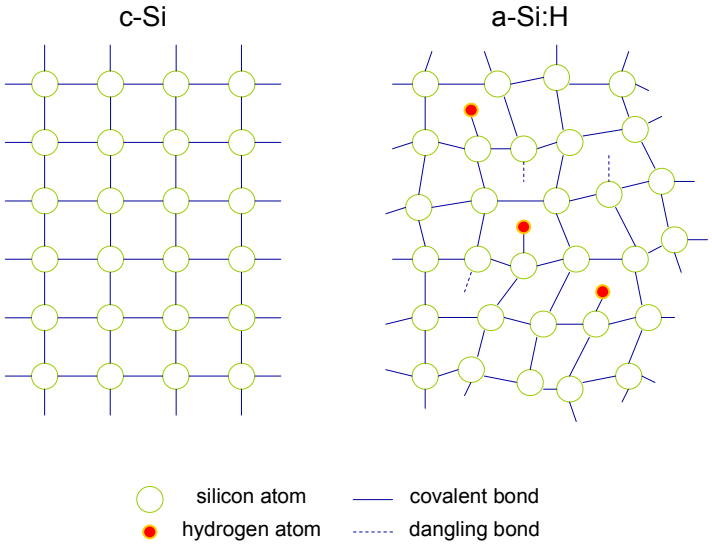

Figure 2.1 : Schematic drawing of the atomic structure of (left) crystalline silicon and (right) hydrogenated amorphous silicon.

2.2.2 Structural properties of µc-Si:H

Hydrogenated microcrystalline silicon (µc-Si:H) is a composite material of crystalline regions, column boundaries, disordered (amorphous) regions and voids (Luysberg et al., 1997; Houben et al., 1998a). It has to be differentiated from polycrystalline silicon (poly-Si) which consists only of crystalline silicon grains. µc-Si:H is also known as nanocrystalline silicon (n-Si). A schematic picture of the structural composition of µc-Si:H is shown in Fig. 2.2. Under highly crystalline growth conditions, i.e. low silane concentration (see section 2.2.4), columnar clusters with small grains of coherent crystalline regions are found (Fig. 2.2, left hand side). The columns are separated from each other by a-Si:H or voids, depending on

the deposition conditions and the substrate (Tzolov et al., 1997). By increasing the silane concentration a decrease of the crystalline fraction leads to interruptions of the columnar crystalline structure and smaller coherent grains are embedded in the amorphous matrix (Fig. 2.2, from left side to right side). For µc-Si:H solar cells, material composition with a structure located at the transition region between amorphous and microcrystalline phase is chosen (Vetterl et al., 2000). Due to the small crystalline domains it does not reach the mobility of poly-Si. On the other hand µc-Si:H is easier to fabricate at large area, as it can be deposited using conventional low temperature a-Si:H deposition techniques, such as PECVD. It has to be noted that µc-Si:H material exhibits increased stability in comparison to a-Si:H.

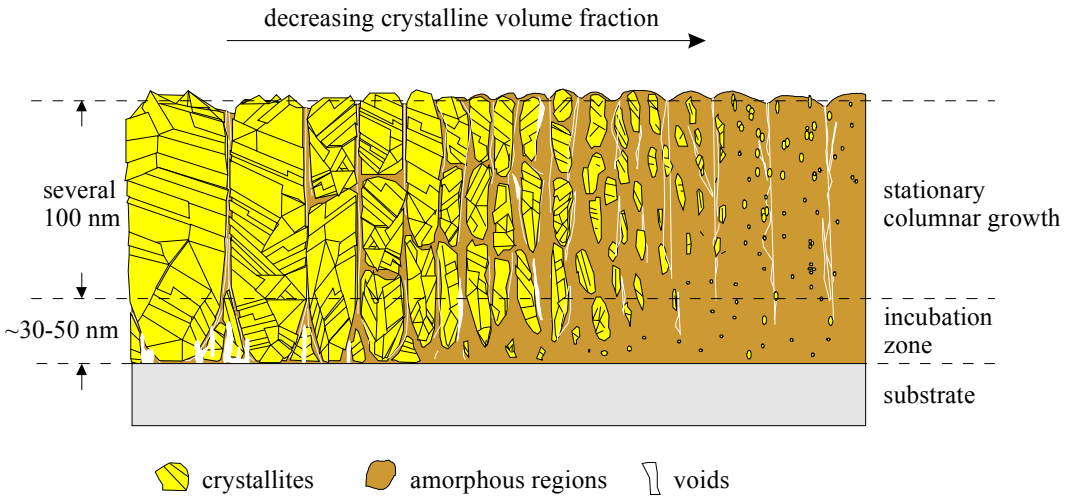

Figure 2.2 : Schematic diagram showing the prominent microstructure characteristics of µc-Si:H grown by high frequency PECVD. From the left to the right, the film composition changes from highly crystalline to predominantly amorphous. The figure is taken from Finger et al. (2000).

2.2.3 Optical properties of c-Si, a-Si:H and µc-Si:H

Fundamental light absorption in a semiconductor refers to absorption of photons by excitation of an electron from the valence band (Ev) into the conduction band (Ec). For a direct-bandgap semiconductor, light absorption occurs when the photon energy of incoming light is larger than the bandgap (Eg) of the semiconductor. Eg is defined as the energy difference between the valence band and the conduction band edges.

Optical properties of c-Si

c-Si which has a bandgap of 1.12 eV at room temperature and air pressure is an indirect-bandgap semiconductor, i.e. the lowest energy minimum of the conduction band is not at the same momentum $\vec{k}$ as the highest maximum of the valence band. For direct transitions of electrons from the valence to the conduction band, photon energies much larger than the forbidden gap are required. Transitions can also occur at lower energies by a two-step process involving not only photons and electrons but also phonons. As a result of the indirect band gap, the optical absorption is significantly reduced in the visible spectral region because the absorption of photons involves phonons for momentum conservation.

Optical properties of a-Si:H

Since in a-Si:H the conservation of the momentum $\vec{k}$ in the electronic transitions is not longer granted (Jackson et al., 1985), the material acts as a 'quasi'-direct semiconductor with a much higher absorption probability of photons in the visible spectral region (photon energies above 1.8 eV), compared to c-Si (Fig. 2.3). Therefore, for a-Si:H film thicknesses of about 500 nm are sufficient to absorb the light with wavelengths $\lambda \leq 600\,\text{nm}$. Below 1.8 eV, the absorption in a-Si:H is determined by the density of tail states (shallow states) and dangling bonds (deep defects).

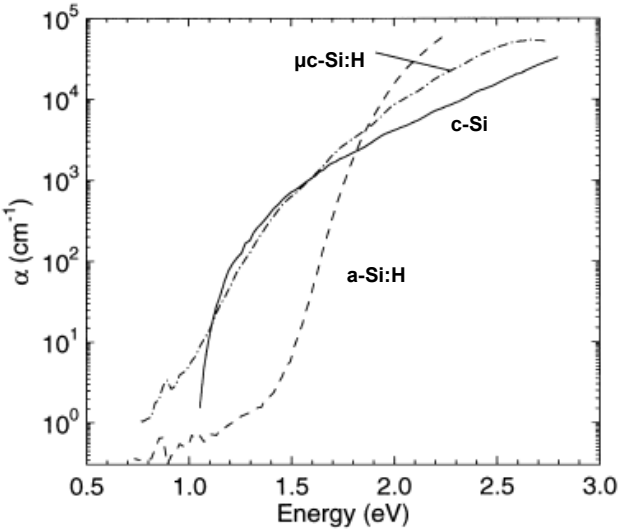

Figure 2.3 : Absorption coefficient α of crystalline silicon (c-Si), hydrogenated amorphous silicon (a-Si:H) and microcrystalline silicon (μc-Si:H) measured by photothermal deflection spectroscopy (PDS). The data are taken from Carius et al. (1997).

Optical properties of µc-Si:H

The optical absorption spectra shown in Fig. 2.3 suggest a higher absorption coefficient for µc-Si:H than for c-Si in the visible spectral region (at photon energies above 1.6 eV). Absorption in a-Si:H phase and internal light scattering in µc-Si:H have been proposed as possible reasons for this effect (Diehl et al., 1998; Beck et al., 1996). Between 1.1 eV and 1.6 eV, µc-Si:H nearly reproduces the absorption coefficient values of c-Si. Thus its absorption is higher than a-Si:H in the red and infrared. In the sub-band gap absorption region (at energies below 1.1 eV), the absorption coefficient of µc-Si:H significantly exceeds the one of c-Si and is slightly higher than the one of a-Si:H. This can be explained by the presence of band tails (at grain boundaries) and deep defects similar to those found in a-Si:H (Jackson et al., 1983; Beck et al., 1996).

2.2.4 Deposition of a-Si:H and µc-Si:H by PECVD process

Plasma enhanced chemical vapor deposition (PECVD) is one of the most prominent methods for depositing a-Si:H and µc-Si:H. The moderate temperatures commonly used in PECVD process offer the possibility to use a large variety of substrate materials such as glass (in our case), stainless steel and plastic. Stainless steels or plastic foils are promising candidates for a roll-to-roll process. Moreover, PECVD provides low energy consumption in industrial-scale process compared to e.g. crystalline technology, which requires temperatures larger than 1000 °C. The relatively lower electronic performance of a-Si:H and µc-Si:H solar cells is thus overcompensated by a cheaper production and high-volume production.
To deposit a-Si:H and µc-Si:H films, decomposition of silane gas (SiH_4) is the most common way. Thermal dissociation of silane occurs at temperature larger than 450 °C but usually leads to the growth of low quality material. PECVD process provides the necessary dissociation energy under vacuum conditions (~ 10^{-8} mbar) and at lower temperatures (typically ~ 200 °C) in a low pressure glow discharge. The plasma is created by means of a high electric field applied between two parallel electrodes. Detailed information about the PECVD method is given in the books written by Chapman (1980), Haefer (1987), or Frey and Kienel (1987). An excitation frequency of 13.56 MHz is commonly used for large area application (RF-PECVD). The schematic outline of the PECVD process between planar electrodes is illustrated in Fig. 2.4. When SiH_4 is used as a source gas in the glow discharge process, reactive neutral species, e.g. SiH, SiH_2, SiH_3, Si_2H_6, H and ionized species, e.g. SiH^+, SiH_2^+ are created in the plasma by electron impact.

The possible dissociation reactions, which can be of importance for the growth processes are given by the following equations (Doyle et al. 1990):

$$e^- + SiH_4 \rightarrow SiH_2 + 2H + e^- \quad (2.1)$$

$$e^- + SiH_4 \rightarrow SiH_3 + H + e^- \quad (2.2)$$

Which of the two dissociation products, SiH_2 or SiH_3 contribute to the growth of the solid films onto the substrate is under debate (Vepřek et al., 1989; Gallagher et al., 1989; Perrin, 1991).

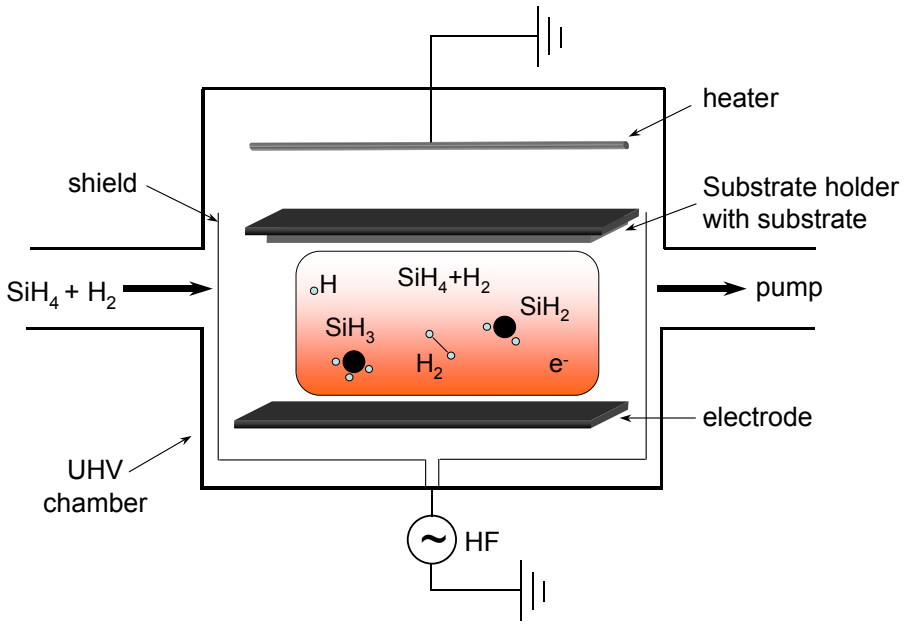

Figure 2.4 : Schematic outline of the PECVD process of SiH_4+H_2 decomposition in RF-glow discharge between planar electrodes.

The properties of the resulting films and especially whether its structure is microcrystalline or amorphous depend on the deposition parameters such as silane to hydrogen ratio in the gas phase, plasma excitation frequency, substrate temperature, discharge power density and total gas pressure. The material properties can be determined by Raman spectroscopy (see chapter 3). One of the most important process parameters to control the structure of the material is silane concentration *SC*, i.e. the ratio of silane gas flow and total gas flow $\left(SC = [SiH_4]/[SiH_4 + H_2]\right)$. In particular, a high concentration of hydrogen in the plasma or high discharge power can establish microcrystalline growth conditions. To obtain p-type or n-type doped silicon material, boron- or phosphorus-containing source gases are introduced into the reactor.

2.3 TCO deposition by magnetron sputtering

Magnetron sputtering is commonly applied for the preparation of Transparent Conductive Oxide (TCO) coatings – in our case ZnO:Al with Al concentration of 0.5 % to 1 %. Detailed information about this method is found in literature (Chopra et al., 1983; Vossen J.C., 1977; Pulker et al., 1984). In the sputter process, ions (usually Ar^+) are created by a low pressure glow discharge and are accelerated towards a target by means of an electric field (DC or RF) induced by two electrodes. By mechanical impact, target material (ZnO:Al) is carried off and condenses on a substrate. Temperature, pressure and applied electric power at the electrodes can be varied independently to obtain different properties of the ZnO coating. In this work, most of the depositions were performed at room temperature (RT). Only the 800 nm thick TCO front contact of p-i-n solar cells was deposited at 400 °C to provide a high transparency and high conductivity at a large deposition rate. Sputter process was also used for depositing the Ag back contact of solar cells with the n-i-p configuration (see section 2.4.5). Indeed, Ag layers with thickness larger than ~ 100 nm sputtered on glass show a good adhesion of Ag on the substrate. On the contrary, evaporated thick Ag layers on Corning glass are found to pill off.

2.4 Crystalline silicon and thin-film silicon solar cells

2.4.1 Working principle of c-Si solar cells

To get a better understanding of the working principle of a-Si:H and μc-Si:H thin film solar cells, it is necessary to first describe the functioning principle of conventional crystalline silicon (c-Si) solar cells. Precise and clear description of the operating principles of c-Si solar cells can be found in the book written by M. A. Green (1982). Solar cells based on c-Si are generally carried out as p-n junction obtained by varying the type of doping within the semiconductor. The band diagram of a p-n junction is shown in Fig. 2.5 (left). By light absorption, electrons can be excited from the valence band to the conduction band and holes are generated in the valence band. Both carriers move through the crystal and contribute to the photocurrent. The generated carriers (both electrons and holes) resulting from light absorption in the bulk material can reach by diffusion the space charge and the back contact, respectively. The space charge region with high static electric field results from the difference of potential between p- and n-doped layers. The space charge region of the p-n junction

depends on the doping level and is typically thinner than 1 µm for a wafer based c-Si solar cell. Since the charge carriers diffuse to the p-n junction, crystalline silicon solar cells are called "diffusion solar cells".

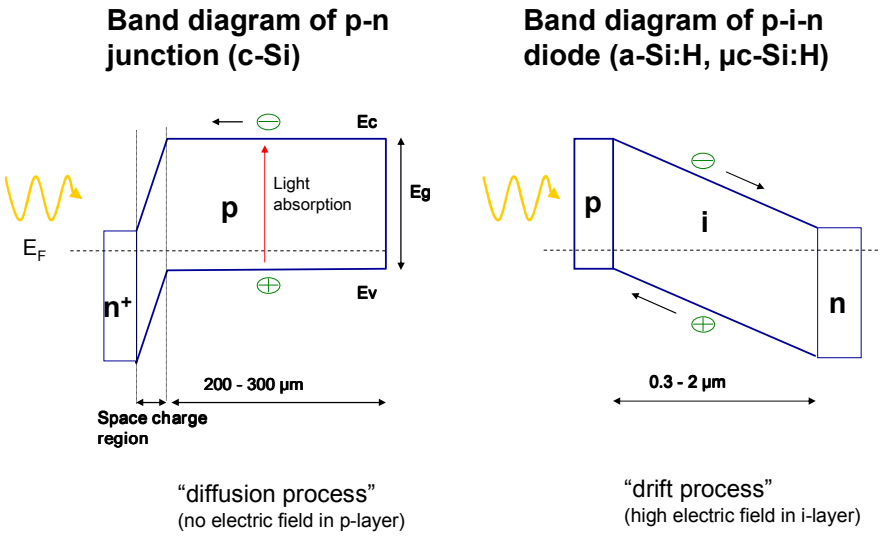

Figure 2.5 : Band diagram of a p-n junction (left) as in the case of c-Si solar cell and of a p-i-n diode (right) as in the case of a-Si:H and µc-Si:H solar cells.

2.4.2 Operating principle of a-Si:H and µc-Si:H solar cells

In contrast to c-Si, a-Si:H material shows a large defect density and consequently short diffusion lengths (i.e. short distances for carriers before they recombine) and a Fermi-level dependent defect state distribution. Thus, no p-n concept is possible for this material (Sauvain et al., 1990). Solar cells based on a-Si:H consist of a p-i-n layer stack. An intrinsic (i-) absorber layer (not intentionally doped, thus not rich in defects) is inserted between the thin p-doped and n-doped layers. The doped layers expand a static electric field over the absorber layer, as illustrated in Fig. 2.5 (right). A direct separation of the photo-generated charge carriers is achieved by drift in this electric field. Since the charge carriers generated by illumination are driven and separated by the electric field, a-Si:H solar cells are called drift cells. For thin-film solar cells based on µc-Si:H – which shows higher diffusion lengths and mobility-lifetime as a-Si:H (Brammer and Stiebig, 2003) – it has turned out that the same *p-i-n* (or *n-i-p*) concept as in amorphous silicon is favorable.

2.4.3 Equivalent circuit of a pin diode

Fig. 2.6 shows a simple equivalent circuit of a pin diode which can be used as model for thin-film silicon solar cells. If we neglect losses and consider a DC input signal (no capacitive effect) the electric behavior of a solar cell in the dark (without illumination) can be described by a simple diode. Under illumination, an additive reverse photocurrent i_{ph} is delivered by the device. Losses in the diode can be represented by the parallel (or shunt) resistance R_p and the series resistance R_S. This latter corresponds to the sum of all resistance contributions, namely resistance of transparent (TCO) and Ag contacts, doped layers, interface and electric wires of the equipment. The parallel resistance describes local shunts (leakages) and depends on the illumination power. The capacity C_p corresponds to the geometric capacity of the device. It is linked with cell area A and thickness of the intrinsic layer d_i through the equation 2.3 :

$$C_p = \varepsilon_r \varepsilon_0 . \frac{A}{d_i} \tag{2.3}$$

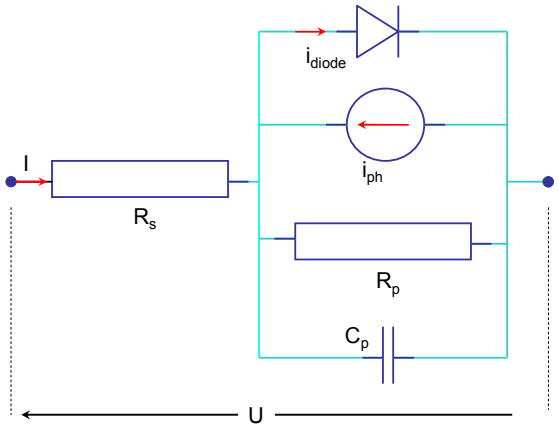

Figure 2.6 : Equivalent circuit of a pin diode.

2.4.4 Thin-film solar cells in p-i-n and n-i-p configuration

In this work, thin-film silicon solar cells based on two different configurations, namely "p-i-n" (also called "superstrate") and "n-i-p" (also referred to as "substrate") were realized and investigated. Fig. 2.7 shows the schematic basic structure of both types of reference cells (= cells without nanoparticles) in the p-i-n and n-i-p configuration. Slight modifications of

the devise structure were made throughout this work. A detailed description of the prepared solar cells is given in the text when the basic structure is modified.

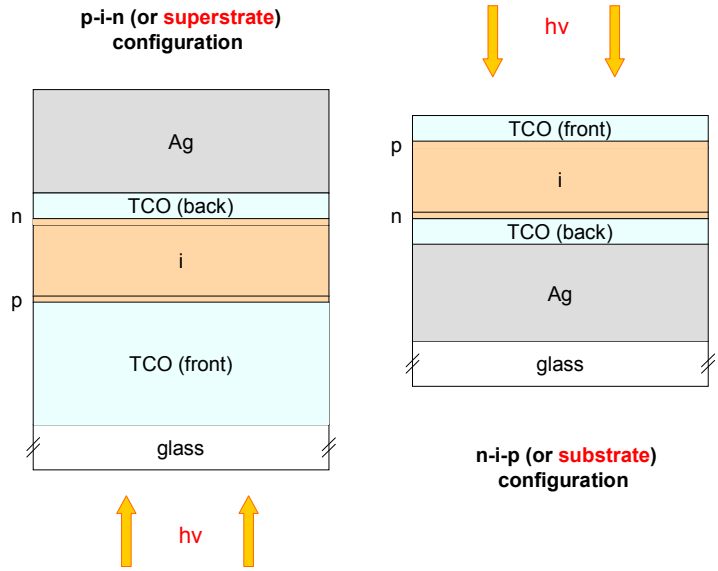

Figure 2.7 : Schematic drawing of thin-film solar cells in the p-i-n configuration (left) and n-i-p configuration (right). The Ag grid of the n-i-p cell, usually deposited on the front TCO contact, is not represented here. The thicknesses of the layers are given in the text.

The labeling “p-i-n” and “n-i-p” only refers to the order of deposition of the n-, i- and p-layer sequence. Almost all solar cells based on a-Si:H and µc-Si:H developed today are illuminated through the p-layer of the device. This is caused by the following reason. The defect distribution of a-Si:H cells is significantly modified in the i-layer close to the interfaces with the doped layers, due to the Fermi level dependent defect state distribution. These regions show a higher defect density than in the bulk i-layer. Therefore they are critical in terms of carrier recombination. Since the red light is absorbed in the bulk of the solar cell, the red response is nearly independent of the illumination side (from the p- or the n-layer). The blue response of solar cells, particularly for a-Si:H solar cells, is more sensitive to the illumination side of the device. Since the mobility of holes in a-Si:H and µc-Si:H is lower than for electrons, (i) the holes should have the shortest distance to their corresponding doped layer and (ii) the cell configuration should be chosen so that the holes resulting from the absorption of blue light (in the i-layer close to the first interface with the doped layer) only have to cross one of the two defect-rich regions of the i-layer, in order to reduce recombination. According to these requirements, illuminating through the p-layer appears to be the best solution. However, there is no fundamental difference in terms of functioning principle for p-i-n and n-i-p configurations. Thus, general requirements can be given for both types of configuration. The differences can be related to a different growth of the thin-films on top of each other.

2.4.5 General requirements for both p-i-n and n-i-p cells

Front TCO

Independently of the configuration, several requirements have to be fulfilled to obtain efficient solar cells. TCO used as front contact should exhibit a high transparency between 300 nm and 1100 nm (which corresponds to the absorption range of μc-Si:H) and a high conductivity to avoid ohmic losses. The thicker the TCO layer is the higher its conductivity is. On the other hand, increasing the TCO thickness also leads to enhanced absorption losses. Another possibility to improve the conductivity is to increase the Al doping concentration of ZnO. But in this case also, more absorption losses in the long-wavelength range are obtained. Thus, a compromise has to be achieved. Due to the fact that very thin silicon layers are involved in a-Si:H and μc-Si:H cells, the most efficient thin-film solar cells developed today are commonly deposited on rough substrate to improve the light in-coupling and the light trapping and consequently to increase the light absorption in the device. This is achieved by "texturing" the sputtered ZnO material surface using wet-chemical etching in diluted hydrochloric acid (HCl) (Kluth et al., 1997). However, in our study nearly all a-Si:H and μc-Si:H were deposited on flat substrate. It is known that metal nanoparticles (or other metal nanostructures presented throughout this work) can lead to strong light scattering depending essentially on their size and their morphology. In order to clearly understand the influence of metal nanoparticles/nanostructures and to separate their optical effect from light scattering obtained with a rough surface, flat substrates (subsequently covered or not covered with nanoparticles / nanostructures) were preferred. Not only optical but also electrical properties are of importance to achieve high efficiencies. For this reason, the fill factor (FF) and the open-circuit voltage (Voc) of solar cells based on a-Si:H and especially μc-Si:H (whose growth is more sensitive to the substrate employed) should not be altered by the TCO.

Silicon layers

The electron-hole pairs generated in the doped layers do (almost) not contribute to the photocurrent, as they are lost by recombination processes. Hence, both p- and n-layers should be as thin as possible and realized using a wide band gap in order to reduce absorption losses. On the other hand, they should be thick enough to build up an efficient electric field across the i-layer. Furthermore, they should exhibit a low perpendicular series resistance. A thickness between 10 nm and 20 nm is suitable for both doped layers. The i-layer has two main functions, namely to provide maximum absorption of the incident light and also enable a good electrical transport of the photo-generated charged carriers. Since defects in the i-layer lead to recombination of the charged carriers, it should exhibit a low defect density in order

to reach an effective carrier collection. With increasing the thickness of the absorber layer, the absorption increases but at the same time the collection efficiency decreases due to reduced electric field $E = U/d_i$ and enhanced defect density $N_d = \sum_{x=0}^{d_i} N_x$ (which lead to increased recombination probability). U is the internal potential difference across the i-layer, d_i is the thickness of the i-layer, N_d is the total defect density and N_x is the defect density at the position x of the i-layer. Therefore, typical thickness values are between 150 nm and 350 nm for a-Si:H cells and between 500 nm and 2 µm for µc-Si:H cells. In this work, cells containing metal nanoparticles/nanostructures with standard absorber thickness as well as very thin solar cells with i-layer thickness reduced to up to 20 nm were prepared, since the investigated electromagnetic field enhancement originating from plasmon effect is located in the surrounding of the nanoparticles (see equation 1.9a).

Back reflector

For both configurations, high efficiencies are achieved by using a back reflector consisting of a thin TCO layer with thickness of 80 nm and an Ag mirror. The thin TCO layer is commonly integrated between silicon and the Ag back contact to improve the reflection of the back reflector and thus the light absorption in solar cells (Stiebig et al., 1994; Yoshida et al., 1992; Beneking et al., 1994). The influence of the thin TCO layer will be stressed out in chapters 7 and 8.

2.4.6 Particular requirements for the p-i-n configuration

Front TCO

In the p-i-n configuration, a 800 nm thick TCO with Al concentration of 0.5 % (to 1 %) is deposited on a glass substrate. Under these conditions, spikes are observed at the surface of the TCO which can be responsible of shunts, i.e. current leakages between the top and the bottom of the solar cell. To remove these peaks, the glass/TCO substrates are dipped in a solution of HCl with low concentration (0.125 %) for 1-2 s. After this chemical process, the TCO film shows a relatively smooth surface. No diffuse scattered light can be measured by using such substrates.

TCO/(a-Si:H)p interface

A very sensitive region in solar cell is the TCO/p interface. At this position, holes generated within the device recombine with electrons delivered by TCO. As mentioned before, the FF and the Voc of cells deposited on ZnO:Al should not be negatively influenced.

However, it was found out that ZnO:Al used as TCO substrate material leads to (i) a significant reduction of FF and (ii) appearance of an S-shape in the dark I-V curves, when using an a-Si:H p-layer. The I-V characteristics and the independence of the series resistance in respect to the thickness of the p-layer indicate that the problem originates from the TCO/(a-Si:H)p interface. The TCO/(a-Si:H)p-contact problem has been reported before (Sakai and Ichikawa, 1991; Kubon et al., 1996). One solution of this problem was already addressed in previous publications of our group (Kubon et al., 1996; Winz et al., 1996). A very thin µc-Si:H buffer p-layer (5-10 nm), which shows much higher doping efficiencies than a-Si:H, has to be inserted between TCO and a-Si:H p-layer.

Back contact

In the p-i-n configuration, the cell geometry (Fig. 2.8, left) is defined by the silver back contact deposited by thermal evaporation.

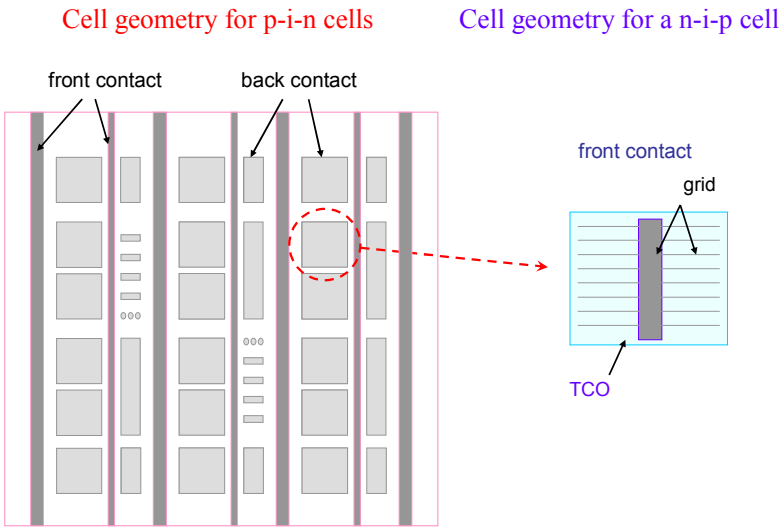

Figure 2.8 : (left) Cell geometry of p-i-n cells with designed areas representing Ag back contacts. (right) Cell geometry of a n-i-p cell : the cell area is defined by TCO covered with an Ag grid to support the current collection.

2.4.7 Particular requirements for the n-i-p configuration

Most of the cells prepared in our institute are based on a p-i-n configuration. Thus, deposition conditions used for the realization of n-i-p diodes are not optimized. However, many efforts were made to obtain satisfying results. Information about the preparation of

n-i-p solar cells is found in the Ph.D work of O. Kluth (1996) and S. Wieder (1999). Note that the highest efficiencies reported so far in the literature are achieved for cells in the n-i-p configuration (a-Si:H/a-SiGe:H/a-SiGe:H-triple junction solar cells) highlighted by a stabilized active area efficiency of 13 % (Yang and al., 1997; Rech and Wagner, 1999).

Back contact

In the n-i-p configuration, the Ag back contact is firstly deposited by sputtering on a glass substrate. To avoid the appearance of spikes at the surface of the Ag bulk material, likely due to stress of Ag (more pronounced at high temperature), the Ag deposition is performed at RT. Afterwards a thin TCO film with thickness of 80 nm is deposited. Deposition at RT is also preferred to avoid the generation of spikes.

(a-Si:H)p/TCO interface

As in the case of the a-Si:H cell with a p-i-n configuration, the p/TCO interface plays an important role. To overcome the mentioned contact problem a μc-Si:H p-layer was deposited on a-Si:H i-layer. In the starting phase, the nucleation of the μc-Si:H p-layer starts with high amount of amorphous phase. Thus, an appropriate i/p interface is achieved to build up a high Voc. The p-layer should be thick enough to provide a microcrystalline phase far enough from the nucleation region. In our case, a 40 nm thick μc-Si:H p-layer has been used to fulfill this condition.

Front contact

In n-i-p configuration, the cell geometry is defined by the TCO top contact. The typical film thickness of a front TCO is around 80 nm to fulfill the anti-reflection condition. Due to low lateral conductivity of the thin ZnO film, a silver grid is thermally evaporated on TCO to support the current collection (Fig. 2.8, right). Important improvements of device performances such as Voc can be achieved by increasing the Al doping concentration of ZnO (not shown). Since the front TCO film is relatively thin, no significant reduction of the short circuit current due to absorption losses in ZnO:Al is measured for an Al concentration varied from 0.5 % to 2 %. However, the base-line process for thin-film silicon solar cells at our institute is based on a p-i-n configuration. Thick front TCO films (of approximately 800 nm) prepared at high temperatures (> 300 °C) are used that require low Al concentration to provide high transparency. Thus, for most of the n-i-p cells presented in this work, ZnO films with Al concentration of 0.5 % are used as a front contact. In the case the front TCO is deposited at 200 °C, the n-i-p cells show only a slight increase of the Voc and a slight decrease of the photocurrent (not shown) compared to the case the front TCO is deposited at RT. Therefore, most of the TCO front contacts of the n-i-p cells have been deposited at RT.

2.5 Summary

The Ag, Au and Al films necessary to obtain nanoparticles or other metal structures are deposited by thermal evaporation.
In contrast to its c-Si counterpart, a-Si shows variations in bond lengths and angles. Due to the disordered nature of the material, a-Si contains defects which can partially be passivated with hydrogen (a-Si:H). µc-Si:H is a composite material of crystalline regions, column boundaries, amorphous regions and voids. a-Si:H efficiently absorbs light between 300 and 800 nm. µc-Si:H efficiently absorbs light in the visible as well as in the red and infrared wavelength regions. Both a-Si:H and µc-Si:H are deposited by PECVD at around 180 °C. The properties of the resulting films – whether their structure is microcrystalline or amorphous – depend on the deposition parameters (silane to hydrogen ratio in the gas phase, plasma excitation frequency, substrate temperature, etc.). The TCO layers consisting of ZnO:Al are deposited by magnetron sputtering at temperatures up to 400 °C.
Due to the large defect density and consequently the short diffusion lengths of a-Si:H and µc-Si:H, solar cells based on a-Si:H and µc-Si:H consist of a p-i-n (or n-i-p) layer stack. The thin p- and n-doped layers expand a static electric field over the i-layer (the absorber layer) to efficiently separate the photo-generated carriers.
Standard thin-film silicon solar cells rely on a randomly textured substrate to achieve an efficient light trapping. In this work, a large amount of cells has been deposited on a flat substrate in order to clearly distinguish the contribution of the metal nanoparticles or nanostructures from that of the light scattering at rough surfaces. The denotation “p-i-n” and “n-i-p” only refers to the order of deposition of the n-, i- and p-layers. Almost all the cells prepared in this work are illuminated through the p-layer. In the p-i-n configuration, the front contact is realized with a 800 nm thick TCO layer. In the n-i-p configuration, the front contact (TCO) consists of a 80 nm thick anti-reflection layer covered with an Ag grid to support the current collection. For both configurations, a 80 nm thick TCO layer is inserted between the n-layer and the Ag mirror in order to increase the reflectivity of the back contact.

Chapter 3

Characterization Methods

We present here the main characterization methods used throughout this work and explain their physical background. First, we describe the measuring systems applied for the characterizaton of the electrical device properties. We explain how to interpret the current-voltage characteristics and how to extract the important information. We introduce the key-parameters of solar cells, namely the short-circuit current I_{sc}, the open-circuit voltage V_{oc}, the fill factor FF and the efficiency. Afterwards we describe the methods used for the optical characterization of the solar cells and samples. These methods are e.g. optical spectroscopy, angle-resolved scattering and Raman spectroscopy. We close this chapter with a discussion about the Surface Enhanced Raman Spectroscopy (SERS) effect and the role of the Raman spectroscopy for probing the electromagnetic field in the surrounding of metal nanoparticles.

3.1 Current-voltage characteristics

The current-voltage characteristics (I-V characteristics) of the solar cells were measured in the dark and under illumination. Since the temperature influences the electrical device properties, all measurements were carried out at room temperature. The absolute values of the dark I-V characteristics are generally plotted in a logarithmic scale (see Fig. 3.1, left). Different information about electrical device properties can be extracted from this curve. Dark I-V characteristics plotted in a logarithmic scale show three distinct regions (here referred to as A, B and C). Each region corresponds to a different working mode of the device. For negative and small voltages (zone A), the I-V curve behavior is dominated by the shunt resistance while for larger positive voltages (zone C), the series resistance of the solar cell leads to a deviation from the expected exponential diode characteristic. In zone B, the current increases exponentially with applied voltage, resulting in a linear behavior in a logarithmic scale. The dark I-V characteristic of a simple p-i-n diode (without losses) is described by equation 3.1 :

$$I(U) = I_O \cdot \left(\exp \frac{qU}{nkT} - 1 \right) \tag{3.1}$$

where $I(U)$ is the current density, U the applied voltage, I_0 the saturation current density, n the ideality factor or diode factor (which is correlated with recombination mechanisms and usually varies between 1 and 2) and T the temperature.

Taking into account the series resistance R_S and shunt resistance R_p, the equation of a thin-film silicon solar cell becomes :

$$I(U) = I_O \cdot \left(\exp \frac{q(U - I(U)R_s}{nkT} - 1 \right) + \frac{U - I(U)R_s}{R_p} \tag{3.2}$$

From the linear fit of the I-V curve, I_0 and n can be determined if the values of R_S and R_p are low and high enough, respectively.

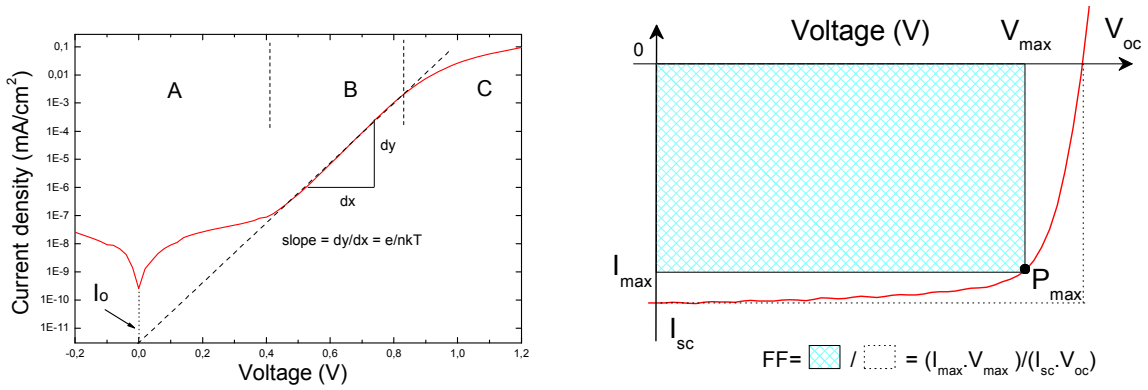

Figure 3.1 : I-V characteristics in the dark (left) and under illumination (right) of a pin diode.

The I-V characteristics under illumination were measured with a two-source solar simulator, which is so-called "class A" simulator creating a calibrated AM 1.5 spectrum with 1 kW.m^{-2} light intensity. Under illumination, charge carriers are generated in the i-layer of the p-i-n solar cell. Driven by the high static electric field existing in the i-layer, the electrons can reach the n-layer and the holes can reach the p-layer. This results in the creation of a photocurrent, mentioned above as i_{ph} (see Fig. 2.6). Assuming a superposition of dark current and photocurrent, the total current I(U) under illumination can be expressed by adding both contributions, the current in the dark and the photocurrent. Thus the total current is given by equation 3.3. In this case, recombination losses of the photo-generated carriers are neglected. However, this approach is not valid in particular for a-Si:H based solar cells.

$$I(U) = I_O.\left(\exp\frac{q(U - I(U)R_s}{nkT} - 1\right) + \frac{U - I(U)R_s}{R_p} - I_{ph} \quad (3.3)$$

From the I-V current under illumination (Fig. 3.1, right), one can determine several parameters:

- The short circuit current density I_{sc} which corresponds to the current obtained under short-circuit condition (for U = 0).

- The open-circuit voltage V_{oc} which is the voltage measured in an open-circuit mode (for I = 0). This parameter can be determined from equation 3.3. If we neglect losses ($I_{ph} \neq f(U)$, Rs = 0 and R_{shunt} very large) and consider Isc = I_{ph}, it can be written as :

$$V_{oc} = \left(\frac{nkT}{q}\right)\ln\left(\frac{I_{sc}}{I_o} + 1\right) \quad (3.4)$$

- The efficiency η defined as the ratio of the maximum power generated by the device (given by $P_{max}=I_{max}.V_{max}$) (see Fig. 3.1, right) and the incident radiation power.

- The fill factor FF defined as

$$FF = \frac{I_{\max}.V_{\max}}{I_{sc}V_{oc}} \quad (3.5)$$

  gives description of the "rectangularness" of the light I-V characteristic and is a measure of the collection efficiency of the photo-generated carriers at the maximum power point.

3.2 Spectral response

The spectral response (SR) of a solar cell gives more insight into the functioning of the device than the I-V characteristic under illumination. From SR data, conclusions about the optical losses and field distribution in the solar cell can be drawn. The absolute SR (λ) of a solar cell is defined by :

$$SR(\lambda) = \frac{I_{ph}(\lambda)}{B} \tag{3.6}$$

with $I_{ph}(\lambda)$ the generated photocurrent density per wavelength and B the power per area of incident light. From absolute SR data one can calculate the quantum efficiency $QE(\lambda)$ of the device by :

$$QE(\lambda) = \frac{I_{ph}(\lambda)}{e\Phi(\lambda)} = SR(\lambda)\frac{hc}{\lambda e} \tag{3.7}$$

with $\Phi(\lambda)$ the photonflux, corresponding to the number of photons provided by the light source at the wavelength λ per time unit and area.

The quantum efficiency can be interpreted as the probability that a photon with specific energy (at a specific wavelength) generates an electron-hole pair and that each generated carrier reaches its contact. The total photocurrent can be calculated by integration of the sun spectrum weighted by the QE of the device.

$$J_{ph}(V) = e\int QE(V,\lambda)\Phi(\lambda)d\lambda \tag{3.8}$$

In our measurements, $\Phi(\lambda)$ of (3.8) corresponds to the photon flux delivered by the sun simulator which creates a calibrated AM 1.5 spectrum.

3.3 Optical spectroscopy

Reflection and transmission measurements were carried out using a two-beam spectrometer (Perkin Elmer, Lambda 19) allowing optical characterization in the ultraviolet, visible and infrared range, i.e. from 185 nm to 3200 nm. In this system, the sample is placed at the ports of an Ulbrich sphere, permitting to evaluate the contribution of the diffuse scattered light to the total light in both reflection and transmission. The absorption (A=1-T-R) can be deduced from the measured reflection (R) and transmission (T) data. To calculate the absorption, reflection and transmission measurements were carried out at the same position of the sample since inhomogeneities in the film thickness and/or in the surface roughness can cause errors when combining the values. Each of the two detectors used in the two-beam spectrometer only covers a part of the wavelength range – namely 185 nm to approximately 850 nm for the first detector and 850 nm to 2500 nm for the second detector. Moreover the

diffraction gratings within the spectrometer which permit to separate the beam of white light into its constituent spectral colors is changed at approximately 850 nm, too. The transition of the two detectors and the change of the two diffraction gratings are responsible of the appearance of extrema in the reflectance or the transmitance at 850 nm. The amplitude of the extrema is more pronounced when aperture plates with small diameter – necessary for the optical characterizaton of small areas – are used.

3.4 Angle resolved scattering measurements

In order to evaluate the angle distribution of the diffuse scattered light found at rough surfaces (e.g. textured TCO, substrates covered with large nanoparticles or nanostructures), angle resolved scattering measurements were carried out using a photogoniometer, as illustrated in Fig. 3.2. In our experiments, the samples were illuminated with different lasers with a wavelength of 550 nm, 633 nm and 897 nm.

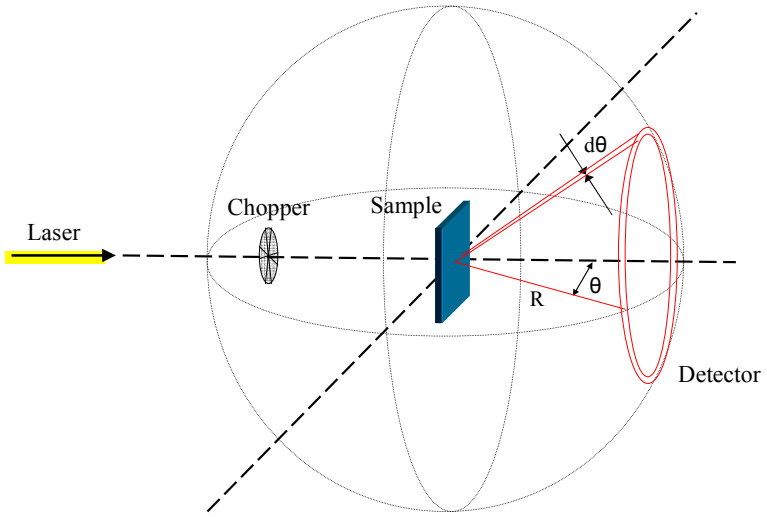

Figure 3.2 : Measurement principle of the angle resolved scattering spectroscopy.

The light intensity of the diffuse scattered light is measured with a photodiode which can be moved automatically around the sample. The signal received by the photodiode is amplified by means of a Lock-in amplifier which, applied in combination with a light chopper positioned between the laser source and the sample, allows to eliminate the contribution of the parasitic light (e.g. light within the room). This set-up thus permits to detect low intensity

signals. The intensity of the scattered light measured at an angle θ is normalized with the intensity of the laser beam measured at 0 ° without the sample. The angle θ is defined according to Fig. 3.2. The angles 90 ° < θ < 270 ° correspond to the light which is reflected. Transmitted light is scattered in angles between -90 ° and 90 °. In this work, we only investigated the scattering properties of opaque reflectors. Therefore, we limited the measurements to the reflection mode. Since all the investigated reflectors behave as isotropic scatterers, the results show a symmetrical angle distribution in respect to the illumination axis. Consequently only the reflection in the range 90 ° < θ < 180 ° is given.

3.5 Raman spectroscopy

3.5.1 Raman spectroscopy, principle

Raman spectroscopy is used in condensed matter physics and chemistry to study vibrational, rotational, and other low-frequency modes in a system. It relies on inelastic scattering (Raman scattering) of monochromatic light, usually from a laser in the visible, near infrared, or near ultraviolet range. The laser light interacts with phonons or other excitations in the system, resulting in the energy of the laser photons being shifted up by absorption of a phonon (anti-Stokes process) or down by generation of a phonon (Stokes process). The shift in energy gives information about the phonon modes in the system and thus about the structural properties of the material. Consequently each material has its own corresponding Raman spectra. An extensive discussion of the theory of the method is given in the literature (e.g. Long, 1977; Cardona, 1982). Fig. 3.3 shows typical Raman spectra of crystalline (c-Si), amorphous (a-Si:H) and microcrystalline silicon (μc-Si:H), obtained in the spectral range 400 cm^{-1} to 560 cm^{-1} of the transverse optical phonon mode in crystalline and amorphous silicon. The main feature in the Raman spectrum of c-Si is a band with a full width at half maximum (FWHM) below 15 cm^{-1} centred at 520 cm^{-1} corresponding to the excitation of the Γ'_{25} phonon. A broad band with FWHM of about 70 cm^{-1}, centered at 480 cm^{-1} characterises the Raman spectrum of a-Si:H. Both features are observed in the Raman spectra of μc-Si:H with different contributions. An additional contribution from structural defects of the crystalline phase leads to the shoulder at 492 cm^{-1}. This was previously found in the presence of hexagonal silicon (Kobliska and Solin, 1973). Due to finite grain size and stress in μc-Si:H, the peak arising from the crystalline signal contribution is often shifted with respect to the resonance of the Γ'_{25} phonon in c-Si and broadened (Richter et al. 1981). Raman measurements can provide qualitative information but also quantitative information if the

measurements are carefully performed. The Raman intensity is proportional to the square of the polarity *p* of the molecule being studied expressed as :

$$p = \alpha E \tag{3.9}$$

α is the polarizability of the material and E denotes the incident electric field. The polarizability of a material corresponds to the relative tendency of the electron cloud to be distorted from its normal shape by an external electric field. Only the changes in vibration which are accompanied by a modification of the polarizability can be detected by Raman measurements.

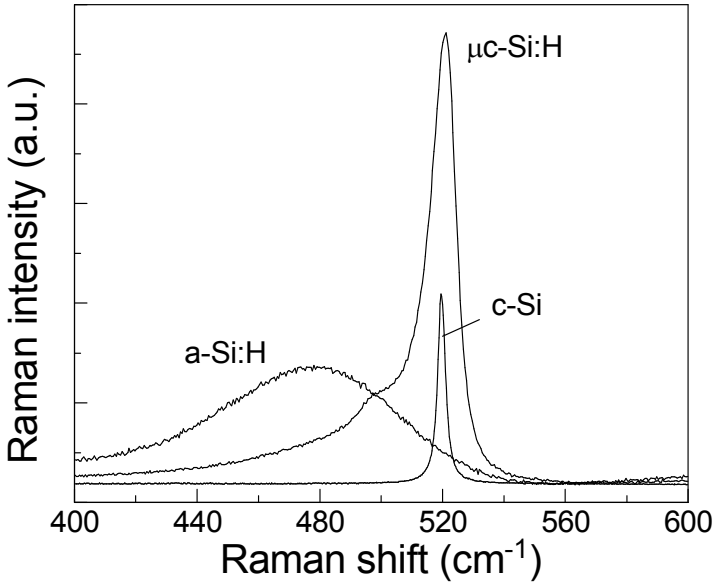

Figure 3.3 : Raman spectra of crystalline silicon (c-Si) together with amorphous silicon (a-Si:H) and microcrystalline silicon (μc-Si:H). Note, that the height of the latter two Raman spectra was chosen to have equal intensity.

It is known that metal nanoparticles as well as rough metal surfaces can lead to a strong amplification of the Raman intensity of molecules adsorbed on the metal. This technique which is known as Surface Enhanced Raman Spectroscopy is often abbreviated SERS and is sensitive enough to detect single molecules adsorbed on metal surface (Nie and Emory, 1997; Kneipp et al., 1997; Vlckova et al. 2007). Colloidal Au and Ag in solution can render SERS active by adsorbate-induced particles aggregation (Chang and Furtak, 1982; Lee and Meisel, 1982). An amplification of the Raman signal which correlates with a strong decrease of the reflectivity, was found by Sukmanowski et al. (2000) for systems based on a-Si:H containing metal films. This is ascribed to an improved light absorption in the a-Si:H material origniating from an increased electromagnetic field *E* in the vicinity of the metal film.

3.5.2 SERS effect and its origin

Retrospective about the SERS effect is made by Moskovits (2005, 2006) and Kneipp et al. (2002). The exact mechanism of the enhancement effect of SERS is still a matter of debate in the literature. There are two primary theories and while their mechanisms are different from each other, distinguishing them experimentally is not straightforward. The first one is electromagnetic theory, proposed by Jeanmaire and Van Duyne (1977) which relies upon the excitation of localized surface plasmons. The second one, chemical theory proposed by Albrecht and Creighton (1977), is based on charge-transfer (resulting in a variation of the molecule polarizability). The chemical theory only applies for species which have formed a bond with the metal surface, so it clearly cannot explain the observed signal enhancement in all cases, while the electromagnetic theory can apply even in those cases where the specimen is only physisorbed to the surface. The electromagnetic theory of SERS accounts for all major SERS observations (Moskovits, 2005). Therefore, a detailed description of this theory is given here.

When an incident light strikes a metal surface, localized surface plasmons are excited. The field enhancement is greatest when the plasmon frequency, ω_p, is in resonance with the radiation. Furthermore, in order for scattering to occur, the plasmon oscillations must be perpendicular to the surface. If they are in-plane with the surface, no scattering will occur. It is because of this requirement that roughened surfaces or nanoparticles are typically employed in SERS experiments as these surfaces provide an area on which the localized surface plasmons can take place (Smith and Dent, 2005). The reason that the SERS effect is so pronounced is because the field enhancement occurs twice. Moskovits (2005, 2006) explains this phenomenon for metal nanoparticles. If we define g as the field enhancement averaged over the surface of the particle, the average magnitude of the field E_s radiated by the particle (in the close vicinity) is $E_s = gE_0$, where E_0 is the magnitude of the incident field. Thus a molecule adsorbed on the surface of the nanoparticle will be excited by a field of magnitude E_s and the Raman scattered light produced by the molecule will have a magnitude of $\alpha_R E_s$, where α_R is the appropriate combination of components of the Raman tensor. The Raman signal is then further amplified by the nanoparticle by the same mechanism as the incident light was. The amplitude of the SERS-scattered field will be given by $E_{SERS} \propto \alpha_R gg' E_0$, with g' the enhancement factor of the field at the shifted wavelength of the Raman scattered light. The average SERS intensity will thus be proportional to the square modulus of E_{SERS}, i.e. $I_{SERS} \propto |\alpha_R|^2 |gg'|^2 I_0$, with I_{SERS} and I_0 the intensities of the SERS-scattered light and

incident light, respectively. The enhancement is not equal for all frequencies. For the frequencies for which the Raman signal is only slightly shifted from the incident light, both the incident laser light and the Raman signal can be near resonance with the plasmon frequency. Under these conditions, the SERS intensity will be enhanced by a factor proportional to the fourth power of the enhancement of the local incident near-field. When the frequency shift is large, the incident light and the Raman signal cannot both be on resonance with ω_p, thus the enhancement at both stages cannot be maximal (Campion and Kambhampati, 1998).

3.6 Summary

The dark I-V characteristics plotted in a logarithmic scale can be separated in three distinct regions. The low- and high-voltage regions are dominated by the shunt resistance and the series resistance, respectively. In the mid-bias region, an exponential behavior is observed. The I-V characteristics under illumination (AM 1.5 = 1 $kW.m^{-2}$) allow to determine the short circuit current (I_{sc}), the open-circuit voltage (V_{oc}), the fill factor (FF) and thus the efficiency of a solar cell. The QE corresponds to the probability that a photon with specific energy generates an electron-hole pair and that each generated carrier reaches its contact.
The optical spectrometer using an integrating sphere allows to measure the total and diffuse fraction of both transmitted and reflected light of a sample. The absorption can be deduced from the measured data. The angle resolved scattering measurements enable the establishment of the angular intensity distribution of the scattered light.
Raman measurements are commonly used to characterize the structural properties of a material. Metal nanoparticles as well as rough metal surfaces can lead to a strong increase of the Raman signal of molecules adsorbed on the metal (SERS effect). This is mainly explained by the enhanced electromagnetic field present in the vicinity of the metal nanoparticles or metal surfaces induced by localized surface plasmons (LSP). In this work we aim to use Raman spectroscopy to give evidence of (i) the existence of a local enhancement of the electromagnetic field resulting from the LSP and/or (ii) the contribution of other effects such as charge transfer.

Chapter 4

Structural and optical characterization of metal films

We open this chapter with a description of the structural properties of thin silver, gold and aluminum films deposited on ZnO:Al and a-Si:H. The influence of the substrate and the effect of an annealing treatment on the morphology of the metal films are discussed. In a subsequent step, the metal films are characterized optically. The medium surrounding the metal films is then varied in order to understand its impact on the optical response. To finish, Raman measurements of a-Si:H-based layer stacks with embedded metal films are performed in order to identify the existence of a local electromagnetic field enhancement.

4.1 Structural characterization of Ag, Au and Al films deposited on ZnO and amorphous silicon

In order to make use of the effect of metal nanoparticles to increase the photocurrent of a-Si:H solar cells, the nanoparticles have to be deposited on TCO (ZnO:Al) or amorphous silicon (a-Si:H) – the two major materials constituting a-Si:H solar cells.
Ag films with thickness of a few nanometers deposited by thermal evaporation on TCO show an island film structure, i.e. separated nanoparticles. For metal films thicker than 5 nm, the Ag film shows a percolation continuum, i.e. random clusters that are connected to each other. A SEM picture of a 3 nm Ag film deposited on TCO, showing a structure close to the percolation threshold (i.e. particles of various shapes and sizes nearly connected to each other) is presented as an example in Fig. 4.1 (left). A thermal treatment of 1 h at 180 °C – corresponding to the duration and temperature of the pre-heating step required to deposit a-Si:H – leads to the formation of well separated particles with ellipsoidal shapes. For 3 nm Ag, particles with an average diameter of around 30 nm are found (see Fig. 4.1, right). For longer annealing time (several hours) and/or higher temperature (up to 300 °C), the inter-

particle distance further increases and Ag nanoparticles with slightly larger sizes can be obtained.

Au and Al films with thickness up to 3 nm were deposited as well. Au films thinner than 2 nm show separated particles before annealing. Thicker films exhibit a percolation continuum. As an example, Fig. 4.2 (left) shows a SEM picture of 3 nm Au on TCO before thermal treatment. Annealing the sample at a temperature of 180 °C for 1 h leads to a modification of the film morphology. The Au coalescences and the surface area covered by the metal is reduced. Nevertheless a structure showing a percolation continuum is still observed after the thermal treatment (Fig. 4.2, right).

Al films of a few nanometers deposited on TCO exhibit a continuous layer structure before annealing, as shown in the case of 3 nm Al (Fig. 4.3, left). Annealing the sample has no significant influence on the Al film morphology (Fig. 4.3, right).

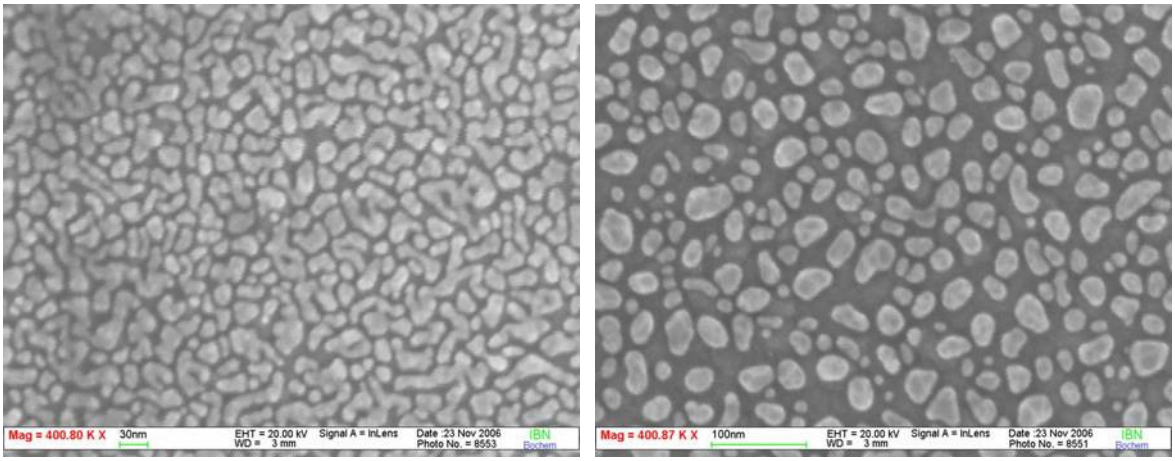

Figure 4.1 : SEM pictures of 3 nm Ag deposited on glass/Ag/TCO before (left) and after (right) annealing in vacuum at 180 °C for 1 h.

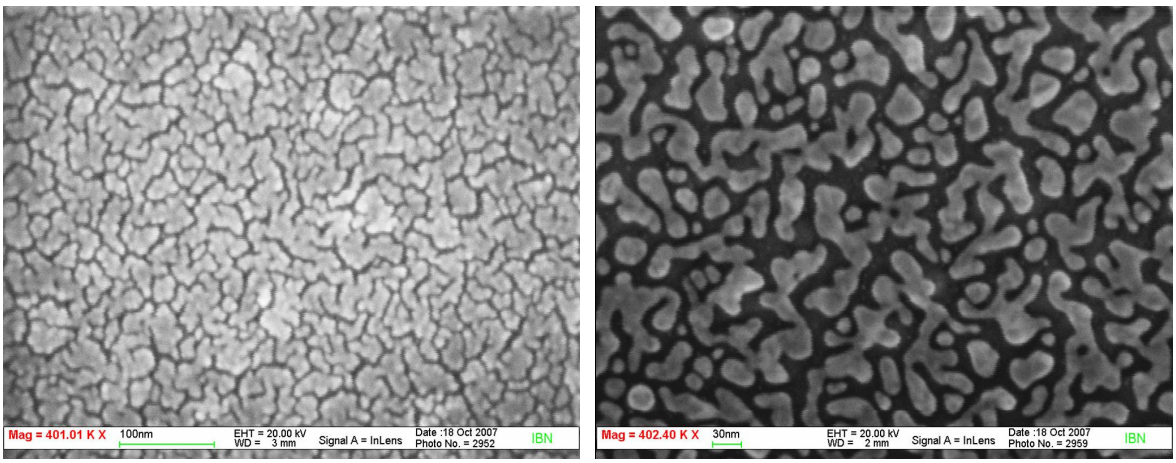

Figure 4.2 : SEM pictures of 3 nm Au deposited on glass/Ag/TCO before (left) and after (right) annealing in vacuum at 180 °C for 1 h.

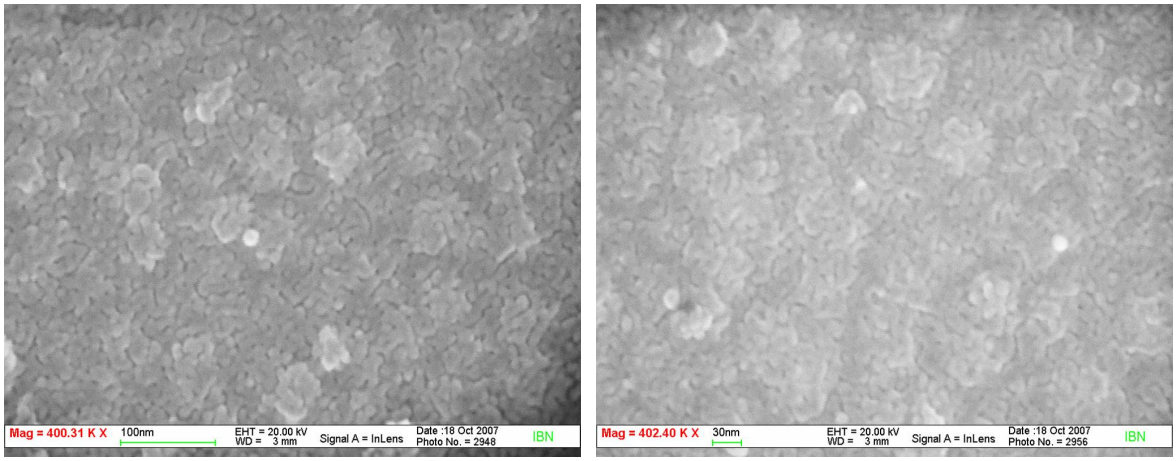

Figure 4.3 : SEM pictures of 3 nm Al deposited on glass/Ag/TCO before (left) and after (right) annealing in vacuum at 180 °C for 1 h.

Similar trends are observed when the metal films are deposited on a-Si:H. Before annealing, Ag and Au films thinner than around 1 nm show separated particles. For thicker films, Ag and Au films exhibit a percolation continuum (Fig. 4.4 and 4.5, left, respectively). In contrast, Al shows a continuous layer structure for films of a few nanometers (Fig. 4.6, left). After an annealing treatment in vacuum of 1 h at a temperature of 180 °C, well separated nanoparticles are formed with Ag (Fig. 4.4, right). The Au film structure is modified but it still shows a percolation continuum for thicknesses thicker than around 1 nm (Fig. 4.5, right). The Al film morphology is not influenced by the temperature treatment (Fig. 4.6, right). Annealing the sample for several hours leads to a slight modification of the film morphology but a continuous layer structure is still observed after that.

To conclude, the thermally evaporated metal films (Ag, Au and Al) show similar structures on both types of substrates (a-Si:H and TCO). Independently of the Ag film thickness (thinner than 10 nm), well separated Ag nanoparticles with ellipsoidal shapes can easily be obtained on a-Si:H and TCO by performing an annealing treatment at a relatively low temperature. Only for metal films thinner than 1-2 nm, separated particles can be found with Au. In the case of Al, nanoparticles can be obtained for films thinner than 0.5 nm (see section 4.3.4).

A different structural behavior was found when metal films were evaporated on Corning glass (see chapter 7).

The nucleation conditions of Ag films deposited on c-Si also differ. Separated particles are already observed before annealing for Ag films thinner than 10 nm (not shown).

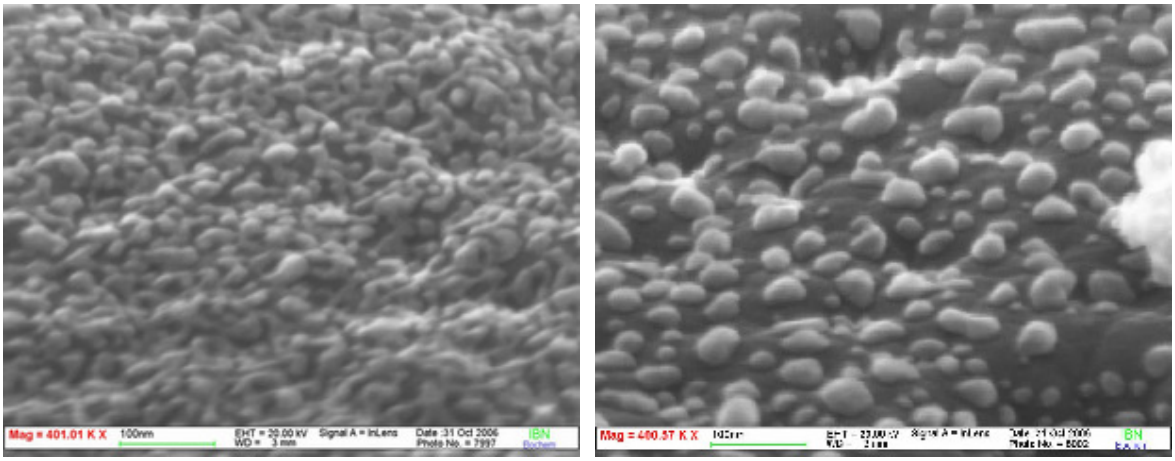

Figure 4.4 : SEM pictures of 3 nm Ag deposited on glass/a-Si:H before (left) and after (right) annealing at 180 °C for 1 h. The measurements were conducted at an angle of inclination of 60 ° with respect to the surface horizontal to determine the height of the obtained structures.

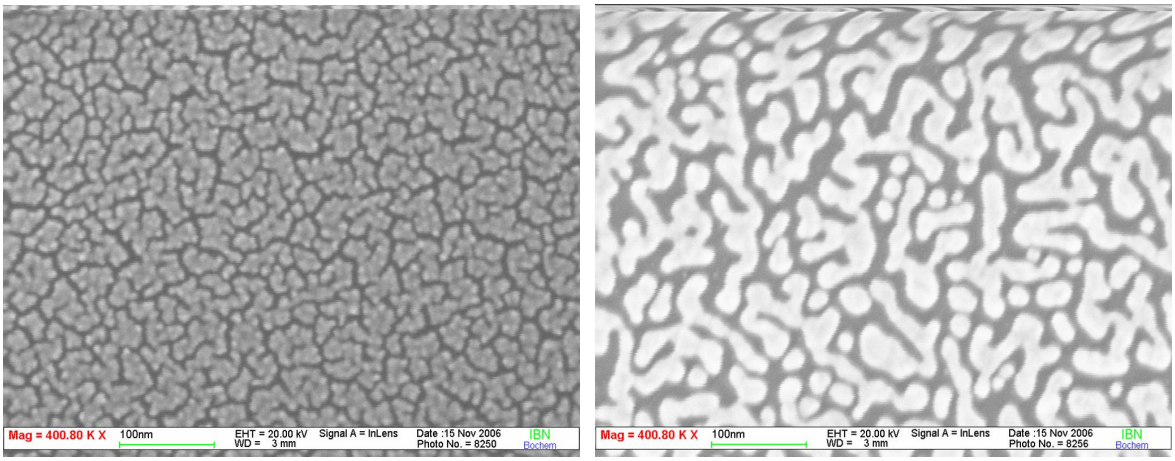

Figure 4.5 : SEM pictures of 3 nm Au deposited on glass/a-Si:H before (left) and after (right) annealing in vacuum at 180 °C for 1 h.

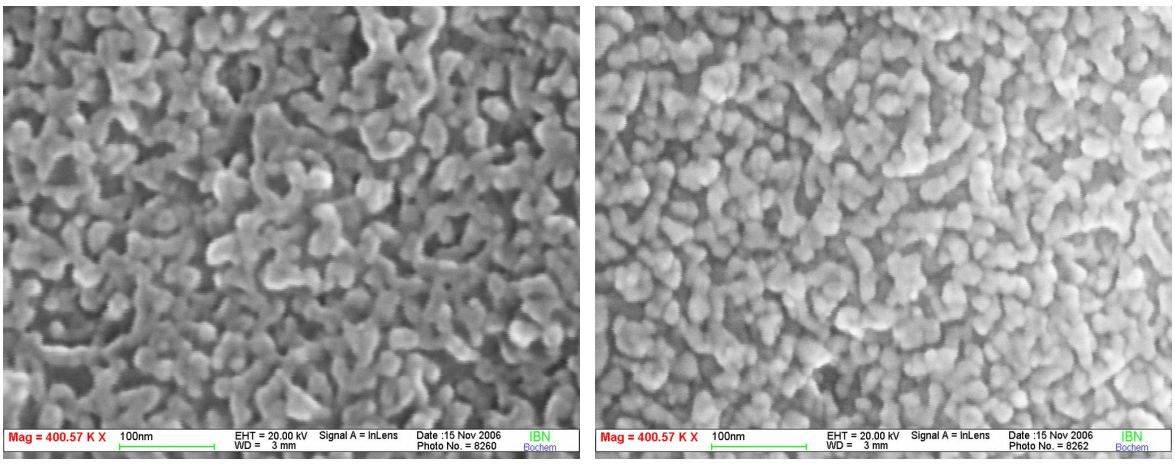

Figure 4.6 : SEM pictures of 3 nm Al deposited on glass/a-Si:H before (left) and after (right) annealing in vacuum at 180 °C for 1 h.

4.2 Optical characterisation of Ag, Au and Al films deposited on ZnO and amorphous silicon

The optical behavior of metal films depends on the considered material but also on the morphology. It is also influenced by the surrounding medium (cf. Fig. 1.3). It is thus important to study the optical response of Ag, Au and Al films in the particular case they are deposited on silicon and ZnO. For the present study, two different layer stacks were prepared, the first one consisting of glass/a-Si:H and the second one consisting of glass/ZnO, both covered on their half with a metal film (see Fig. 4.7). The Corning glass provides a high transparency as well as a very smooth surface. To minimize the light absorption in silicon or ZnO and therefore clearly distinguish the optical contribution of the metal film from that of the "substrate", very thin a-Si:H and ZnO layers of 10 nm and 80 nm, respectively, were used. The metal films were prepared by thermal evaporation of 3 nm Ag, Au and Al and post annealing at 180 °C for 1 h. Reflection and transmission measurements were performed by using an integrating sphere. The light absorption was deduced from the measured data. The layer stacks were alternately illuminated from both sides.

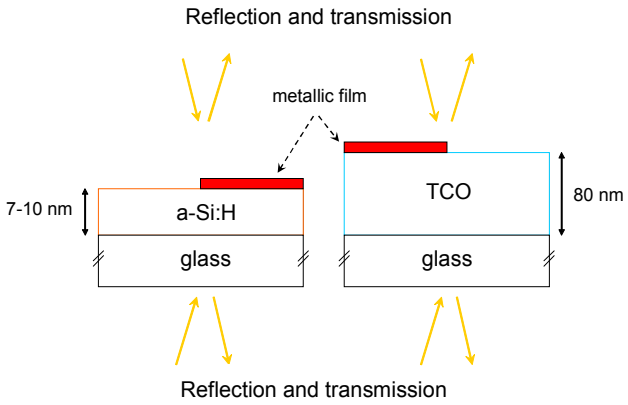

Figure 4.7 : Schematic drawing of a metal film deposited on (left) glass/a-Si:H and on (right) glass/TCO. Very thin a-Si:H and ZnO layers with thickness of ~ 10 nm and 80 nm are used. Reflection and transmission measurements are performed from both sides of the layer stacks.

4.2.1 Optical response of metal films deposited on glass/a-Si:H

Fig. 4.8 to Fig. 4.10 show the optical measurements of glass/a-Si:H layer stacks with and without metal film, after annealing at 180 °C for 1 h, illuminated from the glass side (left) and from the a-Si:H side (right). The layer stack without metal film shows a similar light

transmission in the whole spectral range irrespective of the side of illumination. For wavelengths longer than 400 nm, the reflectivity is also identical from both sides of the layer stack. For shorter wavelengths the reflection measured from the glass side drops and becomes significantly smaller than the reflection measured from the a-Si:H side. The enhanced absorption in the short wavelength range may be due to a better light incoupling when the light illuminates from the glass side. Indeed, a better matching of the refractive indices *n* is obtained for light propagating in the air ($n_{air} \sim 1$) and penetrating from the glass side ($n_{glass} \sim 1.5$) than when light penetrates from the a-Si:H side ($n_{a\text{-}Si:H} \sim 4$). The light absorption of the glass/a-Si:H layer stack covered with Ag nanoparticles (cf. Fig. 4.4, right) exhibits a distinct peak at around 500 nm which is not found in the absorption spectrum of the layer stack without nanoparticles. This maximum is attributed to the localized surface plasmon (LSP) absorption (c.f. section 1.1) of the Ag nanoparticles. Compared with the optical response of glass/a-Si:H/Ag-film before annealing, showing a distinct peak at around 520 nm (Fig. 4.8, left, squares), the annealing process causes a blue shift of the resonance. This is likely due to the temperature-induced modification of the Ag film morphology (before annealing : structure close to the percolation threshold, after annealing : well separated nanoparticles).

The triangles in Fig. 4.8 (left) represent the absorption gain in presence of nanoparticles, i.e. $Abs_{with\ NP} - Abs_{without\ NP}$. This gain corresponds to the LSP resonance of the Ag nanoparticles and occurs at around 480 nm. For spherical and isolated Ag nanoparticles in air ($n_{air} \approx 1$), with diameter much smaller than the wavelength of the incoming light, the LSP resonance is expected to occur at around 3.5 eV – which corresponds to a wavelength of ≈ 350 nm (see Fig. 1.3). The observed discrepancy in the peak position of the resonance may originate from (i) the influence of the a-Si:H-based substrate ($n_{a\text{-}Si:H} \sim 4$), (ii) the ellipsoidal shape of the nanoparticles (see Fig. 1.5), (iii) the size of the nanoparticles (see Fig. 1.6) (Sönnichsen et al., 2000-2002) and/or (iv) the interaction of the nanoparticles which are separated from each other by only a few nanometers (Liu et al., 1998). A reasonable approximation for the effect (i) is to replace the spherical particle on the a-Si:H substrate by a spherical particle in a medium with an averaged dielectric function ε_a in between the air value and that of the a-Si:H material (Kreibig and Vollmer, 1995). $\varepsilon_a \sim ½(1+ \varepsilon_{a\text{-}Si:H})$. In this case, the LSP resonance occurs at around 2.7 eV (see Fig. 1.8, for $\varepsilon_1 = -2.\varepsilon_a$), i.e at 460 nm. This already provides a good agreement with the experimental data. If we consider the effects (ii), (iii) and (iv), a red-shift of the LSP resonance is expected. The broadening of the measured LSP resonance is probably due to the broad distribution in size and shape of the nanoparticles. When the layer stack is illuminated from the glass side, the LSP absorption of the Ag nanoparticles found at 480 nm is probably associated with an increased light absorption in a-Si:H, due to an enhancement of the electromagnetic field in the surrounding of the Ag nanoparticles (see section 1.1). For an illumination from the a-Si:H side, no absorption peak can be recognized in presence of Ag nanoparticles compared to the layer stack without nanoparticles.

The optical response of 3 nm Au and Al films deposited on glass/a-Si:H layer stack after annealing is shown in Fig. 4.9 and 4.10, respectively. Nearly identical trends as those presented here are found before annealing (not shown). This correlates with the fact that the film morphology is not considerably altered by the annealing treatment. Both metal films lead to a strong decrease in reflection and transmission when light penetrates from the glass side. When light enters the layer stack from the a-Si:H side, the transmission is strongly reduced in presence of the Au and Al films compared to the case of the layer stack without metal film. On the other hand, a slight increase in reflection can be observed. The enhanced light absorption found in the whole spectral range for the samples with Au and Al films results from absorption losses in the metal. This optical behavior differs from the one of the Ag film which shows a relatively distinct absorption peak.

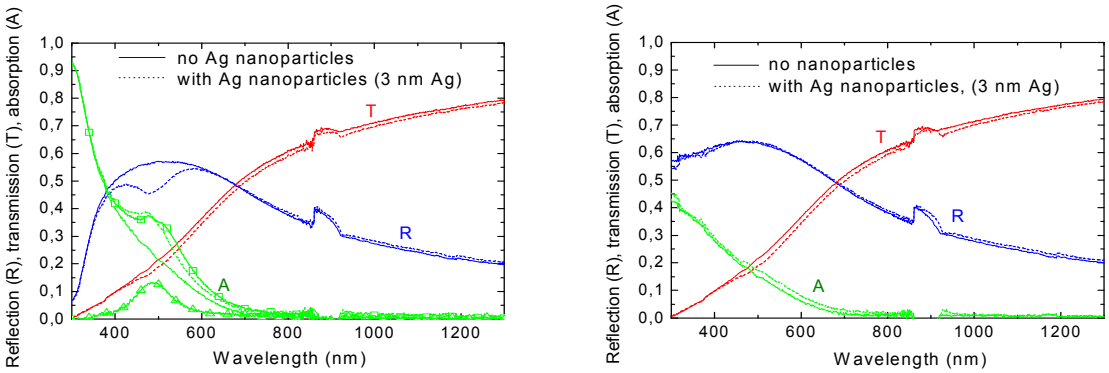

Figure 4.8 : Transmission (T), reflection (R) and absorption (A) of glass/a-Si:H (Fig. 4.7, left) with and without Ag nanoparticles after annealing at 180 °C for 1 h. The sample is illuminated from the glass side (left) and from the a-Si:H side (right). The squares represent the absorption of glass/a-Si:H/Ag-film before annealing. The triangles correspond to the absorption gain obtained by covering the sample with Ag nanoparticles ($A_{\text{with NP}} - A_{\text{without NP}}$).

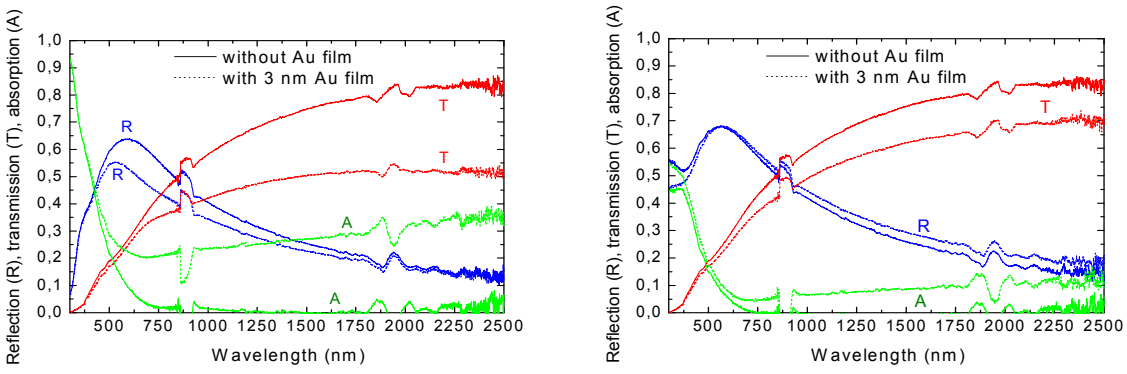

Figure 4.9 : Transmission (T), reflection (R) and absorption (A) of glass/a-Si:H (Fig. 4.7, left) with and without Au film after annealing at 180 °C for 1 h. The sample is illuminated from the glass side (left) and from the a-Si:H side (right).

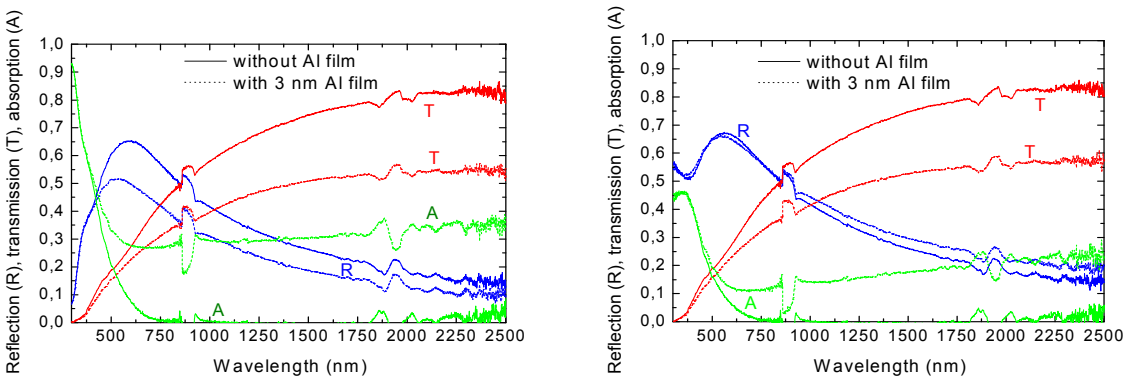

Figure 4.10 : Transmission (T), reflection (R) and absorption (A) of glass/a-Si:H (Fig. 4.7, left) with and without Al film after annealing at 180 °C for 1 h. The sample is illuminated from the glass side (left) and from the a-Si:H side (right).

4.2.2 Optical response of Ag nanoparticles of various sizes on glass/TCO

In order to investigate the influence of the particle size and the inter-particle distance of Ag nanoparticles on the optical response, glass/TCO layer stacks (Fig. 4.7, right) were covered with Ag films annealed at 180 °C with thickness varied between 0.2 nm and 5 nm. SEM pictures of the resulting nanoparticles are shown in Fig. 4.11. For Ag film thicknesses varied between 0.2 nm and 2 nm, the average size of the obtained particles remains nearly constant, equal to approximately 10 nm, but the inter-particle distance decreases. For thicker Ag films, the average size of the nanoparticles increases and particles with a lateral diameter of around 30 nm are found for a 5 nm thick Ag film.

Fig. 4.12 shows the absorption gain obtained in presence of Ag nanoparticles, i.e. $Abs_{with\ NP} - Abs_{without\ NP}$, for glass/TCO/(nanoparticles) layer stacks illuminated from the glass side. The layer stacks with nanoparticles exhibit a resonant absorption peak in comparison to the layer stack without nanoparticles, ascribed to localized surface plasmon (LSP) of the nanoparticles. The absorption is more pronounced in the case light penetrates from the glass side of the system than when light penetrates from the other side (comparison not shown). Independently of the illumination side, a general increase of the amplitude associated with a red-shift of the LSP peak and a broadening of the line-width are found for smaller inter-particle distances (from 0.2 nm to 2 nm Ag) and larger average particle sizes (from 2 nm to 5 nm Ag). The variation of the position and shape of the LSP resonance with respect to the average particle size follows the calculated trends presented in Fig. 1.6 (Mie theory). Similar trends are reported by Sönnichsen et al. (2000-2002) and Liu et al. (1998). For 3 nm Ag deposited on glass/TCO, Fig. 4.12 shows an absorption peak at around 600 nm. This differs from the result obtained for 3 nm Ag deposited on glass/a-Si:H where an absorption peak was observed at

around 500 nm (Fig. 4.8, left). This discrepancy is attributed to a deviation of the deposited Ag film structure due to the different applied substrates. The nanoparticles deposited on TCO probably present a lower aspect ratio (see Fig. 1.5) than the nanoparticles deposited on a-Si:H.

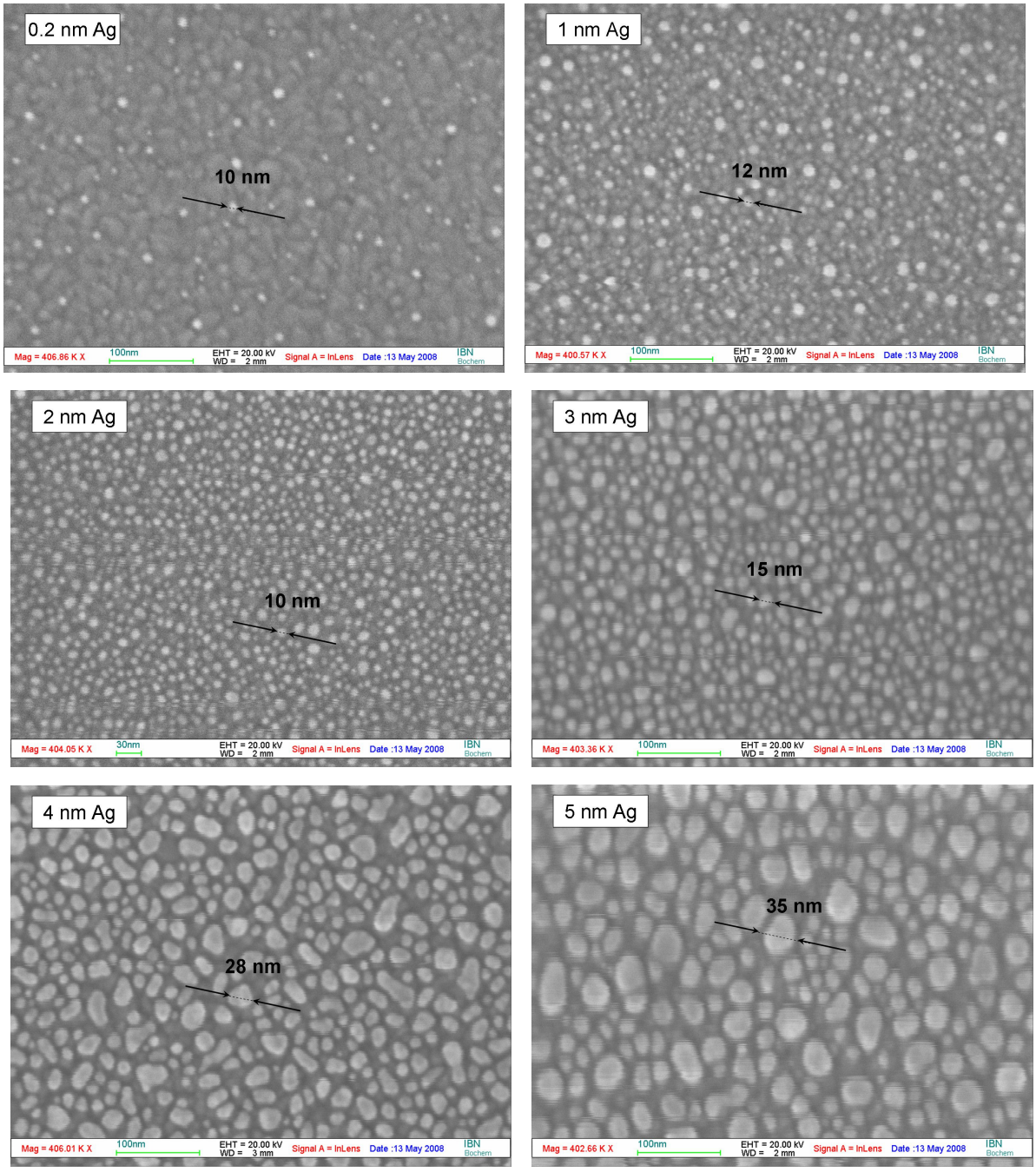

Figure 4.11 : SEM pictures of Ag films with thickness varied between 0.2 nm and 5 nm deposited on glass/TCO(80 nm) after annealing at 180 °C for 2 h.

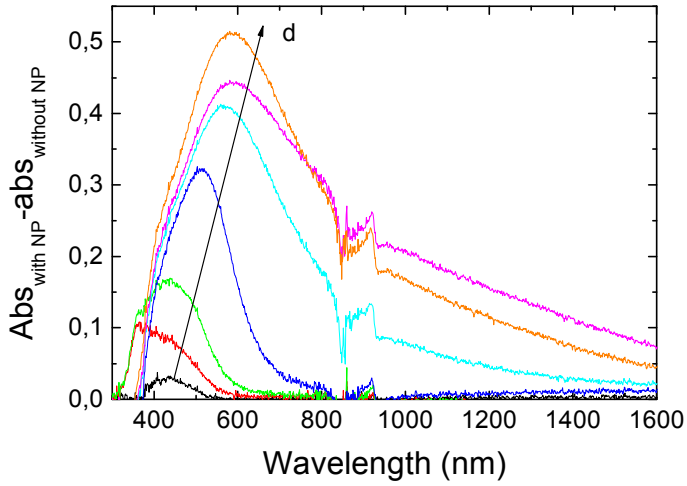

Figure 4.12 : Absorption gain of glass/TCO layer stacks covered with Ag nanoparticles, i.e $Abs_{with\ NP}$-$Abs_{without\ NP}$. The thickness *d* of the Ag film is varied between 0.2, 0.5, 1, 2, 3, 4 and 5 nm in order to obtain nanoparticles of various sizes. The sample is illuminated from the glass side.

4.3 Optical characterisation of Ag, Au and Al films covered with amorphous silicon

4.3.1 Absorption of metal films covered with amorphous silicon

As mentioned before, the optical behavior of metal films can be influenced by their surrounding medium. For metal nanoparticles for example, the position of the LSP resonance is strongly correlated with the refractive index of their embedding medium (equation 1.8 and Fig. 1.3). Both glass/a-Si:H and glass/ZnO layer stacks introduced in section 4.2, with and without metal film (3 nm Ag, Au and Al), were covered with a thin a-Si:H layer of approximately 10 nm, as shown in Fig. 4.13. The transmission and reflection measurements were performed for an illumination from the glass side and from the a-Si:H side. Fig. 4.14, 4.15, 4.16 show the absorption of layer stacks with 3 nm Ag, Au and Al, respectively. The absorption data of the layer stacks without the second a-Si:H layer – already shown is the previous section (Fig. 4.8 to Fig. 4.10) – are replotted for comparison. Covering glass/a-Si:H with a second a-Si:H layer leads to an enhanced light absorption in the blue wavelength region for both illumination sides, due to the larger layer thickness and the high absorption coefficient of a-Si:H material in this wavelength range. Independently of the illumination

side, the layer stack with Ag nanoparticles embedded in a-Si:H shows a strong absorption peak at around 750 nm compared to the layer stack without metal film. The position of the LSP resonance is in good agreement with the one predicted by Mie in the case of a spherical Ag nanoparticle of radius 10 nm (see Fig. 1.3). The discrepancy is probably due to the ellipsoidal shape of the deposited particles. In Fig. 4.14, a larger absorption is obtained if light enters from the glass side. However the opposite behavior was observed when 50 nm thick a-Si:H layers were applied (not shown). In this case, a higher absorption was measured for an illumination from the a-Si:H side. It is therefore not straightforward to conclude if it is an illumination from the glass side or from the other side – according or not to the growth direction of the nanoparticles – that leads to a larger light absorption.

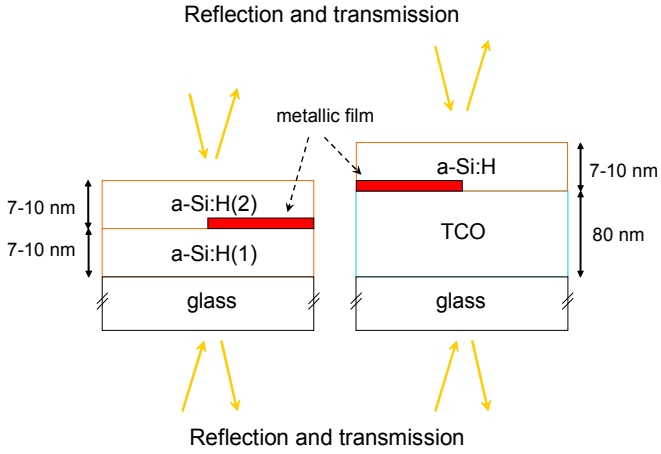

Figure 4.13 : Schematic drawing of a metal film deposited on glass/a-Si:H (left) and glass/TCO (right) covered with a 10 nm a-Si:H layer. The reflection and transmission measurements are alternately performed from both sides of the systems.

The absorption peak observed when the nanoparticles are in contact with air moves towards longer wavelengths when they are embedded in a-Si:H. This effect is due to the higher refractive index of silicon ($n_{a\text{-}Si:H} \sim 4$) in comparison to the one of air ($n_{air} \sim 1$), according to equation 1.8.

The amplitude of the absorption peak (and especially the amplitude of the absorption gain, i.e. $abs_{with\ nanoparticles}$-$abs_{without\ nanoparticles}$) increases for nanoparticles covered with a-Si:H. This result is similar to the one presented in Fig. 1.3. However it is not possible at this stage to say if the resonant light absorption occuring in the Ag nanoparticles is accompanied by an enhanced light absorption in a-Si:H due to a local increase in the electromagnetic field

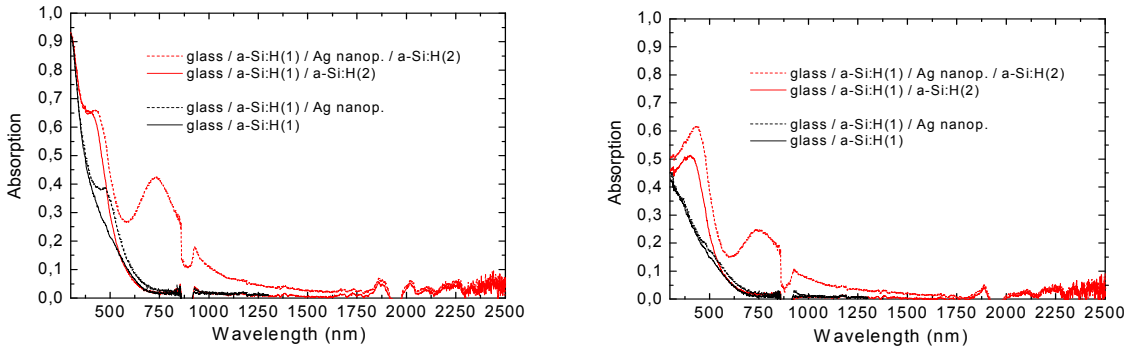

Figure 4.14 : Absorption of glass/a-Si:H(1)/a-Si:H(2) with and without Ag nanoparticles. The sample is illuminated from the glass side (left) and from the a-Si:H side (right). For comparison, the absorption of the layer stack without a-Si:H(2) is replotted.

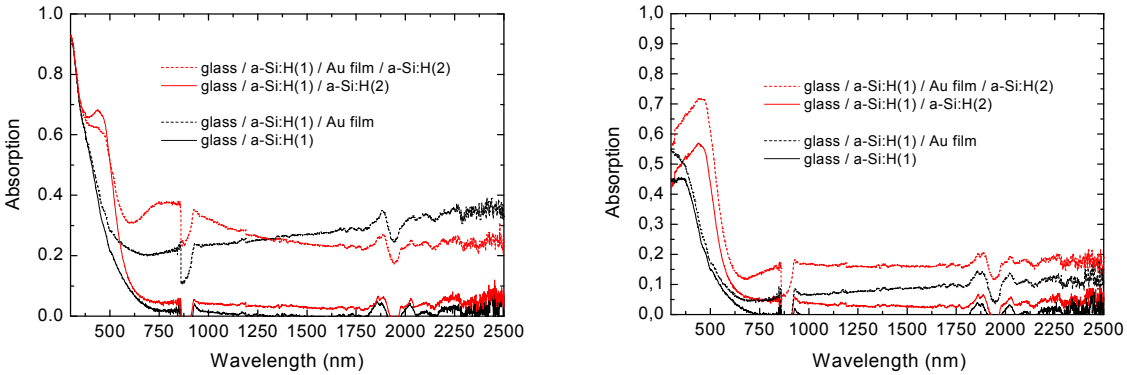

Figure 4.15 : Absorption of glass/a-Si:H(1)/a-Si:H(2) with and without Au film. The sample is illuminated from the glass side (left) and from the a-Si:H side (right). For comparison, the absorption of the layer stack without a-Si:H(2) is replotted.

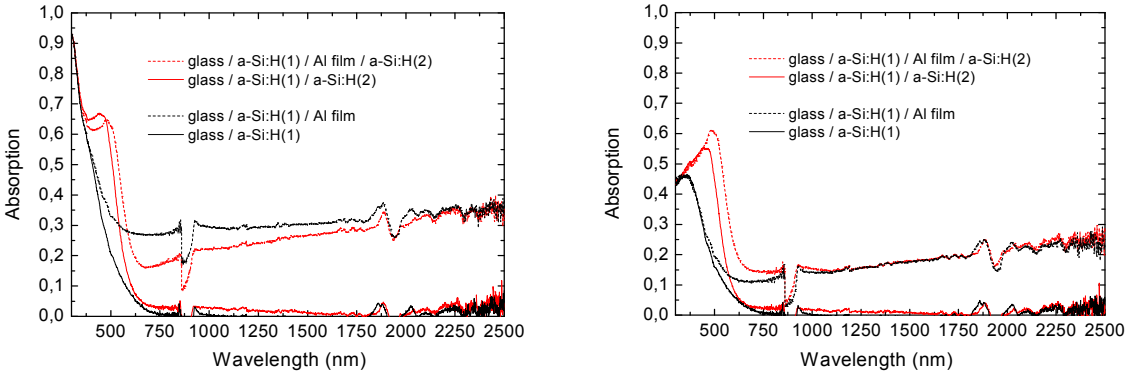

Figure 4.16 : Absorption of glass/a-Si:H(1)/a-Si:H(2) with and without Al film. The sample is illuminated from the glass side (left) and from the a-Si:H side (right). For comparison, the absorption of the layer stack without a-Si:H(2) is replotted.

For an illumination from the glass side, embedding the Au film in a-Si:H originates in an increased absorption for $\lambda < 1250$ nm with a broad maximum at 800 nm compared to the case the Au film is not covered with a-Si:H (Fig. 4.15, left). For an illumination from the a-Si:H side, covering the Au film with a-Si:H leads to an increase in absorption in the whole spectral range. However, no distinct peak is observed. Covering the Al film with a-Si:H does not result in an enhancement of the light absorption in the layer stack (Fig. 4.16). Even a decrease in the absorption for $\lambda > 600$ nm is found for an illumination from the glass side.
To conclude, only the layer stack containing Ag nanoparticles shows a distinct peak in the absorption. This resonant absorption, associated with localized surface plasmon excitation, is likely due to the particular morphology of the Ag film which exhibits separated nanoparticles. On the contrary, Au and Al films show a structure close to the percolation threshold and a continuous surface, respectively. None of them lead to a resonant light absorption.

4.3.2 Absorption of Ag nanoparticles of various sizes covered with a-Si:H

In section 4.2.2, we have shown the absorption spectra of glass/TCO substrates covered with Ag nanoparticles of various sizes and various inter-particle distances. Here we present the optical response of these substrates in the case the nanoparticles are covered with a thin layer of a-Si:H (cf. Fig. 4.13, right). The graph in Fig. 4.17 depicts the absorption gain, i.e. $abs_{\text{with nanoparticles}}$-$abs_{\text{without nanoparticles}}$ (Fig. 4.17) of the layer stack.

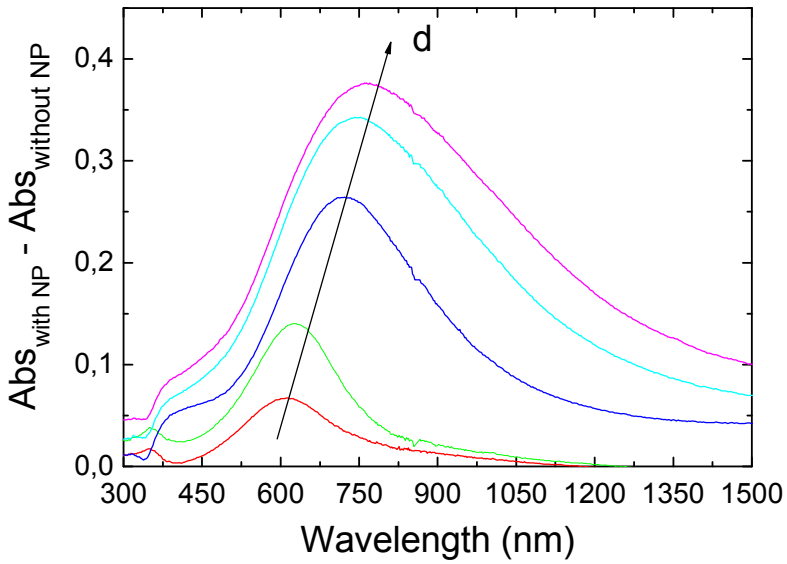

Figure 4.17 : Absorption gain of glass/TCO/Ag-nanoparticles/a-Si:H compared to glass/TCO/a-Si:H. The thickness *d* of the Ag film is varied between 0.5, 1, 2, 3 and 4 nm in order to obtain nanoparticles of various sizes and various inter-particle distances.

In presence of Ag nanoparticles a distinct peak in the absorption gain is observed which corresponds to the LSP resonance of the nanoparticles embedded in a-Si:H. The position of the LSP resonance shifts towards longer wavelengths for Ag nanoparticles covered with a-Si:H. This red-shift is explained by the higher refractive index of a-Si:H compared to the one of air ($n_{a\text{-}Si:H} \sim 4$, $n_{air} \sim 1$). As observed in section 4.2.2, an enhanced amplitude accompanied by a red-shift of the LSP resonance and a broadening of the full width at half maximum (FWHM) are found for increasing Ag film thicknesses.

4.3.3 Raman measurements of a-Si:H layer stacks with embedded metal films

Many authors have reported on the enhancement of the light absorption for organic and inorganic materials using integrated plasmonic metal films. However, it is often a challenge to determine which fraction of the incident light is actually absorbed by the surrounding material and which fraction of the light is lost in the metal. In the previous section, we have shown that a-Si:H-based layer stacks with embedded Ag nanoparticles exhibit a resonant light absorption in the red wavelength region, attributed to LSP. In order to determine whether the incoming light is not only absorbed by the nanoparticles but also by the a-Si:H, Raman measurements have been performed. In other words, Raman spectroscopy has been used as an indicator for revealing the existence of an enhanced electromagnetic field in the vicinity of the nanoparticles (leading to an improved absorption in the a-Si:H).

Metal nanoparticles and metal nanostructures can lead to a strong amplification of the Raman signal by several orders of magnitude (SERS effect, section 3.5.2) for molecules adsorbed on the metal surface. This amplification is mainly attributed to the local electromagnetic field enhancement associated with the localized surface plasmons of the metal. For molecules adsorbed on metal nanoparticles, the SERS intensity can be enhanced by a factor proportional to $|g|^4$, with g referring to the electromagnetic field enhancement averaged over the nanoparticle (Moskovitz et al., 2005). In this section, we present Raman spectra measured at 647 nm and 785 nm of layer stacks based on a-Si:H (as depicted in Fig. 4.13 on the left hand side) containing Ag, Au or Al films. Measurements were also conducted at 488 nm but no Raman enhancement was observed at this wavelength range in presence of metal films (not shown). It is necessary to mention that quantitative Raman measurements require caution. Even if the spot of the laser used for the experiments is relatively large (2 mm times 60 μm), Raman measurements of the same probe performed at different positions can give large discrepancies in the results. This is caused by (i) the slight inclination of the sample holder which leads to a modification of the distance between the probe and both laser source and detector, (ii) the inhomogeneity (thickness and roughness) of the sample. To minimize the

discrepancies, the distance between the measured areas was chosen as small as possible. However, it is important to emphasize that the amplifications of the Raman spectra shown in this work have to be regarded only as indicators of the actual amplifications.

Fig. 4.18 (left) shows Raman spectra of a glass/a-Si:H/Ag-nanoparticles/a-Si:H layer stack alternately illuminated from the glass side and the a-Si:H side. The measurements were performed at 785 nm. This wavelength nearly corresponds to the maximum of the resonant light absorption (see Fig. 4.18, right). Irrespective of the illumination side, an increase in the Raman signal is found for the layer stack with Ag nanoparticles in comparison to the layer stack without nanoparticles. The integration of Ag nanoparticles in the layer stack results in an amplification of the Raman signal by a factor of around 10 for an illumination from the glass side. An amplification by a factor of around 7 is found when light strikes on the a-Si:H side. The Raman spectrum of the layer stack with Ag nanoparticles exhibits a high background signal which increases with decreasing wavenumber. This effect results in a shift of the characteristic Raman peak of a-Si:H from 485 cm^{-1} to 470 cm^{-1}.

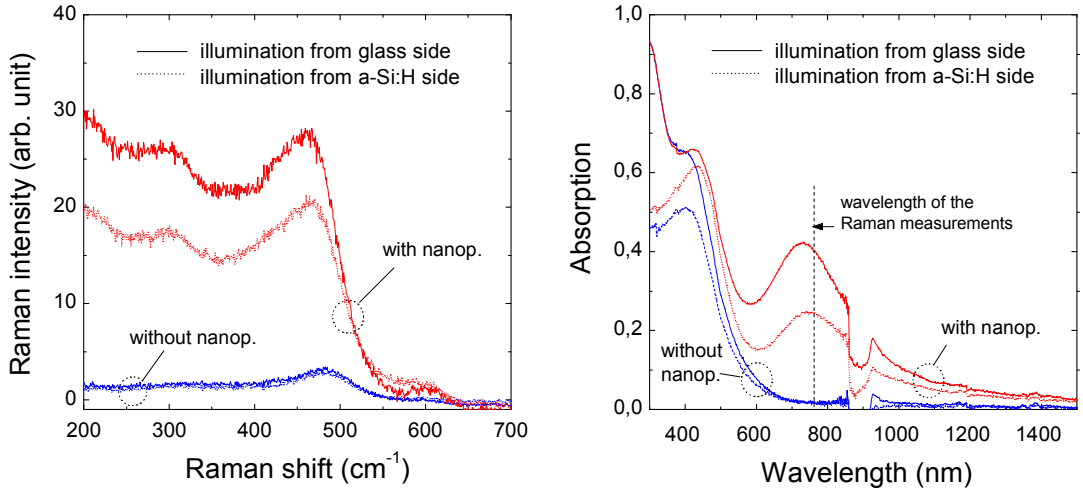

Figure 4.18 : (left) Raman spectrum at 785 nm of an a-Si:H layer stack with and without embedded Ag nanoparticles of diameter 25 nm. The dashed/continuous lines represent the measured Raman intensity when the layer stack is illuminated from the a-Si:H/glass side. (right) Corresponding light absorption spectrum.

Fig. 4.19 shows Raman measurements at 647 nm of glass/Ag/a-Si:H/metal-film/a-Si:H layer stacks. The metal films consist of 3 nm Ag, Au and Al films (or a combination of these metals) deposited by thermal evaporation and subsequently annealed at 180 °C. A strong amplification of the Raman intensity is found for layer stacks containing Ag nanoparticles in comparison to the layer stack of reference, i.e. without metal film. This amplification is

correlated with the enhanced light absorption observed in the red wavelength region for layer stacks containing Ag nanoparticles.

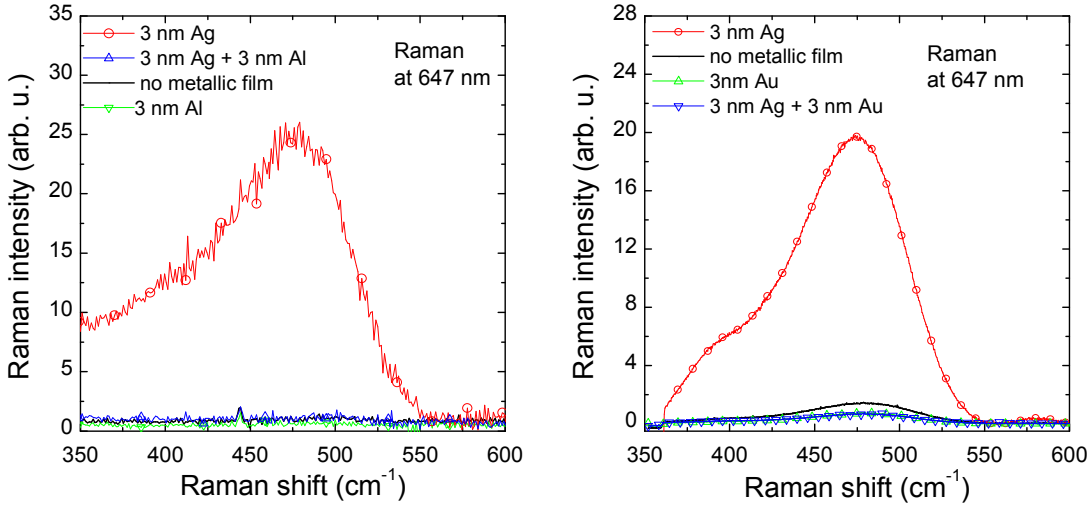

Figure 4.19 : Raman measurements at 647 nm of layer stacks based on a-Si:H containing Ag nanoparticles and/or Al film (left), Ag nanoparticles and/or Au film (right).

Despite an enhanced light absorption in the whole spectral range (see Fig. 4.15 and Fig. 4.16), a-Si:H-based layer stacks containing Au and/or Al films show a reduction of the Raman signal compared to the layer stack of reference. In general, similar trends were found for nearly all investigated layer stacks with Ag, Al and Au films. Since only the Ag film shows well separated nanoparticles after annealing and both Au and Al films show a structure close to or above the percolation threshold, we attribute the enhancement of the Raman signal to the specific nanoparticle structure of the Ag film.

The highest Raman enhancement found in this work – of a factor of around 65 at 647 nm (Fig. 4.20, left) – was obtained for small Ag nanoparticles (Fig. 4.20, right) deposited on a glass/Ag/TCO reflector and covered with a 30 nm thick a-Si:H layer. A thickness of 80 nm was used for the TCO layer. In this configuration, the reflective Ag mirror at the back side of the layer stack results in interferences caused by the superposition of the incident and reflected electromagnetic waves. The electromagnetic field distribution in the TCO layer thus shows maxima and minima of the light intensity which are located at a distance of $(2k+1)\lambda/4n_{TCO}$ and $(2k)\lambda/4n_{TCO}$, respectively, from the mirror. For a 80 nm thick TCO ($n_{TCO} \approx 2$), the Ag nanoparticles are consequently positioned at a maximum of the light intensity. Therefore they can result in a more significant contribution to the Raman amplification. This effect referred to as Interference-Enhanced Raman Scattering (IERS) was reported by several authors (Nemanich et al., 1980; Fortner et al., 1990). A schematic drawing of its functioning principle is presented in Fig. 4.21.

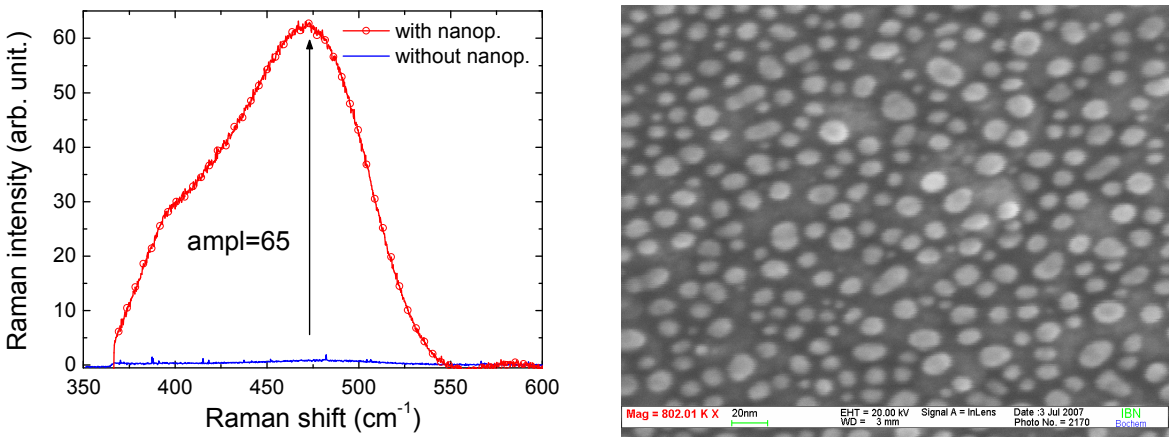

Figure 4.20 : (left) Raman spectrum of glass/Ag/TCO/a-Si:H with (dashed line) and without (solid line) Ag nanoparticles positioned at the TCO/a-Si:H interface. The TCO thickness is optimized to obtain a maximum of the light intensity at the position of the nanoparticles (IERS effect). The Ag nanoparticles (right) are obtained by thermal evaporation of a 3 nm Ag film and a subsequent annealing step at 180 °C.

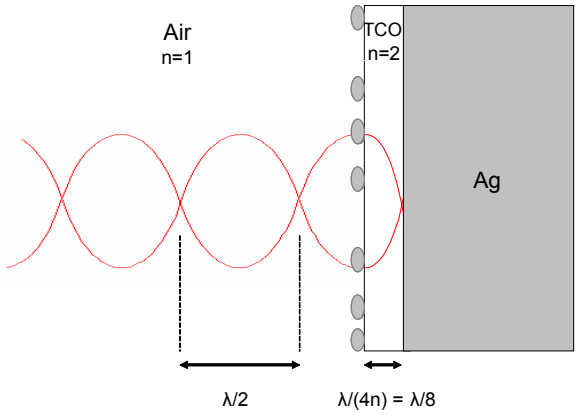

Figure 4.21 : Sketch of the layer stack used for the IERS effect. For simplification, the a-Si:H layer is not represented. The nanoparticles are separated from the Ag back reflector by a TCO layer having a thickness of $\lambda/(4n_{TCO})$. The electromagnetic field profile of a standing wave of wavelength λ is shown.

4.3.4 Au and Al nanoparticles

The fact that the Raman signal is not amplified for layer stacks based on a-Si:H containing Au and Al films of a few nanometers is probably due to the structure of the deposited metal films. As shown before, Au and Al films of a few nanometers exhibit a percolation continuum and a continuous surface, respectively. Therefore no localized surface

plasmon resonance can be observed in their absorption spectrum when they are embedded in a-Si:H. In contrast a-Si:H-based layer stacks containing Ag nanoparticles show a resonant light absorption that is associated with an enhancement of the Raman signal. In order to obtain separated Au and Al nanoparticles, we reduced the thickness of the evaporated Au and Al films to 0.5 nm.

Au nanoparticles

Fig. 4.22 shows SEM images after an annealing treatment at 180 °C of Au films with thickness of 1.5 nm (left) and 0.5 nm (right) deposited on glass/Ag/TCO. For 1.5 nm Au, the film morphology exhibits a structure close to the percolation threshold while for 0.5 nm Au, well separated nanoparticles with an average diameter of around 5 nm can be observed. Reflection measurements of glass/Ag/TCO layer stacks covered with nanoparticles of radius 5 nm show a broad minimum at around 700 nm (not shown). Raman measurements of a-Si:H-based layer stacks containing such nanoparticles were conducted but no enhancement of the signal was observed in comparison to layer stacks without nanoparticles (not shown). Au nanoparticles should exhibit a strong localized surface plasmon resonance for diameters down to 5 nm (Kreibig and Vollmer, 2005). It is therefore presently not clear why the Raman signal is not amplified in this case.

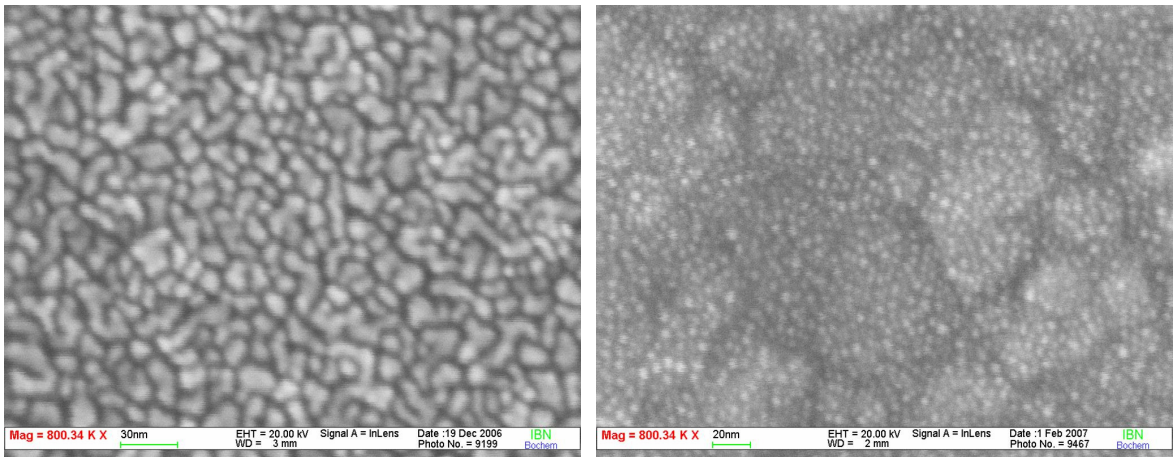

Figure 4.22 : SEM pictures of Au films with thickness of 1.5 nm (left) and 0.5 nm (right) deposited on glass/Ag/TCO after annealing at 180 °C for 1 h.

Al nanoparticles

Fig. 4.23 shows SEM micrographs of 2 nm and 0.5 nm Al films deposited on glass/Ag/TCO before annealing. The film structure was characterized directly after the Al deposition in order to reduce the influence of the air contamination. For 2 nm Al, a continuous surface is observed while for 0.5 nm Al, well separated nanoparticles with an average diameter of around 5 nm are found. Annealing the layer stack at 180 °C has no effect on the

structure of the deposited films. Reflection measurements of glass/Ag/TCO covered with 2 nm Al show a broad minimum in the reflectivity at around 675 nm (Fig. 4.24, left, triangles). On the contrary, Al films thinner than 2 nm show a similar reflectivity to that of the layer stack without Al film (Fig. 4.24, left, squares and circles). XPS (X-ray Photoelectron Spectroscopy) measurements were carried out in order to investigate the chemical composition of the obtained Al film (Fig. 4.24, right).

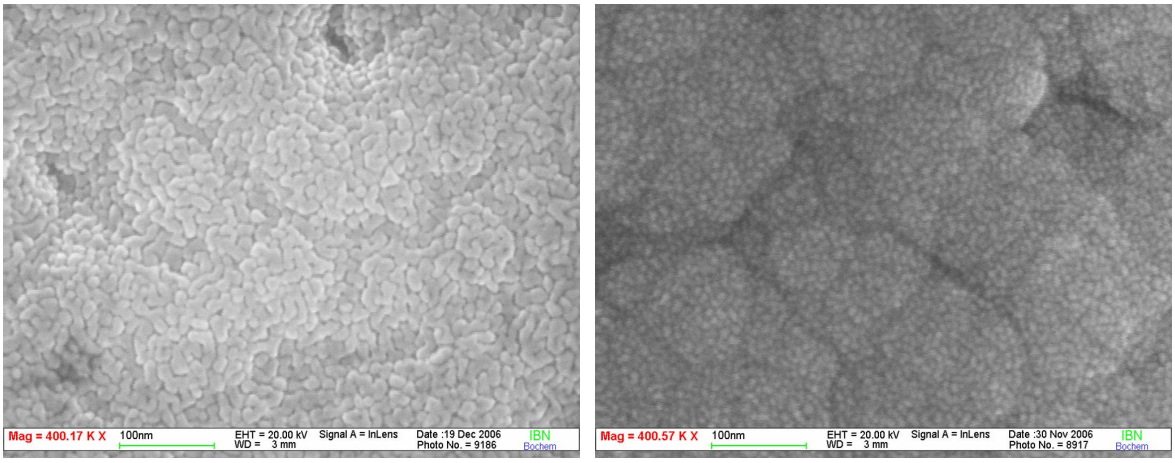

Figure 4.23 : SEM pictures of Al film with thickness of 1.5 nm (left) and 0.5 nm (right) deposited on glass/Ag/TCO. No annealing treatment was performed.

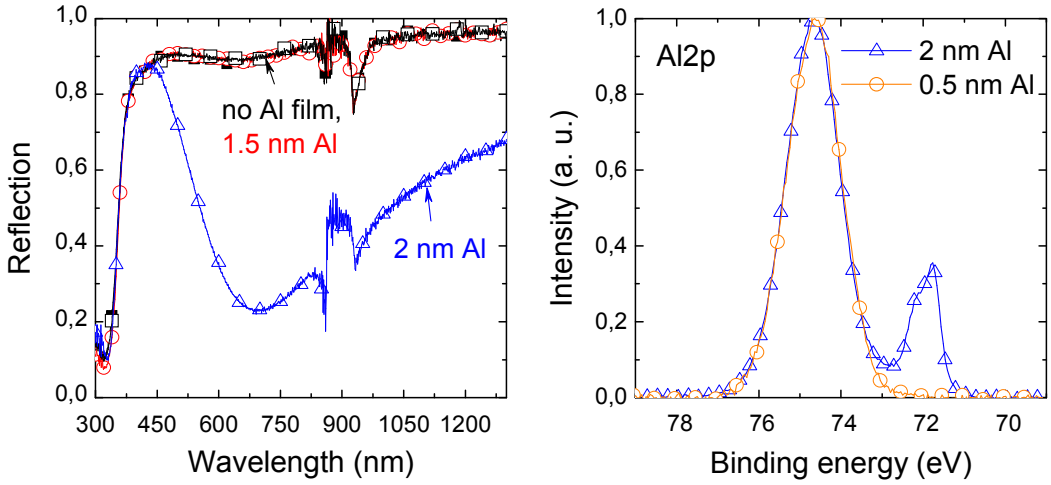

Figure 4.24 : Reflectivity (left) and XPS (right) measurements of glass/Ag/TCO with and without Al films. The thickness of the Al film is varied between 0.5 nm and 2 nm.

XPS measurements of glass/Ag/TCO covered by Al films of thickness larger than 2 nm exhibit an intensity peak at 72 eV which is characteristic of Al material. An intensity peak at 75 eV also appears in the XPS spectrum, which is characteristic of Al_2O_3. In the case of 0.5

nm Al on glass/Ag/TCO in contact with air no contribution of the Al material is found in the XPS spectrum. Only the characterisic peak of Al_2O_3 is observed. The presence of Al_2O_3 results from the rapid oxidation of the thin Al layer. Since Al_2O_3 is transparent, identical optical responses are obtained for the layer stack with 0.5 nm Al and for the layer stack of reference. For slighly thicker Al thicknesses (between 0.5 nm and 1.5 nm), separated Al particles may be obtained. However, also for 1.5 nm Al no LSP absorption resonance is found in the investigated wavelength range. The LSP resonance of ellipsoidal Al nanoparticles embedded in a-Si:H is expected to occur in the visible range (Fig. 1.9, right). However, air contamination leads to the formation of Al_2O_3 at the Al surface which probably results in a blue-shift of the LSP peak to the ultraviolet wavelength range. Thus no amplification of the Raman intensity is expected in the studied wavelength range for layer stacks containing Al films thinner than 2 nm. For thicker films, Al shows a continuous structure and no separated nanoparticles can be observed. Therefore the absorption extremum observed at 675 nm may originate from absorption losses in Al. These losses have to be differenciated from localized surface plasmons since they are not accompanied by strongly enhanced electromagnetic fields in the vicinity of the metal. This probably explains why a-Si:H-based layer stacks containing Al film thicker than 2 nm exhibit a decreased Raman signal at 647 nm (section 4.3.3).

4.4 Summary

Au and Al films thermally evaporated on glass/a-Si:H and glass/TCO exhibit a percolation continuum already for film thicknesses of a few nanometers. Annealing the layer stacks at 180 °C (or higher temperature) for several hours has no significant effect on the film morphology. Au and Al nanoparticles can only be obtained for metal films thinner than 0.5-1 nm. Ag nanoparticles of various sizes can easily be obtained on glass/a-Si:H and glass/TCO substrates by performing an annealing treatment in vacuum of 1 h at 180 °C. While layer stacks with Au or Al films do not show a distinct peak in the absorption spectrum, glass/a-Si:H and glass/TCO layer stacks covered with Ag nanoparticles exhibit a resonant absorption. For larger Ag nanoparticles the resonance is red-shifted. The red-shift is accompanied by an increase in amplitude and line-width of the resonance. For systems containing Au and Al films covered with a thin a-Si:H layer, no distinct peak in the absorption spectrum can be observed. By covering the Ag nanoparticles with a thin a-Si:H layer, the LSP resonance is red-shifted. This effect is attributed to the higher refractive index of a-Si:H compared to the one of air. Au and Al films incorporated in a-Si:H layer stacks are not appropriate for enhancing the Raman signal of a-Si:H. On the contrary, Ag films embedded in a-Si:H lead to an amplification of the Raman signal of a-Si:H for excitation

wavelengths of 647 nm and 785 nm. An amplification of a factor of 65 has been found for a-Si:H-based layer stacks having the proper configuration and containing Ag nanoparticles of diameter 20 nm.

Chapter 5

Small Ag nanoparticles in thin-film silicon solar cells and in photosensitive devices

It has been shown in the previous chapter that layer stacks based on a-Si:H containing small Ag nanoparticles (Ø < 35 nm) exhibit a strong light absorption in the red and infrared wavelength regions, due to localized surface plasmons. Raman measurements conducted at 647 nm and 785 nm exhibit an amplification of the characteristic Raman signal of a-Si:H, indicating a possible increase in the light absorption in this layer. In order to study the local effect of the nanoparticles and make use of the enhanced light absorption, we prepared a-Si:H solar cells in the p-i-n and n-i-p configuration with an i-layer thickness of 100 nm as well as i-p and i-n photosensitive devices (i.e. cells without an n-layer and p-layer, respectively) having an i-layer thickness of 20 nm. Ag nanoparticles with average lateral sizes up to 30 nm were integrated at different positions within the cells. The optoelectronic properties of the devices are discussed.

5.1 Small Ag particles in a-Si:H p-i-n solar cells

Ag nanoparticles with an average lateral size of 30 nm, obtained by thermal evaporation of a 3 nm Ag film and post annealing treatement (see section 2.1), were integrated in p-i-n solar cells. The nanoparticles were incorporated in flat cells (cells deposited on a flat substrate) to avoid light scattering at rough interfaces. Standard a-Si:H solar cells with an absorber layer thickness of 350 nm show a relatively high light absorption in the red wavelength range. In order to obtain a clear effect of the nanoparticles on the optical response of the cells in the long wavelength range, the absorber i-layer was reduced to 100 nm.

5.1.1 Small Ag nanoparticles located at the i-n interface

First we positioned the nanoparticles at the i-n interface of the solar cell, as illustrated in Fig. 5.1. At both i-n and i-p interfaces, a high electrostatic field exists. Consequently, we expect at these positions an efficient extraction of the photo-generated charge carriers. Therefore an increase in the photocurrent should be observed in this configuration if the localized surface plasmon (LSP) resonance of the nanoparticles effectively leads to a local improvement of the light absorption in a-Si:H.

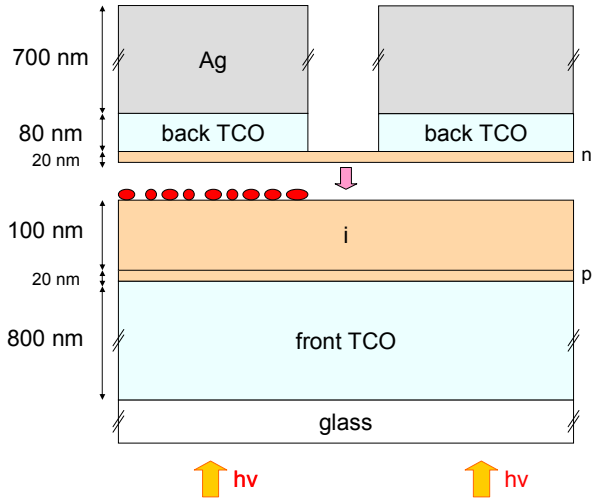

Figure 5.1 : Schematic drawing of two co-deposited a-Si:H cells in a superstrate (p-i-n) configuration with and without Ag nanoparticles. The nanoparticles having an average lateral size of around 30 nm are positioned at the i-n interface.

The reflection of the co-deposited cells with and without Ag nanoparticles shows nearly comparable values for wavelengths λ up to 575 nm (Fig. 5.2a). In this wavelength range, a large fraction of the light is absorbed before it reaches the rear side of the cell. Furthermore, light of short wavelengths is only weakly absorbed by the nanoparticles (see Fig. 4.17). For longer wavelengths, a strong decrease in the reflection is found for the cell with nanoparticles. In contrast to the case of the glass/a-Si:H/nanoparticles/a-Si:H layer stack (depicted in Fig. 4.13), the distinct resonant absorption peak normally found at around 750 nm (see Fig. 4.14) caused by the LSP of the Ag nanoparticles in a-Si:H is not clearly visible. Interference fringes originating from the superposition of the incident light with that reflected at the silver back reflector mask the distinct LSP resonance peak.
Fig. 5.2b shows the quantum efficiency (QE) measured under short-circuit condition (at 0 V) and at reverse bias (-0.5 V) for both types of cells. Despite the fact the reflection of the cell

with nanoparticles is only smaller in the red wavelength region, the QE of the device with nanoparticles is reduced in the whole spectral range compared to that of the device without nanoparticles. This reduction can be explained by (i) charge carrier recombination at the nanoparticle surface, (ii) charge carrier recombination in defects present in the vicinity of the nanoparticles and/or (iii) charge carrier recombination in the bulk of the solar cell caused by a disturbance of the electrostatic field in the i-layer. QE measurements at reverse bias (-0.5V) were carried out in order to improve the extraction of the photo-generated charge carriers. At reverse bias, only a slight increase in QE is observed for both cells. In the red wavelength region, the QE of the cell with nanoparticles remains below that of the cell without nanoparticles. The excepted enhancement of the charge carrier generation in the i-layer resulting from the LSP effect of the nanoparticles is not found. In this configuration, the nanoparticles are covered with the n-layer which is rich in defects. Consequently most of the charge carriers generated in the close vicinity of the nanoparticles may directly recombine in the n-layer.

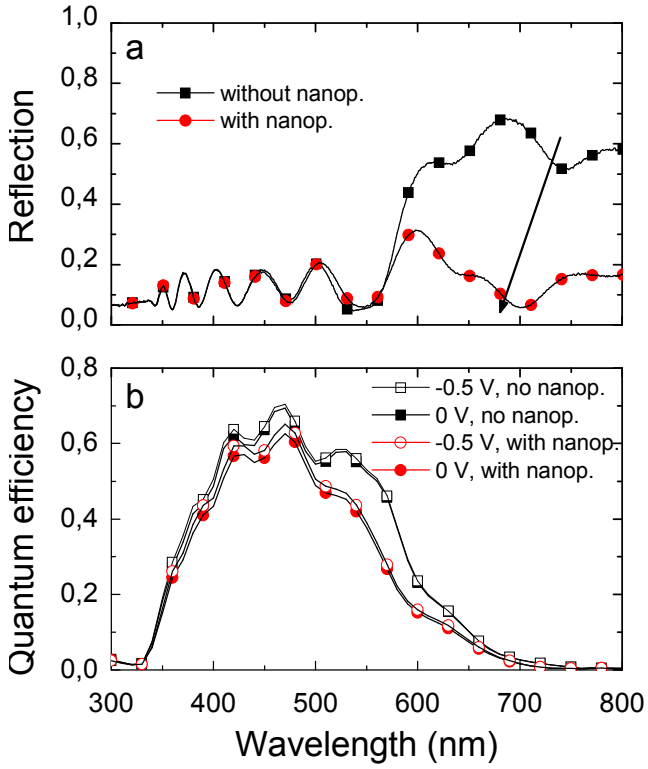

Figure 5.2 : Reflection (a) and quantum efficiency (b) of a-Si:H cells in the p-i-n configuration with (circles) and without (squares) Ag nanoparticles positioned at the i-n interface. The full and open symbols represent the QE measurements performed at 0V and -0.5 V, respectively.

Current-voltage (I-V) measurements in the dark and under illumination are shown in Fig. 5.3 (left and right, respectively). The vacuum break required to deposit the nanoparticles – on the half of the substrate only – does not lead to a significant alteration of the electrical device properties. In the dark, the cells without nanoparticles exhibit an exponential behavior (Fig. 5.3, left, squares), indicating that the current flow in the p-i-n diode is not adversely affected. A high shunt resistance (> 10 MΩ) as well as a low series resistance (< 10 Ω) are measured. Under illumination, the cell without nanoparticles gives a short-circuit current (Isc) of 8.15 mA.cm^{-2}, an open-circuit voltage (Voc) of 880 mV and a fill factor (FF) of 71% (Fig. 5.3, right, squares). Incorporating Ag nanoparticles at the i-n interface of the cell leads to a drastic modification of the electrical device properties. A non-exponential behavior of the I-V curve is observed (Fig. 5.3, left, circles). The current in the dark is enhanced for voltages smaller than 0.75 V, indicating an enhanced carrier recombination. For higher voltages, the current in the dark is decreased compared to the cell without nanoparticles, likely due to a charge transport limitation and an increased series resistance. Under illumination, the cell with nanoparticles exhibits a S-shape for voltages larger than 0.4 V (Fig. 5.3, right, circles). A Voc value of only 595 mV is measured. Furthermore, the integration of the nanoparticles at the i-n interface results in a reduction of the short-circuit photocurrent from 8.15 mA.cm^{-2} to 6.9 mA.cm^{-2} which correlates with the decreased QE. In conclusion, the Ag nanoparticles are found to negatively affect the electrical properties of the solar cells when they are incorporated at the i-n interface.

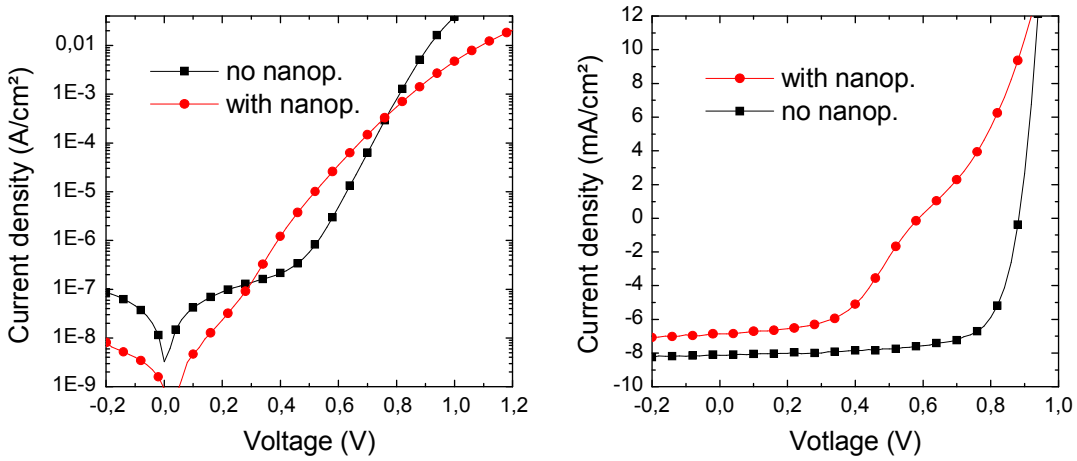

Figure 5.3 : I-V characteristic in the dark (left) and under illumination (right) of a-Si:H cells in the p-i-n configuration with (circles) and without (squares) Ag nanoparticles. The nanoparticles are located at the i-n interface.

In other experiments, the Ag nanoparticles were incorporated in the i-layer or in the n-layer of the solar cell. For these devices, similar results were found. Despite a higher light absorption in the long wavelength range, a decrease in QE in the whole spectrum was observed. Dark characteristics also showed a non-exponential behavior for cells with nanoparticles, due to an alteration of the electrical device properties. We thus decided to position the nanoparticles at the n-TCO interface in order to avoid the "interruption" of the p-i-n layer sequence and to prevent any perturbation of the electronical properties of the p-i-n diode.

5.1.2 Small Ag nanoparticles located at the n-TCO interface

Small Ag nanoparticles were deposited at the n-TCO interface of a-Si:H solar cells having the p-i-n configuration. Prior to the deposition of the back TCO (performed at room temperature), an annealing treatment of 1 h at 180 °C was carried out in order to obtain well separated nanoparticles. A schematic drawing of two co-deposited cells with and without nanoparticles is depicted in Fig. 5.4.

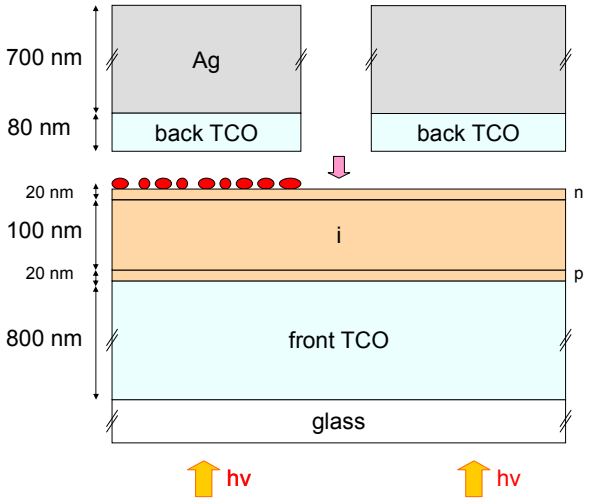

Figure 5.4 : Schematic drawing of two co-deposited a-Si:H cells in the p-i-n configuration with and without Ag nanoparticles. The nanoparticles are positioned at the n-TCO interface.

The I-V characteristics of the cells in the dark and under illumination are shown in Fig. 5.5 (left and right, respectively). For cells with and without nanoparticles, the dark I-V curves remain nearly identical for voltages up to 0.8V. The exponential behavior observed here suggests that the electrical device properties are not significantly affected by the presence of the nanoparticles at the n-TCO interface. Only an increase of the series resistance is observed, probably due to a contact alteration. Under illumination, the I-V curve shows a reduction of the fill factor, likely related to the increased series resistance observed in the dark I-V curve.

Furthermore, the incorporation of the nanoparticles leads to a decrease of the short-circuit current from 9 $mA.cm^{-2}$ to 8 $mA.cm^{-2}$.

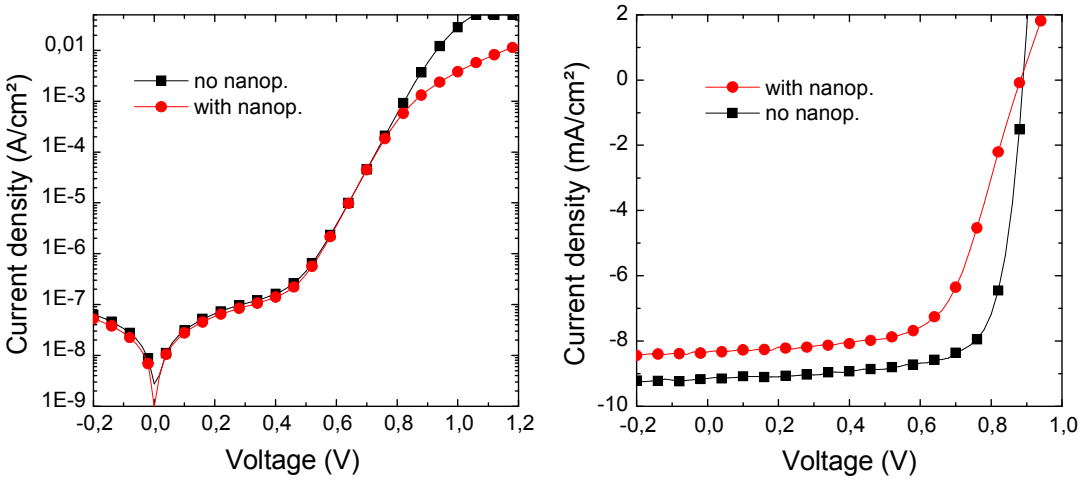

Figure 5.5 : Measured I-V curve in the dark (left) and under illumination (right) of a-Si:H solar cells in the p-i-n configuration with (circles) and without (squares) Ag nanoparticles. The nanoparticles having an average lateral size of 30 nm are positioned at the n-TCO interface.

Despite a reduction of the reflectivity in the red wavelength range (Fig. 5.6, left), the Raman intensity is not enhanced at 647 nm for devices with nanoparticles (Fig. 5.6, right). In this configuration, the Ag nanoparticles are covered with TCO. When Ag nanoparticles with radius of around 30 nm (obtained by evaporation of 3 nm Ag and subsequent annealing) are embedded in silicon ($n_{a\text{-}Si:H} \sim 4$), the LSP resonance occurs in the infrared at around 750 nm (Fig. 4.14) and a strong amplification of the Raman signal is observed at 647 nm and 785 nm (see section 4.3.3). When the Ag nanoparticles are covered with TCO ($n_{TCO} \sim 2$) the LSP resonance shifts to shorter wavelengths, as illustrated in Fig. 1.3. This probably explains why the Raman signal at 647 nm is not amplified in presence of Ag nanoparticles. Raman measurements were also performed at 514 nm. At this wavelength, the light is mainly absorbed before it reaches the nanoparticles. Thus, also in this case, no amplification of the Raman signal was measured for the cell containing Ag nanoparticles.

The lower Isc value is also reflected in the lower QE (Fig. 5.7). However, the QE is not reduced in the whole spectral range as it was observed for structures with nanoparticles located at the i-n interface or in the i-layer (see section 5.1.1). Identical QE values are found in the short and long wavelength ranges for cells with and without nanoparticles. This confirms that the integration of Ag nanoparticles at the n-TCO interface does not lead to a significant alteration of the electrical device properties. An efficient extraction and collection of the photo-generated charge carriers is provided. Only a decrease between 500 nm and 625 nm is observed in the QE data for cells with nanoparticles compared to cells without

nanoparticles, likely due to absorption losses in the nanoparticles. In this configuration also, the photo-generated charge carriers resulting from the expected effect of the nanoparticles, i.e. an amplification of the electromagnetic field in the vicinity of the nanoparticles at the LSP resonance, may recombine directly at the metal surface and/or in the vicinity of the nanoparticles (i.e. in defects).

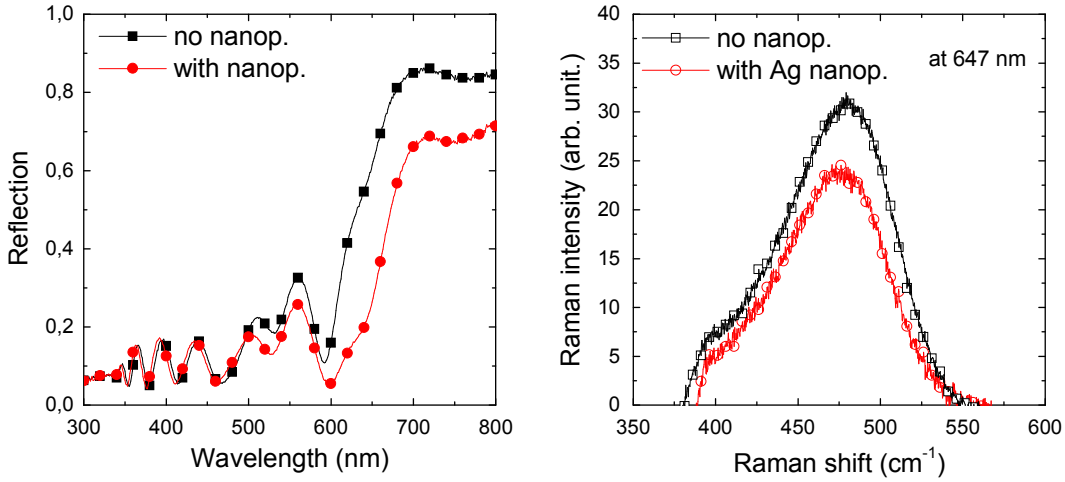

Figure 5.6 : Reflection (left) and Raman signal (right) of a-Si:H cells in the p-i-n configuration with (circles) and without (squares) nanoparticles. The nanoparticles are located at the n-TCO interface.

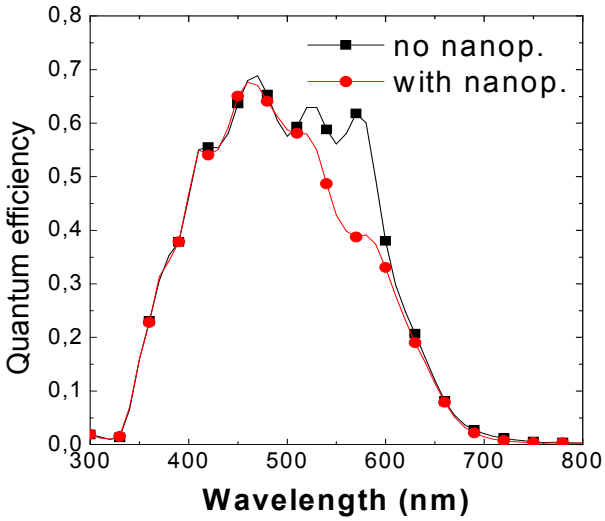

Figure 5.7 : Quantum efficiency of a-Si:H cells in the p-i-n configuration with (circles) and without (squares) Ag nanoparticles. The nanoparticles are positioned at the n-TCO interface.

5.2 Small Ag nanoparticles in a-Si:H n-i-p solar cells

When Ag nanoparticles are positioned at the i-n interface of p-i-n solar cells, a strong disturbance of the electrical device properties, indicated by a non-exponential behavior of the dark I-V curve, is found. For Ag nanoparticles incorporated at the n-TCO interface of p-i-n cells in the superstrate configuration, no significant alteration of the electrical device properties is observed. However, in this configuration the Ag nanoparticles are covered with TCO and the localized surface plasmon (LSP) resonance is expected to occur in the short wavelength range. To overcome this problem, a-Si:H solar cells in the substrate (n-i-p) configuration were prepared with small Ag nanoparticles positioned at the TCO-n interface so that the nanoparticles are embedded in a-Si:H. A schematic drawing of the co-deposited cells with and without nanoparticles is depicted in Fig. 5.8.

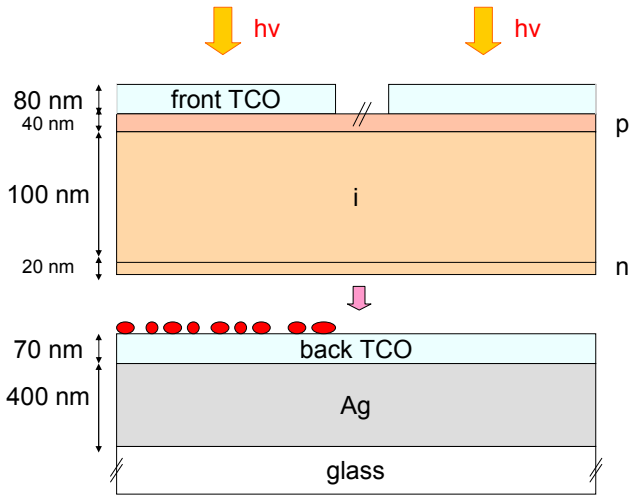

Figure 5.8 : Schematic drawing of co-deposited a-Si:H cells in the substrate (n-i-p) configuration with and without Ag nanoparticles. The nanoparticles are positioned at the TCO-n interface.

Reflection measurements of solar cells with and without nanoparticles are shown in Fig. 5.9a. For wavelengths $\lambda < 570$ nm, comparable values are observed. In this wavelength range, the light is mainly absorbed before it reaches the back contact of the solar cell. A strong decrease of the reflection in the long wavelength range is measured for cells with nanoparticles. Despite the enhanced light absorption in the red wavelength range, the QE of the device with nanoparticles is reduced for wavelengths larger than 525 nm in comparison to the cell without nanoparticles (cf. Fig. 5.9b). Since the QE of both types of cells is identical in the short wavelength range, a significant alteration of the electric device performance due to the presence of nanoparticles can be excluded. Consequently, the decrease in QE can be

explained by (i) recombination (at the particle surface, at the TCO back contact or in the n-layer rich in defects) of the charge carriers generated in the vicinity of the nanoparticles at the LSP resonance and/or by (ii) optical losses in the nanoparticles which are not compensated by the gain resulting from the enhanced electromagnetic field associated with LSP.

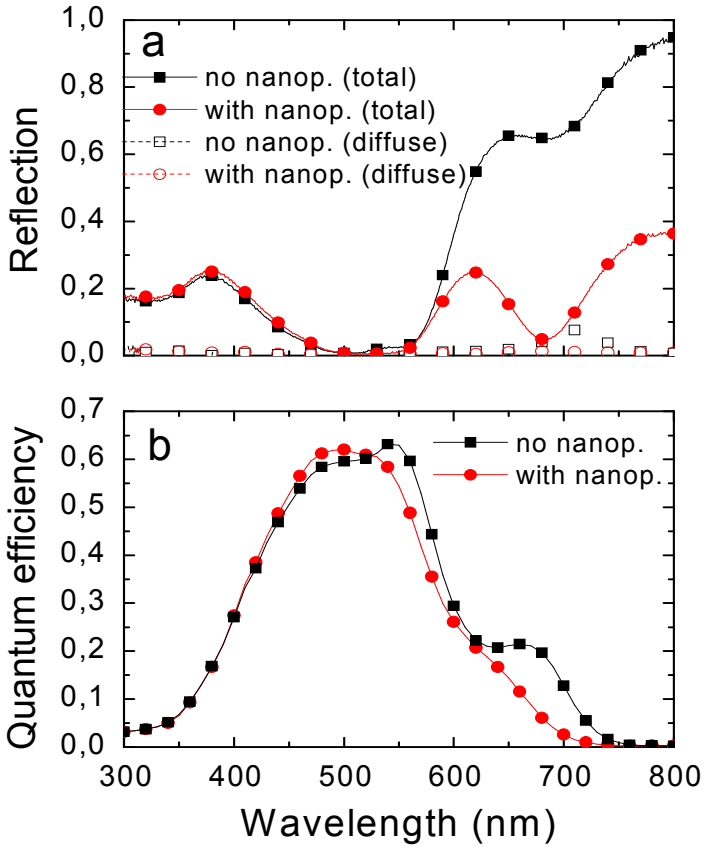

Figure 5.9 : Reflection (top) and quantum efficiency (bottom) of a-Si:H cells in the n-i-p configuration with (circles) and without (squares) Ag nanoparticles. The nanoparticles are positioned at the TCO-n interface.

Fig. 5.10 shows the measured current density in the dark (left) and under illumination (right) of the cells with and without nanoparticles. I-V characteristics of both cells exhibit an exponential behavior, confirming that the electrical device properties are not disturbed by the introduction of the nanoparticles at the TCO-n interface. For voltages larger than 0.8 V, the cell with nanoparticles even shows a higher current than the cell without nanoparticles, likely due to an improvement of the contact at the TCO-n interface. I-V measurements under illumination show a nearly identical FF (66 %) and V_{oc} (0.88 V) for both cells. In agreement with the QE data, a reduction of Isc from 5.9 to 4.9 $mA.cm^{-2}$ is measured for the cell with nanoparticles in comparison to the cell without nanoparticles. As mentioned above, a possible

reason for the reduction of the photocurrent in the red region is the recombination in the n-layer of the photo-generated charge carriers resulting from the effect of the nanoparticles. In order to investigate this possibility, we prepared a-Si:H photosensitive devices in the i-p and i-n configuration (i.e. solar cells with no n-layer and no p-layer, respectively) containing small Ag nanoparticles positioned at the TCO-i interface (see next section).

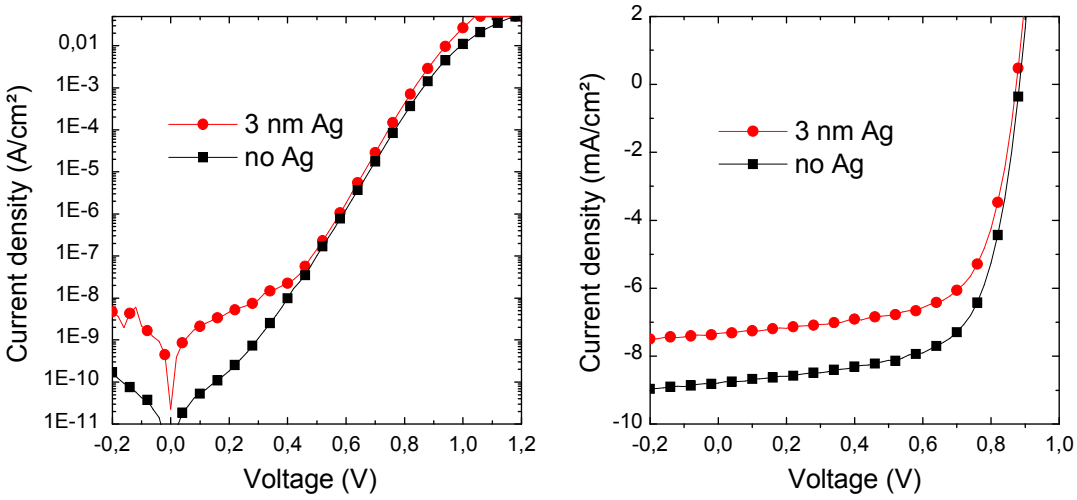

Figure 5.10 : Measured current density in the dark (left) and under illumination (right) of a-Si:H cells in the n-i-p configuration with (circles) and without (squares) Ag nanoparticles. The nanoparticles are positioned at the TCO-n interface.

5.3 Ag nanoparticles at the TCO-i interface of i-p and i-n photosensitive devices

5.3.1 i-p devices with an i-layer thickness of 100 nm

Irrespective of the cell configuration (p-i-n or n-i-p), no enhanced photocurrent in the visible region has been observed so far for a-Si:H solar cells containing Ag nanoparticles. When the nanoparticles interrupt the p-i-n layer sequence, a strong disturbance of the electrical device properties is observed. Only when the nanoparticles are positioned at the n-TCO interface, no significant alteration of the electrical cell performance is observed. In the p-i-n configuration, the nanoparticles deposited at the n-TCO interface are covered with TCO ($n_{TCO} \approx 2$). Thus, the plasmon resonance occurs in the short wavelength range and no amplification of the Raman signal is found. In the n-i-p configuration, the Ag nanoparticles

positioned at the TCO-n interface are embedded in a-Si:H ($n_{\text{a-Si:H}} \approx 4$). The plasmon resonance occurs in the red region where an amplification of the Raman intensity has been measured (see section 4.3.3). However, the generated carriers resulting from the effect of the nanoparticles probably recombine in the n-layer, rich in defects. In order to avoid carrier recombination in the n-layer, a-Si:H i-p solar devices (i.e solar cells without the n-layer) have been prepared with Ag nanoparticles positioned at the TCO-i interface. An illustration is given in Fig. 5.11. In this configuration, the nanoparticles are in direct contact with the absorber layer where the generated carriers can more easily be extracted and then contribute to the photocurrent.

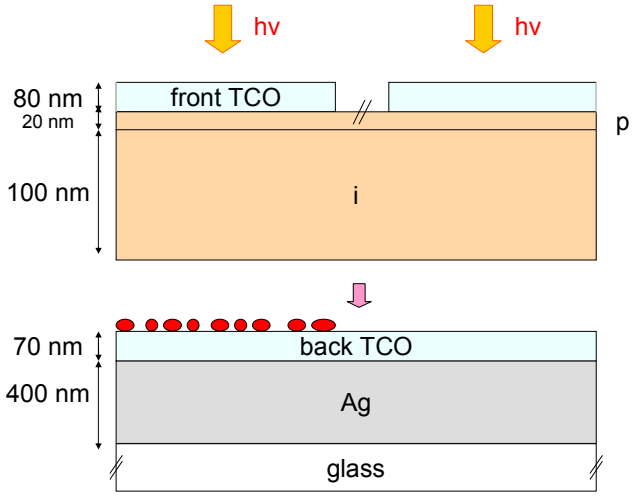

Figure 5.11 : Schematic drawing of co-deposited a-Si:H devices in the i-p configuration with and without Ag nanoparticles. The nanoparticles are positioned at the TCO-i interface.

Fig. 5.12 shows the I-V characteristics in the dark (left) and under illumination (right) of co-deposited i-p solar cells with and without nanoparticles. Both cells exhibit an exponential behavior. However, both devices show a particularly high series resistance, indicating a charge transport limitation and/or a contact problem at the i-layer/TCO interface. The absence of n-layer leads to a reduction of the device performance under illumination (Fig. 5.12, right) compared to cells deposited in the n-i-p configuration. An Isc value of around 8 $mA.cm^{-2}$, a FF of 44 % and a Voc of 530 mV are obtained for the device without nanoparticles. A S-shape in the AM 1.5 I-V characteristic is observed for high voltages. It correlates with the high series resistance indicated by the low saturation level of the dark I-V curve. Also in this configuration, the structure with incorporated nanoparticles exhibits a higher dark current (section 5.1.1), indicating that recombination of charge carriers is enhanced. The incorporation of nanoparticles results in a decrease of the photocurrent by around 1 $mA.cm^{-2}$ and a reduction of the FF from 44 % to 40 %. The Voc is strongly decreased from 530 mV to

400 mV. This effect is attributed to the high charge carrier recombination suggested by the larger dark current.

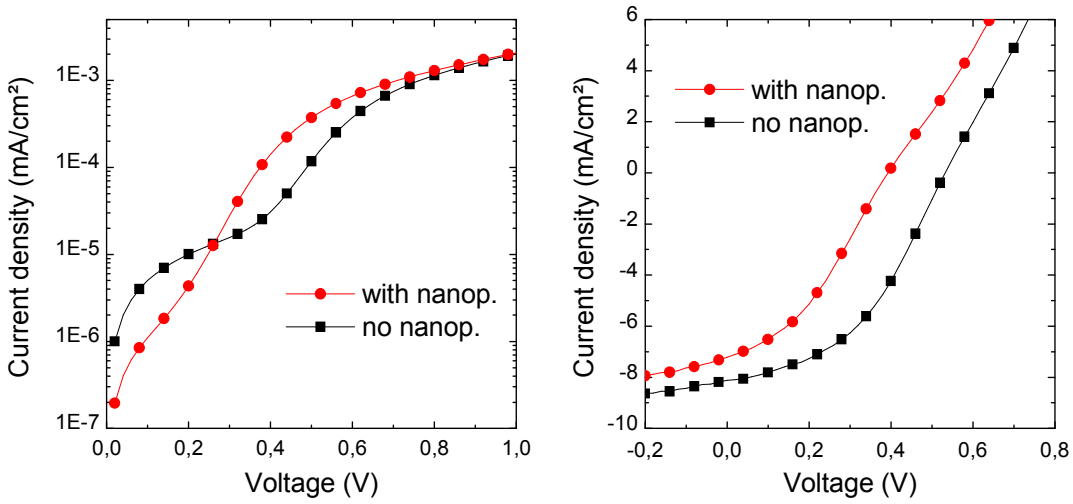

Figure 5.12 : I-V characteristic in the dark (left) and under illumination (right) of a-Si:H cells in the i-p configuration with (circles) and without (squares) Ag nanoparticles. The nanoparticles are positioned at the TCO-i interface.

Despite the enhanced light absorption in the red region, no improvement of the QE is measured under short-circuit condition for the cell containing Ag nanoparticles (Fig. 5.13, left). QE measurements performed at negative voltages – applied in order to improve the extraction of the charge carriers – only show a slight increase of the photocurrent in the long wavelength range (Fig. 5.13, right, QE in a logarithmic scale). However, due to the structure of the prepared cells, the static electrostatic field built in the i-layer – and especially in the vicinity of the nanoparticles – is probably not sufficient to extract the charge carriers resulting from the local effects of the nanoparticles. Even at - 1 V, no considerable enhancement of the QE is found in the long wavelength range and the signal shows a strong noise contribution. It is therefore difficult to conclude if the nanoparticles actually result in an improved photocurrent. In order to significantly enhance the electrostatic field in the vicinity of the nanoparticles and thus further improve the collection of the charge carriers, we reduced the thickness of the i-layer from 100 nm to 20 nm.

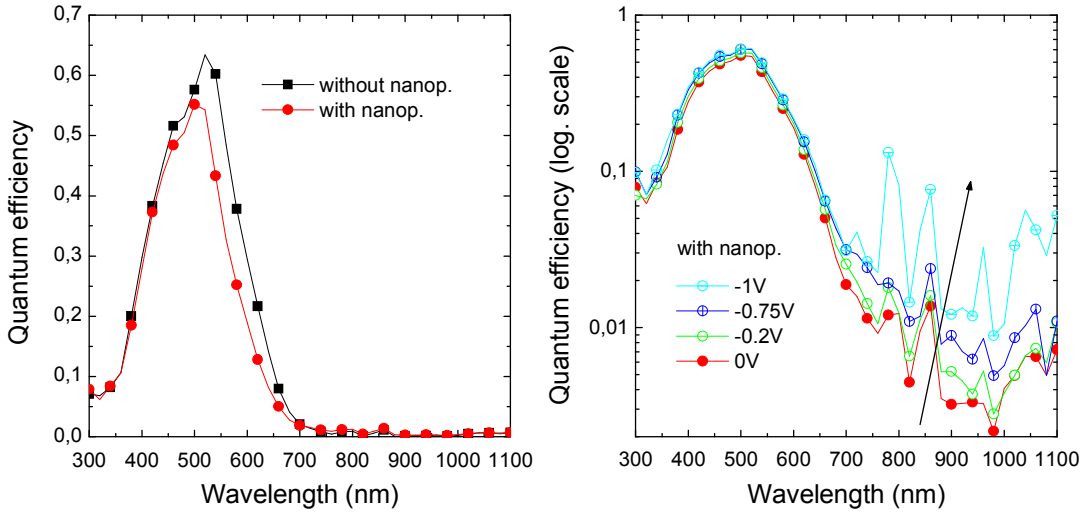

Figure 5.13 : (left) Quantum efficiency at 0 V of a-Si:H cells in the i-p configuration with (circles) and without (squares) Ag nanoparticles positioned at the TCO-i interface. (right) Quantum efficiency under negative voltages of cells containing Ag nanoparticles (log. scale).

5.3.2 Ultra-thin i-p and i-n photosensitive cells with i-layer thickness of 20 nm

In order to achieve an electrostatic field significantly larger than that usually obtained in the i-layer of standard solar cells, ultra-thin a-Si:H i-p and i-n photosensitive devices with an i-layer thickness of 20 nm have been prepared. The Ag nanoparticles are integrated at the TCO-i interface of the devices, as illustrated in Fig. 5.14. In this section, the average size of the nanoparticles has been varied by depositing Ag films with thickness between 2 nm and 5 nm.

Fig. 5.15 (left) and Fig. 5.15 (right) show the reflectivity of the i-p and i-n devices, respectively, with and without Ag nanoparticles. For both i-p and i-n configuration, devices with Ag nanoparticles show a strong decrease in the reflectivity for wavelengths larger than 500 nm in comparison to devices without nanoparticles. As the thickness of the Ag film is increased from 2 nm to 5 nm, the minimum in the reflectivity is red-shifted due to the larger sizes of the obtained nanoparticles (Fig. 1.6). The broad minimum in the reflectivity is attributed to the large distribution of shapes and sizes of the nanoparticles (Fig. 5.14, right). The presence of the Ag back reflector leads to interferences which mask the distinct LSP resonance. Indeed a distinct – though broad – absorption peak was found in the red region of the spectrum for glass/TCO/Ag-nanoparticles/a-Si:H and glass/a-Si:H/Ag-nanoparticles/a-Si:H layer stacks (see section 4.3.1).

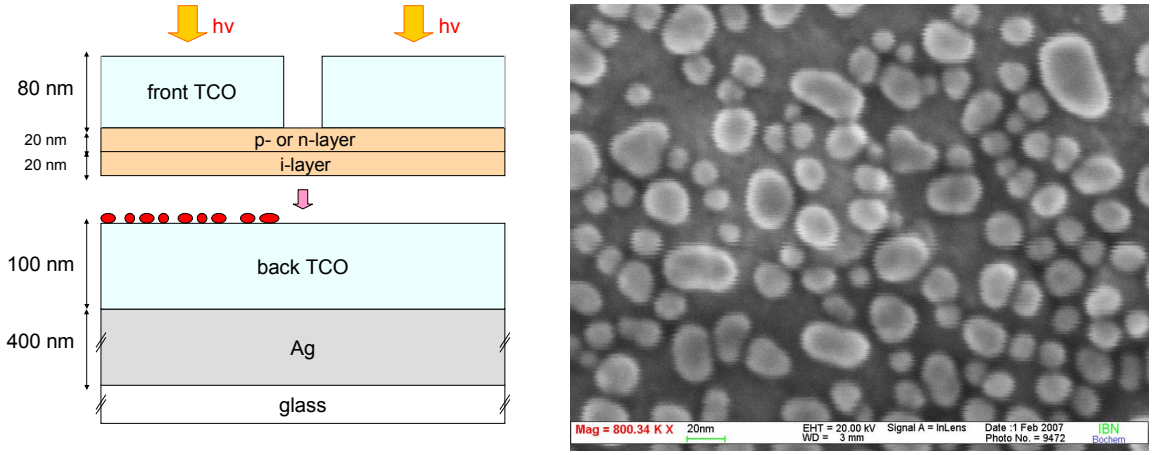

Figure 5.14 : (left) Schematic drawing of ultra-thin a-Si:H photosensitive devices in the Ag/TCO/i/n/TCO and Ag/TCO/i/p/TCO configuration with an i-layer thickness of 20 nm. The Ag nanoparticles are positioned at the TCO-i interface. (right) SEM picture of a 2 nm Ag film thermally evaporated on glass/Ag/TCO after annealing treatment at 180 °C for 90 min.

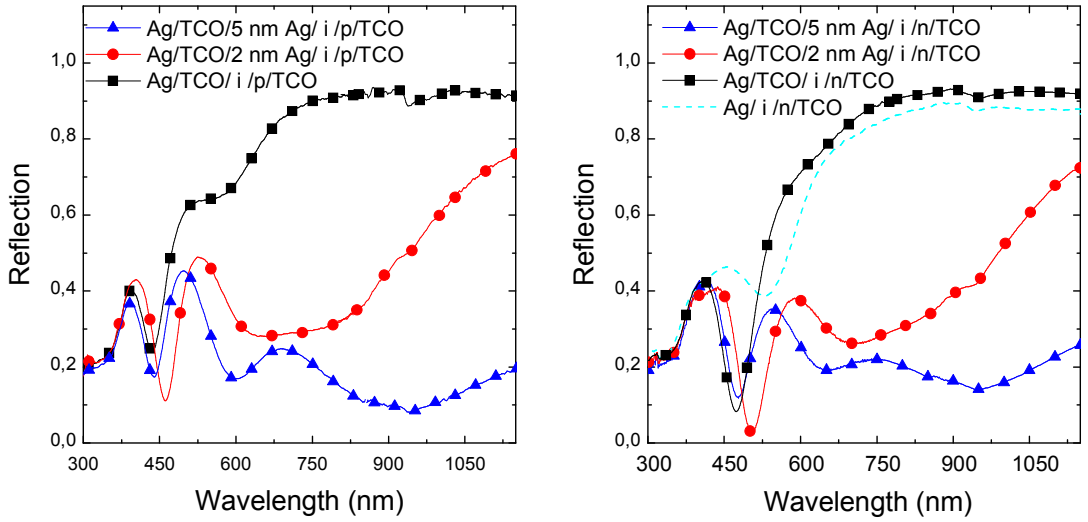

Figure 5.15 : Reflection of ultra-thin a-Si:H i-p (left) and i-n (right) photosensitive devices with and without Ag nanoparticles. The nanoparticles are deposited at the the TCO-i interface by thermal evaporation of a 2 nm (circles) and 5 nm (triangles) Ag film. For comparison, the reflection of glass/Ag/i/n/TCO layer stack is also shown (dashed line).

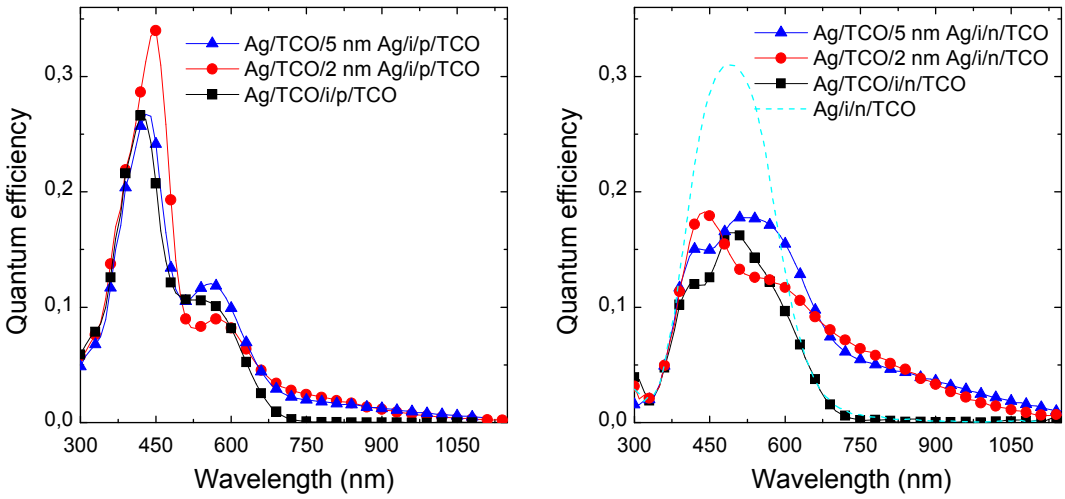

Figure 5.16 : Quantum efficiency of ultra-thin a-Si:H i-p (left) and i-n (right) photosensitive devices with and without Ag nanoparticles. The nanoparticles are deposited at the TCO-i interface by thermal evaporation of a 2 nm (circles) and 5 nm (triangles) Ag film. For comparison, the quantum efficiency of glass/Ag/i/n/TCO layer stack is also shown (dashed line).

QEs of i-p and i-n devices are plotted in Fig. 5.16 (left) and Fig. 5.16 (right), respectively. For $\lambda < 600$ nm, the QE of the solar devices with and without Ag nanoparticles is nearly identical. In this wavelength range, interferences lead to the small discrepancies observed between QE with nanoparticles and QE without nanoparticles. Solar devices containing Ag nanoparticles show an enhanced photocurrent for $\lambda > 600$ nm compared to devices without nanoparticles. For $\lambda > 750$ nm, no photocurrent can be measured for solar devices without nanoparticles, due to (i) the very thin thickness of the employed i-layer and (ii) the low absorption coefficient of a-Si:H in this wavelength range. In contrast, the photocurrent measured in presence of Ag nanoparticles extends to the near infrared (NIR) region, a spectral range that corresponds to photon energies smaller than the bandgap of a-Si:H. The broad enhancement of the photocurrent correlates with the broad reflectivity minimum found in presence of nanoparticles. By increasing the Ag film thickness from 2 nm to 5 nm, and consequently the average size of the obtained nanoparticles, the contribution of the photocurrent slightly shifts to longer wavelengths. This correlates with the observed shift in the reflectivity found for larger Ag film thicknesses. To verify the accuracy of the QE measurements in the NIR spectral range, we have measured the QE signal given by the system under open-circuit conditions. For $\lambda > 750$ nm, this signal has been found to nearly perfectly follow the QE characteristic of the device without nanoparticles, confirming that the photocurrent found in

the NIR region with nanoparticles is not an artifact. The Raman signal – enhanced by a factor of around 6 with nanoparticles (Fig. 5.17) – does not reveal the presence of a Raman peak at 520 cm^{-1}, characteristic of µc-Si:H (see Fig. 3.3). Crystallisation of a-Si:H in the vicinity of the nanoparticles, associated with a reduction of the optical bandgap, can therefore be excluded as a possible reason to explain the enhanced absorption and photocurrent in the NIR spectral region.

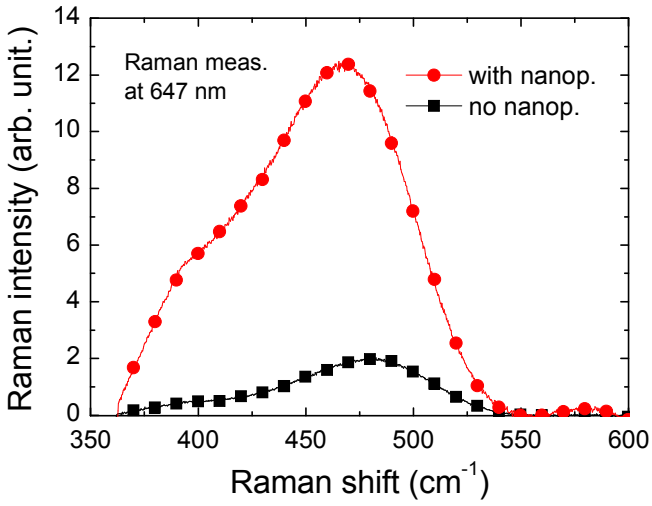

Figure 5.17 : Raman spectrum of an i-n solar cell with (circles) and without (squares) Ag nanoparticles positioned at the TCO-i interface.

Recently, several authors have reported enhancements of the photovoltaic conversion efficiency of organic solar cells by making use of the LSP of metal nanoparticles (Westphalen et al., 2000; Stenzel et al., 1995; Wen et al., 2000). The positive contribution of surface plasmons (SP) on the photocurrent of inorganic semiconductor/metal Schottky junctions has also been reported using the method of attenuated total reflection (Daboo et al., 1991). Two main reasons are found in the literature to explain the increased photocurrent. (i) The enhancement of the local electromagnetic field in the vicinity of the nanoparticles due to LSP. (ii) Photoemission of electrons – excited by light at the LSP resonance – from the nanoparticles to their surrounding medium. Lombardi et al. (1986) and Campion and Kambhampati (1998) have found that metal nanoparticles in contact with organic material can be employed as charge-transfer intermediates allowing spectroscopic transitions normally taking place in the UV to be excited by visible light.

Since a-Si:H only efficiently absorbs light of wavelengths up to 750 nm, the measured photocurrent in the NIR can obviously not be explained by an enhanced carrier generation resulting from an improved light absorption in the bulk a-Si:H i-layer (corresponding to an optical transition from the valence- to the conduction-band of a-Si:H). LSP-induced

photoemission of electrons from the nanoparticles or from states in their close vicinity may be responsible of the increased QE in the NIR spectral region. Fig. 5.18 shows two schematic models illustrating the possible photoemission processes involved in the carrier-generation mechanism of the i-p and i-n devices. Note that the nanoparticle / i-layer junction forms a Schottky contact. In the case of the i-p structure, photo-excited electrons from the valence band of the a-Si:H i-layer having a sufficient energy will be able to reach the Fermi level. The electrostatic field built by the p-layer will enable the transport and collection of the resulting holes from the i-layer to the p-contact. For the i-n configuration, photo-excited electrons of the nanoparticles having a sufficient energy will overcome the Schottky barrier formed by the nanoparticle / i-layer contact and reach the conduction band of the i-layer where they will be driven to the n-contact. Here, photoemission from defect states present in the vicinity of the nanoparticles (Fig. 5.18, mechanism 2) may also come into play. For both device configurations, an enhanced electromagnetic field inside and in the close vicinity of the nanoparticles is expected at the LSP resonance (see equation 1.6). The photoemission effect is therefore most probably amplified by the LSP effect of the nanoparticles.

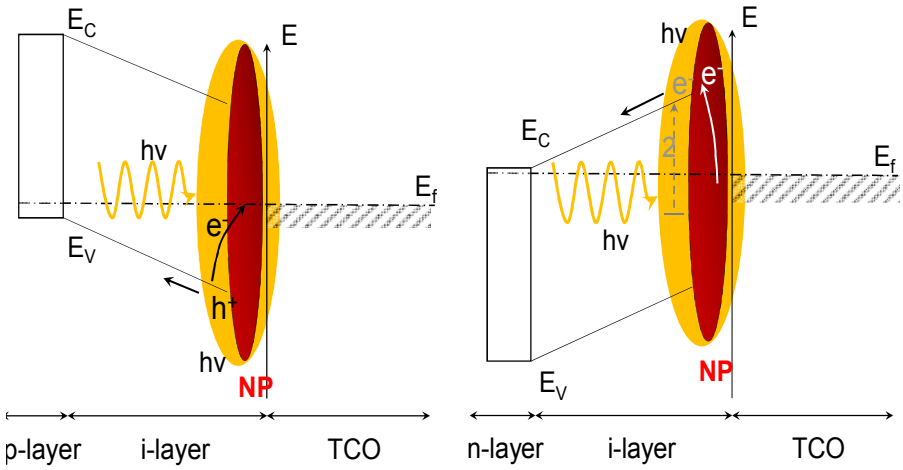

Figure 5.18 : Illustration of possible photoemission processes occuring in the i-p (left) and i-n (right) device. Photoexcitation from states outside and inside the nanoparticles at the localized surface plasmon resonance and the transport processes are depicted. The mechanism 2 (on the right) illustrates the photoemission of electrons from defect states close to the nanoparticles.

The enhancement of the photocurrent observed in presence of nanoparticles is more pronounced for the i-n configuration than for the i-p configuration. A more efficient photo-generation mechanism of carriers in the case of the i-n configuration may explain this result. However, due to the lower mobility of the carriers involved in the transport of the i-p configuration (namely the holes), a lower collection efficiency of the photo-generated carriers cannot be excluded as a possible reason to explain the limitation of the photocurrent for this

configuration. A negative bias voltage has been applied in order to improve the carrier extraction and collection. However, due to the very thin layers employed in these devices, the application of negative voltages leads to shunt problems.

In order to verify if the photocurrent enhancement is actually caused by the resonant light absorption in the nanoparticles due to LSP, a glass/Ag/i/n/TCO layer stack was prepared. The Ag layer consists of a 700 nm Ag film deposited by thermal evaporation. Reflection measurements of the glass/Ag/i/n/TCO layer stack show a slight decrease of the reflectivity in the long wavelength range compared to the glass/Ag/TCO/i/n layer stack (Fig. 5.15, right, dashed line), probably due to optical losses in Ag (Springer et al., 2004). QE of the prepared layer stack exhibits a high signal in the short wavelength range. However no photocurrent is measured for wavelength larger than 800 nm (Fig. 5.16, right, dashed line). Thus, the enhanced photocurrent found for $\lambda > 800$ nm with nanoparticles is most probably caused by the resonant LSP absorption.

Despite the enhanced photocurrent obtained for devices with Ag nanoparticles in comparison to devices without nanoparticles, the QE does not reflect the strong light absorption observed in the long wavelength range. Absorption losses in Ag nanoparticles and/or recombination of the generated charge carriers at the metal surface may occur. Only in the case the nanoparticles are in direct contact with the i-layer, a beneficial contribution on the photocurrent can be observed. Indeed, an enhanced photocurrent in the infrared region was also measured for ultra-thin a-Si:H p-i-n photosensitive devices with Ag nanoparticles located in the i-layer (not shown). However, no photocurrent enhancement is measured in the long wavelength range for ultra-thin p-i-n devices when the nanoparticles are deposited at the TCO-n interface (not shown). Under these conditions, we assume that charge carriers resulting from a photoemission process induced by LSP recombine directly in the nanoparticles or in the defect rich n-layer, due to the absence of electrostatic field necessary for the extraction of the carriers.

5.3.3 Ag nanoparticles embedded in TCO

In the previous section, we have shown that Ag nanoparticles incorporated at the TCO-i interface of a-Si:H solar cells with an i-layer thickness of 20 nm can lead to an increased photocurrent in the red and infrared spectral regions. We attributed this effect to an increased photoemission of electrons, at the Schottky contact formed by the i-layer / nanoparticle interface, induced by the enhanced electromagnetic field inside and in the close vicinity of the nanoparticles at the LSP resonance.

The amplification of the electromagnetic field in the surrounding of the nanoparticles may be of great use for enhancing light absorption with optical transitions above the bandgap. In the

red wavelength region – where the LSP resonance is maximum – the absorption coefficient of a-Si:H is relatively small (see Fig. 2.3). In order to shift the LSP resonance of the nanoparticles to shorter wavelengths, where the absorption coefficient of a-Si:H is larger (i.e. where optical transitions above the bandgap are more probable), the nanoparticles were covered with a thin layer of TCO with thickness around 10 nm. The refractive index n of TCO ($n_{ZnO} \sim 2$) is smaller than the one of a-Si:H ($n_{a\text{-}Si:H} \sim 4$). Therefore, according to equation 1.8, we expect the LSP resonance to be shift towards shorter wavelengths (Fig. 1.3). A schematic drawing of an a-Si:H i-n solar cell with an i-layer thickness of 20 nm and with nanoparticles embedded in TCO is shown in Fig. 5.19. When the nanoparticles are embedded in TCO, charge carriers resulting from a photoemission process may "recombine" directly within the nanoparticles, at the particle surface or in TCO since no efficient extraction of the electrons and holes can be provided. Embedding the nanoparticles in a transparent TCO thus permits to (i) eliminate the contribution of a charge transfert effect to the photocurrent and (ii) consider only the effect of an electromagnetic field enhancement occuring in the vicinity of the nanoparticles. The TCO layer was chosen as thin as possible so that (i) the local electromagnetic field resulting from the nanoparticles can reach the i-layer and (ii) optical losses in TCO are reduced.

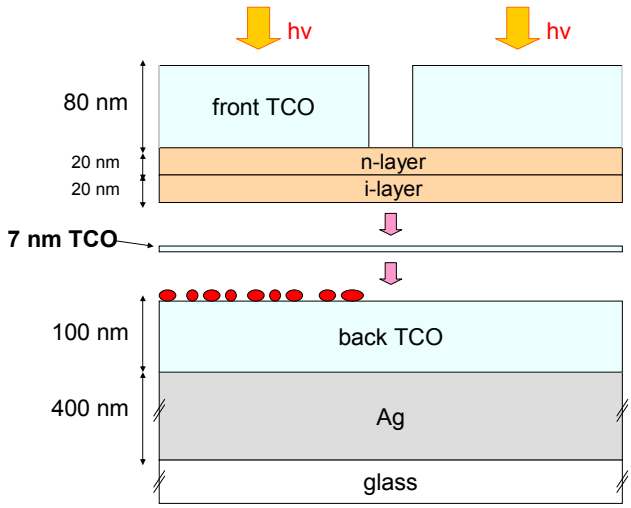

Figure 5.19 : Schematic drawing of very thin a-Si:H solar cells in the Ag/TCO/i/n/TCO configuration with an i-layer thickness of 20 nm. The Ag nanoparticles are embedded in TCO.

The reflection of the cell with nanoparticles (Fig. 5.20, left, for 3 nm Ag) shows a sharp minimum at 600 nm. We can clearly see from the measurements that the position of the LSP peak is blue-shifted in comparison to the case the nanoparticles are directly covered with a-Si:H. Moreover, the extremum in the reflection spectrum is sharper than in the previous case. This correlates with the theoretical results found in Fig. 1.3. For the device without

nanoparticles the Raman spectrum shows a broad maximum centered at 480 cm^{-1} which is characteristic of a-Si:H (Fig. 5.20, right). In contrast, the Raman signal found for the device with nanoparticles does not correspond to that of a-Si:H. A peak at 560 cm^{-1} is observed. Tzolov et al. (2000) have reported an intensive band in the Raman spectra of Al-doped ZnO films at approximately 570 cm^{-1}. The peak has been assigned to electric field-induced Raman scattering on longitudinal optical phonons. As already shown, the incorporation of Ag nanoparticles in a-Si:H can result in a shift of the a-Si:H Raman peak by up to 15 cm^{-1} to shorter wavenumbers (see Fig. 4.18, left), due to an increased background signal in presence of nanoparticles. It is therefore possible that the peak observed at 560 cm^{-1} results from an enhanced Raman signal of the TCO material, due to (i) a charge transfer and/or (ii) an enhanced electromagnetic field in the surrounding of the nanoparticles.

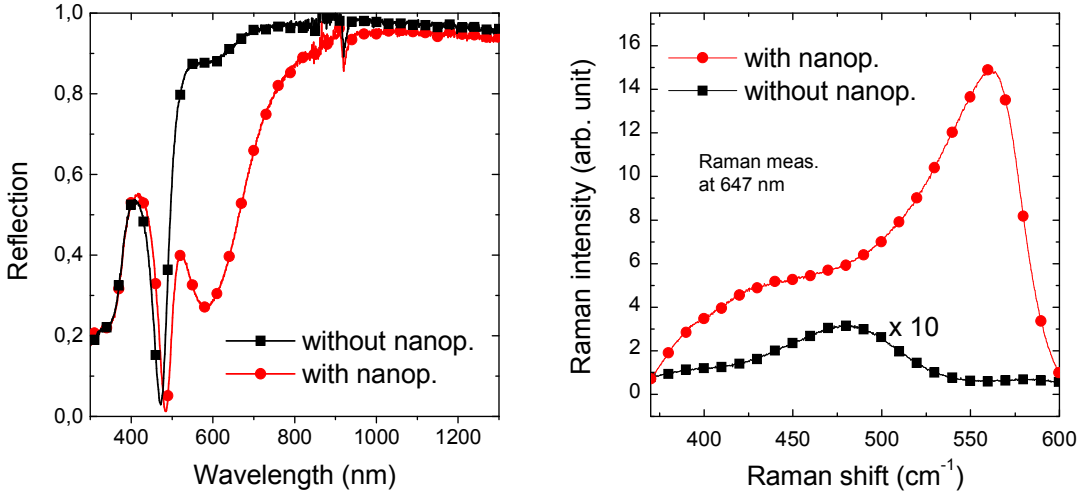

Figure 5.20 : Reflection (left) and Raman spectrum (right) of i-n devices with (circles) and without (squares) Ag nanoparticles. The nanoparticles are embedded in TCO.

QE measurements of the prepared cells show a higher photocurrent between 300 nm and 550 nm in presence of nanoparticles (cf. Fig. 5.21). Since the absorption spectrum of the devices with and without nanoparticles is similar in the short wavelength range (Fig. 5.20, left), the increase in blue response can be attributed to an improved electrical contact property in presence of nanoparticles. However, a smaller QE is measured for longer wavelengths and especially at 600 nm. Since the cell with Ag nanoparticles exhibits an increased absorption at 600 nm accompanied by a high Raman signal of ZnO, the enhanced electromagnetic field associated with LSP is probably confined in the TCO layer.

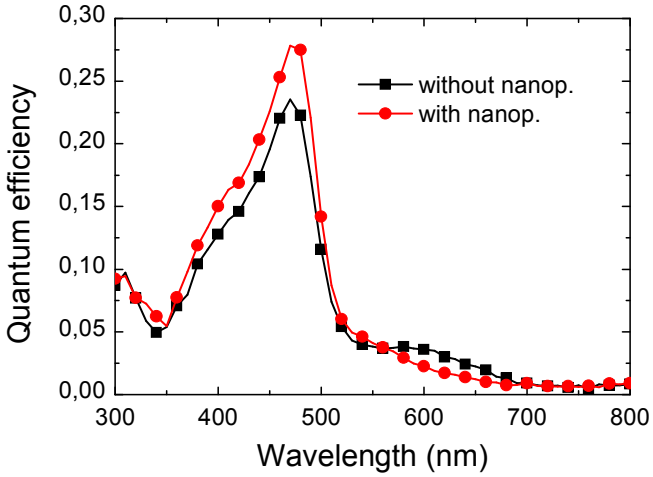

Figure 5.21 : Quantum efficiency of i-n solar cells with (circles) and without (squares) Ag nanoparticles. The nanoparticles are embedded in TCO.

5.3.4 LSP excitation with illumination from both sides of a bifacial device

In section 4.3, we have shown the optical response of a transparent bifacial glass/TCO/Ag-nanoparticles/a-Si:H/TCO layer stack. Despite the fact that the layer stack is not symetrical (the nanoparticles are deposited on TCO and covered with a-Si:H), a resonant light absorption accompanied by an enhancement of the Raman signal is measured for both illumination sides. In order to determine for which illumination side the effect of the nanoparticles has a stronger impact on the photocurrent, a bifacial solar device in the glass/TCO/(nanoparticles)/i-n/TCO configuration has been prepared. A schematic drawing of the device is depicted in Fig. 5.22.

For an illumination from the grid side (from the top of the device, in Fig. 5.22), identical QE values are found with and without nanoparticles in the short wavelength range at 0 V (cf. Fig. 5.23, left). For $\lambda > 650$ nm, the solar cell with nanoparticles exhibits an increased photocurrent compared to the cell without nanoparticles. Applying a negative bias voltage leads to an enhanced photocurrent of the device with nanoparticles in the whole spectral range (Fig. 5.23, left, at -0.75 V). For bias voltage of -0.5 V a saturation of the photocurrent is observed for both types of cells. The generation of charge carriers resulting from the LSP of Ag nanoparticles in the long wavelength range is probably limited by the efficiency of the photoemission process. Carrier recombination at the metal surface of the nanoparticles and optical losses probably also contribute to the photocurrent limitation.

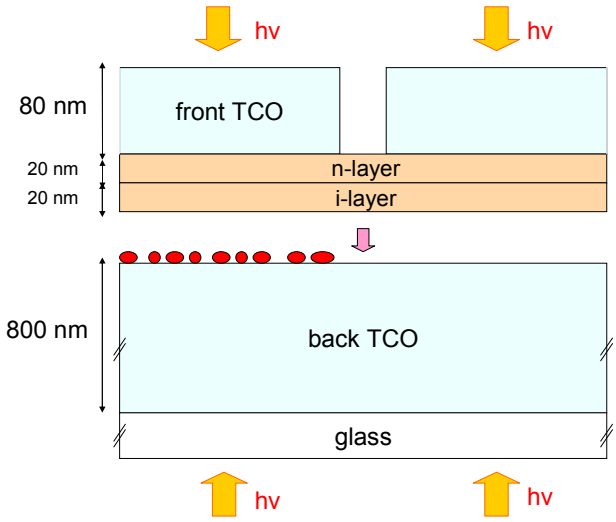

Figure 5.22 : Schematic drawing of two co-deposited a-Si:H i-n devices with and without Ag nanoparticles. The nanoparticles are positioned at the TCO-i interface. The device can be illuminated from both sides.

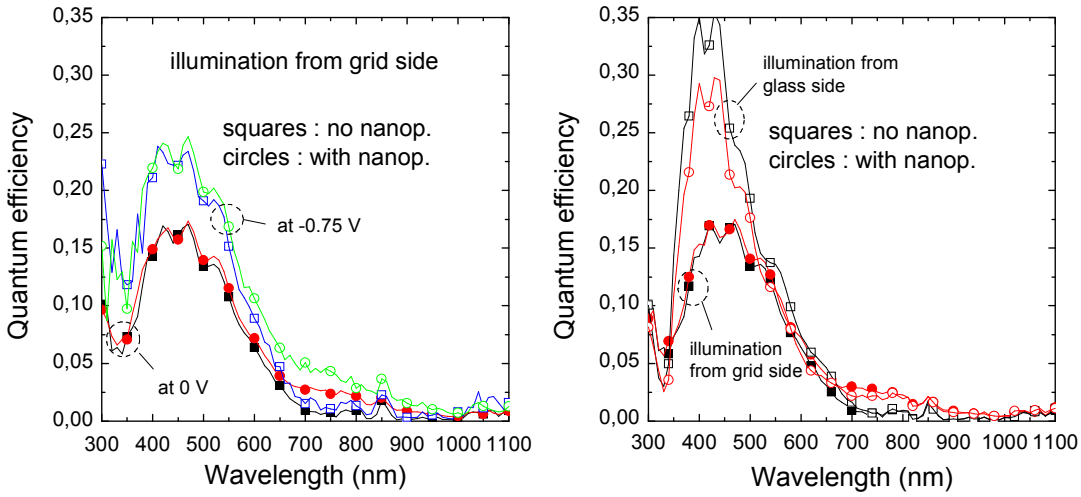

Figure 5.23 : (left) Quantum efficiency at 0 V and -0.75 V of a glass/TCO/i/n/TCO layer stack with and without Ag nanoparticles located at the TCO-i interface for an illumination from the grid side. Quantum efficiency at 0 V for illumination from grid side (full symbols) and glass side (open symbols).

When light enters from the glass side, a lower QE is measured in presence of nanoparticles in the short wavelength range (Fig. 5.23, right). Even if the LSP resonance mainly occurs in the red and infrared regions, the nanoparticles partly absorb light of short wavelengths before it

reaches the active layer of the device. However it is clear that the integration of nanoparticles also leads to an improved photocurrent in the infrared wavelength region for an illumination from the glass side. Therefore for small nanoparticles, LSPs can be excited independently of the illumination side of the nanoparticles and photoemission processes can be activated leading to a photocurrent enhancement.

5.4 Summary

Ag nanoparticles with an average diameter smaller than 35 nm deposited by thermal evaporation in a-Si:H solar cells lead to a significant enhancement of the light absorption in the red and infrared wavelength regions, due to localized surface plasmons (LSPs). Raman measurements performed at 647 nm show in most of the cases an amplification of the Raman signal for a-Si:H layer stacks containing Ag nanoparticles in comparison to layer stacks without nanoparticles. When the nanoparticles are incorporated inside the pin layer sequence of the p-i-n and n-i-p cells, a strong alteration of the electrical device properties is observed. Only if the nanoparticles are integrated at the TCO-n (or TCO-p) interface, no disturbances of the electrical device properties are found. However, under these conditions the photo-generated carriers resulting from the LSP-induced enhancement of the electromagnetic field in the vicinity of the nanoparticles may recombine directly in the n-layer rich of defects. For ultra-thin i-p cells and i-n photosensitive devices with Ag nanoparticles incorporated at the TCO-i interface, an enhanced photocurrent attributed to LSP-assisted photoemission of electrons from the nanoparticles or from states in their close vicinity is observed in the red and infrared spectral regions. This photocurrent is higher for the i-n configuration than for the i-p configuration. Further efforts have to be made to (i) clearly understand the photoelectronic mechanism of the involved process(es) and (ii) evaluate the limitation of the charge carrier generation.

Chapter 6

Large Ag nanoparticles for an improved light scattering

The scattering cross-section of spherical nanoparticles increases rapidly with their diameter (see equation 1.11a). Several authors have made use of this property to enhance light absorption in crystalline silicon and thin-film silicon solar cells. Most of the applications found in the literature consist of using large nanoparticles on top of solar cells to improve the light incoupling. In this chapter, we propose another approach based on the application of large nanoparticles at the rear side of solar cells. First, we discuss the structural and optical properties of the nanoparticles. Afterwards, we present the results obtained for μc-Si:H and a-Si:H solar cells in the n-i-p configuration applying the modified back reflector with large nanoparticles. The optoelectronic device properties are discussed.

6.1 Preparation of large Ag nanoparticles on glass/Ag/TCO

Large nanoparticles were prepared using the same technique as applied for depositing small nanoparticles (with a lateral size < 50 nm), i.e. the thermal evaporation of a thin Ag film and a post annealing treatment. The thickness of the Ag film was varied between 10 nm and 35 nm. A glass/Ag/TCO layer stack was used as a substrate. For 10 nm Ag, a percolation continuum is observed before thermal treatment (Fig. 6.1, left). For thicker Ag films, the voids separating the percolated Ag structures become smaller and a continuous and homogeneous surface is found for 20 nm Ag (Fig. 6.1, right). Annealing the layer stack at 180 °C for 30 min is sufficient to observe significant changes in the Ag-film structure. However since the samples were annealed in the vacuum chamber of a PECVD system because of its high vacuum (< $1e^{-6}$ mBar), the annealing process was conducted overnight (i.e. for several hours). For Ag film thicknesses of 10 nm and 20 nm well separated nanoparticles are formed after the annealing treatment with average lateral size of 100 nm (Fig. 6.2, left) and 300 nm (Fig. 6.2, middle), respectively. A broad range of particle sizes extending from 20 nm to 250 nm is found after the annealing treatment of a 10 nm Ag film. A more uniform

size distribution is observed in the case of a 20 nm Ag film. For thicker Ag films, the annealing treatment leads to a modification of the film morphology from a continuous and homogenous surface to a percolation continuum (Fig. 6.2, right, in the case of a 35 nm thick Ag film). Even with a longer annealing time and higher temperatures no isolated particles can be obtained.

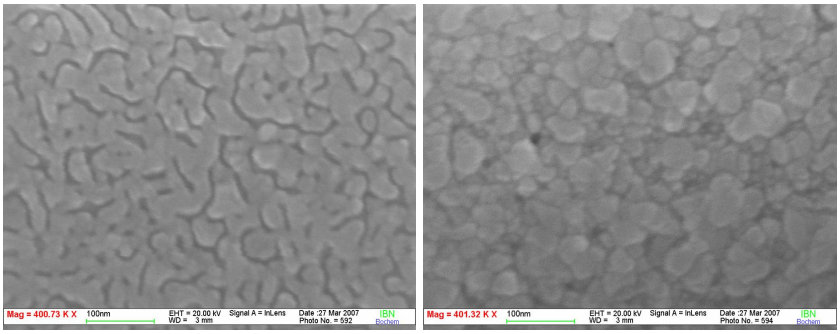

Figure 6.1 : SEM pictures of a 10 nm (left) and 20 nm (right) Ag film deposited on a glass/Ag/TCO layer stack before thermal treatment.

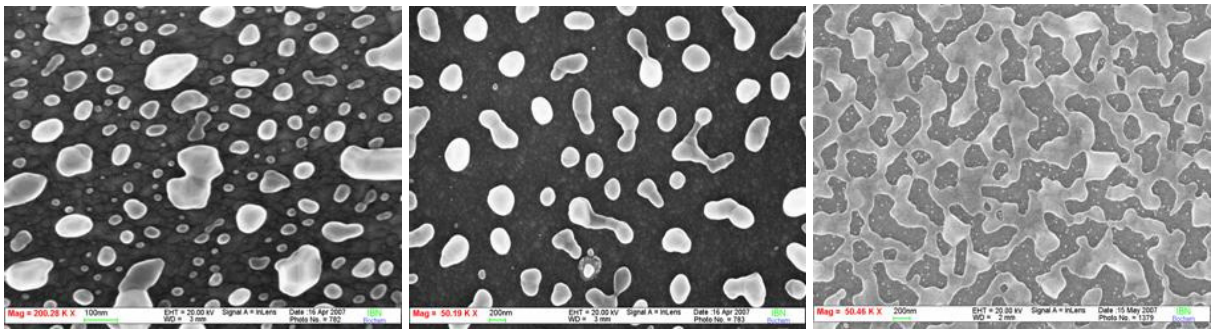

Figure 6.2 : SEM pictures of a 10 nm (left), 20 nm (middle) and 35 nm (right) Ag film deposited on a glass/Ag/TCO layer stack after annealing at 180 °C for 90 min. Note the different scales used for the SEM micrographs.

6.2 Optical characterization of large Ag nanoparticles deposited on glass/Ag/TCO

Fig. 6.3 shows reflection measurements of a glass/Ag/TCO reflector covered with a 10 nm (left) and 20 nm (right) Ag film before annealing. The reflectivity of glass/Ag/TCO without Ag film is plotted as a reference (Fig. 6.3, left, solid line). Between 450 nm and 1300 nm the layer stack shows a high reflectivity. For wavelengths smaller than 450 nm, a strong decrease of the reflection is found, due to light absorption in the TCO and in the Ag mirror. Two minima are observed at 340 nm and 420 nm which are attributed to the plasma

frequency and surface plasmon resonance of Ag embedded in TCO (Springer et al., 2004). The reflector covered with a 10 nm thick Ag film exhibits a broad minimum in the reflectivity at approximately 650 nm (Fig. 6.3, left, squares). The reflector covered with a 20 nm thick Ag film shows a nearly identical reflectivity as the reflector without Ag film, except a distinct minimum at approximately 550 nm (Fig. 6.3, right, squares).

To understand the origin of the minima in the reflectivity, reflection simulations of glass/Ag/TCO/Ag systems using the optical constant of bulk Ag material for the Ag film were carried out. In the case of the 10 nm thick Ag film no match between simulation and experiment could be achieved (Fig. 6.3, left, comparison of the dashed line and squares). This may be due to the fact that before annealing the 10 nm thick Ag film shows a percolation continuum while ideal bulk materials were considered in the calculation of the Ag nano-layer. Simulation of the 20 nm thick Ag layer on glass/Ag/TCO shows a good agreement with the experimental data (Fig. 6.3, right, comparison of the dashed line and squares). However the distinct minimum in the calculated reflectivity reaches a value of 0.65 and appears at 500 nm. By increasing the thickness of the Ag film in the simulations, the minimum in the reflectivity shifts towards shorter wavelengths and becomes sharper. This behavior is represented by the simulation considering a 30 nm thick Ag bulk layer on top of the TCO layer (Fig. 6.3, right, dots). By decreasing the TCO layer thickness by a few nanometers, the distinct minimum also experiences a blue-shift (not shown). The position of the distinct minimum at 550 nm strongly depends on the TCO layer thickness. This indicates that the minimum originates from interference effects. Thus we assume that the difference observed between the measurements and the calculations of the layer stack covered with 20 nm Ag originates from a slight discrepancy between both the actual and the simulated thicknesses of the TCO and Ag films. In the simulations, surface plasmons of Ag are not considered.

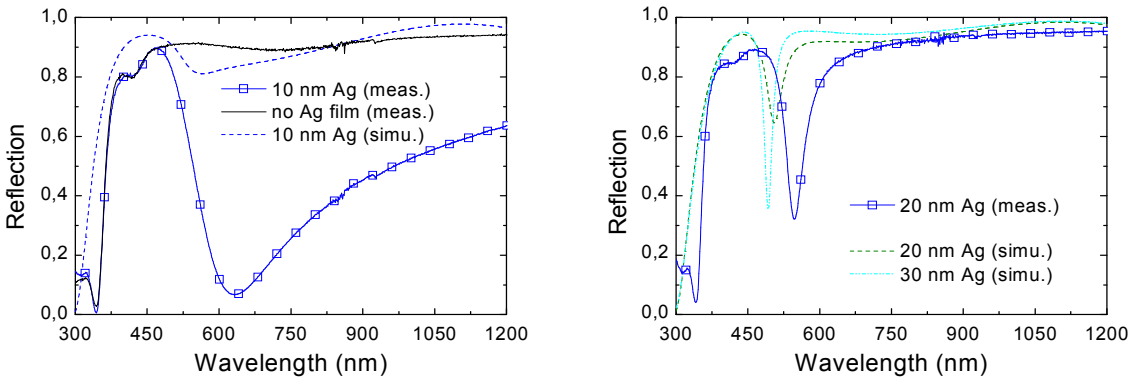

Figure 6.3 : Measured and calculated reflection of 10 nm Ag (left) and 20 nm Ag (right) deposited on a glass/Ag/TCO reflector before annealing. The solid line (left) represents the reflectivity of the glass/Ag/TCO reflector without Ag film on the top.

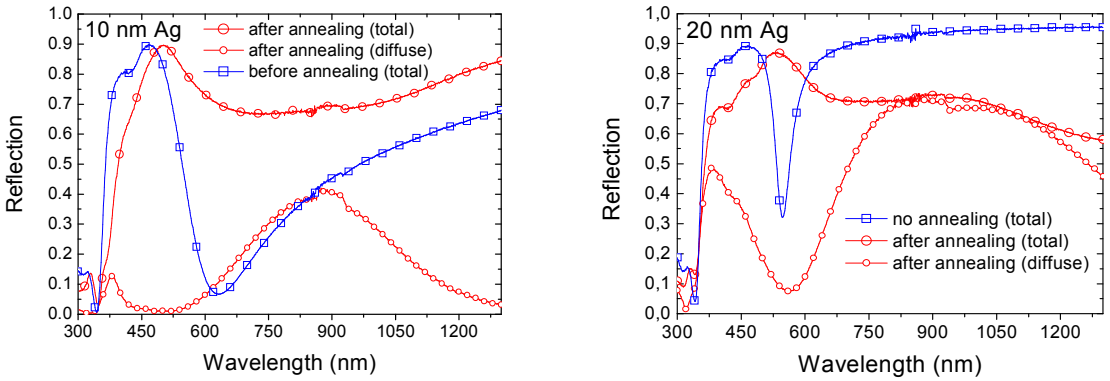

Figure 6.4 : Diffuse and total reflection of 10 nm Ag (left) and 20 nm Ag (right) deposited on a glass/Ag/TCO reflector before and after annealing at 180 °C.

After an annealing treatment at 180°C (Fig. 6.4), the distinct minima of the glass/Ag/TCO reflectors covered with 10 nm and 20 nm Ag film disappear. Two broad peaks in the diffuse part of the reflected light with maxima at 400 nm and 900 nm are found in both cases (Fig. 6.4, small circles), likely due to light scattering at the surface of the large Ag nanoparticles. When reflectors with a thinner TCO layer are used, a shift of the minimum of the diffuse part to shorter wavelengths is observed (not shown). Since its position is nearly independent of the nanoparticle diameter originating from different Ag film thicknesses and depends strongly on the TCO layer thickness, it may be caused by an interference effect. Optical losses indicated by the decreased total reflection of the substrate with nanoparticles (Fig. 6.4, large circles) can be attributed to (i) light confinement in the TCO due to the enhanced light scattering and (ii) light absorption in the nanoparticles.

By etching the modified back contact system with HCl, the TCO is removed at areas which are not covered with the nanoparticles as verified by SEM and reflection measurements (Fig. 6.5, left and right, respectively). The nanoparticles act as etching masks. Since their diameter can be varied over a wide range, this approach may be useful for other applications. After etching of the TCO layer, the two maxima in the diffuse scattered light disappear and a broad and single peak at around 500 nm is observed (Fig. 6.5, right). Moreover the intensity of the diffuse scattered light is decreased after etching of the TCO. By removing the TCO ($n_{TCO} \approx 2$), the optical path length of the light which is reflected at the Ag back reflector is reduced. Thus, the phase shift between the light which is reflected at the nanoparticle surface and the light which is reflected at the Ag back contact is decreased. This is equivalent to reduce the surface roughness of the back reflector. Under these conditions, according to the Rayleigh criterion for rough surfaces (see equation 6.1), the fraction of scattered light decreases (Stiebig et al., 2006a):

$$Haze = \frac{diffuse \quad scattered \quad reflection}{total \quad reflection} = 1 - \exp\left[-\left(\frac{4\pi\delta}{\lambda}\right)^2\right] \tag{6.1}$$

, with δ the root mean square roughness and λ the excitation wavelength.
Moreover, the total reflectivity increases in the long wavelength range after etching. This indicates that most of the absorption losses observed for the system glass/Ag/TCO/nanoparticles (before HCl dip) originate from the trapping of light in the TCO layer rather than light absorption in the nanoparticles.

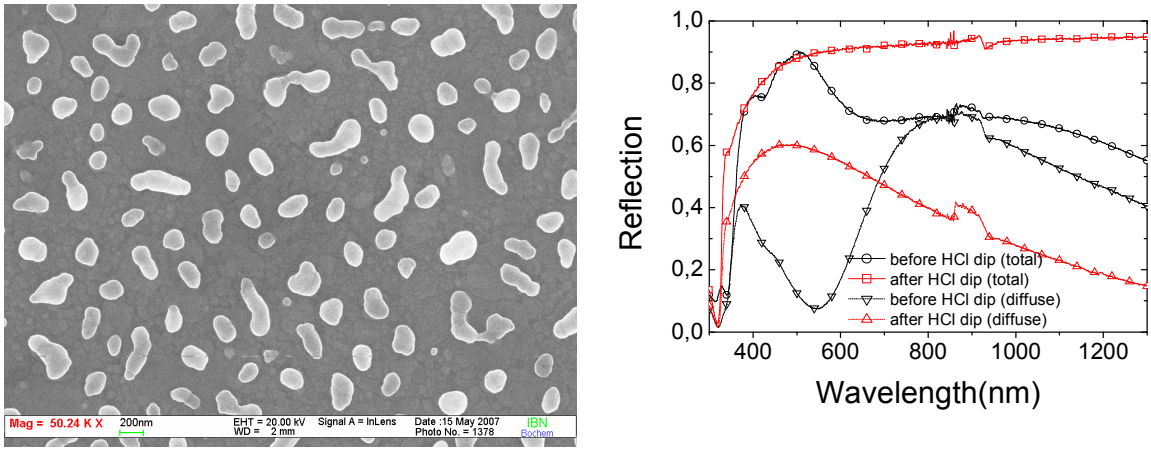

Figure 6.5 : (left) SEM picture of a glass/Ag/TCO/large-nanoparticles layer stack after HCl dip. By etching the layer stack with HCl, the TCO is removed at areas which are not covered with the nanoparticles. The nanoparticles act as etching masks. (right) Diffuse and total reflection of the system before and after HCl dip.

6.3 Large silver nanoparticles in µc-Si:H n-i-p solar cells

Since the glass/Ag/TCO reflector with large Ag nanoparticles shows promising scattering properties, it was applied as a back contact in µc-Si:H n-i-p solar cells. The nanoparticles – obtained by evaporation of a 20 nm Ag film followed by an annealing treatment – were deposited through a mask so that they cover only the half of the substrate. AFM measurements of the modified reflector show ellipsoidal nanoparticles with an average lateral size of 300 nm and height of 50 nm after annealing at 180 °C for several hours (Fig. 6.6, left). A root mean square roughness of 27.5 nm is measured. On top of this substrate a µc-Si:H n-i-p solar cell with an i-layer thickness of 1 µm was deposited. A schematic drawing of the device is shown in Fig. 6.6 (right).

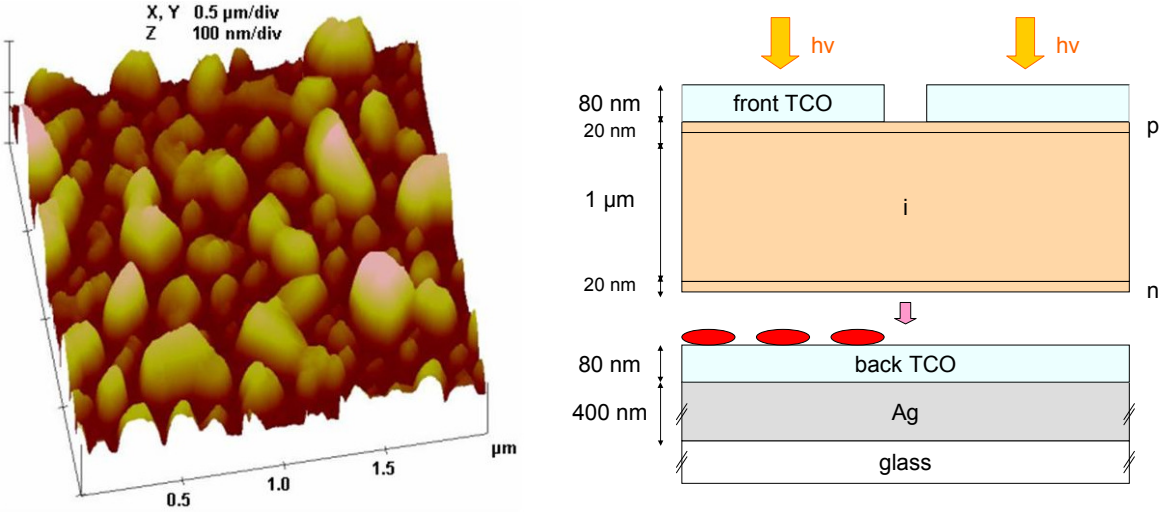

Figure 6.6 : (left) 2x2 µm² AFM scan of a 20 nm Ag film deposited on a glass/Ag/TCO layer stack after annealing at 180 °C for several hours. (right) Schematic drawing of two co-deposited µc-Si:H n-i-p solar cells with (left) and without (right) large Ag nanoparticles.

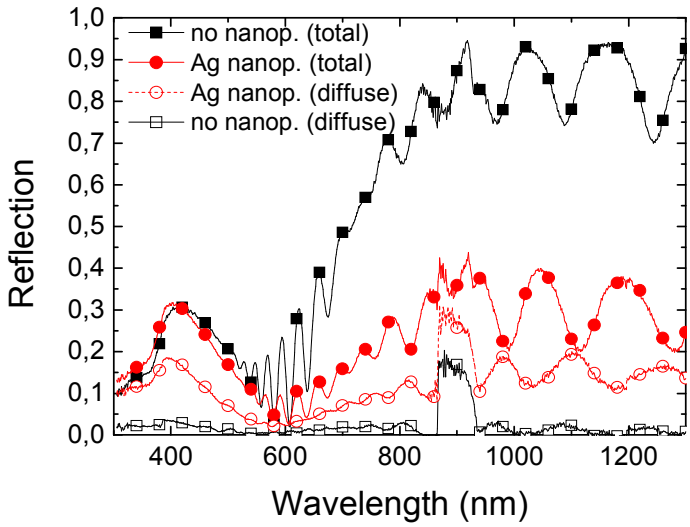

Figure 6.7 : Diffuse (open symbols) and total (full symbols) reflection of µc-Si:H n-i-p solar cells deposited on glass/Ag/TCO with (circles) and without (squares) Ag nanoparticles.

Reflection measurements of both types of cells with and without nanoparticles are shown in Fig. 6.7. For the solar cell with nanoparticles, the fraction of diffuse scattered light (open circles) is increased in the whole spectral range in comparison to the cell without nanoparticles (open squares). Due to light scattering at the back contact, the light path in the cell is enhanced and the total absorption is increased. This corresponds to a reduction of the reflection (full circles) compared to the case of a flat cell (full squares).

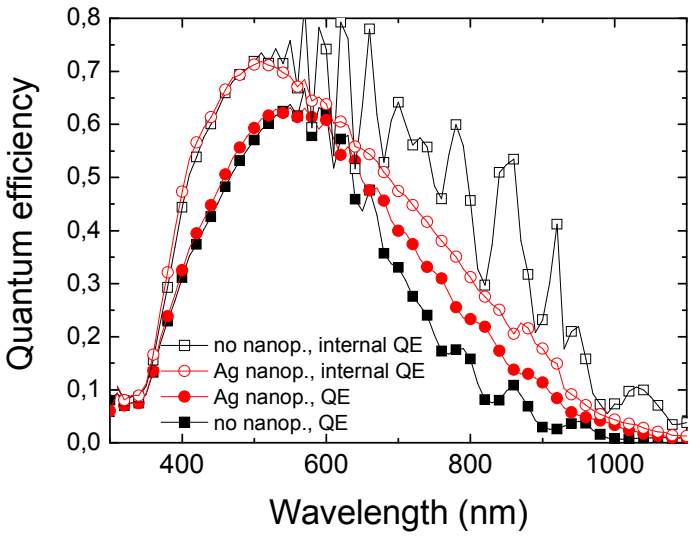

Figure 6.8 : External quantum efficiency (full symbols) of n-i-p µc-Si:H solar cells with (circles) and without (squares) large nanoparticles. The calculated internal quantum efficiency is also plotted (open symbols).

An increased external QE is measured in the long wavelength range for the cell with nanoparticles compared to the cell without nanoparticles (Fig. 6.8, full symbols) because of the improved light scattering. Due to the nearly conformal deposition of the µc-Si:H and TCO layers, the front surface topography of the solar cell approximately follows the topography of the back reflector. The resulting nanotexture at the front surface leads to a slight improvement in the light incoupling, indicated by the small increase in the blue response. This increase is associated with a reduction of the cell reflection in the short wavelength range compared to the case of the flat cell (Fig. 6.7, full circles compared to full squares). The enhancement of the QE for $\lambda > 600$ nm does not correspond to the strong increase in absorption found in the long wavelength range. The internal QE, given by equation 6.2:

$$QE_{internal} = QE / (1 - \text{total reflection}) \qquad (6.2)$$

has been calculated to evaluate the parasitic absorption losses in the solar cell. In the long wavelength range, $QE_{internal}$ is smaller for the cell with nanoparticles than for the reference cell (see Fig. 6.8, open circles compared to open squares). The reduced internal QE may originate from plasmonic absorption losses in the silver nanoparticles. These optical losses are probably emphasized by the multiple light reflections within the cell due to the enhanced light scattering. The spectral range of the observed absorption losses fits with the position of the localized surface plasmon absorption of individual Ag nanoparticles that can be found at wavelengths between 500 nm and 2 µm depending on the particle size, shape and embedding

material (Mertens et al., 2004). Nevertheless, the decrease in the internal QE in the NIR wavelength region may also be explained by (i) an enhanced absorption in the back TCO caused by light trapping between the silber back reflector and the nanoparticles, (ii) recombination of charge carriers in defects present in the vicinity of the nanoparticles and/or (iii) surface recombination of charge carriers at the metal particle surface.

Despite an increase in the short-circuit current, the electronic properties of the solar cells with large nanoparticles are adversely affected. Both FF and Voc are reduced from 73 to 69 % and from 510 mV to 480 mV, respectively (cf. Fig. 6.9). The lower cell performance may originate from an alteration of the µc-Si:H growth on the substrate due to the presence of the nanoparticles. It is known that the substrate roughness has a large influence on the growth mechanism of µc-Si:H (H. Li, 2007). The decrease of Voc may result from an enhanced carrier recombination due to the formation of defects and voids. The two following reasons for that are found in the literature. (i) When grown on large nanoparticles, the silicon columns of the µc-Si:H that grow perpendicularly to the nanoparticle surface may collide with each other in the i-layer, leading to a higher electronic defect density caused by the higher grain boundary density. (ii) µc-Si:H deposited on large nanoparticles fails to conformally cover the nanoparticles. Consequently, voids which develop along the deposition direction and extend into the bulk of the i-layer may appear in the solar cell. These voids are suggested to be the path where impurities such as water vapor and oxygen move in and dope the material.

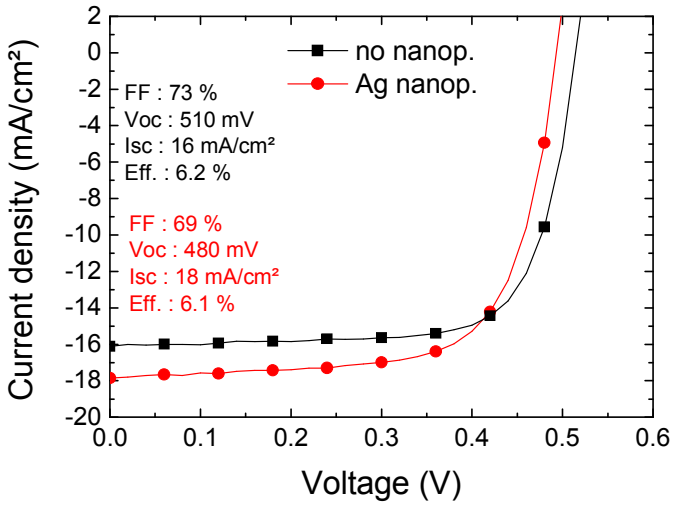

Figure 6.9 : Current-voltage characteristic under AM 1.5 illumination of n-i-p µc-Si:H solar cells with (circles) and without (squares) Ag nanoparticles.

6.4 Large silver nanoparticles in a-Si:H n-i-p solar cells

6.4.1 Ag nanoparticles at the TCO/n interface

A reflector with large Ag nanoparticles similar to the one shown in section 6.3 was integrated at the rear side of a-Si:H n-i-p solar cells. The nanoparticles are ellipsoidal with average lateral size of 300 nm and height of 50 nm (cf. Fig. 6.6, left). The nip diode consists of a-Si:H n- and i-layers and a µc-Si:H p-layer. An absorber layer thickness of 350 nm was used, as illustrated in Fig. 6.10. Detailed information about the n-i-p cell preparation and requirements are given in sections 2.4.5 and 2.4.7.

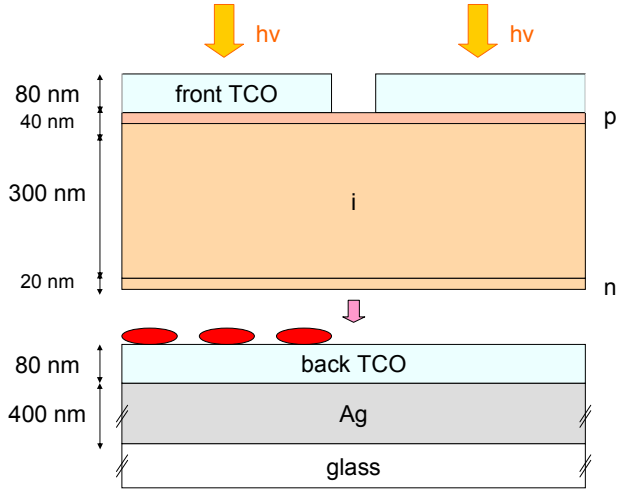

Figure 6.10 : Schematic drawing of two co-deposited a-Si:H n-i-p solar cells with and without Ag nanoparticles.

Reflection measurements of a-Si:H cells show similar trends to those found in the case of µc-Si:H cells. In presence of the nanoparticles, the fraction of diffuse scattered light is increased in the whole spectral range (open circles) compared to flat cells (open squares). Thus, the light path in the solar cells is enhanced and the total reflection is reduced (full circles compared to full squares).
Fig. 6.12 shows the corresponding Quantum Efficiency curves. The external QE (Fig. 6.12, top) is increased in the long wavelength range for the cell with nanoparticles in comparison to the cell without nanoparticles. Nevertheless, the increase in QE in the long wavelength range is again not representative of the strong decrease in reflection. A smaller $QE_{internal}$ is observed for cells with nanoparticles (Fig. 6.12, bottom), probably due to plasmonic losses in the Ag nanoparticles.

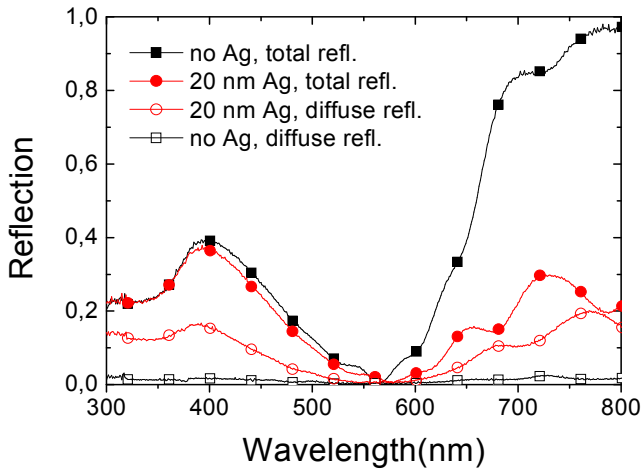

Figure 6.11 : Diffuse (open symbols) and total (full symbols) reflection of a-Si:H n-i-p solar cells based on glass/Ag/TCO with (circles) and without (squares) large Ag nanoparticles.

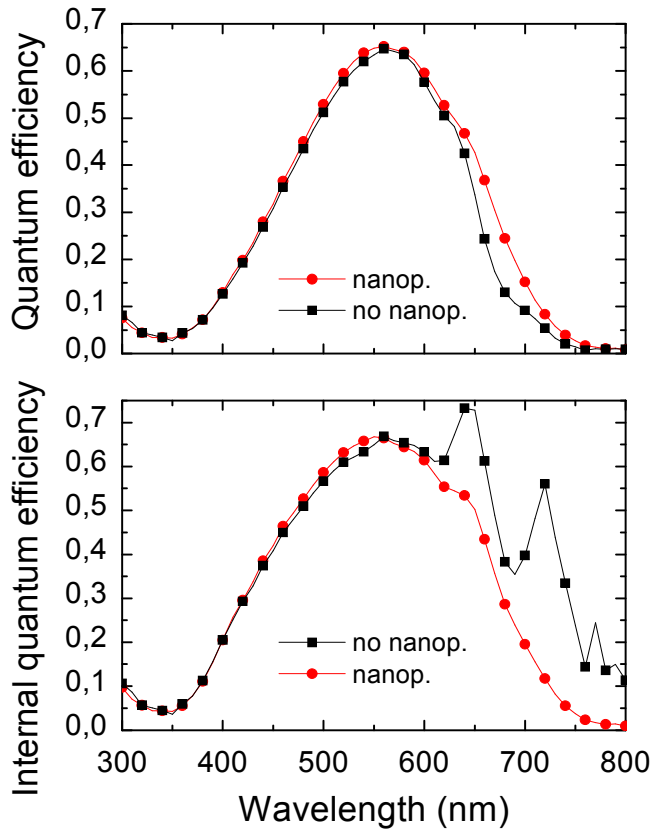

Figure 6.12 : External (top) and internal (bottom) quantum efficiency of a-Si:H n-i-p cells deposited on substrates with (circles) and without (squares) large nanoparticles.

Fig. 6.13 shows the I-V curve under illumination of the a-Si:H solar cell with and without large Ag nanoparticles. The short-circuit current (Isc) and the fill factor (FF) increase from 11.1 mA.cm^{-2} to 12.1 mA.cm^{-2} and from 57.3 % to 58.4 %, respectively, by incorporating the nanoparticles. This results in an increase in efficiency of 0.5 %. The Voc is decreased from 882 mV to 862 mV in presence of the nanoparticles, probably due to (i) surface recombination at the metal particle surface and/or (ii) recombination of charge carriers in defects introduced by the nanoparticles. Note however that the electric properties of the a-Si:H solar cells are less affected by the presence of the nanoparticles than those of the µc-Si:H cells. Therefore the significant decrease in FF and Voc found for the µc-Si:H cells deposited on the modified reflector (see section 6.3) is most probably due to a more severe alteration of the material growth. To conclude, large Ag nanoparticles incorporated at the back side of a-Si:H solar cells in the n-i-p configuration have a beneficial influence (i.e. an enhanced efficiency). However the observed gain in photocurrent may be attenuated by (i) optical losses in the nanoparticles, (ii) optical losses in the back TCO, (iii) recombination at the surface of the metal particles and/or (iv) recombination of charge carriers in defects introduced by the nanoparticles. To reduce the influence of (i) and (iii), a thin TCO layer was deposited on the nanoparticles, as shown in the next section.

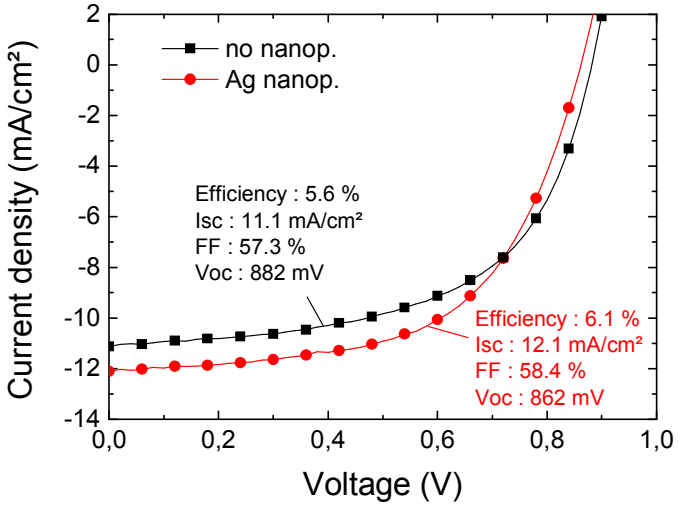

Figure 6.13 : Current density under illumination of a-Si:H solar cells in the n-i-p configuration with (circles) and without (squares) large Ag nanoparticles.

6.4.2 Ag nanoparticles embedded in TCO

Significant optical losses in textured silver back reflectors have been observed in the case the silver is in direct contact with silicon (Stiebig et al., 1994). These optical losses are caused by surface plasmon polaritons in Ag and are influenced by (i) the nucleation region of

the Ag film (for p-i-n cells), (ii) the deposition conditions used for Ag, (iii) the surface texture (Springer et al., 2004; Sainju et al., 2006) and (iv) the embedding medium. In the case of large isolated Ag nanoparticles embedded in a-Si:H ($n_{a\text{-}Si:H} \approx 4$), plasmon absorption may as well occur in the red region depending on the particle size, shape and embedding material (Mertens et al., 2004; Sönnichsen et al., 2000-2001). It is well known that the integration of a thin TCO layer between the silicon and the metal back contact (Ag or Al) usually leads to a significant enhancement of the photocurrent (Stiebig et al., 1994; Schultz, 1994; Beneking et al., 1994; Yoshida et al., 1992). For cells deposited on a rough substrate this enhancement is even larger than for cells deposited on a flat substrate. This effect is ascribed to (i) the multiple light reflections at the back reflector and (ii) the increased localized surface plasmon absorption at textured metal surfaces. The improved efficiency found in presence of an additional TCO layer is explained by an increased reflection at the back contact caused by a reduction of the plasmonic absorption losses in the metal. As explained in chapter 1, the localized surface plasmon resonance of small Ag nanoparticles shifts towards shorter wavelengths as the refractive index n of their embedding medium is decreased (see Fig. 1.3). For large nanoparticles, the same effect is expected. Fig. 6.14 illustrates the blue-shift of the LSP absorption resonances of large Ag nanoparticles of radius R=60 nm when the refractive index of the matrix is varied from 3.6 ($\approx n_{a\text{-}Si:H}$) to 2 ($\approx n_{TCO}$).

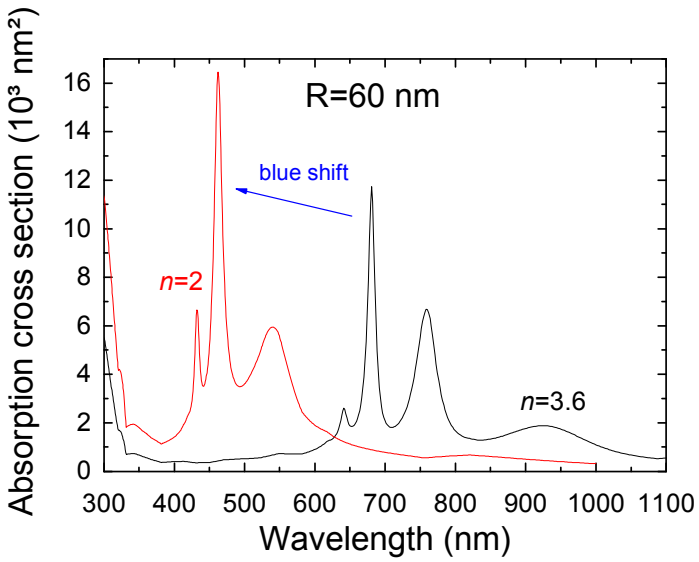

Figure 6.14 : Absorption cross section of Ag nanoparticles of radius R=60 nm in a matrix with refractive index n=2 (~ n_{TCO}) and n=3.6 (~$n_{a\text{-}Si:H}$), according to the Mie theory.

An additional TCO layer with thickness around 80 nm, referred to as TCO3, has been incorporated between the nanoparticles and the silicon layers (cf. Fig. 6.15). The additional TCO3 layer leads to a decrease in the QE in the whole wavelength range (Fig. 6.16). The deposition and growth conditions applied for the TCO3 layer or simply the vacuum break

necessary to deposit this layer apparently results in the deterioration of the electric quality of the back contact. Nevertheless, we note that the TCO3 layer leads to a considerable enhancement of the QE of the cell with nanoparticles for $\lambda > 600$ nm. For the cells applying the TCO3 layer, the internal QE is nearly identical with and without nanoparticles (result not shown), confirming the significant reduction of the plasmonic losses in the nanoparticles.

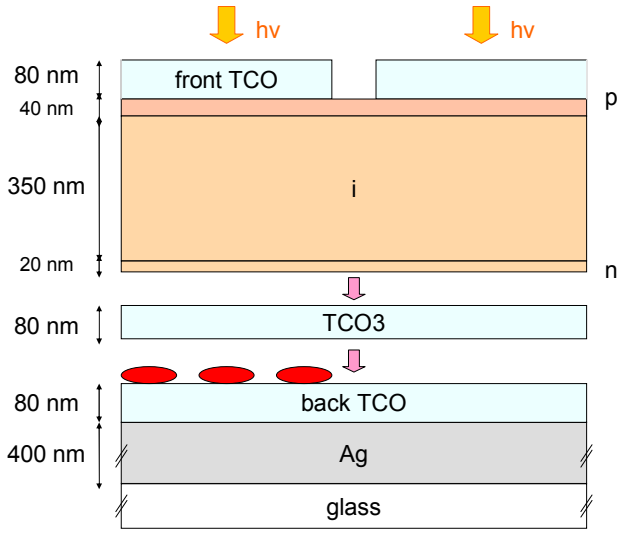

Figure 6.15 : Schematic drawing of two co-deposited a-Si:H n-i-p cells with and without Ag nanoparticles. A thin TCO layer is incorporated between the particles and the silicon layers.

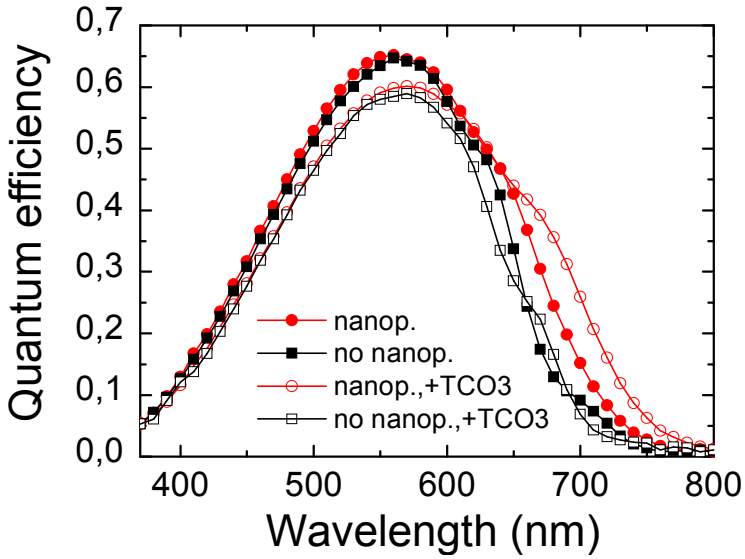

Figure 6.16 : Quantum efficiency of a-Si:H n-i-p cells with (circles) and without (squares) nanoparticles. The open/full lines represent the QE of cells with/without a TCO3 layer.

6.5 Summary

Large Ag nanoparticles with an average lateral size up to 300 nm have been deposited on glass/Ag/TCO by thermal evaporation followed by an annealing treatment at 180 °C. The reflection measurements of this layer system show two peaks in the diffuse scattered light. The amplitude of the maxima increases with the size of the deposited nanoparticles. The minimum of the diffuse light is ascribed to interferences. Optical losses indicated by the decreased total reflectivity are found which are attributed to (i) light confinement in the TCO and (ii) light absorption in the nanoparticles.

Large Ag nanoparticles have been incorporated at the rear side of μc-Si:H and a-Si:H solar cells. The reflection of the cells with nanoparticles is significantly smaller in the long wavelength range than the reflection of the reference cells. This result is caused by the improved light trapping resulting from the enhanced light scattering at the nanoparticles. For both μc-Si:H and a-Si:H cells, the QE is increased in the long wavelength region. However, plasmonic losses in the metal nanoparticles lower the positive effect of the nanoparticles. By covering the nanoparticles with an 80 nm thick TCO layer, the plasmonic losses are shifted towards shorter wavelengths and the QE increases in the long wavelength range. Solar cells containing large Ag nanoparticles exhibit an improved photocurrent. However, the presence of the nanoparticles leads to a considerable degradation of the electric device performance (more pronounced for the μc-Si:H cells), likely due to an alteration of the material growth on the modified back reflector.

Chapter 7

Nanostructured Ag back reflector

Most of the thin-film silicon solar cells produced today rely on a randomly textured substrate with crater-like or pyramid-like structures in the micrometer range in order to achieve an efficient light trapping and a high conversion efficiency. In this chapter, we present an approach based on an Ag nanostructured back reflector to provide light scattering at the rear side of thin-film silicon solar cells. After an annealing treatment, thin Ag films (< 50 nm) deposited on glass by thermal evaporation show a large variety of structures with heights of several nanometers. After these structures are covered with a bulk Ag layer of moderate thickness, the obtained reflectors – showing a topography made of nanostructures – can serve the purpose of scattering the light at the rear side of solar cells. Indeed, for Ag films with the proper thickness, reflection and angle distribution measurements of the resulting nanostructures reveal interesting optical properties. The Ag nanostructures are here used as back reflectors in a-Si:H and μc-Si:H solar cells in the n-i-p configuration. The optoelectronic properties of the obtained solar cells are compared with those of solar cells deposited on a standard back reflector.

7.1 Structural and optical characterization of Ag films on glass

Ag films with thickness varied between 3 nm and 50 nm were deposited on Corning glass by thermal evaporation. Annealing the samples in vacuum at a temperature of 180 °C leads to a modification of the metal film morphology. For Ag films thinner than 5 nm, separated nanoparticles are obtained after annealing treatment due to (i) surface diffusion of Ag and (ii) surface tension of the resulting isolated particles. For thicker Ag films, a percolation continuum (i.e. particles that are connected to each other) is found after thermal treatment. Reflection and transmission measurements of glass/Ag-film after annealing treatment at 180 °C were performed in order to characterize the optical behavior of the resulting Ag films.

In the case of glass/Ag-film with metal film thickness up to 5 nm, densely packed ellipsoidal nanoparticles with an average lateral size and height of several nanometers are found after

annealing at 180 °C. A distinct minimum in the transmittance is observed at approximately 425 nm (Fig. 7.1, full squares). Since the reflection of the prepared system only shows a slight increase at this wavelength (Fig. 7.1, full circles), the calculated absorption exhibits a maximum which also peaks at around 425 nm. This absorption is ascribed to localized surface plasmon absorption of the nanoparticles. Compared with the optical response of the glass/Ag-film before annealing, showing a distinct peak at 460 nm (Fig. 7.1, dashed line), we note that the annealing process causes a blue shift of the resonant maximum of the absorption by 35 nm that is accompanied by a narrowing of the FWHM of the absorption peak by 30 nm (Fig. 7.1, triangles). Considering the relatively small dimensions of the nanoparticles, no diffuse scattered light can be measured (Fig. 7.1, open symbols). The position of the absorption peak at 425 nm does not correspond to the expected theoretical dipolar plasmonic absorption of small individual Ag nanoparticles in air ($n_{air} \sim 1$) – normally occuring at 350 nm. The discrepancy is attributed to (i) the larger sizes of the obtained particles (see Fig. 1.6), (ii) their ellipsoidal shape (see Fig. 1.5), (iii) the small inter-particle distances which lead to interactions between the nanoparticles (Liu et al., 1998) and (iv) the fact that the symmetry of the medium surrouding the nanoparticles is modified by the presence of the glass substrate ($n_{glass} \sim 1.45$).

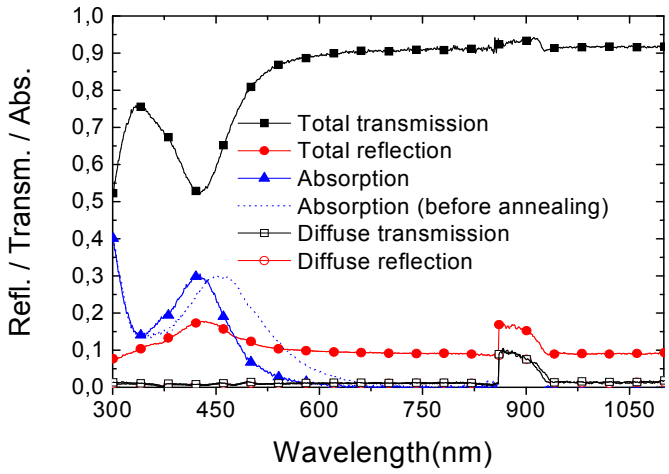

Figure 7.1 : Reflection, transmission and absorption of a 5 nm Ag film on Corning glass. The dashed line represents the light absorption before annealing.

By increasing the thickness of the Ag film from 5 nm to 20 nm a structure close to the percolation threshold is found after annealing at 180 °C (Fig. 7.2, left). Although the absorption maximum at 425 nm is less pronounced it can still be recognized. A second peak is observed at around 340 nm (Fig. 7.2, right) which is probably due to surface plasmon (SP) absorption. Both diffuse transmission and diffuse reflection are enhanced in the whole investigated wavelength range. By further increasing the Ag film thickness to 40 nm, a percolation continuum is obtained after annealing at 180 °C (Fig. 7.3, left). Structures with an

average height and lateral size of around 80 nm and 800 nm, respectively, are obtained. A root mean square roughness of 30 nm is measured. The absorption peak at 340 nm remains (Fig. 7.3, right). However the extremum previously observed at 425 nm – due to localized surface plasmon absorption of single nanoparticles – disappears as no isolated nanoparticles can be found for the 40 nm thick Ag film. The extrema in the diffuse reflectance and transmittance observed at 320 nm (Fig. 7.3, right, red arrow) correspond to the plasma frequency. The diffuse scattered light is increased in both reflection and transmission modes compared to the 20 nm thick Ag film.

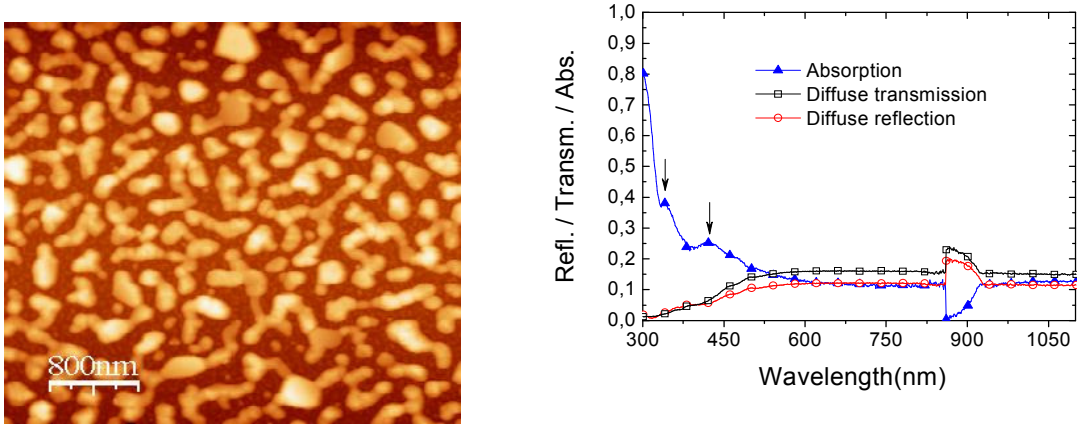

Figure 7.2 : (left) AFM scan of a 20 nm Ag film on Corning glass after annealing in vacuum at 180 °C. (right) Reflection, transmission and absorption of the sample.

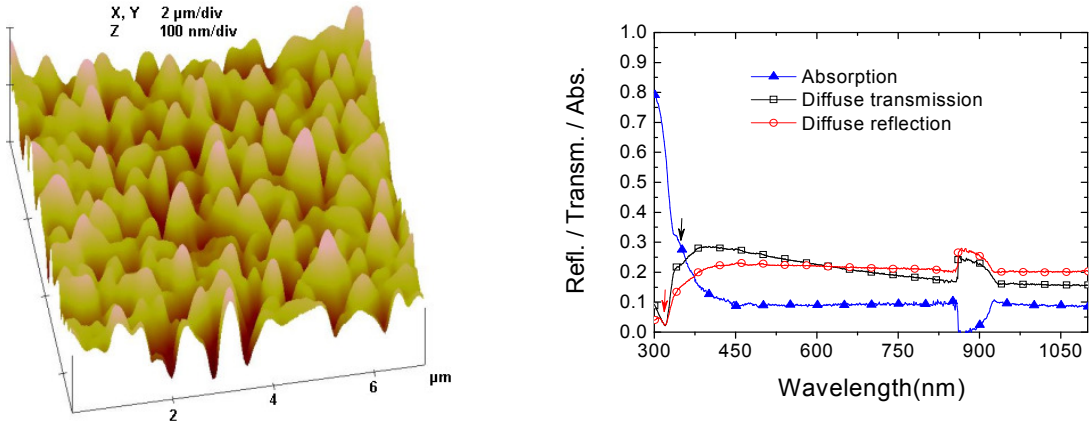

Figure 7.3 : (left) AFM scan of a 40 nm Ag film on Corning glass after annealing in vacuum at 180 °C. (right) Reflection, transmission and absorption of the sample.

7.2 Optical characterization of the nanostructured Ag reflector

Glass/Ag-film samples annealed in vacuum at 180 °C show an increasing light scattering for increasing Ag-film thicknesses. However the thicker the Ag film is the lower the total transmission is. In order to make use of the enhanced scattered light of glass/Ag-film systems for application as back reflectors in n-i-p solar cells, they were covered with a bulk Ag layer having a thickness of 200 nm. Due to the conformal deposition of the bulk Ag layer, the Ag surface follows the morphology of the glass/nanostructured Ag-film. The presence of the bulk Ag layer leads to a high reflection. Moreover the structures formed at its surface – denoted as nanostructures – provide an efficient light scattering for the proper roughness of the Ag-film. Reflection measurements of nanostructures obtained for Ag-film thicknesses varied between 30 nm and 50 nm are shown in Fig. 7.4.

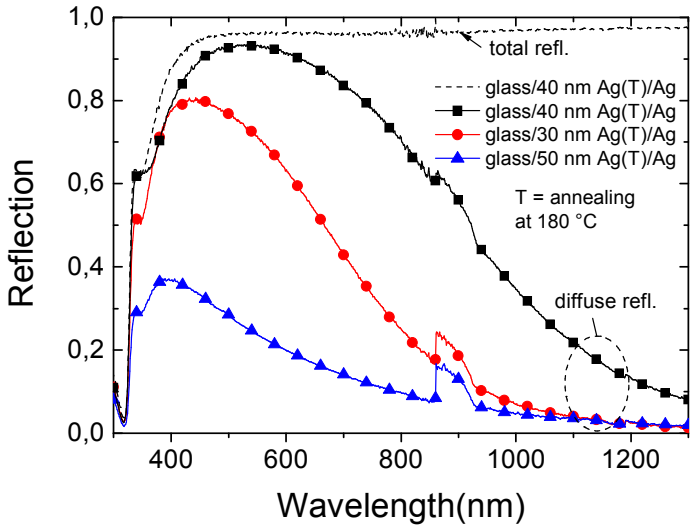

Figure 7.4 : Diffuse and total reflection of a glass/Ag-film/Ag(200 nm) reflector with Ag film thickness of 30 nm, 40 nm and 50 nm. Prior to the deposition of the 200 nm thick Ag layer, the glass/Ag-film is annealed at 180 °C (denoted as *T* in the graph).

For Ag films thinner than 40 nm the diffuse part of the light increases with the roughness of the nanostructured surface, i.e. with the Ag film thickness. For an Ag film thickness of 40 nm, the total reflectivity exceeds 95 % for 450 nm < λ < 1300 nm and the diffuse part of the light reaches 93 % at 500 nm. By further increasing the thickness of the Ag film, the diffuse part of the light decreases as shown in the case of a 50 nm thick Ag film. This is due to the fact that the Ag film becomes more compact and exhibits a reduced roughness. The extinction peaks found at 320 nm and 350 nm originate from light absorption associated with the plasma oscillation and the SP resonance of Ag in air, respectively (Springer et al., 2004). Fig. 7.5

shows the angular intensity distribution (AID) at 550 nm and 897 nm of the nanostructured Ag reflector – in the case of an Ag film thickness of 40 nm covered with a 500 nm thick Ag layer. The maximum of the AID is shifted by 15 ° to smaller angles when the wavelength of the incoming light is increased from 550 nm to 897 nm. This significant wavelength dependence indicates that geometric scattering at the rough surface only can not explain the observed scattering properties of the reflector. The nanostructured surface morphology may behave as large nanoparticles connected to each other. Therefore, Mie scattering may also contribute to the wavelength-dependent angle distribution of the nanostructures.

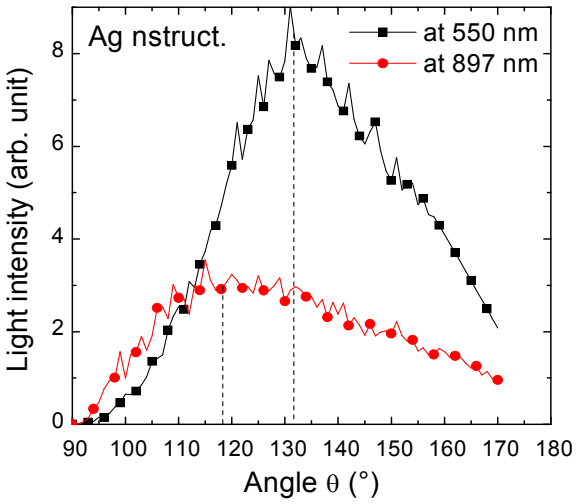

Figure 7.5 : Angular intensity distribution at 550 nm and 897 nm of a nanostructured Ag reflector. θ is the angle between the incoming light and the reflected light (cf. section 3.2).

7.3 µc-Si:H n-i-p solar cells with a nanostructured back reflector

Since the nanostructured Ag reflector introduced in the previous section shows a high reflection and a high light scattering (into large angles), it was applied as a back reflector in µc-Si:H n-i-p solar cells. Solar devices deposited on a flat reflector and on the nanostructured reflector were co-deposited (see Fig. 7.6). An absorber layer thickness of 1 µm was used.
The solar cell based on the nanostructured back reflector exhibits a reduction of the total reflection in the whole spectral range (Fig. 7.7, full circles) compared to the flat cell (full squares). The enhanced absorption in the long wavelength region is attributed to the increased light path within the cell caused by the improved light scattering at the nanostructured Ag surface (open circles).

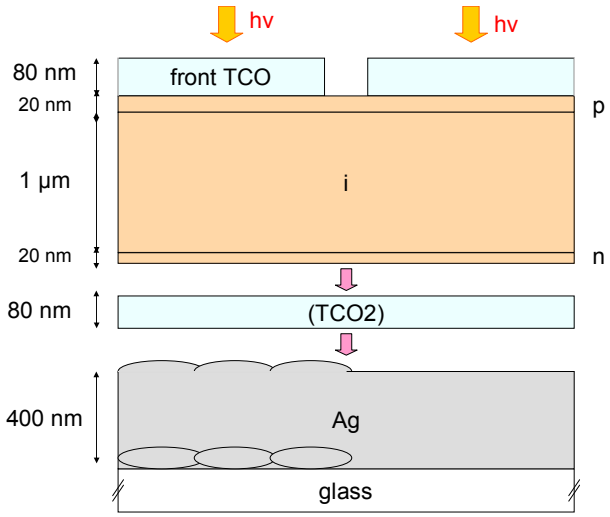

Figure 7.6 : Schematic drawing of two co-deposited µc-Si:H n-i-p solar cells deposited on a nanostructured (left) and a flat (right) Ag back reflector. The TCO2 layer is optional and is not used unless stated in the text.

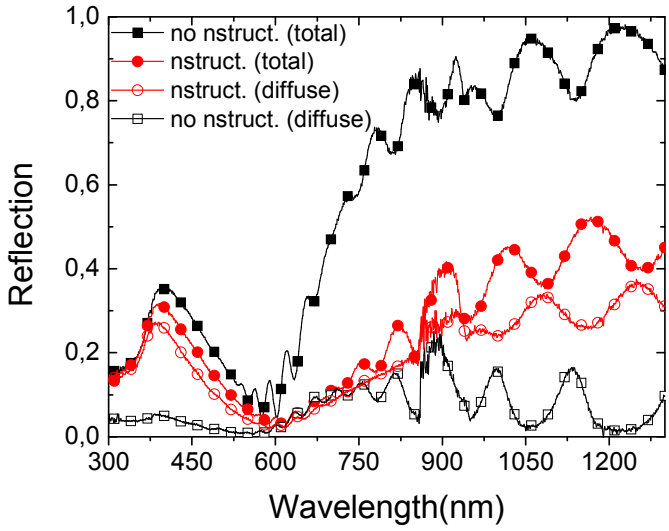

Figure 7.7 : Diffuse (open symbols) and total (full symbols) reflection of cells deposited on a nanostructured (circles) and a flat (squares) Ag back reflector.

Fig. 7.8 (top, full symbols) depicts the corresponding QE curves. For the cell based on the nanostructured back reflector, the QE is increased in the long wavelength range (Fig. 7.8, top, full circles compared to full squares). For wavelengths smaller than 600 nm, an increase in QE is also observed, due to an improvement in the light incoupling resulting from the conformal deposition of the thin-film layers on the nanostructured back reflector (Stiebig et al., 2006b; Haase and Stiebig, 2006). The higher blue response correlates with the lower cell reflectivity (Fig. 7.7, full circles compared to full squares).

The increase in QE in the long wavelength range does not express the strong decrease in reflectance. The internal QE of the cell deposited on the nanostructured reflector is noticeably smaller than that of the reference cell for $\lambda > 600$ nm (Fig. 7.8, bottom, full circles compared to full squares). A photocurrent loss is found which may originate from parasitic absorption associated with surface plasmons (Maier, 2007; Haug et al., 2008) or localized surface plasmons of the nanostructured Ag surface embedded in silicon. In order to shift the plasmonic losses in Ag towards shorter wavelengths (see section 6.4.2 for detailed explanations), the reflector was covered with a thin TCO layer (cf. Fig. 7.6).

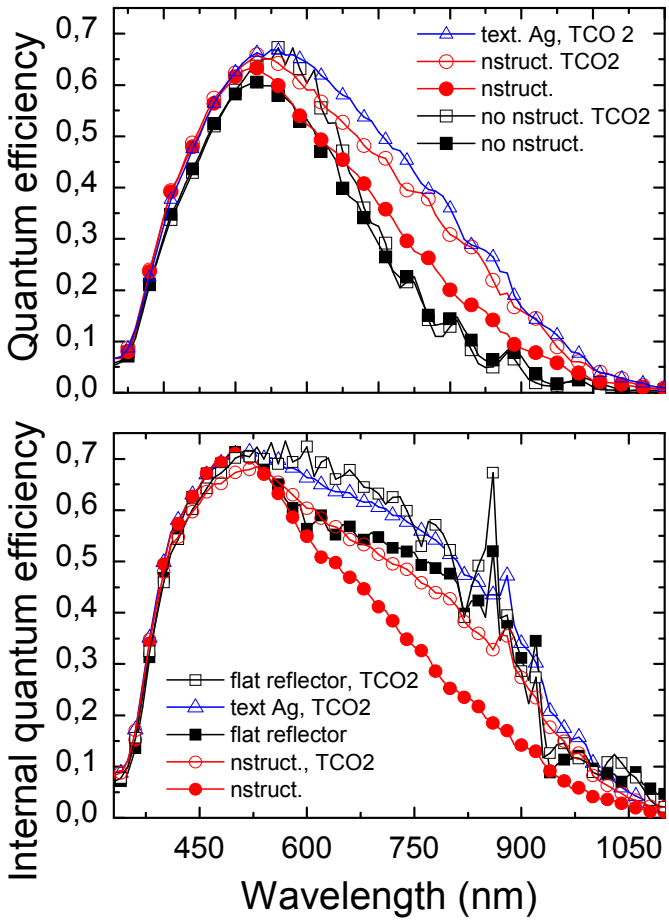

Figure 7.8 : Quantum efficiency (top) and internal quantum efficiency (bottom) of cells based on a nanostructured (circles) and a flat (squares) back reflector. The results of a cell deposited on a standard back reflector are also plotted (triangles). The full/open symbols represent the quantum efficiencies of cells without/with TCO2.

For the flat cell, the incorporation of the TCO2 layer leads to an increase in QE between 500 nm and 700 nm (Fig. 7.8, top, open squares compared to full squares), due to a reduction of the absorption losses in the back reflector. This is confirmed by the enhanced internal QE

in the wavelength range 500 nm – 800 nm after insertion of TCO2 (Fig. 7.8, bottom, open squares compared to full squares). The Ag surface of the "flat" reflector is altered by the deposition of the subsequent silicon layers performed at 180 °C. This effect is indicated by the contribution of the diffuse scattered light measured for the "flat" cell (Fig. 7.7, open squares). Since the Ag surface is not perfectly flat, plasmonic absorption losses are expected at the rear side of the device. For the cell based on the nanostructured back reflector, the incorporation of the TCO2 layer also leads to an increase in both the external and internal QE in the long wavelength range (Fig. 7.8, top and bottom, open circles compared to full circles). The influence of the TCO2 layer on the QE is more pronounced for the cell deposited on the nanostructured back reflector than for the reference cell. This effect is more significant in the infrared wavelength region. This is ascribed to (i) the multiple reflections at the back reflector resulting from the enhanced light scattering, (ii) the increased plasmonic absorption losses with increasing surface roughness and size of the nanostructures (Fig. 1.6, Sönnichsen et al., 2000-2001).

The standard concept adopted for n-i-p thin-film silicon solar cells to achieve a good light-trapping consists of applying a textured TCO/Ag back reflector. The surface texture of the TCO is obtained by dipping the glass/TCO substrate in a solution of HCl. Under the proper preparation conditions (i.e. the adequate HCl concentration, temperature and duration of the etching process), an optimized crater- or pyramid-like TCO texture with a root mean square roughness of around 150 nm can be obtained. An AFM picture of an 800 nm thick TCO layer etched during 30 s in a solution of HCl with a concentration of 0.5 % is shown in Fig. 7.9 (left). The highest efficiencies achieved so far for a-Si:H and μc-Si:H solar cells are obtained by using this type of surface texture. In order to compare the optical properties of the nanostructured Ag back reflector with those of a standard textured reflector, μc-Si:H solar cells in the n-i-p configuration were deposited on both types of back reflector covered with a thin TCO layer (cf. Fig. 7.9, right). The external and internal QE of the cell based on the standard back reflector are plotted in Fig. 7.8. For $\lambda > 550$ nm, a higher QE is measured for the cell based on the textured reflector (Fig. 7.8, top, open triangles compared to open circles). The larger fraction of the diffuse scattered light found for the textured Ag reflector in air (not shown) is probably responsible for the observed enhancement. Moreover, despite its larger features, the standard texture leads to significantly less absorption losses than the nanostructured reflector. This is indicated by the higher internal QE (Fig. 7.8, bottom, open triangles compared to open circles). Only a slight difference in the internal QE is found in the red wavelength range between the cell deposited on the textured Ag/TCO and the cell deposited on the flat Ag/TCO reflector (bottom, open triangles compared to open squares).

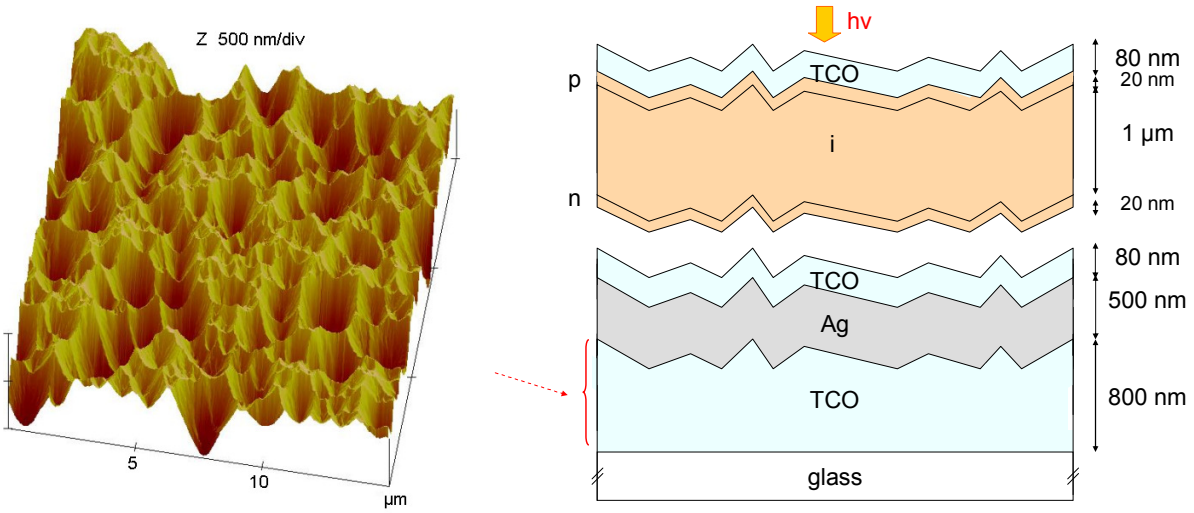

Figure 7.9 : (left) AFM picture of a standard TCO surface texture obtained by chemical etching for 30 sec. in a solution of HCl (0.5 %). (right) Schematic drawing of a µc-Si:H cell deposited on an Ag/TCO back reflector of standard texture.

Despite the increase in the short-circuit current, the solar cell deposited on the nanostructured Ag/TCO reflector shows a reduction in both the FF and the Voc (of 7.8 % and 40 mV) compared to the cell deposited on the flat Ag/TCO reflector (cf. Fig. 7.10). This result is similar to that reported in section 6.3 in the case of a µc-Si:H cell deposited on large Ag nanoparticles. The lower cell performance may originate from an alteration of the µc-Si:H growth on the substrate (see section 6.3). In contrast, the electrical device properties of the cell deposited on the textured Ag/TCO are not altered compared to those of the flat cell. Even a slight increase in the FF from 72.1 % to 72.3 % is observed in this case.

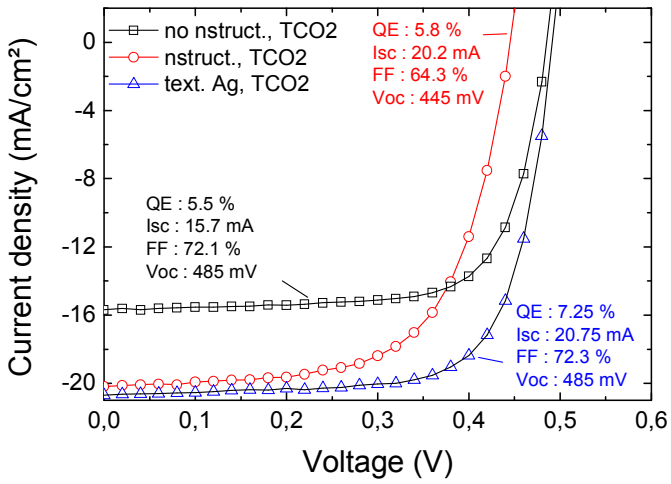

Figure 7.10 : I-V curve under illumination of µc-Si:H n-i-p cells deposited on a flat Ag/TCO (squares), a nanostructured Ag/TCO (circles) and a textured Ag/TCO (triangles) reflector.

7.4 a-Si:H n-i-p solar cells with a nanostructured back reflector

Amorphous silicon solar cells with an absorber layer of 350 nm in the n-i-p configuration were deposited on a flat Ag/TCO back reflector, a nanostructured Ag/TCO reflector (Fig. 7.11, left) and an Ag/TCO reflector of standard texture (right).

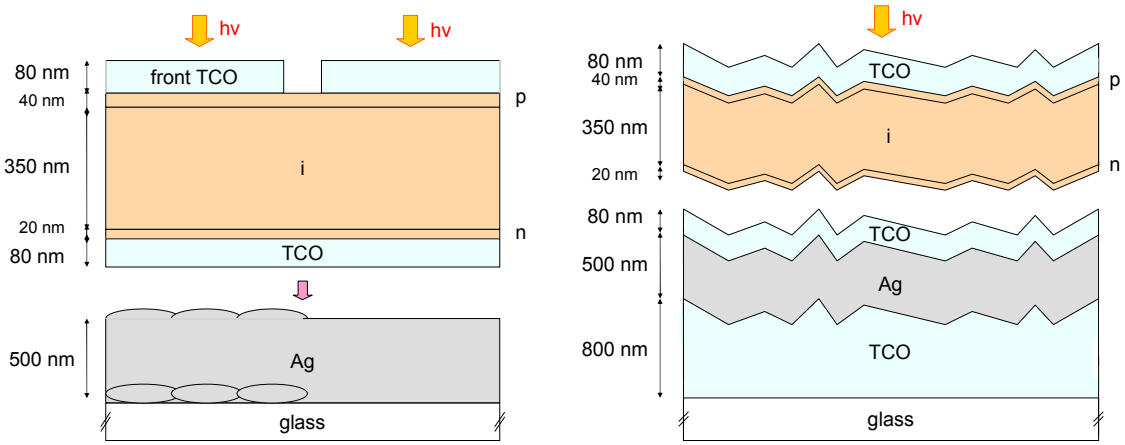

Figure 7.11 : Schematic drawing of an a-Si:H n-i-p solar cell deposited on a nanostructured Ag/TCO reflector (left) and an Ag/TCO reflector of standard texture (right).

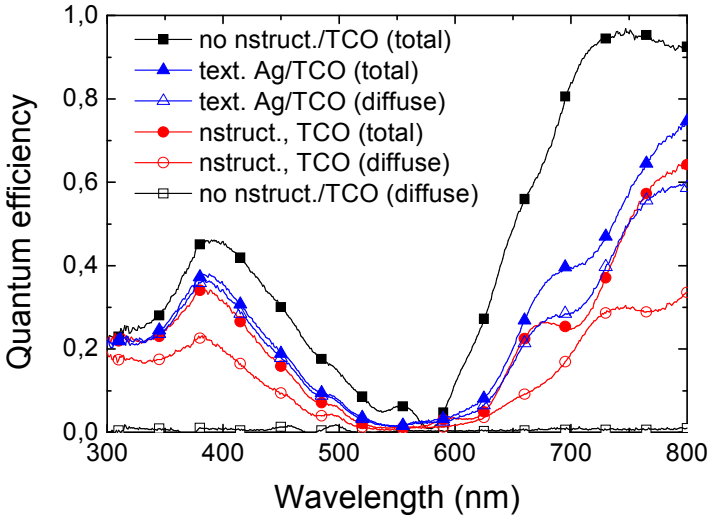

Figure 7.12 : Total (full symbols) and diffuse (open symbols) reflectivity of a-Si:H cells in the n-i-p configuration deposited on flat Ag/TCO (squares), Ag nanostructures/TCO (circles) and textured Ag/TCO (triangles).

The same general trend in terms of optical response is observed for the a-Si:H cells than for the µc-Si:H cells. For the solar cell applying the nanostructured back reflector, a lower reflection is measured compared to the flat cell (Fig. 7.12, full circles compared to full

squares). This effect is attributed to the improved light scattering at the back reflector. In the short wavelength range, the reflection is similar for both types of back reflector. However, for $\lambda > 600$ nm, the reflection of the cell applying the textured Ag is larger than for the nanostructured reflector (Fig. 7.12, full triangles compared to full circles). This is likely due to the dominant plasmonic losses in the nanostructured back reflector (see section 7.3).

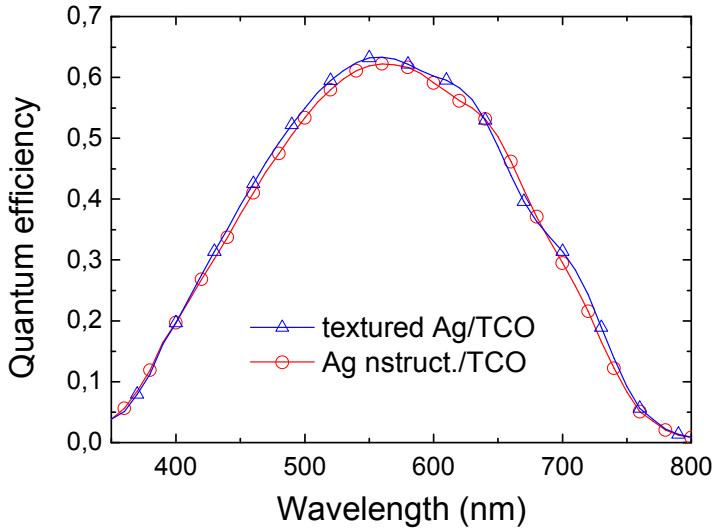

Figure 7.13 : Quantum efficiency of a-Si:H cells in the n-i-p configuration based on the nanostructured Ag/TCO (circles) and textured Ag/TCO (triangles) back reflector.

Fig. 7.13 shows the QE of cells deposited on the nanostructured Ag/TCO back reflector and the Ag/TCO reflector of standard texture. Nearly in the whole spectral range, the standard back reflector gives a higher QE than the nanostructured back reflector. The key parameters extracted from the I-V curves of both types of cells are shown in Table 7.1. In accordance with the QE data, the cell deposited on the standard Ag/TCO reflector shows a higher short-circuit current (Isc ~ 12.9 mA.cm^{-2}) than the other cell (Isc ~ 12.55 mA.cm^{-2}). A decrease in the Voc from 752 mV to 742 mV is observed in comparison to the cell deposited on the standard reflector. Both cells show an identical FF. In conclusion, the cell based on the standard back reflector gives a higher efficiency.

	QE(%)	FF(%)	Voc(mV)	Isc(mA.cm^{-2})
nanostructures/TCO	5.7	62	742	12.55
textured Ag/TCO	6	62	752	12.9

Table 7.1 : Key parameters (QE, FF, Voc, Isc) of a-Si:H cells in the n-i-p configuration deposited on nanostructures/TCO and textured Ag/TCO.

7.5 Summary

Ag films with thickness varied between 3 nm and 50 nm were deposited by thermal evaporation on Corning glass. After annealing in vacuum at 180 °C, Ag films with thickness of a few nanometers exhibit separated nanoparticles. Optical measurements show a distinct peak in the absorption spectrum which is characteristic of localized surface plasmons of the obtained nanoparticles. By increasing the thickness of the deposited Ag film, a percolation continuum is found after the annealing treatment. In this case, both diffuse transmission and diffuse reflection of the glass/Ag-film increase. Covering the glass/Ag-film system with a bulk Ag layer of moderate thickness leads to the formation of nanostructures that provide an efficient light scattering for the proper thickness and annealing treatment of the Ag-film. Angle resolved measurements show a significant wavelength dependence of the scattered light distribution. Therefore the scattering properties of the nanostructures are not ascribed to geometric scattering only.

Integrated at the back side of μc-Si:H and a-Si:H n-i-p solar cells, the nanostructured back reflector leads to an improved light absorption in the long wavelength range, due to an enhanced optical path provided by the light scattering. In terms of short-circuit photocurrent, solar cells deposited on the nanostructured back reflector and on a standard back reflector give comparable results. However, cells based on the nanostructured Ag reflector suffer from a degradation of the electrical device properties. This deterioration is more pronounced in the case of μc-Si:H cells, probably due to an alteration of the material growth on the nanostructures. In conclusion, the efficiency of both μc-Si:H and a-Si:H solar cells deposited on Ag nanostructures is slightly lower than the efficiency of solar cells deposited on a back reflector of standard texture. Further work is necessary to optimize the geometry of the nanostructures in order to obtain a better light scattering and lower plasmonic losses.

Chapter 8

Impedance measurements and simulations of a-Si:H and µ-Si:H solar cells

In paralell to the study of metal nanoparticles integrated in thin-film silicon solar cells, a comparison of the dynamic properties of a-Si:H and µc-Si:H solar cells deposited on a standard textured substrate was made using impedance measurements – capacitance and conductance. After introducing the applied method, we show the transient behavior of a-Si:H and µc-Si:H solar cells of various i-layer thicknesses in the dark. Discrepancies in the capacitance behavior of both types of cells are observed in the high frequency and high bias range. In order to discuss the dynamic properties of a-Si:H and µc-Si:H solar cells in the dark and to describe the recharching behavior of the localized states involved in the capacitive effects, SPICE simulations were performed. Calculations with the simulator AFORS-HET were conducted to understand the origin of the discrepancy between the capacitance behavior of both types of cells in the high frequency and high voltage range. We close the first part of this chapter by discussing the effect of illumination on the impedance of the cells. The second part deals with the influence of light soaking on the frequency dependent impedance of a-Si:H and µc-Si:H cells. The transient behavior of the cells exhibits a high sensitivity to degradation which correlates with the alteration of the optoelectrical device properties, indicated by variations in the dark I-V curves and in the quantum efficiency.

8.1 Experimental details

In this study, we investigate the dynamic properties of standard a-Si:H and µc-Si:H solar cells by measuring the voltage- and frequency-dependent impedance. The impedance Z is calculated from the current I flowing through the solar cell in response to the applied voltage U. U consists of an alternative (AC) signal in superposition with a continuous (DC) signal. Z is given by the formula:

$$Z = U/I = |Z|e^{j\varphi} \tag{8.1}$$

,with $|Z| = |U/I|$ and φ the phase shift between the applied voltage and the resulting current signal. In our experiments, the voltage- and frequency-dependent impedance was measured with a LCR meter using a four-point measuring set-up. The DC voltage was varied between -0.5 V and 0.8 V for a-Si:H cells and between -0.5 V and 0.5 V for µc-Si:H cells. A small harmonic signal with amplitude of 10 mV and frequency varied between 100 mHz and 1 MHz was applied. The measurements were carried out at room temperature. For measurements under illumination, a filter was used between the light source of the sun simulator (creating a calibrated AM 1.5 spectrum with 1 $kW.m^{-2}$ light intensity) and the solar cell to reach an illumination of 1000 lux, determined by a luxmeter.

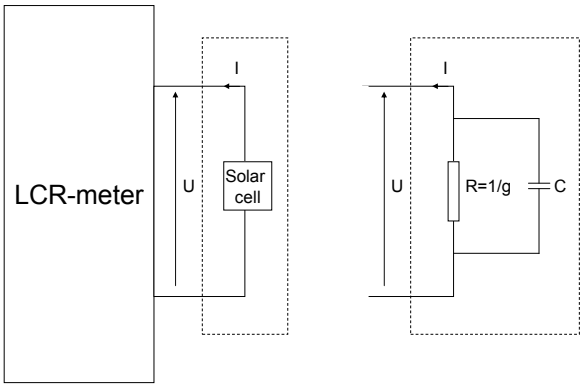

Figure 8.1 : R//C equivalent circuit of a solar cell : the capacitance and the conductance are calculated from the impedance by considering the studied device to be equivalent to a resistance in parallel with a capacitance.

The impedance of the solar cells was discussed in terms of capacitance and conductance. Both values were calculated from the impedance by considering the studied device to be equivalent to a resistance in parallel with a capacitance (see Fig. 8.1). In this condition, the admittance *Y=1/Z* can be written as :

$$Y = g + jC\omega = \frac{1}{|Z|}e^{-j\varphi} \tag{8.2}$$

Consequently, g and C can be expressed as :

$$g = \frac{1}{|Z|}\cos\varphi \tag{8.3a}$$

$$C = -\frac{1}{\omega|Z|}\sin\varphi \tag{8.3b}$$

8.2 Capacitance and conductance in the dark and under illumination

8.2.1 Impedance measurements in the dark

The measured capacitance and conductance in the dark of a-Si:H and µc-Si:H p-i-n solar cells with an i-layer thickness of 500 nm is shown in Fig. 8.2 and Fig. 8.3, respectively. The frequency range of the input signal was varied between 100 Hz and 1 MHz. At negative voltages and at 0 V, the capacitance is constant in the whole frequency range for both a-Si:H and µc-Si:H solar cells and corresponds to the geometric capacitance C_g of the solar cell, given by :

$$C_g = \varepsilon_r \varepsilon_0 . \frac{A}{d_i} \tag{8.4}$$

, with A the area of the solar cell, defined by the contact area and d_i the i-layer thickness.

For positive DC signal, the capacitance of both types of cell increases with increasing bias. This enhancement is more pronounced for smaller frequencies. In the high frequency and high voltage range the a-Si:H cell and the µc-Si:H cell exhibit a discrepancy in the capacitance behavior. By increasing the frequency of the input signal, the capacitance of the a-Si:H cell convergences to the geometric capacitance while the capacitance of the µc-Si:H cell converges to a higher value (compared to C_g), which increases with increasing bias.
The capacitance increase with elevating bias for both types of cells can be explained by the increased number of charge carriers that are trapped in the intrinsic region of the device. Since emission and capture processes are not instantaneous, traps in the material lead to a delay in the charge carrier displacement with regard to the applied input signal. As this delay increases the capacitance increases as well. For small frequencies charge carriers can follow the variations of the input signal and can consequently contribute to the capacitive effect. By increasing the frequency of the applied signal over a certain value, charge carriers are not able to respond to the signal and can not participate to the capacitive effect.

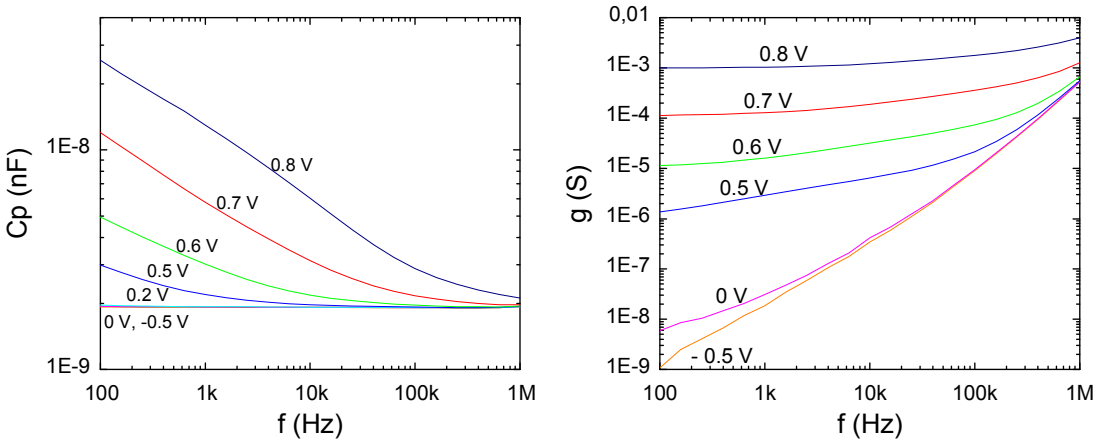

Figure 8.2 : Capacitance (left) and conductance (right) in the dark of an a-Si:H solar cell with i-layer thickness of 500 nm.

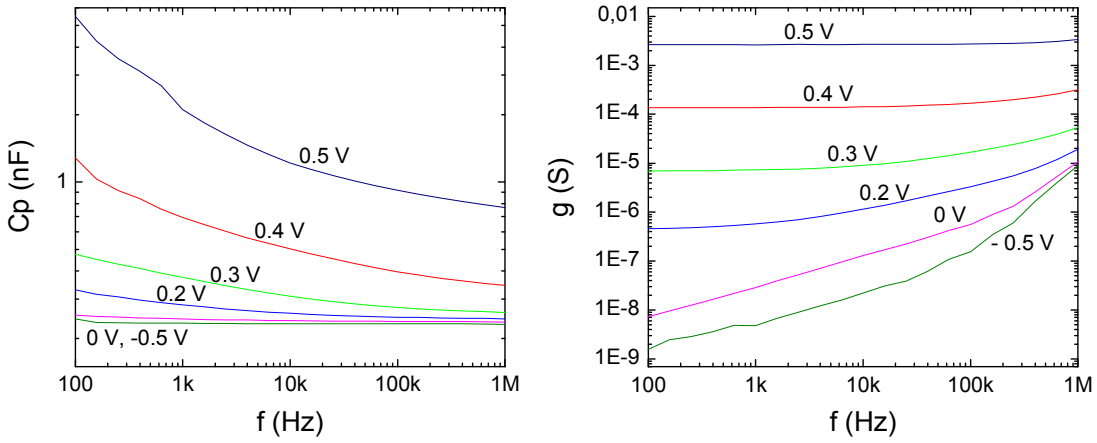

Figure 8.3 : Capacitance (left) and conductance (right) in the dark of a µc-Si:H solar cell with i-layer thickness of 500 nm.

The conductance of both types of cell exhibits a similar behavior. By elevating the frequency of the harmonic signal the conductance is enhanced. Increasing the bias voltage also leads to an enhancement of the conductance, due to the increased number of carriers injected in the i-layer and participating to the current. The enhancement is more pronounced in the small frequency range. For high bias voltages and f < 1 kHz the conductance converges to a nearly constant value. This value corresponds to the conductance in DC mode (referred to as g_{DC}) that can be deduced from the dark I-V characteristic.

$$g_{DC} = \frac{1}{R_{diff}} = \left(\frac{dI}{dV} \right)_{V_{DC}} \tag{8.5}$$

SPICE (Simulation Program with Integrated Circuit Emphasis) simulations were performed to discuss the dynamic properties of a-Si:H and µc-Si:H solar cells in the dark and to describe the recharging behavior of the localized states.

8.2.2 SPICE simulations

The SPICE equivalent circuit used to model the investigated solar cells consists of a series resistance (Rs), a geometric capacitance (Cg) mainly determined by the i-layer thickness, a shunt resistance (Rshunt) caused by local shunts, a differential resistance of the diode (Rdif) and additional voltage- and frequency-dependent RC circuits connected in parallel to Cg. The RC elements consider (i) the variation of charges that are trapped in localized states and (ii) the finite capture and emission mechanisms of these charges in the localized states. As mentioned in section 8.2.1, (ii) leads to a certain phase shift in the charge variation regarding to the applied signal. Therefore, it determines the capacitance behavior of the cell.

The electronic equivalent circuit used to fit the experimental data of an a-Si:H solar cell with an i-layer thickness of 700 nm is shown in Fig. 8.4. Table 8.1 shows the values of the electronic components used in the model. The values of the series resistance R_s, the differential resistance R_{dif} and the shunt resistance R_{shunt} were determined by taking the derivative of the dark I-V curve in the high voltage range, in the range of exponential behavior and in the negative voltage range, respectively. The dynamic properties of a-Si:H diodes are described by three first-order R(V)C(V) elements connected in parallel to Cg. With this approach a good agreement between the simulations and experimental data was already achieved (Stiebig et al., 2002). From table 8.1, R1(V)C1(V), R2(V)C2(V) and R3(V)C3(V) describe the dynamic behavior of the device in the low frequency range, the mid-frequency range and the high frequency range, respectively. Therefore we generally have R1 > R2 > R3 and C1 > C2 > C3 (especially in the high voltage range) to traduce the decreased resistance and capacitance with elevating the frequency. The values used for R1, R2 and R3 are lowered in the high bias voltage range in order to account for the general decrease in the resistance, due to the enhanced number of charge carriers injected in the device. On the contrary, the values of C1, C2 and C3 have to be elevated to correctly describe the enhanced capacitance, due to the increased number of states involved in the recharging and emitting process resulting from the splitting of the quasi-Fermi levels. Fig. 8.5 shows the calculated capacitance and conductance of an a-Si:H cell with i-layer thickness of 700 nm in comparison with the measured data. A good agreement is found between the simulation and the

experimental data. Two first-order voltage-dependent R(V)C(V) circuits cannot reproduce the measured frequency dependence of a-Si:H cells (Fig. 8.5, triangles). For high frequencies the conductance is determined by the geometric capacitance and the series resistance of the solar cell. The tangent to the conductance can be obtained by considering only the capacity C_g in series with the resistance R_s (see Fig. 8.5, right). Therefore it is possible to deduce R_s from the tangent of the conductance in the high frequency range.

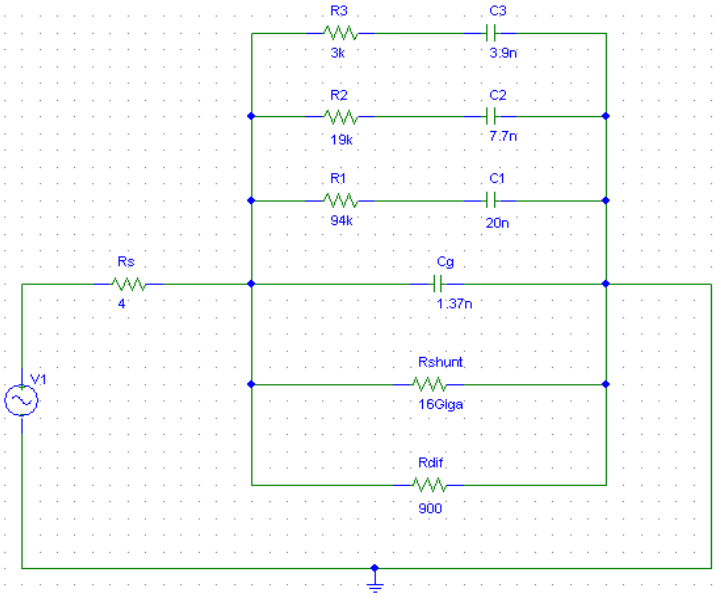

Figure 8.4 : Dynamic electrical model of a 700 nm thick a-Si:H solar cell.

	-0,5V	**-0,2V**	**0V**	**0,2V**	**0,5V**	**0,6V**	**0,7V**	**0,8V**
Rdif				1,96Giga	1Mega	72k	9,7k	900
R1	600Mega	300Mega	200Mega	80Mega	950k	575k	260k	94k
R2	25Mega	25Mega	80Mega	30Mega	750k	135k	60k	19k
R3	1Mega	1Mega	1Mega	1Mega	250k	50k	10k	3k
C1	0,002n	0,004n	0,005n	0,003n	1n	4n	10n	20n
C2	0,002n	0,002n	0,003n	0,1n	0,22n	1,5n	4n	7,7n
C3	0,005n	0,005n	0,007n	0,007n	0,03n	0,3n	2n	3,9n

Table 8.1 : Values of the electronic components used in the equivalent circuit model of an a-Si:H solar cell with i-layer thickness of 700 nm.

As shown in Fig. 8.6, the measured C(f) values of µc-Si:H cells in the high frequency range do not converge to the geometric capacitance and increase with increasing bias. In particular this deviation from Cg requires a more complicate equivalent circuit to describe the dynamic properties of µc-Si:H cells. SPICE simulations of µc-Si:H diodes reveal that between 4 and 5 first order elements have to be considered to fit the experimental data (Fig. 8.6). The capacitor C5 (see Fig. 8.7) is used to reflect the capacitance offset found in the high frequency range.

The capacitor C4 and the resistance R4 are employed to describe the slight decrease of the capacitance in the high frequency range as the capacitance does not show a constant value. Table 8.2 shows the values of the components used to fit the experimental data. A similar trend is observed as for the a-Si:H cell. R1>R2>R3>R4 and C1>C2>C3>C4. Moreover, with elevating bias voltages, the values of R(V) are decreased and the values of C(V) are increased to traduce the enhanced conductance and capacitance, respectively.

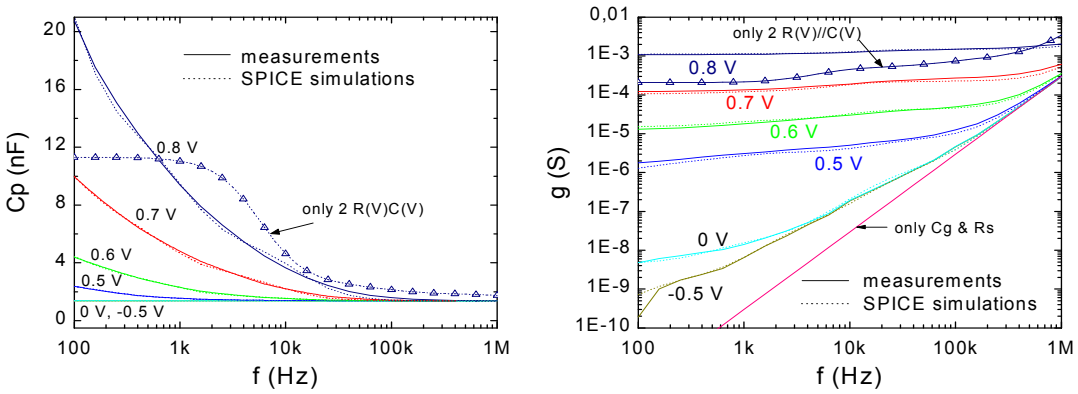

Figure 8.5 : Capacitance (left) and conductance (right) measurements in the dark (solid lines) and calculations using SPICE simulator (dashed lines) in the case of an a-Si:H solar cell with i-layer thickness of 700 nm.The lines with triangles represent the simulations performed by considering only two first-order voltage-dependent R(V)C(V) elements connected in parallel to Cg. The tangent curve plotted in the right graph is the conductance when only R_s and C_g are considered in the model.

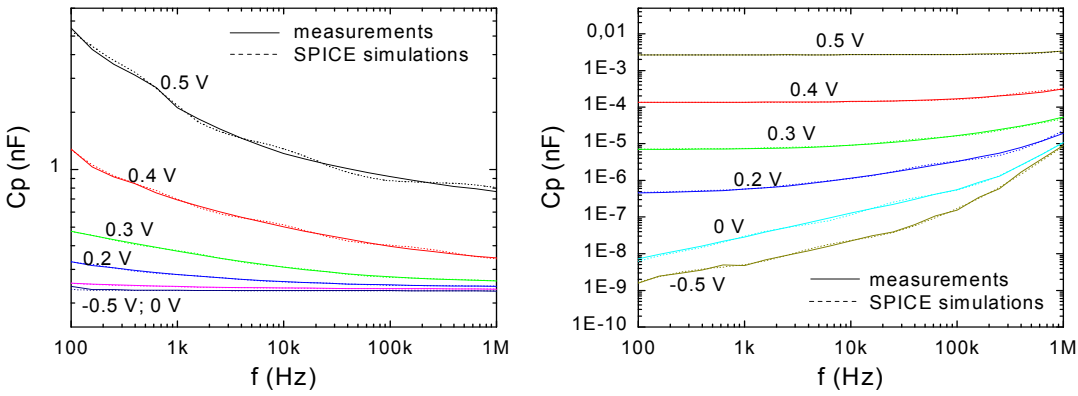

Figure 8.6 : Capacitance (left) and conductance (right) measurements in the dark (solid lines) and calculations using SPICE simulator (dashed lines) in the case of a µc-Si:H solar cell with i-layer thickness of 500 nm.

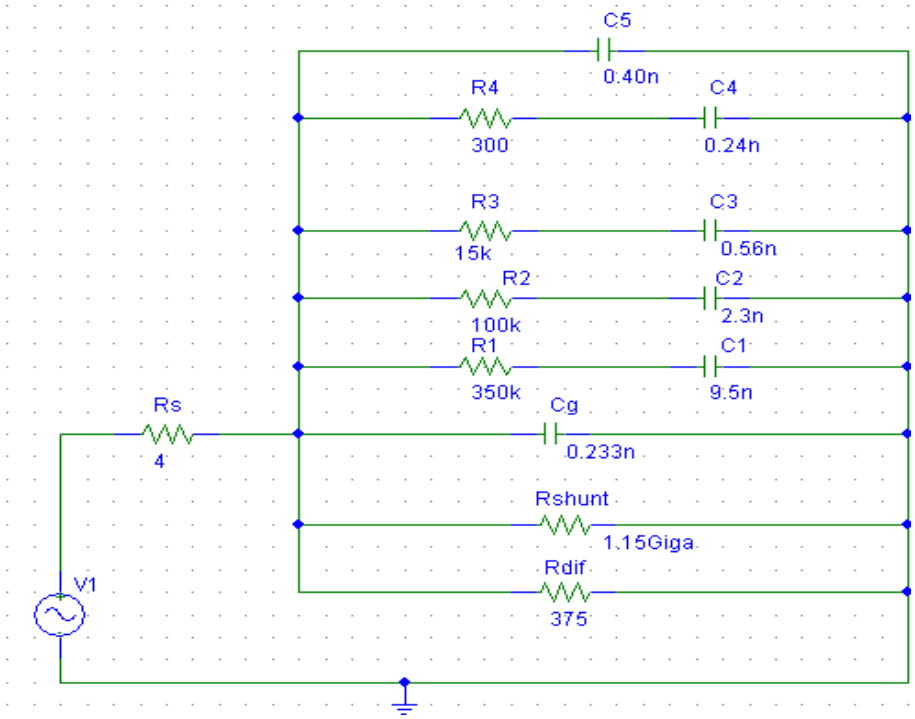

Figure 8.7 : Dynamic electrical model of a 500 nm thick µc-Si:H solar cell.

	-0,5V	**-0,2V**	**0V**	**0,1V**	**0,2V**	**0,3V**	**0,4V**	**0,5V**
Rdif				30Mega	2,2Mega	140k	7,5k	375
R1	300Mega	250Mega	90Mega	35Mega	13Mega	7,2Mega	1,85Mega	350k
R2	50Mega	30Mega	13Mega	6Mega	2,1Mega	950k	560k	100k
R3	10Mega	5Mega	2Mega	1Mega	400k	150k	65k	15k
R4			50k	25k	20k	40k	6k	300
C1	0,003n	0,005n	0,017n	0,024n	0,056n	0,11n	1,1n	9,5n
C2	0,0007n	0,002n	0,0065n	0,01n	0,025n	0,075n	0,3n	2,3n
C3	0,0002n	0,0007n	0,0018n	0,004n	0,01n	0,04n	0,15n	0,56n
C4			0,001n	0,002n	0,04n	0,01n	0,07n	0,24n
C5				0,006n	0,01n	0,028n	0,1n	0,4n

Table 9.2 : Values of the electronic components used in the equivalent circuit model of a µc-Si:H solar cell with i-layer thickness of 500 nm.

8.2.3 AFORS-HET simulations

Before starting the description of the realized simulations, it is necessary to understand the electronic band structure and defect distribution of a-Si:H and µc-Si:H. As mentioned in section 2.2.1, amorphous silicon is a material where the atomic structure shows some degree

of disorder. Variations in bond lengths and angles lead to a lack of far field order which results in localized defects within the bandgap referred to as *tail states* (Overhof, 1998) and *dangling bonds*. The dangling bonds, which can partially be passivated by hydrogen, exist in the three differently charged states D^-, D^0 and D^+. Electronic states arising from a particular type of defect do not have identical energy level. The random nature of a-Si:H leads to a broad distribution of energy levels of electronic states associated with a particular type of defect. In amorphous silicon, the band tails extend from the band edges into the gap over an energy range of about 0.2 eV for the conduction band tail and 0.3-0.4 eV for the valence band tail (Stutzmann, 1987). High defect density leads to material with worse semiconductor properties. Saturation by hydrogen reduces the density of dangling bonds and localized band tail states and the electronic properties of the material are improved. Fig. 8.18 shows the schematic representation of the electronic density of states in a-Si:H according to the standard model (Mott and Davis, 1979). Shown are the extended states in the valence and the conduction band, the states originating from dangling bonds and the valence and conduction tails-states. It is assumed that the density of states in µc-Si:H material is similar to the one of a-Si:H (Brammer and Stiebig, 2003). In µc-Si:H the disordered regions and voids which separate the grain cluster columns (see Fig. 2.2) are believed to contain the majority of defects and hydrogen atoms in µc-Si:H thin films (Werner and Peisl, 1985).

The capacitance behavior is mainly determined by the emission and capture processes of the charge carriers that are trapped in defects present in the intrinsic region of the device. For small frequencies charge carriers can follow the variations of the input signal and can consequently contribute to the capacitive effect. By increasing the frequency of the applied signal over a certain value, charge carriers are not able to respond to the signal and can not participate to the capacitive effect. This property establishes a *demarcation energy* E_d, corresponding to the threshold energy that is required for a charge carrier to be trapped in/released from a defect, written as :

$$E_d = kT \ln(\nu / f) \tag{8.6}$$

, where ν is the thermal emission prefactor (10^{12}-10^{13} cm^{-1}). Defects with energy positions below E_d (having higher response frequency, referred to as *fast* defects) will be able to respond to the signal, but those defects with energy positions above this level (with slower response time, referred to as *slow* defects) will not be able to follow the signal.

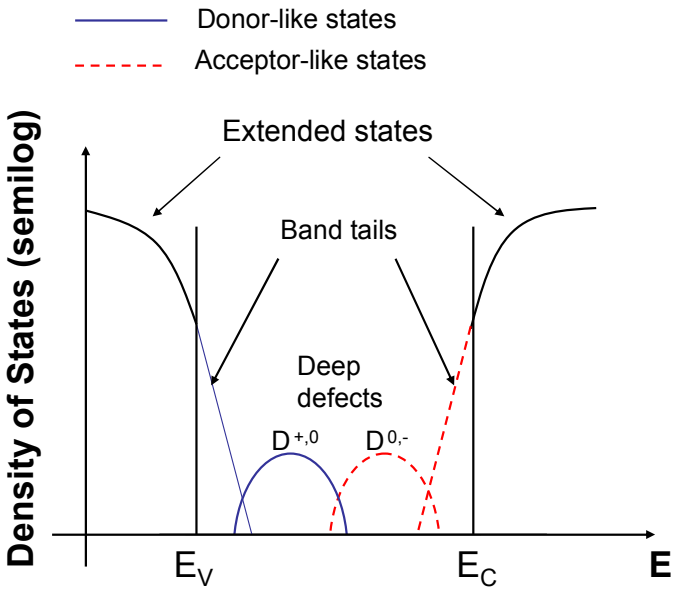

Figure 8.8 : Schematic drawing of the density of states in a-Si:H (similar to the one in µc-Si:H).

In order to understand the origin of the discrepancy in the capacitance behavior between a-Si:H and µc-Si:H solar cells in the high frequency range (see section 8.2.1), simulations were performed with AFORS-HET (Stangl et al., 2005). Parameters similar to the values used for modelling of the steady-state behavior were used (Brammer and Stiebig, 2003). The simulation demonstrates that for µc-Si:H cells the dynamic properties of shallow states (tail states) in the i-layer are responsible for the higher Cp value (compared to Cg) measured at high bias and high frequency. The shallow defects can follow the variation of the harmonic signal in the high frequency range but also in the low frequency range. Thus, they lead to a shift of the capacitance values – offset – in the whole spectral range. This was demonstrated by means of simulations conducted at 0.5 V of µc-Si:H cells where the influence of both defects, the dangling bonds and the tail states, were considered separately (Fig. 8.9, left). The calculations show that dangling bonds determine the capacitance behavior in the low frequency range only, whereas tail states are responsible of a capacitance offset in the whole investigated spectral range. Increasing the bandgap within the simulation from 1.12 eV (bandgap of µc-Si:H) to 1.7 eV (bandgap of a-Si:H) and keeping all other parameters constant, the increase in Cp at 1 MHz shifts to higher bias (Fig. 8.9, right). Thus, the discrepancy of the capacitance found for a-Si:H and µc-Si:H measured at high frequency and high voltage is determined by the occupation of shallow states. Since the tails continue the

density of states at the band edges, the shallow states also shift with increasing band gap. Consequently, the high capacitance signal for high frequencies can be likely explained by the release and occupation of carriers in the shallow states as a function of the applied bias rather than a general different transient behavior of µc-Si:H diodes in comparison to a-Si:H diodes.

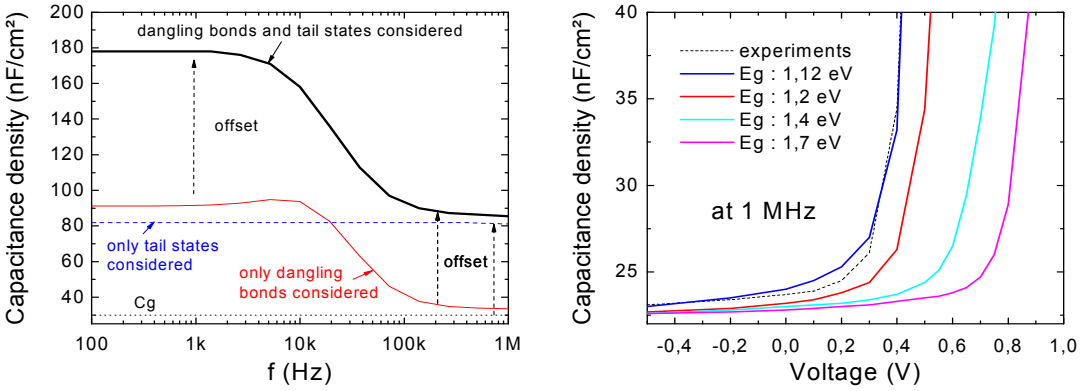

Figure 8.9 : (left) Influence of both types of defect, dangling bonds and tail states, on the capacitance behavior of simulated solar cells. (right) Capacitance simulations at 1 MHz in function of the applied bias voltage for different bandgap energies.

8.2.4 Impedance measurements under illumination

For both a-Si:H and µc-Si:H solar cells, the capacitance behavior under illumination (Fig. 8.10 and Fig. 8.11, solid lines) is nearly the same as in the dark. The a-Si:H cell under illumination exhibits only slighly lower capacitance values in the low frequency range and slighly higher capacitance in the large frequency range, especially for low bias, in comparison to the cell measured in the dark. An identical – though less pronounced – trend is found for the µc-Si:H solar cell. Under illumination, both a-Si:H and µc-Si:H solar cells show an increased conductance for low frequency and low bias, due to the enhanced number of charge carriers participating to the current.

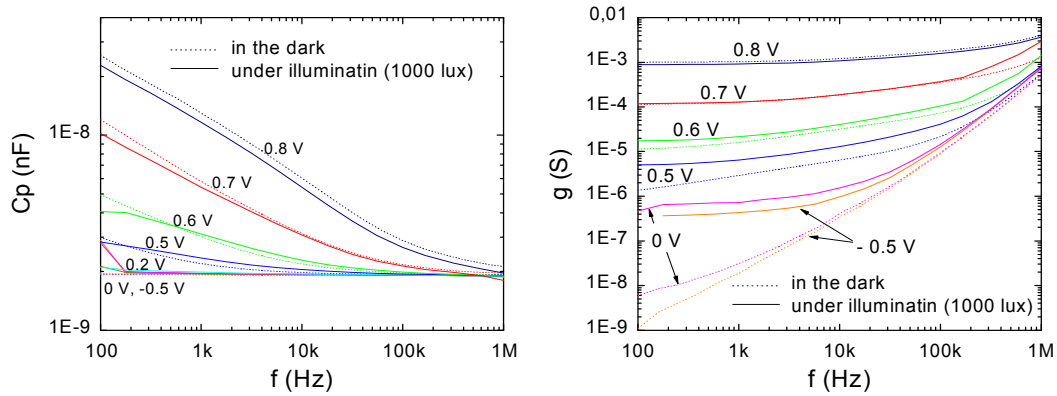

Figure 8.10 : Capacitance (left) and conductance (right) of an a-Si:H solar cell with i-layer thickness of 500 nm, in the dark (dashed lines) and under illumination (solid lines).

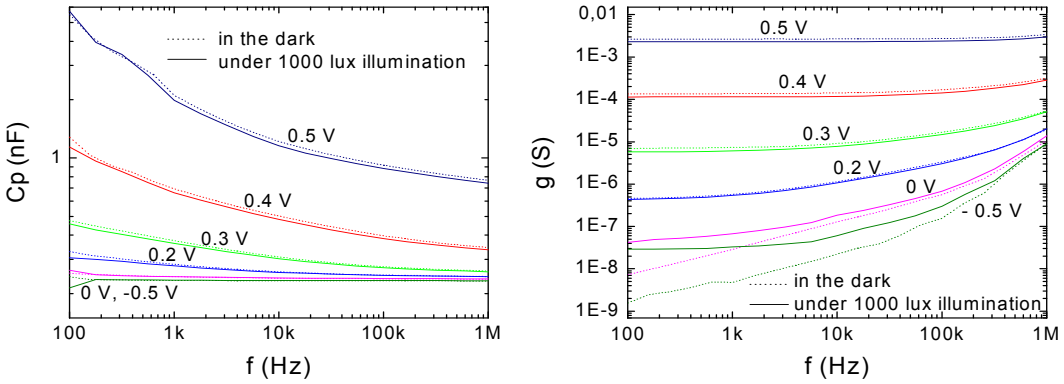

Figure 8.11 : Capacitance (left) and conductance (right) of a µc-Si:H solar cell with i-layer thickness of 500 nm, in the dark (dashed lines) and under illumination (solid lines).

8.3 Impedance measurements after light soaking

8.3.1 Light induced degradation of µc-Si:H cells

Under illumination the performance of a-Si:H solar cells degrades but can be restored by annealing at temperatures of about 180 °C. This degradation effect is known as the Staebler-Wronski effect (SWE) (Staebler and Wronski, 1977). The metastable behavior is attributed to the light-induced defect creation. These metastable defects are created by the breaking of weak or strained Si-Si bonds and act like recombination centers in the material. It was explained in the previous section that deep defects (dangling bonds, considered as *slow*

defects) contribute to the capacitance signal only in the low frequency range while shallow defects (considered as *fast* defects) can participate to the capacitive effect in the whole spectral range. Thus, the effect of light soaking was used to vary the ratio of the shallow and deep states.

The effect of light soaking on the electrical device properties of a-Si:H and µc-Si:H solar cells was studied. QE, I-V in the dark and impedance measurements were carried out for cells subjected to intense light exposure of various durations. The measurements were performed with another system as the one used in the previous section. This system allows to work in a very low frequecy range (f < 1 µs). However this system shows a higher noise signal especially for f < 100 Hz. The measurements were carried out in a frequency range 100 mHz < f < 100 kHz. Fig. 8.12 (left) shows the capacitance of a µc-Si:H solar cell with an absorber layer of 870 nm before (lines) and after light soaking of 40 h (squares). Irrespective of the applied bias, the degraded cell shows an increase in the capacitance. The increase is more pronounced in the low frequency range. The conductance is not significantly modified after 40 h light soaking (Fig. 8.12, right).

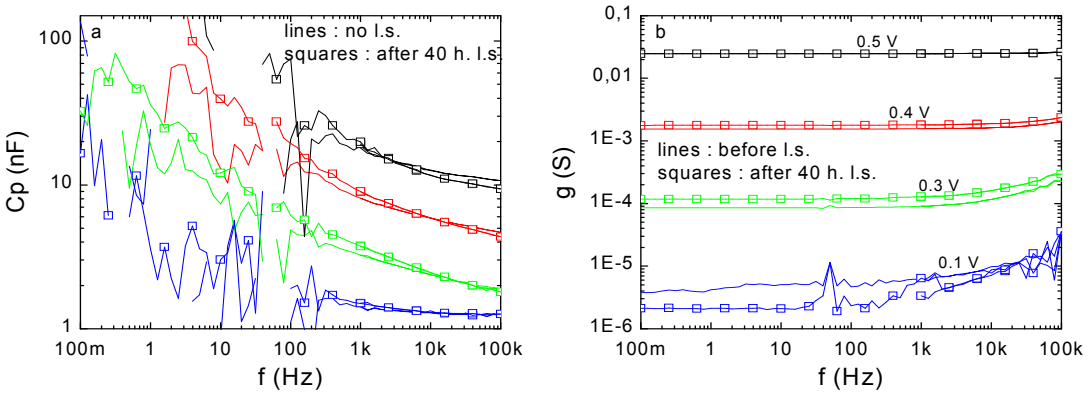

Figure 8.12 : Capacitance (left) and conductance (right) of µc-Si:H solar cell with i-layer thickness of 870 nm, before (lines) and after (squares) 40 h light soaking (l.s.).

Light soaking of 600 h results in a larger discrepancy of the capacitance compared to the values of the not-degraded cell (Fig. 8.13, left). The conductance increases after 600 h of light soaking, especially for low voltages (Fig. 8.13, right). Despite these results, light soaking has no significant influence on the dark I-V characteristic (see Fig. 8.6, left, for 40 h light soaking). Light soaking may induce defects in the a-Si:H phase surrounding the crystals of the µc-Si:H material. These defects probably contribute to the local capture and emission of charge carriers, thereby leading to a variation of the device capacitance. However, since the current is mostly provided by the transport of the charge carriers in the percolated columnar grain clusters, the dark I-V curve is not significantly altered by the presence of defects in the a-Si:H phase. QE of the cell after 40 h light soaking also remains unaltered in the whole

spectral range, indicating that the optoelectric properties are not considerably influenced (Fig. 8.14, right).

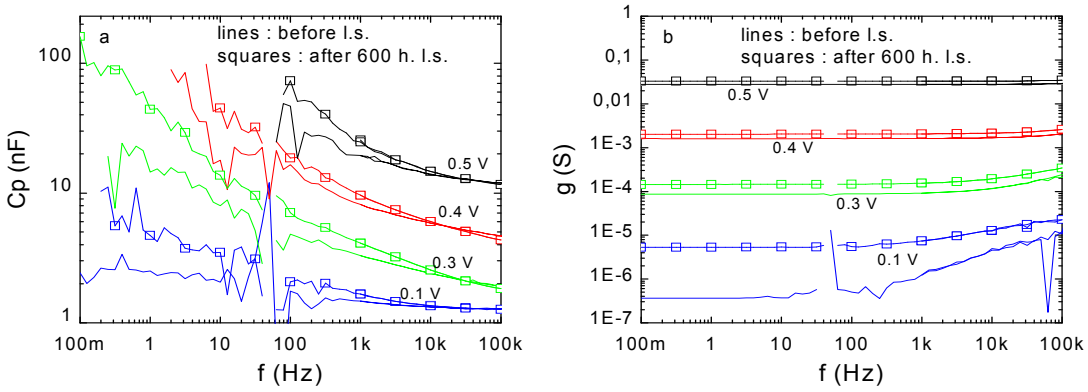

Figure 8.13 : Capacitance (left) and conductance (right) of µc-Si:H solar cell with i-layer thickness of 870 nm, before (lines) and after (squares) 600 h light soaking (l.s.).

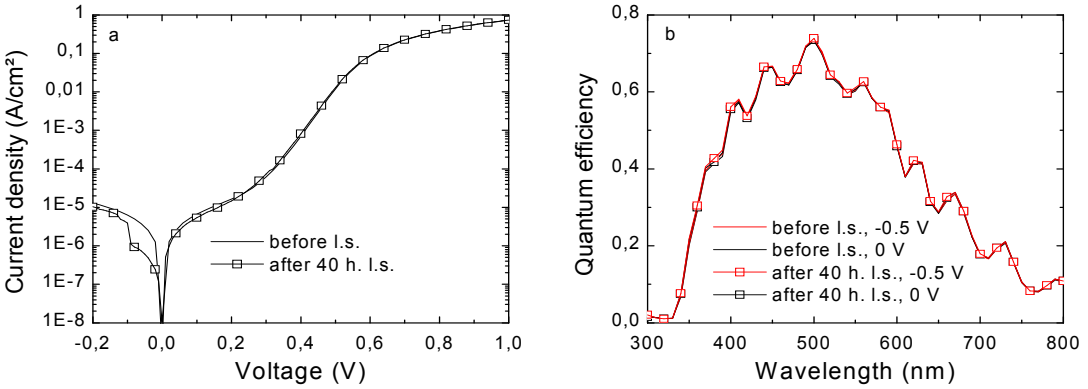

Figure 8.14 : Dark I-V and QE before (lines) and after (squares) 40 h light soaking (l.s.).

Similar results were obtained for a µc-Si:H solar cell having an intrinsic layer of 500 nm. Despite the thinner thickness of the absorber layer which should lead to a less pronounced degradation, an increase in the capacitance is also observed for low frequencies in comparison to the reference cell (see Fig. 8.15, left, for light soaking of 600 h). As observed for the thicker cell, an increase in the conductance – more pronounced for low voltages – is found after light soaking (Fig. 8.15, right). Nevertheless, light soaking of 40 h has no influence on the I-V curve in the dark and the QE. Therefore a strong degradation in the bulk of the µc-Si:H cell can be excluded.

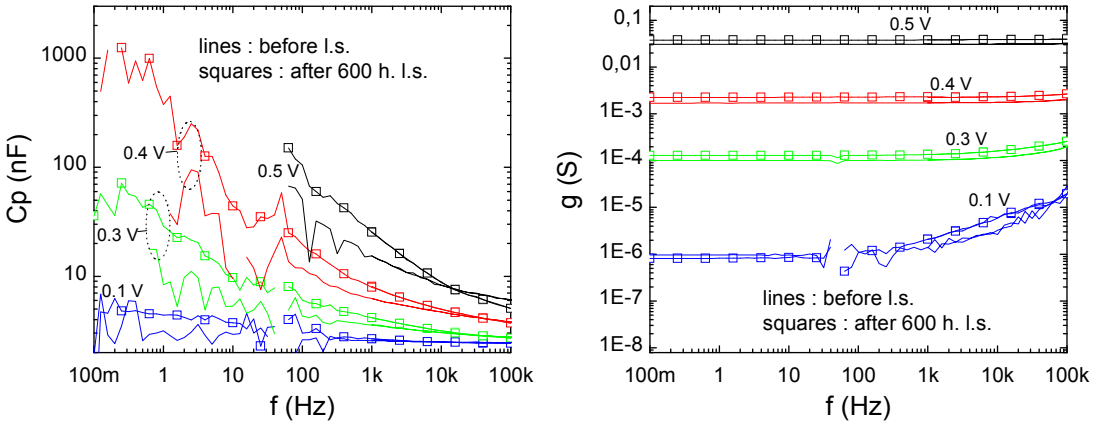

Figure 8.15 : Capacitance (left) and conductance (right) of µc-Si:H solar cell with i-layer thickness of 500 nm, before (lines) and after (squares) 600 h light soaking (l.s.).

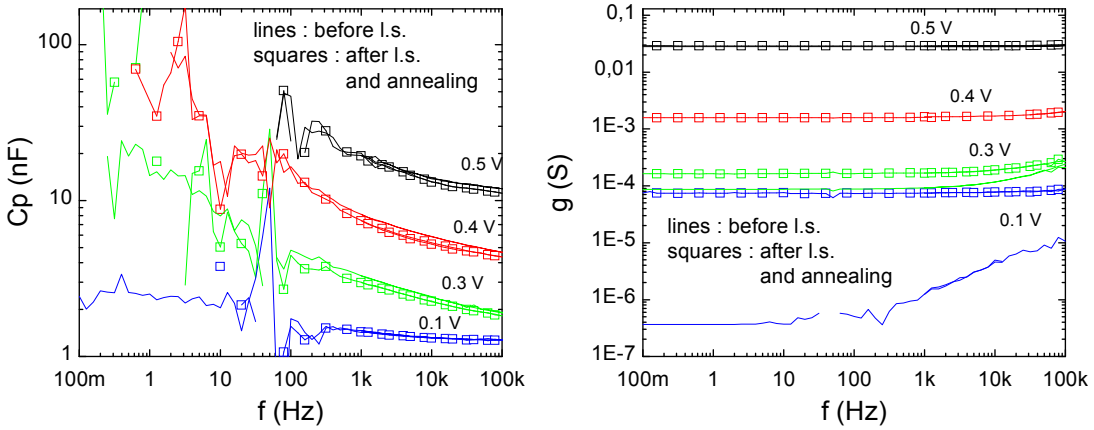

Figure 8.16 : Capacitance (left) and conductance (right) of µc-Si:H solar cell with i-layer thickness of 870 nm, before light soaking (l.s.) (lines) and after light soaking + post annealing at 180 °C for 30 min (squares).

Independently of the duration of the light soaking treatment, annealing the cells at 180 °C for around 30 min leads to a nearly full recovery of the device properties. After annealing, both capacitance and conductance exhibit similar values to the ones found before light soaking (Fig. 8.16, left and Fig. 8.16, right). Only at 0.1 V, the conductance after light soaking and subsequent annealing does not show the initial value (Fig, 8.16, right, blue squares). This is attributed to a shunt problem. From these measurements we can conclude that the light induced defect mechanism is nearly fully reversible, also for the µc-Si:H cell.

8.3.2 Light induced degradation of a-Si:H cells

Capacitance and conductance measurements of a-Si:H solar cells with an i-layer thickness of 700 nm are shown in Fig. 8.17 (left) and Fig. 8.17 (right), respectively, before and after light soaking. After only 2 h light soaking, the capacitance of the solar cell drops in the whole investigated spectral range, especially for low frequencies and high voltages where negative capacitance values are measured, due to light induced defect creation and probably due to a variation of the potential distribution within the cell. As observed in the case of µc-Si:H solar cells, an increase in the conductance – more pronounced in the low bias range – is measured after light soaking, likely due an enhanced density of charge carriers originating from defects and participating to the current.

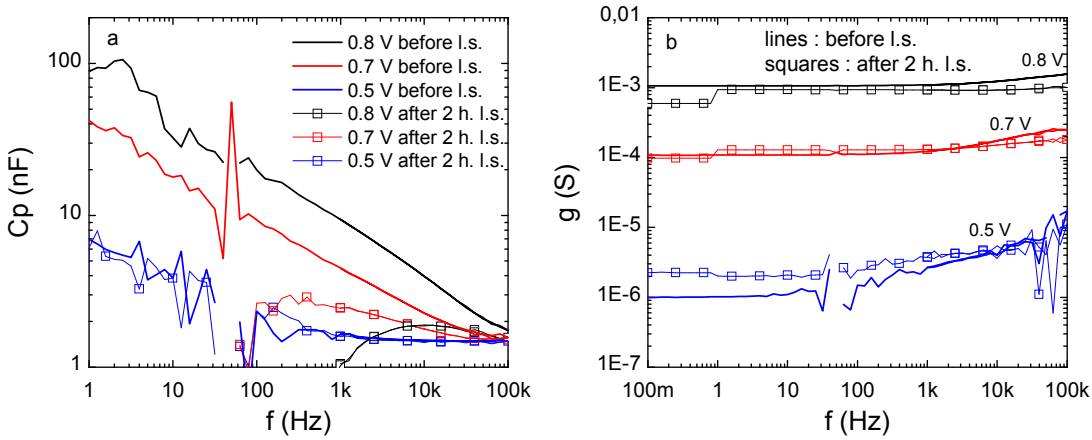

Figure 8.17 : Capacitance (left) and conductance (right) of an a-Si:H solar cell with an i-layer thickness of 700 nm, before (lines) and after (squares) 2 h light soaking (l.s.).

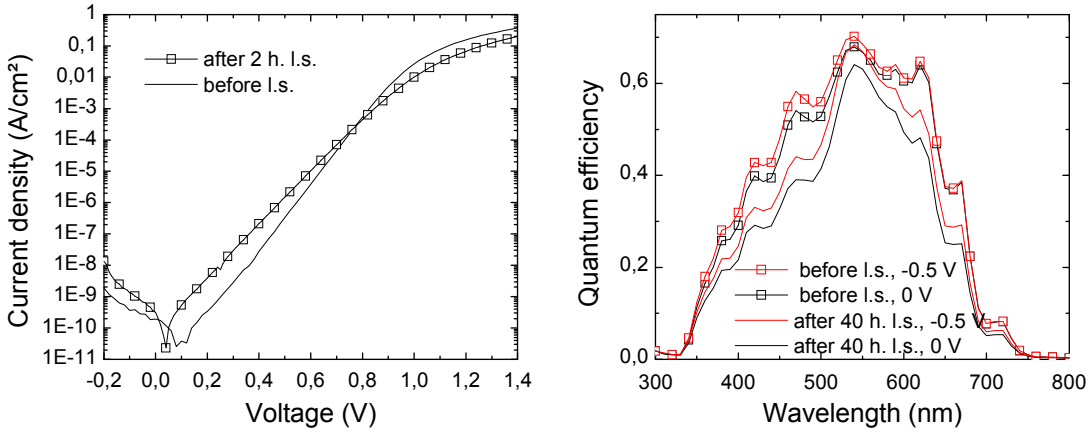

Figure 8.18 : Dark I-V (left) and QE (right) before (lines) and after (squares) 40 h light soaking (l.s.).

After degradation, the dark I-V curve exhibits an enhanced current for voltages smaller than 0.8 V (Fig. 8.18, left), associated with an increase in both quality factor n and I_0, due to light induced defect creation. A charge carrier transport limitation is observed after light soaking. This is indicated by the decreased current for bias larger than 0.8 V. A reduction of the QE is the whole spectral range, indicating a pronounced degradation of the bulk properties is observed after 40 h light soaking (Fig. 8.18, right).
In order to better understand the effect of light induced degradation on the capacitance behavior of a-Si:H cells, we prepared an a-Si:H solar cell with an i-layer thickness of 500 nm. As observed for the a-Si:H solar cell with an i-layer thickness of 700 nm, a drop of the capacitance is found for low frequencies and high voltages after 40 h light soaking (Fig. 8.19, left). The conductance is also enhanced in the low bias range (Fig. 8.19, right).

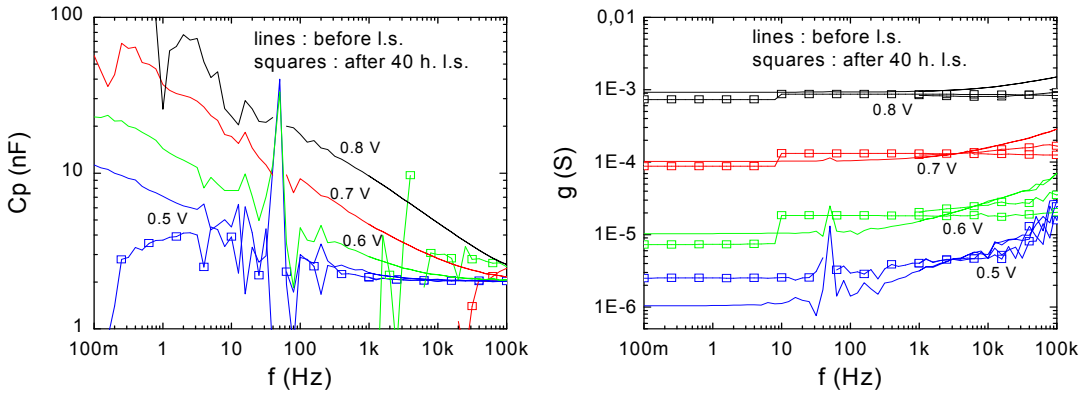

Figure 8.19 : Capacitance (left) and conductance (right) of an a-Si:H solar cell with an i-layer thickness of 500 nm, before (lines) and after (squares) 40 h light soaking (l.s.).

Nevertheless, the decrease in capacitance is not so pronounced as in the previous case (Fig. 8.20, left, for light soaking of 2 h). This is attributed to the thinner thickness of the i-layer which results in a smaller degradation. The I-V characteristic in the dark (Fig. 8.21, left, after 40 h light soaking) shows the same behavior as in the case of the a-Si:H solar cell with absorber layer thickness of 700 nm, namely an increase current for bias smaller than 0.8 V and a decreased current for larger voltages, due to enhanced defect density and degradation of the contact, respectively. QE measurements at 0 V and -0.5 V of the degradated cell exhibit slighly smaller values in the whole spectral range than the reference cell (Fig. 8.21, right, after light soaking of 40 h), confirming the strong sensitivity of a-Si:H material to light soaking.

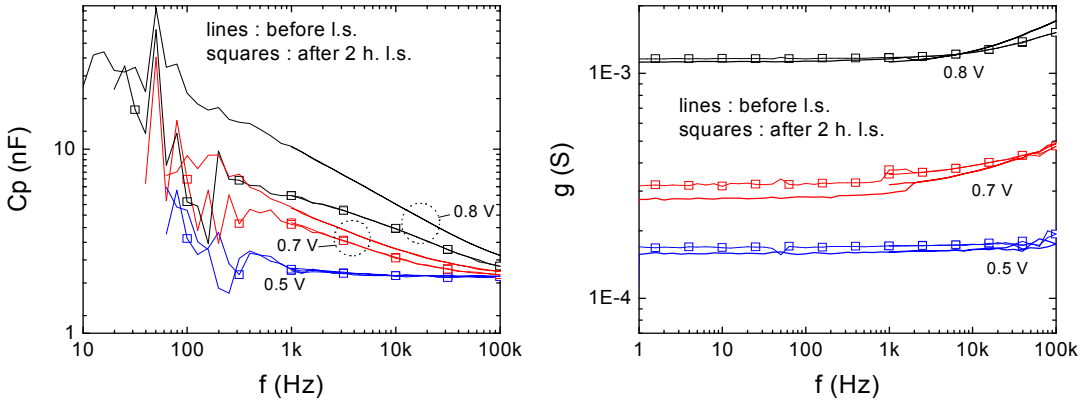

Figure 8.20 : Capacitance (left) and conductance (right) of an a-Si:H solar cell with an i-layer thickness of 500 nm, before (lines) and after (squares) 2 h light soaking (l.s.).

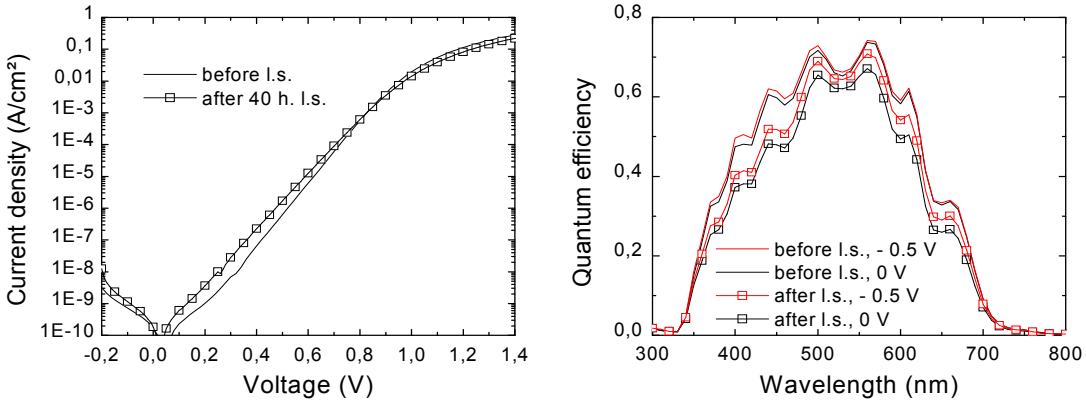

Figure 8.21 : Dark I-V (left) and QE (right) before (lines) and after (squares) 40 h light soaking (l.s.)

8.4 Summary

At 0 V and for negative voltages, the capacitance of both a-Si:H and µc-Si:H solar cells is constant, equal to the geometric capacitance, in the whole frequency range. For positive voltages, the capacitance increases with increasing bias. The enhancement is more pronounced in the small frequency range. By increasing the frequency of the harmonic signal, the capacitance of a-Si:H cells converges to the geometric capacitance while the capacitance of µc-Si:H cells converges to a higher value which increases with elevating bias. For small frequencies, charge carriers can follow the variations of the input signal and can contribute to

capacitive effects. For higher frequencies, the charge carriers are not able to respond to the fast signal. Therefore the capacitance decreases. The conductance of both types of cells exhibits a similar behavior. The conductance is enhanced by increasing the frequency of the input signal. Increasing the bias voltage also leads to an enhancement of the conductance, due to an increased number of charge carriers injected in the i-layer of the cell. SPICE simulations show that three first-order voltage-dependent R(V)C(V) circuits are needed to adequately describe the recharching behavior of the localized states within a-Si:H cells. For µc-Si:H cells, even more R(V)C(V) are required. AFORS-HET simulations show that the discrepancy of the capacitance found for a-Si:H and µc-Si:H measured at high frequency and high voltage is determined by the occupation of shallow states.

The transient response of both a-Si:H and µc-Si:H is strongly influenced by light soaking. For low frequencies and high voltages, µc-Si:H solar cells exhibit an increased capacitance and a-Si:H solar cells show a drop of the capacitance (in some cases to negative values) after light soaking. This effect is more pronounced for thicker cells. For all cells, light soaking results in an increased conductance in the small bias range. Only a-Si:H solar cells show an alteration of the electrical device properties in DC mode (I-V and QE measurements). Annealing the cell at 180 °C for 30 min leads to a nearly full recovery of the device performance.

Conclusions

This work has been motivated by the desire to combine plasmonics with thin-film silicon solar cell technology in order to address new light trapping concepts. We have made use of the optical properties of metal nanoparticles and metal nanostructures to improve the light absorption in thin-film silicon solar cells.

The first concept investigated in this thesis is based on the application of localized surface plasmons of small metal nanoparticles to enhance the local electromagnetic field and achieve a higher light absorption. More precisely, we have investigated the influence of metal nanoparticles of diameter smaller than 50 nm on the photocurrent of a-Si:H solar cells and a-Si:H ultra-thin photosensitive devices.

In a second approach, the ability of large metal particles (with dimensions above 50 nm) to scatter the light has been demonstrated. In order to make use of the scattering properties, large silver nanoparticles have been incorporated at the rear side of thin-film silicon solar cells. Additionally, a light trapping scheme based on a nanostructured Ag back reflector has been suggested as an alternative to the standard back reflector.

Prior to the integration of the metal structures in the solar cells, we have investigated the structural and optical properties of Ag, Au and Al films deposited by thermal evaporation on different substrates, such as a-Si:H and TCO (ZnO:Al). We have shown that Ag nanoparticles can easily be obtained on a-Si:H and TCO by thermal evaporation and by applying a subsequent annealing treatment. The average size of the Ag nanoparticles and the inter-particle distance can be controlled by varying the thickness of the deposited Ag film as well as the temperature and the duration of the thermal treatment. Small and large Ag nanoparticles with an average lateral size varied from 5 nm to 300 nm have been prepared.

On the contrary, separated Au and Al nanoparticles have only been obtained with metal films thinner than approximately 0.5-1 nm. For thicker films, a percolation continuum has been found for Au and a continuous surface has been found for Al. In all cases, a thermal treatment in vacuum at moderate temperature has shown no significant influence on the film morphology.

Ag nanoparticles with an average diameter smaller than around 35 nm deposited on glass/TCO or glass/a-Si:H system exhibit a resonant absorption, which is attributed to localized surface plasmons (LSPs). By covering the nanoparticles with a thin layer of a-Si:H, the position of the resonance is red-shifted due to the higher refractive index n of a-Si:H compared to the one of air ($n_{\text{a-Si:H}} \approx 4$, $n_{\text{air}} = 1$). By increasing the size of the formed nanoparticles from 10 nm to 30 nm, the LSP peak also moves towards longer wavelengths.

This red-shift is accompanied by an increase in both the amplitude and the line-width of the LSP peak.

Au and Al films of a few nanometers deposited on glass/TCO or glass/a-Si:H show a strong light absorption in the whole investigated wavelength range (300 nm – 2.5 μm). Covering the metal films with a thin layer of a-Si-H has no considerable effect on the optical behavior of the system. No resonant peak in the absorption spectrum can be recognized. Raman measurements, used as indicators of the existence of an enhanced electromagnetic field in the vicinity of the metal films, exhibit a higher Raman signal for layer stacks containing small Ag nanoparticles compared to layer stacks without nanoparticles. In contrast, no enhancement of the Raman intensity is found for a-Si:H-based layer stacks containing Au and Al films. This effect is attributed to the morphology of the deposited metal films. For Au and Al films thinner than 1 nm, nanoparticles with diameter down to 5 nm can be obtained. Nevertheless, also in this case no enhancement of the Raman signal has been measured in the visible range. The LSP resonance of ellipsoidal Al nanoparticles embedded in a-Si:H is expected to occur in the visible range. However, air contamination leads to the oxydation of the Al film surface (Al_2O_3) which probably results in a blue-shift of the LSP peak in the ultraviolet.

Since a resonant light absorption accompanied with an enhanced Raman signal has been found for a-Si:H-based systems containing small Ag nanoparticles, a-Si:H solar cells with an i-layer thickness of 100 nm containing small Ag nanoparticles have been prepared. Independently of the device configuration (p-i-n or n-i-p), all deposited cells with nanoparticles have shown a reduced device reflectivity in the red region of the spectrum in comparison to cells without nanoparticles, attributed to the LSP resonance of the nanoparticles. However, no improvement in the photocurrent has been measured in presence of Ag nanoparticles in the long wavelength range. Even a decrease of the quantum efficiency (QE) has been observed. Irrespective of the position of the nanoparticles within the pin layer sequence (i.e. in the i-layer, at the i-n interface or in one of the doped layers), the electrical device properties are strongly altered. This effect is ascribed to (i) charge carrier recombination at the surface of the nanoparticles, (ii) carrier recombination in defects present in the vicinity of the nanoparticles, (iii) carrier recombination in the bulk of the cells due to an alteration of the electrostatic field in the i-layer. The nanoparticles themselves may hinder the current flow. Only when the nanoparticles are incorporated at the TCO/doped-layer interface, no strong alteration of the electrical cell performances is observed. However, independently of the device configuration, also no increase in the QE has been measured in the red wavelength range for cells with Ag nanoparticles located at the n-TCO interface.

A positive contribution of the Ag nanoparticles on the photocurrent of ultra-thin photosensitive devices has been found in the case the nanoparticles are in direct contact with the i-layer. This is shown for i-p and i-n devices having an i-layer thickness of 20 nm and containing Ag nanoparticles located at the TCO-i interface. Both types of devices with

nanoparticles exhibit an increased photocurrent in the red and infrared wavelength ranges compared to devices without nanoparticles. Since a-Si:H only efficiently absorbs light of wavelengths up to 750 nm, the enhanced photocurrent found for longer wavelengths is explained by an LSP-assisted photoemission mechanism of electrons (or holes) from the nanoparticles (or from states close to the nanoparticles). A model has been proposed to illustrate the possible processes involved in the charge carrier generation mechanism. In the case the nanoparticles are covered with a thin TCO layer (≈ 7 nm), no enhancement of the photocurrent of the photosensitive device has been observed. Under these conditions the increased electromagnetic field resulting from the effect of the nanoparticles is probably confined in the TCO layer. The generated carriers resulting from the photoemission process may thus recombine directly in the nanoparticles or in the TCO layer since no efficient static electric field is provided to extract the carriers.

Large Ag nanoparticles (with diameter larger than 50 nm) deposited on glass/Ag/TCO lead to a high light scattering into large angles. Integrated at the TCO-n interface of n-i-p a-Si:H and μc-Si:H solar cells, they lead to an improved light absorption caused by the enhanced light scattering at the rear side. The increased absorption is accompanied by an improved QE in the long wavelength range. However the increase in QE does not express the strong increase in absorption. Absorption losses attributed to plasmonic losses in Ag are observed in the red and infrared wavelength regions when the nanoparticles are in direct contact with silicon. The incorporation of a thin layer of TCO (of thickness around 80 nm) between the metal nanoparticles and the silicon layers results in a shift towards shorter wavelengths of the localized surface plasmons, leading to an increase in photocurrent in the long wavelength range.
For both μc-Si:H and a-Si:H cells, reduced electrical device performances have been observed in presence of the nanoparticles. This deterioration is more pronounced for the μc-Si:H cells where a decrease of the Voc of around 30 mV has been measured in comparison to cells without nanoparticles. The disadvantage of the cells deposited on the reflector with large nanoparticles may result from an alteration of the material growth on the ellipsoidal particles.

A reflector denoted as nanostructured back reflector has been proposed as an alternative for improving the light trapping in thin-film silicon solar cells in the n-i-p configuration. Ag films of a few nanometers (from 10 nm to 50 nm) deposited on glass and subjected to an annealing treatment lead to a high light scattering. Covered with a bulk Ag film of moderate thickness (200 nm – 500 nm), the obtained nanostructured reflector shows a high reflectivity and scatters light into large angles. We have shown that the maximum of the angular intensity distribution shifts towards smaller angles as the wavelength of the incoming light increases. Incorporated at the rear side of a-Si:H and μc-Si:H solar cells, the nanostructured reflector

leads to an increased QE in the long wavelength range. Covering the nanostructured back reflector with an 80 nm thick TCO layer results in a further increase in the photocurrent. However, as observed with the large silver nanoparticles, the I-V measurements in the dark and under illumination of the cells applying the nanostructured Ag/TCO back reflector reveal a severe deterioration of the electrical device performances. This deterioration is more pronounced for the μc-Si:H cells. It is likely due to an alteration of the growth of the silicon material. Solar cells deposited on a back reflector of standard texture exhibit a slighly higher short-circuit current and FF but a significantly larger Voc.

In parallel to the study related to the integration of plasmonic structures in thin-film silicon solar cells, impedance measurements and calculations have been carried out to investigate the dynamic electrical properties of a-Si:H and μc-Si:H solar cells. The same general trend has been found for both types of cells. Only a discrepancy in the high frequency and high bias range has been observed between a-Si:H and μc-Si:H cells. The capacitance of a-Si:H converges to the geometric capacitance while the capacitance of the μc-Si:H cells converges to a higher value which increases with elevating bias voltage. SPICE simulations and AFORS simulations have been performed in order to get a deeper insight into the functioning principle of the cells. Simulations have shown that the high capacitance signal of the μc-Si:H cells for high frequencies and high bias can be explained by the release and occupation of carriers in the shallow states as function of the applied bias rather than a general difference in the behavior of both types of cells.
Light soaking has a strong effect on the dynamic response of μc-Si:H and a-Si:H cells. After light soaking, the μc-Si:H cells show an increase in both the capacitance and the conductance values which is more pronounced in the small frequency range. However, the dark I-V curves and the QE are not modified after 40 h light soaking. Defect creation in the a-Si:H phase of the μc-Si:H material may explain the results. The capacitance of a-Si:H cells drops in the low frequency range after only 2 h light soaking, due to light induced defect creation and likely due to an associated variation of the potential distribution within the i-layer of the cell. For both types of cells, an annealing treatment at 180 °C for 30 min leads to a nearly full recovery of the dynamic optoelectrical device performance.

References

[1] http://www.sharp.co.uk/page/solarproducts

Albrecht M.G., Creighton J.A. "Anomalously Intense Raman Spectra of Pyridine at a Silver Electrode", J. of the American Chemical Society, vol. 99 (1977) 5215-5219.

Ashcroft N. W., Mermin N. D., "Solid State Physics", Holt-Saunders, Tokyo (1981).

Banerjee A., Yang J., Guha S., "Optimization of high efficiency amorphous silicon alloy based triple-junction modules", Mater. Res. Soc. Symp. Proc., vol. 557 (1999) 743-748.

Beck N., Meier J., Fric J., Remes Z., Poruba A., Fluckiger R., Pohl J., Shah A., Vanecek M., "Enhanced optical absorption in microcrystalline silicon", J. of Non-Crystalline Solids, vol. 200 (1996) 903-906.

Beneking C., Rech B., Eickhoff T., Michael Y.G., Schultz N. and Wagner H., "Preparation and Light Stability of a-Si/a-Si Stacked Solar Cells". In Proceedings of the 12th EC PVSEC, Amsterdam, (1994) 683-686.

Bohren C. F., Huffman D. R., "Absorption and Scattering of light by small particles", John Wiley and Sons, Inc., New York, NY, first edition (1983).

Brammer T., Stiebig H., "Defect density and recombination lifetime in microcrystalline silicon absorbers of highly efficient thin-film solar cells determined by numerical device simulations", J. Appl. Phys., vol. 94 (2003) 1035-1042.

Campion A. and Kambhampati P., "Surface-enchanced Raman scattering", Chemical Society Reviews, vol. 27 (1998) 241-250.

Cardona M., "Light Scattering in Solids", Springer, Berlin (1982).

Carius R., Finger F., Backhausen U., Luysberg M., Hapke P., Otte M., Overhof H., "Electronic properties of microcrystalline silicon", Mat. Res. Soc. Symp. Proc., vol. 467 (1997) 283-294.

Catchpole K.R., Pillai S., "Surface plasmons for enhanced silicon light-emitting diodes and solar cells", J. of Luminescence, vol. 121 (2006) 315–318.

Chang R.K. and Furtak T.E., "Surface Enhanced Raman Scattering", Plenum Press, New York (1982).

Chapman B., “Glow Discharge Processes”, John Wiley & Sons, New York, Chichester, Brisbane, Toronto, Singapore (1980).

Chopra K.L., Major S., Pandya D.K., “Transparent Conductors - a Status Review”, Thin Solid Films, vol. 102 (1983) 1-46.

Daboo C., Baird M.J., Hughes H. P., Apsley N., Emeny M.T., “Improved surface plasmon enhanced photodetection at an Au-GaAs Schottky junction using a novel molecular beam epitaxy grown otto coupling structure”, Thin Solid Films, vol. 201 (1991) 9-27.

Del Fatti N., Vallée F., Flytzanis C., Hamanaka Y., Nakamura A., “Electron dynamics and surface plasmon resonance nonlinearities in metal nanoparticles”, Chemical Physics, vol. 251 (2000) 215-226.

Deng X. and Schiff E.A., “Amorphous Silicon-based Solar Cells”, Handbook of Photovoltaic Science and Engineering from Antonio Luque and Steven Hegedus, John Wiley & Sons, Chichester (2003) 505-565.

Derkacs D., Lim S.H., Matheu P., Mar W., Yu E.T., “Improved performance of amorphous silicon solar cells via scattering from surface plasmon polaritons in nearby metallic nanoparticles”, Applied Physics Letters, vol. 89 (2006) 093103.

Diehl F., Schröder B., Oechsner H., “Light scattering and enhanced optical absorption in hot wire microcrystalline silicon”, J. of Applied Physics, vol. 84 (1998) 3416-3418.

Dirix Y., Bastiaansen C., Caseri W., Smith P., “Oriented Pearl-necklace arrays of metallic nanoparticles in polymers : a new route toward polarization-dependent color filters”, Advanced Materials, vol. 11 (1999) 223-227.

Doyle J.R., Doughty D.A., Gallagher A., “Silane dissociation products in deposition discharges”, J. of Applied Physics, vol. 68 (1990) 4375-4384.

Drude P., “Zur Elektronentheorie der Metalle”. Annalen der Physik. 1 (1900) 566-613.

Ehrenreich H., Philipp H.R., “Optical properties of Ag and Cu”, Physical Review, vol. 128 (1962) 1622-1629.

Faraday M., Philosophical Transactions of the Royal Society, London, (1857).

Finger F., Vetterl O., Carius R., Lambertz A., Scholten C., Houben L., Luysberg M., “Microcrystalline silicon solar cells: relationship between material properties and device

performance", Proceedings of the Eleventh International School of Condensed Matter Physics, Varna, Bulgaria, (2000) 26.

Fortner J., Yu R.Q., Lannin J.S., "Near-surface Raman scattering in germanium clusters and ultrathin amorphous films", Physical Review B, vol. 42 (1990) 7610-7613.

Frey H. and Kienel G., "Dünnschichttechnologie", VDI Verlag, Düsseldorf (1987).

Gallagher A., Doyle J., Doughty D. "Plasma chemistry in silane and silane-dislane discharge deposition", Mat. Res. Soc. Symp. Proc., vol. 149 (1989) 23-31.

Genov D.A., Sarychev A.K, Shalaev V.M., "Plasmon localization and local field distribution in metal-dielectric films", Physical Review E, vol. 67 (2003) 056611.

Green M.A., "Solar Cells, Operating Principles, Technology and System Applications", Prentice-Hall, Inc, Englewood Cliffs (1982).

Green M.A., Emery K., King D.L., Hishikawa Y., Warta W., "Solar Cell Efficiency Tables (version 28)", Progress in Photovoltaics : Research and Applications, vol. 14 (2006) 455-461.

Grésillon S., Aigouy L., Boccara A.C., Rivoal J.C., Quelin X., Desmarest C., Gadenne P., Shubin V.A., Sarychev A.K., Shalaev V.M., "Experimental Observation of Localized Optical Excitations in Random Metal-Dielectric Films", Physical Review Letters, vol. 82 (1999) 4520-4523.

Grésillon S., Ducourtieux S., Lahrech A., Aigouy L., Rivoal J.C., Boccara A.C., "Nanometer scale apertureless near field microscopy", Appl. Surface Science, vol. 164 (2000) 118-120.

Gupta R., Dyer M.J., Weimer W.A., "Preparation and characterization of surface plasmon resonance tunable gold and silver films", J. of Applied Physics, vol. 92 (2002) 5264-5271.

Haase C., Stiebig H., "Optimized properties of thin-film silicon solar cells with grating couplers", Progress in Photovoltaics, vol. 14 (2006) 629-641.

Haefer R.A., "Oberflächen – und Dünnschicht – Technologie Teil 1, Beschichtungen von Oberflächen", Springer-Verlag, Berlin, Heidelberg, New York, London, Paris, Tokyo (1987).

Haes A.J., Van Duyne R.P., "A unified view of propagating and localized surface plasmon resonance biosensors", Anal. Bioanal. Chem., vol. 379 (2004) 920-930.

Handbook of Optical Constants of Solids, E.D. Palik Academic Press (1985).

Haug F.-J., Söderström T., Cubero O., Terrazzoni-Daudrix V., Ballif C., "Plasmonic absorption in textured silver back reflectors of thin film solar cells", vol. 104 (2008) 064509.

Houben L., "Plasmaabscheidung von mikrokristallinen Silizium: Merkmale der Mikrostruktur und deren Deutung im Sinne von Wachstumsvorgängen", Ph.D. thesis, Heinrich-Heine-Universität Düsseldorf (1998).

(a) Houben L., Luysberg M., Hapke P., Carius R., Finger F., Wagner H., "Structural investigations of microcrystalline silicon in the transition from highly crystalline to amorphous growth", Philosophical Magazine A, vol. 77 (1998) 1447-1460.

Hovel H., Fritz S., Hilger A., Kreibig U., Vollmer M., "Width of cluster plasmon resonances – bulk dielectric functions and chemical interface damping", Phys. Rev. B, vol. 48 (1993) 18178-18188.

Jackson W.B., Johnson N.M., Biegelsen D.K. "Density of gap states of silicon grain boundaries determined by optical absorption", Applied Physics Letters, vol. 43 (1983) 195-197.

Jackson W.B., Kelso S.M., Tsai C.C., Allen J.W., Oh S.J., "Energy dependence of the optical matrix element in hydrogenated amorphous and crystalline silicon", Phys. Rev. B, vol. 31 (1985) 5187-5198.

Jackson J. D., "Classical Electrodynamics", John Wiley & sons, Inc., New York, NY, 3rd edition (1999).

Jeanmaire D.L., van Duyne R.P, "Surface Raman spectroelectrochemistry .1. heterocyclic, aromatic, and aliphatic-amines adsorbed on anodized silver electrode", J. of Electroanalytical Chemistry, vol. 84 (1977) 1-20.

Ji X., Xu S., Wang L., Liu M., Pan K., Yuan H., Ma L., Xu W., Li J., Bai Y., Li T., "Immunoassay using the probe-labeled Au/Ag core-shell nanoparticles based on surface-enhanced Raman scattering", Colloids and Surfaces A-Physicochemical and Engineering Aspects, vol. 257-58 (2005) 171-175.

Johnson P.B., Christy R.W., "Optical-constants of noble-metals", vol. 6 (1972) 4370-4379

Kaveh M., Wiser N., "Electron electron-scattering in conducting materials", Advances In Physics, vol. 33 (1984) 257-372.

Kluth O., "Präparation und Charakterisierung von texturierten Metalloxid Schichten für Dünschichtsolarzellen", Diploma Thesis, RWTH Aachen (1996).

Kluth O., Löffel A., Wieder S., Beneking C., Appenzeller W., Houben L., Rech B., Wagner H., Hoffmann S., Waser R., Anna-Selver J.A., and Keppner H., "Texture etched Al-doped ZnO: A new material for enhanced light trapping in thin film solar cells", Proceedings of the 26th IEEE Photovoltaic Specialists Conference, Anaheim (1997) 715-718.

Kneipp K., Kneipp H., Itzkan I., Dasari R.R., Feld M.S., "Surface-enhanced Raman scattering ans biophysics", J. Phys.: Condens. Matter, vol. 14 (2002) R597-R624.

Kneipp K., Wang Y., Kneipp H., Perelman L.T., Itzkan I., Dasari R.R., Feld M.S., "Single molecule detection using surface-enhanced Raman scattering (SERS)". Physical Review Letters, vol. 78 (1997) 1667-1670.

Kobliska R. and Solin S., "Raman spectrum of wurtzite silicon", Physical Review B, vol. 8 (1973) 3799-3802.

Kreibig U. and Vollmer M., "Optical properties of metal clusters", Springer, Berlin (1995).

Kubon M., Böhmer E., Siebke F., Rech B., Beneking C., Wagner H., "Solution of the ZnO/p Contact Problem in a-Si:H based Solar Cells", Solar Energy Materials, vol. 41-2 (1996) 485-492.

Lee P.C. and Meisel D., "Adsorption and surface-enhanced Raman of dyes on silver and gold sols", J. Physical Chemistry, vol. 86 (1982) 3391-3395.

Li H., "Single and multijunction silicon based thin film solar cells on flexible substrates with absorber layers made by hot-wire CVD", PhD work in Utrecht University (1997).

Liu Z., Wang H., Li H., Wang X., "Red shift of plasmon resonance frequency due to the interacting Ag nanoparticles embedded in single crystal SiO2 by implantation", Applied Physics Letters, vol. 72 (1998) 1823-1825.

Logan N.A., "Survey of Some Early Studies of the Scattering of Plane Waves by a Sphere", Proc. IEEE., vol. 53 (1965) 773-785.

Lombardi J.R., Birke R.L., Lu T., Xu J., "Charge-transfer theory of surface enhanced Raman spectroscopy: Herzberg-Teller contributions", J. of Chemical Physics, vol. 84 (1986) 4174-4180.

Long D.A., "Raman spectroscopy", McGrow-Hill International Book Company, New York (1977).

Luysberg M., Hapke P., Carius R., Finger F., "Structure and growth of microcrystalline silicon: Investigation by TEM and Raman spectroscopy of films grown at different plasma excitation frequencies", Philosophical Magazine A, vol. 75 (1997) 31-47.

Maier S.A., "Plasmonics : Fundamentals and applications", Springer US (2007).

Meier J., Keppner H., Dubail S., Droll U., Torres P., Pernet P., Ziegler Y., Selvan J., Cuperus J., Fischer D., Shah A., Mater. Res. Soc. Symp. Proc., vol. 507 (1998) 139-144.

Mertens H., Verhoeven J., Polman A., Tichelaar F.D., "Infrared surface plasmons in two-dimensional silver nanoparticle arrays in silicon", Applied Physics Letters, vol. 85 (2004) 1317-1319.

Mie G., "Beiträge zur Optik trüber Medien, speziell kolloidaler Metallösungen", Ann. Phys., vol. 25 (1908) 377-452.

Moskovits M., "Surface-enhanced Raman spectroscopy: a brief retrospective", J. of Raman spectroscopy, vol. 36 (2005) 485-496.

Moskovits M., "Surface-Enhanced Raman Spectroscopy: a Brief Perspective". Surface-Enhanced Raman Scattering: Physics and Applications, vol. 103 (2006) 1-17.

Mott N.F., Davis E.A., "Electronic Processes in Non-Crystalline Materials", Clarendon Press (1979).

Nemanich R.J., Tsai C.C., Connell G.A.N., "Interference-Enhanced Raman scattering of Very Thin Titanium and Titanium Oxide films", Physical Review Letters, vol. 44 (1980) 273-276.

Nie S. and Emory S. R., "Probing Single Molecules and Single Nanoparticles by Surface-Enhanced Raman Scattering", vol. 275 (1997) 1102-1106.

Overhof H., "Fundamental concepts in the physics of amorphous semiconductors", J. of Non-Cryst. Solids, vol. 227-230 (1998) 15-22.

Perrin J. "Plasma and surface reactions during a-Si:H film growth", J. of Non-Crystalline Solids 137-138 (1991) 639-644.

Persson B.N., "Polarizability of small spherical metal particles – influence of the matrix environment", Surface Science, vol. 281 (1993) 153-162.

Pillai S., Catchpole K.R., Trupke T., Zhang G., Zhao J., Green M.A., "Enhanced emission from Si-based light-emitting diodes using surface plasmons", Applied Physics Letters, vol. 88 (2006) 161102.

Pillai S., Catchpole K.R., Trupke T., Green M.A., "Surface plasmon enhanced silicon solar cells", Applied Physics Letters, vol. 101 (2007) 093105.

Pinchuk A., Kreibig U., Hilger A., "Optical properties of metallic nanoparticles: influence of interface effects and interband transitions", Surface Science, vol. 557 (2004) 269-280.

Pulker H.K., "Coatings on glass", Elsevier, Amsterdam, Oxford, New York, Tokyo (1984).

Rand B.P., Peumans P. and Forrest S.R., "Long-range absorption enhancement in organic tandem thin-film solar cells containing silver nanoclusters", J. Appl. Phys., vol. 96 (2004) 7519-7526.

Rech B. and Wagner H., "Potential of Amorphous Silicon for Solar Cells", Applied Physics A, vol. 69 (1999) 155-167.

Richter H., Wang Z.P., Ley L., "The one phonon Raman spectrum in microcrystalline silicon", Solid State Communications, vol. 39 (1981) 625-629.

Sainju D., van den Oever P.J., Podraza N.J., Syed M., Stoke J.A., Jie Chen, Xiesen Yang, Xunming Deng and Collins R.W., "Origin of optical losses in Ag/ZnO back-reflectors for thin film Si photovoltaics", 4th World Conference on Photovoltaic Energy (WCPEC), vol. 1-2 (2006) 1732-1735.

Sakai H. and Ichikawa Y., "Process Technology for a-Si/a-Si Double Stacked Tandem Solar Cells with Stabilized 10-percent Efficiency", J. of non-Crystalline Solids, vol. 137 (1991) 1155-1160.

Sauvain A., Shah A., Hubin J., "Measurement of ambipolar mobility-lifetime product and its significance for amorphous silicon solar cells", Proceedings of the 21st IEEE Photovoltaic Specialist Conference, Orlando, vol. 2 (1990) 1560-1563.

Schaadt D. M., Feng B., Yu E. T., "Enhanced semiconductor optical absorption via surface plasmon excitation in metal nanoparticles", Applied Physics Letters, vol. 86 (2005) 063106.

Schultz N., "Präparation und Charakterisierung transparenter Metalloxid-Schichten für Solarzellen aus amorphem Silizium", Diploma thesis, RWTH Aachen (1994).

Shah A., Torres P., Tscharner R., Wyrsch N., Keppner H., "Photovoltaic technology: The case for thin-film solar cells", Science, vol. 285 (1999) 692-698.

Smith J.B. and Ehrenreich H., "Frequency-dependence of the optical relaxation-time in metals", Physical Review B, vol. 25 (1982) 923-930.

Smith E. and Dent G., "Modern Raman Spectroscopy: A Practical Approach", John Wiley and Sons (2005).

Sönnichsen C., Geier S., Hecker N.E., von Plessen G., Feldmann J., Ditlbacher H., Lamprecht B., Krenn J.R., Aussenegg F.R., Chan V. Z-H., Spatz J.P., Moeller M., "Spectroscopy of single metallic nanoparticles using total internal reflection Microscopy", Applied Physics Letters, vol. 77 (2000) 2949-2951.

Sönnichsen C., "Plasmons in metal nanostructures", PhD thesis (2001).

Sönnichsen C., Franzl T., Wilk T., von Plessen G. and Feldmann J., "Plasmon resonances in large noble-metal clusters", New J. of Physics, vol. 4 (2002) 93.1-93.8.

Springer J., Poruba A., Müllerova L., Vanecek M., Kluth O., Rech B., "Absorption loss at nanorough silver back reflector of thin-film silicon solar cells", J. Applied Physics, vol. 95 (2004) 1427-1429.

Springer J., Rech B., Reetz W., Müller J., Vanecek M., "Light trapping and optical losses in microcrystalline silicon pin solar cells deposited on surface-textured glass/ZnO substrates", Solar Energy Materials and Solar Cells, vol. 85 (2005) 1-11.
Staebler D.L. and Wronski C.R., "Reversible conductivity changes in discharge-produced amorphous Si", Appl. Phys. Lett., vol. 31 (1977) 292-294.

Stangl R., Kriegel M., Maydell K.v., Schmidt M., Fuhs W., Proc. 31. IEEE Photovoltaic Specialists Conference and Exhibition, Lake Buena Vista, Florida, USA, 2005.

Stenzel O., Stendal A., Voigtsberger K., von Borczyskowski C., "Enhancement of the photovoltaic conversion efficiency of copper phthalocyanine thin film devices by incorporation of metal clusters", Solar Energy Materials and Solar Cells, vol. 37 (1995) 337-348.

Stiebig H., Kreisel A., Winz K., Schultz N., Beneking C., Eickhoff Th., Wagner H., Meer M., "Spectral response modelling of a-Si:H solar cells using accurate light absorption profiles", Proc. First World Conference on Photovoltaic Energy Conversion (WCPEC), (1994) 603-606.

Stiebig H., Nosan U., Krause M., Jankovec M., Topic M., "Dynamic properties of ultraviolet sensitive detectors", J. Non-Cryst. Solids, vol. 1295 (2002) 299–302.

Stiebig H.(a), Schulte M., Zahren C., Haase C., Rech B., Lechner P., "Light trapping in thin-film silicon solar cells by nano-textured interfaces – art. No. 619701", Photonics Europe 2006 : Optoelectronics and Photonic Materials, SPIE, vol. 6197 (2006) 19701-19701.

Stiebig H.(b), Haase C., Zahren C., Rech B., Senoussaoui N., "Thin-film silicon solar cells with grating couplers – An experimental and numerical study", J. non-cryst. Solids, vol. 352 (2006) 1949-1952.

Stuart H.R., Hall D.G., "Island size effects in nanoparticle-enhanced photodetectors", Applied Physics Letters, vol. 73, (1998) 3815-3817.

Stutzmann M., "Weak bond-dangling bond conversion in amorphous silicon", Phil. Mag. B, vol. 56 (1987) 63-70.

Sukmanowski J., Paulick C., Sohr O., Andert K., Royer F.X., "Light absorption enhancement in thin silicon layers", J. Applied Physics, vol. 88 (2000) 2484-2489.

Tzolov M., Finger F., Carius R., Hapke P., "Optical and transport studies on thin microcrystalline silicon films prepared by very high frequency glow discharge for solar cells applications", Journal of Applied Physics, vol. 81 (1997) 7376-7385.

Tzolov M., Tzenov N., Dimova-Malinovska D., Kalitzova M., Pizzuto C., Vitali G., Zollo G., Ivanov I., "Vibrational properties and structure of undoped and Al-doped ZnO films deposited by RF magnetron sputtering", Thin Solid Films, vol. 379 (2000) 28-36.

Van Dijk M.A., Tchebotareva A. L., Orrit M., Lippitz M., Berciaud S., Lasne D., Cognet L., Lounis B., "Absorption and scattering microscopy of single metal nanoparticles", Physical Chemistry Chemical Physics, vol. 8 (2006) 3486-3495.

Vepřek S., Sarott F.A., Rambert S., Taglauer E., "Surface hydrogen content and passivation of silicon deposited by plasma induced chemical vapor deposition from silan and the implications for the reaction mechanism", J. of Vacuum Science & Technology A7, (1989) 2614-2624.

Vetterl O., Finger F., Carius R., Hapke P., Houben L., Kluth O., Lambertz A., Mück A., Rech B., Wagner H., "Intrinsic microcrystalline silicon: A new material for photovoltaics", Solar Energy Materials & Solar Cells, vol. 62 (2000) 97-108.

Vlckova B., Pavel I., Sladkova M., Siskova K., Slouf M., "Single molecule SERS: Perspectives of analytical applications", J. of Molecular Structure, vol. 834 (2007) 42-47.

Voisin C., Christofilos D., Del Fatti N., Vallée F., Prével B., Cottancin E., Lermé J., Pellarin M., Broyer M., "Size-dependent electron-electron interactions in metal nanoparticles", Phys. Rev. Lett., vol. 85 (2000) 2200-2203.

Vossen J.C, "Transparent Conducting Films", Physics of Thin films, vol. 9 (1977) 1-71.

Wen C., Ishikawa K., Kishima M., Yamada K., "Effects of silver particles on the photovoltaic properties of dye-sensitized TiO2 thin films", Solar Energy Materials and Solar Cells, vol. 61, (2000) 339-351.

Werner J., Peisl M., "Exponential band tails at silicon grain boundaries", Mat. Res. Soc. Symp. Proc., vol. 46 (1985) 575-580.

Westphalen M., Kreibig U., Rostalski J., Lüth H., Meissner D., "Metal cluster enhanced organic solar cells", Solar Energy Materials & Solar Cells, vol. 61 (2000) 97-105.

Wieder S., "Amorphous Silicon Solar Cells, Comparison of p-i-n and n-i-p Structures with Zinc-Oxide Frontcontact", Ph.D thesis, RWTH Aachen (1999).

Wiederrecht G.P., "Near-field optical imaging of noble metal nanoparticles", Eur. Phys. J. Appl. Phys., vol. 20 (2004) 3-18.

Willemen J.A., "Modelling of Amorphous Silicon Single- and Multi-Junction Solar Cells", Ph.D thesis, Delft University of Technology (1998).

Winz K., Rech B., Eickhoff T., Beneking C., Fortmann C.M., Hapke P., Wagner H., "Optoelectronic properties of Thin Amorphous and Microcrystalline p-Type Silicon Based Films Developped for Amorphous Silicon-Based Solar Cells", Mat. Res. Soc. Symp. Proc., vol. 420 (1996) 819-824.

Yang J., Banerjee A., Guha S., "Triple-junction amorphous silicon alloy solar cell with 14.6% initial and 13.0% stable conversion efficiencies", Appl. Phys. Lett., vol. 70 (1997) 2975-2977.

Yoshida S., Yoshino M., Kitahara S., Seki K., Katayama S., Nabeshima K., Nozue K., Yamada A., Konagai M., "Improvement of a-Si/a-Si double junction solar cells by utilizing the ZnO/Ag rear contact", 11th E.C. Photovoltaic Solar Energy Conference, (1992) 590-593.

Zaremba E., Persson B.N., "Dynamic polarizability of small metal particles", Phys. Rev. B, vol. 35 (1987) 596-606.